Departamento de Química Física
y Termodinámica Aplicada
Universidad de Córdoba

SÍNTESIS Y CARACTERIZACIÓN DE PEROVSKITAS HÍBRIDAS Y SU IMPLEMENTACIÓN EN CÉLULAS SOLARES

SYNTHESIS AND CHARACTERIZATION OF HYBRID PEROVSKITES AND THEIR IMPLEMENTATION IN SOLAR CELLS

Química Fina

Directores
Gustavo de Miguel Rojas
Luis Camacho Delgado

Tesis Doctoral
Alexander Zachary Davis Jodlowski

Córdoba, Julio 2018

TITULO: *SÍNTESIS Y CARACTERIZACIÓN DE PEROVSKITAS HÍBRIDAS Y SU IMPLEMENTACIÓN EN CÉLULAS SOLARES*

AUTOR: *Alexander Zachary Davis Jodlowski*

© Edita: UCOPress. 2018
Campus de Rabanales
Ctra. Nacional IV, Km. 396 A
14071 Córdoba

https://www.uco.es/ucopress/index.php/es/
ucopress@uco.es

TÍTULO DE LA TESIS: SÍNTESIS Y CARACTERIZACIÓN DE PEROVSKITAS HÍBRIDAS Y SU IMPLEMENTACIÓN EN CÉLULAS SOLARES.

DOCTORANDO/A: ALEXANDER ZACHARY DAVIS JODLOWSKI

INFORME RAZONADO DEL/DE LOS DIRECTOR/ES DE LA TESIS

(se hará mención a la evolución y desarrollo de la tesis, así como a trabajos y publicaciones derivados de la misma).

D. Luis Camacho Delgado y D. Gustavo de Miguel Rojas, Catedrático y Contratado Ramón y Cajal del Departamento de Química Física y Termodinámica Aplicada de la Universidad de Córdoba, respectivamente, informan que la presente Tesis Doctoral se ha desarrollado en los laboratorios del Departamento de Química Física y Termodinámica Aplicada de la Universidad de Córdoba bajo nuestra dirección. Esta Tesis Doctoral reúne todas las condiciones exigidas según la legislación vigente. Su evolución y desarrollo ha seguido el plan de trabajo inicialmente previsto, alcanzándose los objetivos previamente marcados, como son la síntesis mecanoquímica de perovskitas y la sustitución parcial del catión metilamonio, normalmente usado en fotovoltaica, por el catión guanidinio. Durante la elaboración de la Tesis, el doctorando ha realizado una labor altamente satisfactoria dentro del grupo de investigación. Los resultados de la investigación han sido publicados en 6 artículos, 4 de ellos directamente relacionados con el plan de trabajo de la tesis en las siguientes revistas científicas: *Nature Energy*, *Angewandte Chemie International Edition*, *Advanced Energy Materials y Nano Energy.* El doctorando ha realizado una estancia de 7 meses en los laboratorios del Grupo del Prof. M. K. Nazeeruddin en EPFL (Suiza), donde ha conseguido preparar y caracterizar células solares de hasta 20% de eficiencia.

Por todo ello, se autoriza la presentación de la tesis doctoral.

Córdoba, 18 de julio de 2018

Firma del/de los director/es

Fdo.: Luis Camacho Delgado

Fdo.: Gustavo de Miguel Rojas

SÍNTESIS Y CARACTERIZACIÓN DE PEROVSKITAS HÍBRIDAS Y SU IMPLEMENTACIÓN EN CÉLULAS SOLARES.

LOS DIRECTORES,

Fdo.: Luis Camacho Delgado
Catedrático del Departamento de Química Física y Termodinámica Aplicada de la Universidad de Córdoba

Fdo.: Gustavo de Miguel Rojas
Personal Contratado dentro del Programa Ramón y Cajal

Trabajo presentado para optar al grado de Doctor en Ciencias Químicas

Fdo.: Alexander Zachary Davis Jodlowski
Licenciado en Ciencias Químicas

DEPARTAMENTO DE QUÍMICA FÍSICA
Y TERMODINÁMICA APLICADA
UNIVERSIDAD DE CÓRDOBA

D.ª María Teresa Pineda Rodríguez, Catedrática y Directora del Departamento de Química Física y Termodinámica Aplicada de la Universidad de Córdoba,

INFORMA:

Que el trabajo presentado como Tesis Doctoral por D. Alexander Zachary Davis Jodlowski, titulado "*Síntesis y Caracterización de Perovskitas Hibridas y su Implementación en Células Solares*", ha sido realizado en los laboratorios de este Departamento, así como en las instalaciones del École Polytechnique Fédérale de Lausanne (Sion, Suiza) y reúne las condiciones exigidas según legislación vigente.

Y para que conste, firmo el presente en Córdoba a nueve de julio de dos mil dieciocho.

Fdo. : María Teresa Pineda Rodríguez

Mediante la defensa de esta Tesis se pretende optar a la obtención de "Tesis con mención internacional" habida cuenta que el doctorando reúne los requisitos exigidos para tal mención:

1. Se cuenta con los informes favorables de dos doctores pertenecientes a instituciones de Enseñanza Superior de países europeos distintos al nuestro.
2. En el Tribunal que ha de evaluar la tesis existe un miembro de un centro de Enseñanza Superior de otro país europeo.
3. Parte de la defensa de la Memoria se realizará en la lengua oficial de otro país europeo.
4. El doctorando ha realizado una parte del trabajo experimental en las instalaciones de ÉCOLE POLYTECHNIQUE FÉDÉRALE DE LAUSANNE (Sion, Suiza) en el grupo de "Molecular Engineering of Functional Materials" (GMF). Esta estancia, de siete meses de duración en total, se ha realizado gracias a la concesión de ayudas de la COST-ACTION STSM-MP1307 y la beca de movilidad internacional "DOCTORADO HACIA LA EXCELECNIA" de la Universidad de Córdoba.

LUIS CAMACHO DELGADO, Catedrático del Departamento de Química Física y Termodinámica Aplicada de la Universidad de Córdoba,

INFORMA:

Que el trabajo presentado como Tesis Doctoral por D. Alexander Zachary Davis Jodlowski, titulado “Síntesis y Caracterización de Perovskitas Híbridas y su Implementación en Células Solares”, ha sido realizado bajo mi dirección en los laboratorios de este Departamento y reúne las condiciones exigidas según la legislación vigente.

Y para que conste, firmo el presente en

Córdoba, a diecinueve de Julio de 2018

Firma del/de los director/es

Fdo.:_Luis Camacho Delgado

GUSTAVO DE MIGUEL ROJAS, Personal Contratado dentro del Programa Ramón y Cajal del Departamento de Química Física y Termodinámica Aplicada de la Universidad de Córdoba,

INFORMA:

Que el trabajo presentado como Tesis Doctoral por D. Alexander Zachary Davis Jodlowski, titulado “Síntesis y Caracterización de Perovskitas Híbridas y su Implementación en Células Solares”, ha sido realizado bajo mi dirección en los laboratorios de este Departamento y reúne las condiciones exigidas según la legislación vigente.

Y para que conste, firmo el presente en

Córdoba, a diecinueve de Julio de 2018

Firma del/de los director/es

Fdo.:_Gustavo de Miguel Rojas

TÍTULO DE LA TESIS: SÍNTESIS Y CARACTERIZACIÓN DE PEROVSKITAS HÍBRIDAS Y SU IMPLEMENTACIÓN EN CÉLULAS SOLARES.

DOCTORANDO/A: ALEXANDER ZACHARY DAVIS JODLOWSKI

INFORME RAZONADO DEL/DE LOS DIRECTOR/ES DE LA TESIS

(se hará mención a la evolución y desarrollo de la tesis, así como a trabajos y publicaciones derivados de la misma).

D. Luis Camacho Delgado y D. Gustavo de Miguel Rojas, Catedrático y Contratado Ramón y Cajal del Departamento de Química Física y Termodinámica Aplicada de la Universidad de Córdoba, respectivamente, informan que la presente Tesis Doctoral se ha desarrollado en los laboratorios del Departamento de Química Física y Termodinámica Aplicada de la Universidad de Córdoba bajo nuestra dirección. Esta Tesis Doctoral reúne todas las condiciones exigidas según la legislación vigente. Su evolución y desarrollo ha seguido el plan de trabajo inicialmente previsto, alcanzándose los objetivos previamente marcados, como son la síntesis mecanoquímica de perovskitas y la sustitución parcial del catión metilamonio, normalmente usado en fotovoltaica, por el catión guanidinio. Durante la elaboración de la Tesis, el doctorando ha realizado una labor altamente satisfactoria dentro del grupo de investigación. Los resultados de la investigación han sido publicados en 6 artículos, 4 de ellos directamente relacionados con el plan de trabajo de la tesis en las siguientes revistas científicas: *Nature Energy*, *Angewandte Chemie International Edition*, *Advanced Energy Materials y Nano Energy.* El doctorando ha realizado una estancia de 7 meses en los laboratorios del Grupo del Prof. M. K. Nazeeruddin en EPFL (Suiza), donde ha conseguido preparar y caracterizar células solares de hasta 20% de eficiencia.

Por todo ello, se autoriza la presentación de la tesis doctoral.

Córdoba, 18 de julio de 2018

Firma del/de los director/es

Fdo.: Luis Camacho Delgado

Fdo.: Gustavo de Miguel Rojas

En primer lugar, agradecer a mis Abuelos, Maciej Jodlowski y Juana Torrens, que sin vuestro sacrificio y esfuerzo nunca hubiera llegado a donde estoy.

A mi familia que me ha apoyado en todo momento y me ha dado fuerzas.

A mis directores, D. Gustavo de Miguel Rojas y D. Luis Camacho Delgado, que me han guiado en el desarrollo de esta Tesis. Mi eterno agradecimiento por vuestra paciencia, esfuerzo, apoyo y por introducirme en el complicado pero maravilloso mundo de la investigación.

Gracias a mi grupo FQM204 por apoyarme en todo momento y crear un ambiente de trabajo y de amistad que en pocos lugares se puede ver, nunca los olvidare.

Agradecer a Marta Rosel Pérez Morales, quien fue la primera persona que me introdujo en el mundillo de la investigación cuando estaba en la carrera.

A los amigos que me han apoyado y soportado durante todo este tiempo, y en especial a mi fiel amigo Ramón, gracias por estar siempre ahí.

Por último, pero no menos importante a Cristina Roldán Carmona quien me guío y ayudó en todo momento en mi estancia en Suiza

Special thanks should be given to Prof. Mohammad Khaja Nazeeruddin, for offering me the opportunity to work with him at the École Polytechnique Fédérale de Lausanne (Sion, Switzerland). I am also deeply grateful to his working group for their kindness and help during my stay in Sion. Prof. M. K. Nazeeruddin is a great scientist and an exceptional person. Thanks for the important values you transmitted to me.

A mi familia.

Índice

Objetivos

Aim

Objetivos

- Sintetizar perovskitas en fase solida utilizando métodos mecánicos para su obtención.
- Estudio estructural en función de la temperatura de las distintas fases de las perovskitas hibridas usando como catión orgánico el formamidinio, guanidinio y metilamonio.
- Realizar la síntesis de una perovskita hibrida sustituyendo parcialmente el catión metilamonio usado habitualmente por el guanidinio y llevar a cabo su caracterización estructural.
- Estudio de cómo influye la mezcla de cationes orgánicos en la estructura de perovskitas híbridas y su impacto en el rendimiento y estabilidad de una célula solar bajo iluminación constante.
- Estudio bibliográfico acerca de perovskitas alternativas donde se sustituye el plomo por otro elemento con el fin de eliminar el problema de la toxicidad. También se ha investigado el uso de cationes orgánicos alternativos, nuevas composiciones en perovskitas inorgánicas además de nuevos tipos de estructuras intermedias quasi-2D como las Ruddlesden-Popper.

Resumen

Summary

Resumen

En la presente Tesis, se ha estudiado la síntesis, caracterización y estabilidad de perovskitas hibridas orgánico – inorgánicas utilizando el catión plomo (Pb^{2+}) para la red inorgánica y usando distintos tipos de cationes orgánicos (guanidinio, metilamonio y formamidinio). Además, se fabricaron células solares utilizando como material activo estas perovskitas y se estudió su rendimiento fotovoltaico y estabilidad frente a condiciones ambientales en condiciones operativas. Por último, se ha realizado un trabajo bibliográfico sobre perovskitas alternativas a las tradicionales que actualmente se emplean para células solares.

La organización de los resultados experimentales se ha realizado conforme a la modalidad de compendio de artículos de la Universidad de Córdoba, según la cual, la Tesis doctoral estará constituida por las copias completas de los artículos científicos publicados o aceptados por el Doctorando. Además, se incluyen los objetivos, resumen, introducción y conclusiones.

La introducción que consta del *Capítulo I* toca aspectos básicos que han sido tratados en los artículos. Así la introducción queda dividida en 5 bloques. En el primer bloque, se hace un breve repaso sobre la energía solar y su impacto en la actualidad y las diferentes tecnologías empleadas en fotovoltaica. En el segundo bloque, se habla de las estructuras cristalinas básicas de las perovskitas y sus distintas dimensionalidades. En el tercer bloque, se abordan las propiedades y composiciones de las distintas perovskitas con aplicación en células solares. Para el cuarto bloque, se habla de los distintos métodos de síntesis y deposición en capa fina. Por último, en el quinto apartado se mencionan las distintas arquitecturas de las células solares y se describe el funcionamiento de estas.

El *Capítulo II*, denominado Experimental, describe los diferentes métodos y técnicas más utilizadas durante esta Tesis junto con un pequeño marco teórico en cada apartado.

El *Capítulo III* está compuesto por tres artículos científicos donde se muestran los resultados obtenidos de esta Tesis.

- *Memoria 1.- "Benign-by-Design Solventless Mechanochemical Synthesis of Three-, Two-, and One-Dimensional Hybrid Perovskites"*

En esta memoria se propone la mecano-síntesis como método alternativo a la preparación de perovskitas hibridas orgánico – inorgánicas. En este método no se utilizan disolventes orgánicos (DMSO, DMF) como en los métodos tradicionales de síntesis de perovskita, por esta razón se considera un método más benigno con el medio ambiente ya que no genera residuos orgánicos en el proceso de síntesis. Además, este proceso es rápido, simple y reproducible, con el añadido de poder obtenerse gran cantidad de material en polvo policristalino con alta pureza, el cual facilita considerablemente el proceso de caracterización.

Para demostrar la validez de este método propuesto se sintetizaron cuatro perovskitas distintas, $MAPbI_3$, $FAPbI_3$, $GuaPbI_3$, Gua_2PbI_4 (MA, FA y Gua son metilamonio, formamidinio y guanidinio, respectivamente) y se caracterizaron mediante difracción de rayos X, espectroscopia de absorción UV-vis, espectroscopia de fotoelectrones de rayos X (XPS) y microscopia de barrido electrónico (SEM).

De las cuatro perovskitas descritas, tres de ellas ya habían sido sintetizadas y caracterizadas previamente, pero en este trabajo se sintetizó y caracterizó por primera vez una perovskita basada en guanidinio ($GuaPbI_3$) con una estructura cuasi-1D en forma de cadena. Este resultado es significativo en

el campo de las perovskita porque introduce un nuevo método para sintetizar nuevos materiales de este tipo.

- *Memoria 2.- "Large guanidinium cation mixed with methylammonium in lead iodide perovskites for 19% efficient solar cells"*

Las perovskitas con estructura tridimensional (*Capitulo 1*) presentan las mejores propiedades optoelectrónicas para su implementación en células solares pero poseen una baja estabilidad a la humedad y al oxígeno. Por esta razón se ha propuesto el uso del guanidinio en mezcla con metilamonio para formar una perovskita hibrida multi-catión orgánico y se ha verificado la inserción del guanidinio dentro de la red cristalina mediante difracción de rayos X utilizando el método de Williamson - Hall (*Capítulo I*). Además, se ha demostrado el incremento en la eficiencia de las células solares utilizando esta mezcla de cationes y un aumento en la estabilidad en un test de estrés bajo iluminación constante (*Capítulo III*).

- *Memoria 3.- "Alternative Perovskites for Photovoltaics"*

En la Memoria 3, se presentan los enfoques más recientes realizados para explorar e implementar materiales de perovskitas alternativos e innovadores en células solares. Se busca superar las principales limitaciones que tienen las perovskitas convencionales, incluida la estabilidad y la toxicidad. En esta revisión bibliográfica se recopilan estudios como la sustitución del Pb^{2+} por elementos del grupo 14 como el germanio eliminando el problema de la toxicidad. Además, se muestran diferentes estudios utilizando diferentes cationes como el etilamonio, rubidio, guanidinio así como perovskitas con diferentes dimensionalidades según su estequiometria y sobre todo la familia de perovskitas quasi-2D Ruddlesden – Popper entre otras.

Summary

In this thesis, a study of the organic - inorganic hybrid perovskites using the lead cation (Pb^{2+}) as the inorganic network and different organic cations (guanidinium, methylammonium and formamidinium) has been performed. In addition, solar cells were manufactured using these perovskites as the active material to study their photovoltaic performance and environmental stability under operating conditions. Lastly, a bibliographic work about alternative perovskites used for solar cells applications has been realized. The organization of the experimental results has been carried out according to the modality of compendium of articles of the University of Córdoba. The complete copies of the scientific articles published or accepted authored by the PhD student will constitute the doctoral thesis. In addition, the objectives, summary, introduction, and conclusions have been included.

The introduction is divided into 5 blocks. In the first block, a brief review of the solar energy and its impact to the energy sector is discussed together with the different technologies used in photovoltaic. In the second block, the different crystalline structures of the perovskites and their different dimensionalities are revised. In the third block, the properties and compositions of the different perovskites and their application in solar cells are summarized. In the fourth block, the different methods of synthesis and deposition as thin film are described. Finally, in the fifth section, it is mentioned the different architectures and operation conditions of the solar cells.

Chapter II, called Experimental, describes different methods and techniques used during this Thesis.

The *Chapter III* is composed of three scientific articles where the results obtained from this Thesis are shown.

o *Article 1*.- "Benign-by-Design Solventless Mechanochemical Synthesis of Three-, Two-, and One-Dimensional Hybrid Perovskites"

In this article, the mechano-synthesis is proposed as an alternative method to the preparation of organic-inorganic hybrid perovskites. This method does not use organic solvents (DMSO, DMF) as in traditional perovskite synthesis methods, and therefore it was considered a more benign method to the environment. In addition, this process is fast, simple and reproducible, and capable of obtaining a large amount of polycrystalline powder material with high purity, which considerably facilitates the characterization process.
To demonstrate this method, four different perovskites were synthesized, $MAPbI_3$, $FAPbI_3$, $GuaPbI_3$, Gua_2PbI_4 (MA, FA and Gua are methylammonium, formamidinium and guanidinium, respectively) and were characterized by X-ray diffraction, UV-vis absorption spectroscopy, X-ray photoelectron spectroscopy (XPS) and scanning electron microscopy (SEM). Three of these perovskites had been previously synthesized and characterized, but in this work, a guanidinium-based perovskite ($GuaPbI_3$) with a quasi-1D chain structure was synthesized and characterized for the first time. This result is significant in the field of perovskite because it introduces a new method to synthesize new perovskite materials.

o *Article 2*.- “Large guanidinium cation mixed with methylammonium in lead iodide perovskites for 19% efficient solar cells”

The perovskites with three-dimensional structures (Chapter 1) present the best optoelectronic properties to be implemented in solar cells but they possess low stability to moisture and oxygen. Thus, the use of guanidinium in mixture with methylammonium was proposed to form an organic multi-cation hybrid perovskite and the insertion of guanidinium within the crystalline network was verified by X-ray diffraction using the Williamson-Hall method (Chapter I). In addition, the increase in the efficiency of the solar cells has been demonstrated using this mixture of cations and an increase of stability in a stress test under constant illumination has been detected (Chapter III).

o Article 3.- "Alternative Perovskites for Photovoltaics"

The article 3 is a review of the most recent approaches undertaken to explore and implement alternative and innovative perovskite materials in solar cells. These alternatives focus on the overcoming the main limitations of conventional perovskites, including stability and toxicity. In this review, different studies are reported including the substitution of Pb^{2+} for elements of group 14 such as germanium, removing the problem of toxicity and studies of different cations (methylammonium, rubidium, guanidinium, etc.) to synthesize 2D and quasi-2D perovskites (Ruddlesden-Popper)

Capítulo I

Introducción

Chapter I

Introduction

La energía solar, su impacto en la actualidad y las diferentes tecnologías fotovoltaicas

La búsqueda de nuevas fuentes de energía y la contaminación medioambiental son uno de los principales retos a los que se enfrenta la humanidad en el siglo XXI. El constante aumento de la población mundial y el uso excesivo de fuentes de energía no renovables (carbón, petróleo, gas natural y energía nuclear) han originado que la búsqueda de fuentes de energías renovables y accesibles para la población sea una prioridad en la actualidad. Teniendo estos factores en cuenta, la energía solar es un importante candidato para remplazar a las fuentes de energías no renovables. Una clara prueba de ello es la evolución exponencial de la potencia solar instalada a nivel mundial (Figura 1).

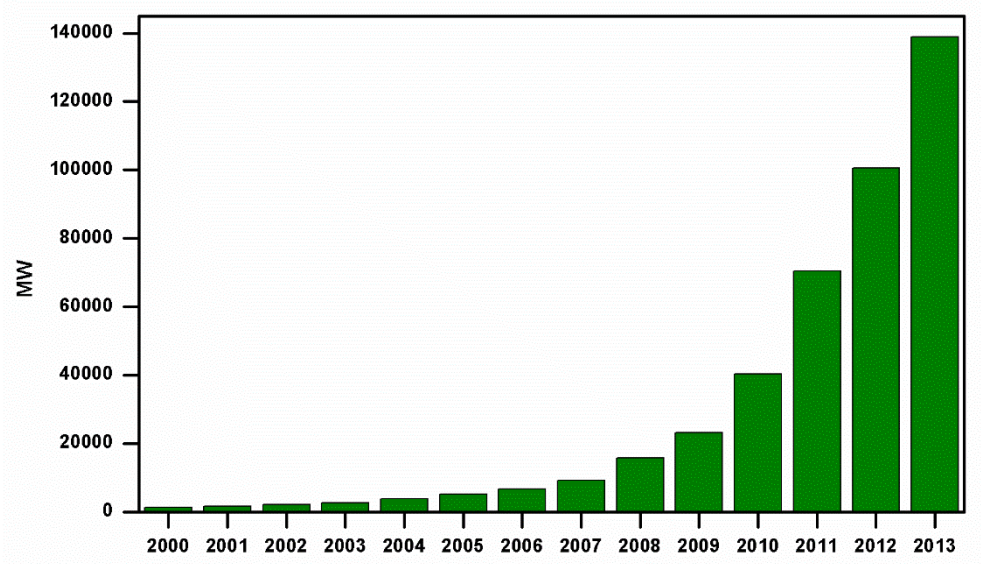

Figura 1. Evolución de la potencia fotovoltaica acumulada 2000-2013 (European Photovoltaic Industry Association)

Las principales ventajas a destacar de esta fuente de energía son:

- La energía solar es abundante, en comparación con el carbón, el petróleo, el gas natural, etc.

- La energía del sol es gratis. A diferencia del petróleo, el gas natural y otras fuentes de energías no renovables el uso de la luz del sol es gratuito.

- La energía solar es limpia. Aunque la conversión de energía solar a energía eléctrica por medio de paneles solares se considera limpia, hay que considerar que la producción de los paneles solares si produce emisiones de CO_2, pero en menor medida que los combustibles fósiles.

- Es beneficioso para los pobres. Este tipo de fuente de energía alternativa reduce la dependencia de los monopolios que controlan las fuentes de energía y tiende a beneficiar a las personas pobres, siempre que se apliquen políticas que lo permitan.

- Su aplicabilidad en regiones remotas. Los países pobres con combustibles fósiles pueden liberar su dependencia de esta energía y gastar sus fondos en otras partidas a través de la aplicación de energía solar.

Debido a todos estos factores, la inversión en I+D+i en nuevas tecnologías fotovoltaicas es fundamental para poder mantener la calidad de vida de la sociedad actual y de las futuras.
La tecnología fotovoltaica tradicionalmente se divide en tres categorías (1ª generación, 2ª generación y 3ª generación).

Primera generación.

La primera generación de células solares esta principalmente basada en silicio. Este tipo de células solares son las que dominan el mercado actualmente y son las que se suelen ver en los tejados de las casas. Sus principales cualidades son su alta estabilidad y altas eficiencias, sin embargo, son rígidas y requieren de mucha energía para su manufacturación.

Hay tres tipos de paneles solares basados en silicio.

I. Células de silicio monocristalinas.

Se fabrica a partir de ingots (bloques de silicio cilíndricos) sin impurezas a los que se le cortan los bordes de manera que quede un prisma rectangular, se desecha abundante silicio, y finalmente se corta en láminas para fabricar los módulos. En relación con otros tipos de células solares basadas en silicio, tienen mayor eficiencia de conversión fotovoltaica (*photovoltaic conversion efficiency*, PCE) pero son más costosas y frágiles que sus homólogas policristalinas.

II. Células de silicio policristalinas.

Los paneles solares basados en células solares de silicio policristalino son más económicos que los monocristalinos. La síntesis se basa en un proceso de fundición, las piezas de silicio se funden en un crisol de cerámica y luego se pasan a un molde de grafito para formar un lingote. A medida que el silicio fundido se enfría, se introduce un cristal de siembra de la estructura cristalina deseada para facilitar la formación.

III. Células de silicio amorfo.

Las células solares basadas en silicio amorfo son las que usualmente se usan en calculadoras, baterías portátiles o dispositivos portátiles pequeños. En lugar de hacer crecer cristales de silicio como se hace al fabricar los dos tipos anteriores, el silicio se deposita en una capa muy delgada sobre un sustrato, como un metal, vidrio o incluso plástico. A veces, varias capas de silicio, dopadas de maneras ligeramente diferentes para responder a la luz con diferentes longitudes de onda, se colocan una sobre otra para mejorar la eficiencia. Los métodos de producción son complejos pero consumen menos energía que los paneles cristalinos, y los precios han bajado a medida que los paneles se fabrican en masa utilizando este proceso.

Una ventaja del uso de capas muy finas de silicio amorfo es que los paneles pueden ser flexibles. La desventaja de los paneles amorfos es que son

mucho menos eficientes por unidad de área (hasta 10%) y generalmente no son adecuados para instalaciones de techos ya que necesitarían casi el doble del área de panel para la misma potencia de salida.

Segunda generación.

Las células solares de segunda generación esta compuestas por los materiales CIGS[1]–[3] ($CuIn_xGa_{(1-x)}Se_2$) y CdTe[4], [5], donde el rendimiento típico es del 10 al 15%. Dado que las células solares de segunda generación evitan el uso de obleas de silicio y tienen un menor consumo de material, ha sido posible reducir los costos de producción de estos tipos de células solares en comparación con la primera generación. Las células solares de segunda generación también son flexibles hasta cierto punto. Sin embargo, como la producción de células solares de segunda generación todavía incluye procesos de vacío y tratamientos a altas temperaturas, hay un gran consumo de energía asociado con la manufacturación de estas células solares. Además, la segunda generación se basa en elementos escasos y este es un factor limitante en el precio.

Tercera generación.

Las células solares de tercera generación son dispositivos procesados en disolución basados en moléculas orgánicas semiconductoras, nanopartículas, semiconductores inorgánicos, células solares sensibilizadas por colorantes (DSSC)[6] y materiales híbridos. En esta última categoría (materiales híbridos) entran las células solares basadas en perovskitas hibrida orgánica-inorgánica.

Esta Tesis se centra en las células solares de perovskita hibridas orgánica - inorgánicas. Las células solares de perovskitas (CSP) salieron a la luz por primera vez en la comunicación del Prof. Miyasaka[7] del 2009 donde se alcanzaron unas eficiencias de 3.81%. Estos resultados no fueron tomados en serio por la comunidad científica debido a las bajas eficiencias obtenidas.

Posteriormente, en 2011, el Prof. Nam-Gyu Park, utilizando quantum-dots de $CH_3NH_3PbI_3$, alcanzó una eficiencia del 6.2%[8], demostrando el alto coeficiente de absorción que presentan las perovskitas hibridas. El principal problema que encontraron fue la inestabilidad de las perovskitas debido al contacto con los electrolitos líquidos, los cuales disolvían a la perovskita. Por esta razón, el Prof. Pak y el Prof. Grätzel remplazaron la disolución de electrolitos por un transportador de huecos en estado sólido como el Spiro-OMeTAD[9].

Esta aportación fue fundamental para impulsar la investigación sobre CSP. Al año siguiente (2013), las publicaciones en este campo pasaron de 4 a 56, en el 2014 a 463 publicaciones hasta llegar a 1849 publicaciones en el 2017. Respecto a la evolución de la eficiencia en CSP, se puede apreciar los cambios en la Figura 2, con un drástico incremento de las eficiencias desde el 2013 (14%) hasta el 2017 con un 22.7% de eficiencia certificado.

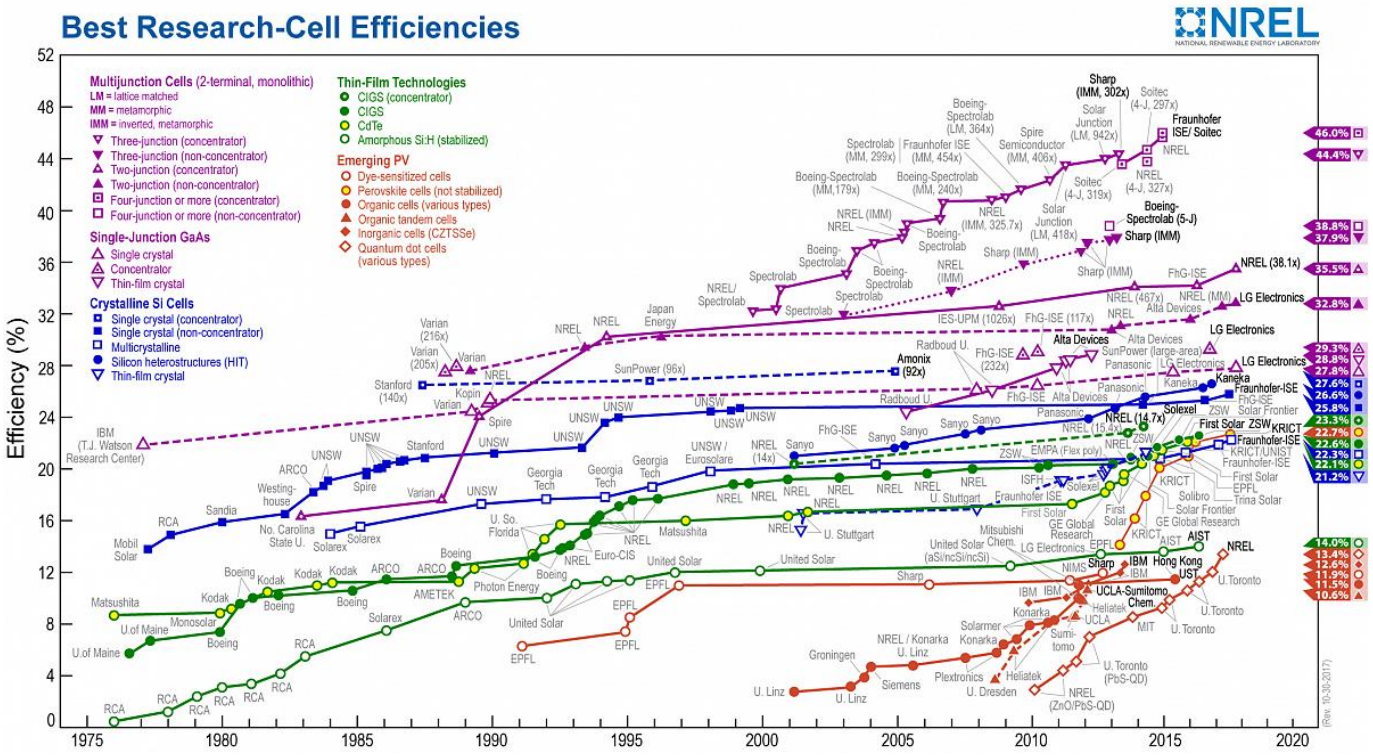

Figura 2. Evolución de las eficiencias en células sol

Estructura básica de las perovskitas

La perovskita se considera un mineral del grupo IV, según la clasificación de Strunz[10] (titanato de calcio, $CaTiO_3$). Fue descubierto en los Montes Urales de Rusia por Gustav Rose en 1839 y nombrado en honor al mineralogista ruso, Lev Aleksevich von Perovski (1792-1856). También recibe el nombre de perovskita el grupo de cristales que toman la misma estructura que el $CaTiO_3$, cuya fórmula química básica es ABX_3, donde "A" y "B" son cationes de diferente tamaño. "A" es un catión grande que puede ser un alcalino, alcalinotérreo, lantánido y, en el caso de las hibridas orgánica-inorgánica, un catión orgánico como el metilamonio (MA, $CH_3NH_3^+$). "B" es un catión de tamaño medio con preferencia por la coordinación octaédrica, normalmente un metal de transición. "X" puede ser oxígeno o, en caso de perovskitas hibridas, un halogenuro[11].

La estructura tipo perovskita consiste en una red tridimensional (3D) de octaedros BX_6 compartiendo esquinas, donde el átomo B es típicamente un catión metálico y X es un anión (Cl^-, Br^-, I^- y en algunos casos S^{2-}), con la carga apropiada para cumplir la neutralidad de la molécula. Los cationes "A" llenan los huecos formados entre los octaedros con 12 puntos de coordinación. De hecho, se define el factor de tolerancia (t) impuesto por las restricciones geométricas basado en un modelo de esfera rígida para la estructura de la perovskita, para poder así establecer que tan grande puede ser el catión "A" considerando los radios iónicos de "B" y "X".

Para un perovskita con empaquetamiento cubico perfecto, las condiciones de los iones "A", "B" y "X" debe ser:

$$(\boldsymbol{R_A} + \boldsymbol{R_X}) = \boldsymbol{t}\sqrt{\boldsymbol{2}}\,(\boldsymbol{R_B} + \boldsymbol{R_X})$$

donde R_A, R_B y R_X son los correspondientes radios iónicos.

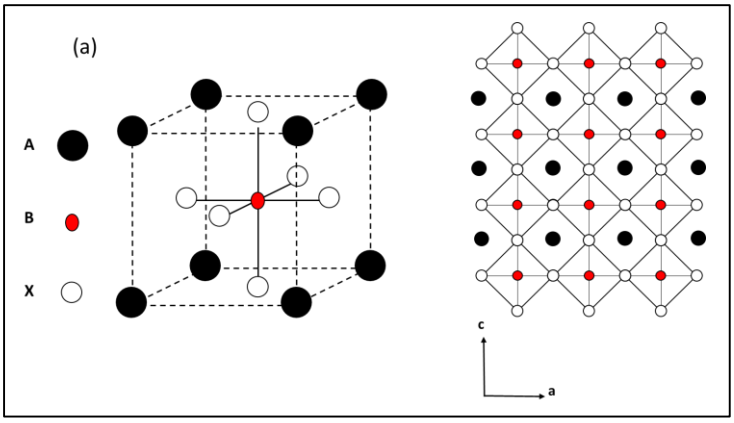

Figura 3. Estructura básica de perovskita ABX_3 (a) y representación de la estructura extendida en las tres dimensiones (b).

Empíricamente se deduce que en la mayoría de las estructuras de perovskitas cúbicas el valor del factor de tolerancia (t) se encuentra entre 0.8 – 1. Estos valores están sujetos a variaciones dependiendo de que tablas se usen para obtener los radios iónicos, sobre todo el radio iónico de la molécula orgánica para el que se hace la suposición que es esférica, lo que conlleva un error añadido. Solo las moléculas orgánicas pequeñas, aquellas que consisten en dos o tres átomos (excluyendo los hidrógenos) pueden entrar para formar una estructura de perovskita 3D. Basándonos en esto, el ion metilamonio cumple las condiciones para formar una perovskita con estructura 3D al usar como "B" el Pb^{2+} y como "X" los aniones Cl^-, Br^- y I^-. Todas estas perovskitas adoptan una estructura cubica a altas temperaturas como se muestra en la Tabla 1.

Tabla 1.. Datos de la estructura de $CH_3NH_3PbX_3$ (X = Cl, Br, I)

X	Temperatura (K)	Sistema cristalino	Grupo espacial
Cl	>178.8	Cubico	*Pm3m*
Cl	172.9-178.8	Tetragonal	*P4/mmm*
Cl	<172.9	Ortorrómbico	$P222_1$
Br	>236.9	Cubico	*Pm3m*
Br	155.1-236.9	Tetragonal	*I4/mmm*
Br	149.5-155.1	Tetragonal	*P4/mmm*
Br	<144.5	Ortorrómbico	$Pna2_1$
I	>327.4	Cubico	*Pm3m*
I	16.2-327.4	Tetragonal	*I4/mcm*
I	<162.2	Ortorrómbico	$Pna2_1$

Cuando los valores de t > 1 la estructura 3D se rompe dando lugar a las perovskitas de baja dimensionalidad (2D, 1D y 0D). En el caso de la estructura perovskita 2D, suelen presentar la formula general A_2BX_4 donde A es $R\text{-}NH_3^+$ o $^+NH_3\text{-}R\text{-}NH_3^+$ siendo R una cadena alifática o un anillo aromático. Estos sistemas consisten en una monocapa de perovskita con orientación (100) separada por una bicapa de cationes orgánicos (ver Figura 4).

En contraste a las estructuras 3D, donde el catión orgánico debe caber en un cavidad rígida y definida, la distancia entre las láminas inorgánicas (BX_4^{2+}) puede variar mucho dependiendo de la longitud del catión orgánico ($R\text{-}NH_3^+$). Los responsables de estabilizar esta estructura son interacciones de los hidrógenos de los grupos amonio que forman puentes de hidrogeno con los halógenos en la red inorgánica (BX_4^{2+}), resultando en una estructura tipo sándwich neutra orgánica-inorgánica. Las láminas en esta estructura están apiladas unas encima de otras manteniéndose unidas por

interacciones de van der Waals entre las cadenas de los cationes orgánicos que mantienen la estructura unida.

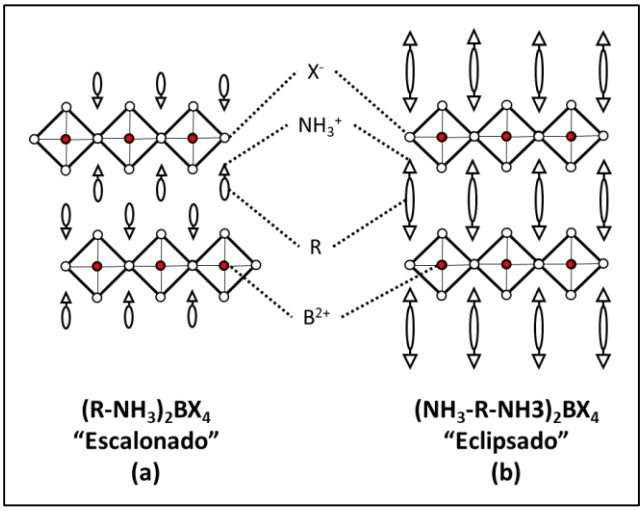

Figura 4. Comparación para n = 1 con orientación de las láminas de perovskita (100) con cationes orgánicos, monoamonio (a) y diamonio (b). Nótese en el caso ideal del sistema con diamonio, los átomos metálicos de las distintas capas inorgánicas están totalmente alineadas (configuración eclipsada). En contraste, el sistema ideal de monoamonio, los átomos metálicos están desplazados entre las láminas inorgánicas adyacentes (configuración escalonada).

El ángulo entre las cadenas de los cationes orgánicos depende de su conformación, así como del espacio entre los cationes orgánicos vecinos más cercanos dentro de la misma capa (controlado por la red inorgánica BX_4^{2+}). Por lo tanto, la longitud de los cationes orgánicos tiene una influencia significativa en el espaciado de la red inorgánica y en consecuencia en sus propiedades físicas.

Este tipo de perovskitas 2D pueden presentar dos tipos de configuraciones, dependiendo si es $R\text{-}NH_3^+$ o $^+NH_3\text{-}R\text{-}NH_3^+$. En el primer caso presentaría un desplazamiento de la lámina de perovskita sucesiva que da como resultado una configuración "escalonada" para las diferentes capas, uniéndose los cationes orgánicos a las láminas solo por un extremo (Figura 4a). En el segundo caso, al tener dos terminaciones $-NH_3^+$ que pueden interaccionar

mediante puentes de hidrogeno con cada lamina sucesiva, se disponen de manera “eclipsada” como se observa en la Figura 4b. Los puentes de hidrogeno entre el grupo (o grupos) $-NH_3^+$ y las láminas de perovskita es otro tema importante que determina la estructura de las perovskitas hibridas orgánica-inorgánica. Influye no solo en la alineación y el espaciamiento de las láminas vecinas, sino también en el grado de inclinación y rotación de las esquinas compartidas del octaedro BX_6 dentro de las láminas y afecta directamente a las transiciones estructurales que varían en función de la temperatura. En principio, la(s) cabeza(s) de amonio de $R\text{-}NH_3^+$ o $^+NH_3\text{-}R\text{-}NH_3^+$ pueden formar puentes de hidrogeno con cualquiera de los 8 halógenos (4 puentes y 4 terminales) que forman la cavidad los octaedros compartidos BX_6. En la práctica, debido a restricciones geométricas del catión orgánico, la interacción N-H----X generalmente se forma entre dos halógenos puentes y un halógeno terminal (configuración halógeno puente) o a dos halógenos terminales y un halógeno puente (configuración halógeno terminal, Figura 5). Estos dos tipos de unión también se conocen como las configuraciones “ortorrómbica” y “monoclínica”, debido a los esquemas de los puentes de hidrogeno.[12] Dicho esto, la simetría de la estructura depende de otros factores además del esquema de enlaces de hidrógeno.

La estructura electrónica y el tamaño de los átomos metálicos de la lámina inorgánica también tienen un impacto importante en la coordinación local y en la estructura cristalina. Aparte de las estructuras 2D ya mencionadas anteriormente también hay un grupo de estructuras 2D denominadas fase Ruddlesden-Popper, las cuales fueron descritas por primera vez en 1957 por S.N. Ruddlesden y P. Popper[13, 14] con fórmula $A_2A'_{n-1}B_nX_{3n+1}$ donde n es un numero entero (las 2D son el caso particular para n = 1), A = $R\text{-}NH_3$, alifático primario ($CH_3CH_2NH_3^+$) o un catión alquilamonio aromático ($Ph\text{-}CH_2CH_2NH_3^+$), A’ es un catión alquilamonio pequeño (ejemplo, $CH_3NH_3^+$), B

es un catión metálico (normalmente Pb^{2+}) y X corresponde a un halogenuro ($X = Cl^-$, Br^+, o I^-).

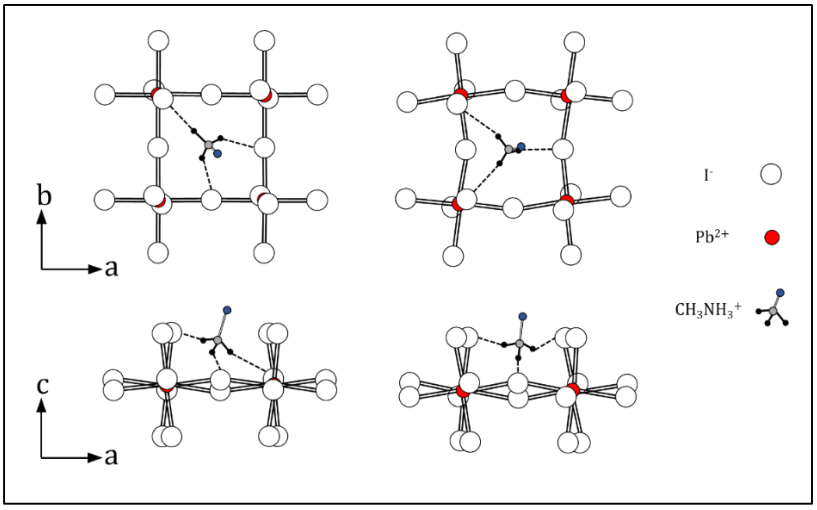

Figura 5. Dos estructuras distintas del enlace de hidrogeno en las perovskitas hibridas orgánicas – inorgánicas observadas en el plano (100). Para simplificar, se muestra un catión de metilamonio como catión orgánico y los hidrógenos unidos al átomo de carbono están reorientados en cada ejemplo. Los cationes alquilamonio más grandes y los que contienen grupos aromáticos también adoptan estos mismos dos esquemas.

Como en el caso de las 2D, el catión A actúa como espaciador entre las láminas de perovskita compuesta por los octaedros BX_6 que comparten esquinas, dando como resultado la formación de capas orgánicas e inorgánicas alternadas que se apilan a lo largo de la dirección *c* (Figura 6). El espesor de las láminas 3D (n) se puede controlar experimentalmente ajustando la relación entre el catión grande (A) y el catión pequeño (A'). Además, debido a la baja dimensionalidad y la diferencia de las propiedades dieléctricas entre los espaciadores orgánicos y las capas de perovskita inorgánica, estos compuestos son estructuras con pozos cuánticos múltiples de origen natural, que dan lugar a excitones estables a temperatura ambiente. Las propiedades ópticas de esta clase de perovskitas varían dependiendo del valor de "n" con band gaps de ~1.5 eV para el caso de

n = ∞ y > 1.6 eV para n ≥ 2, los cuales son ideales para células solares y en general para aplicaciones en optoelectrónica. La principal motivación por la cual existe un interés en el uso de este tipo de estructuras quasi-2D en células solares basadas en perovskita es su mayor resistencia a la humedad en comparación a las perovskitas con estructura 3D.

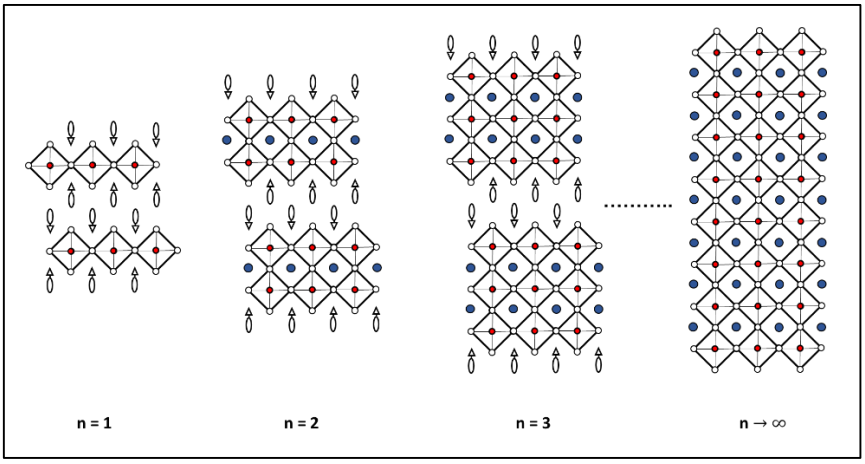

Figura 6. Representación esquemática de la orientación (100) de la familia de perovskitas orgánicas – inorgánicas, $A_2A'_{n-1}B_nX_{3n+1}$ para distintos valores de "n".

La siguiente estructura disminuyendo la dimensionalidad es la perovskita monodimensional (1D).[15], [16] Estos sistemas consisten en cadenas de octaedros que comparten una sola de sus esquinas con el octaedro adyacente (Figura 6). Al ser sistemas donde los cationes orgánicos y las cadenas de la red inorgánica están aisladas unas de otras se restringe la movilidad de los electrones a una sola dimensión y por esta razón no son empleadas en células solares. También existen perovskitas con cero dimensionalidad, 0D[17] (ver Figura 7), las cuales no presentan utilidad práctica en células solares por lo cual no se comentan en esta tesis.

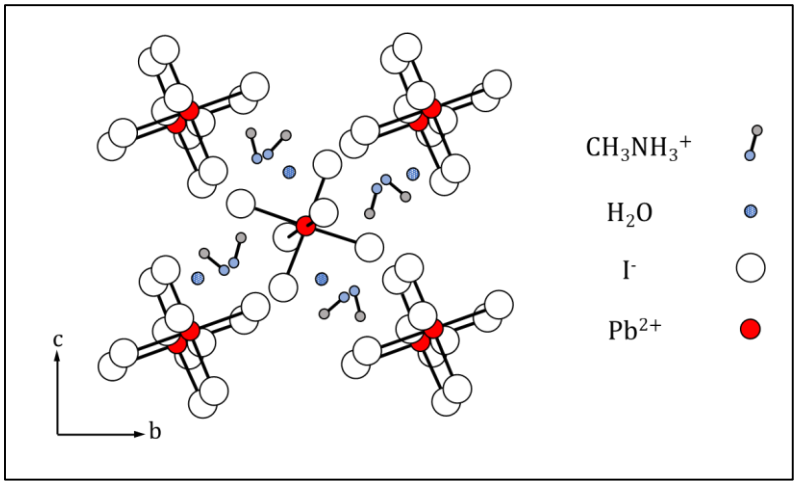

Figura 7. Representación esquemática de la estructura "1D" de la perovskita hidratada $(CH_3NH_3)_4PbI_6 \cdot 2H_2O$, consiste en octaedros PbI_6^{4+} aislados separados por moléculas de metilamonio y agua.

Propiedades y composición química

Considerando todas las estructuras nombradas anteriormente, las 3D son las más utilizadas en fotovoltaica debido a sus excelentes propiedades ópticas, incluido un band gap ≈ 1.6 eV. Este valor se puede considerar óptimo ya que concuerda con el rango de band gaps descrito por el límite de Shockley-Queisser[18]–[20] para las eficiencias máximas. De hecho, la eficiencia máxima teórica para este tipo de materiales estaría rondando el 32% (Figura 8), mientras que para un valor de band gap de 1.34 eV tendría el punto máximo de eficiencia teórica de unos 33.7% (todo esto considerando una energía de incidencia de 1000 W/m^2 y empleando un espectro de AM 1.5 G).

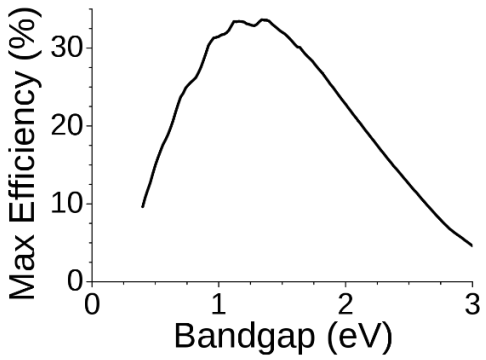

Figura 8. Representación gráfica del límite de Shockley-Queisser teórico en función del band gap.

Además de un óptimo band gap también presentan un alto coeficiente de absorción con valores ≈ 1.5 x 10^4 cm^{-1} a 550 nm lo que implica un orden de magnitud mayor que el colorante N-719, complejo de rutenio ampliamente utilizado en las células solares sensibilizadas por colorante (DSSC)[17]. Este valor tan alto del coeficiente de absorción hace de este material ideal para emplearlo en células solares de capa fina[5],[6]. También presentan una energía de unión del excitón (*exciton binding energy*) muy baja (2-50 meV)[23]–[29] permitiendo la generación de cargas libres, alta movilidad de

cargas[30]–[32] debido a su baja masa efectiva (m_h^* o $m_e^* \approx 0.1m_0$), gran tolerancia a defectos lo cual evita la formación de trampas (*deep trap states*) y una gran longitud de difusión de los portadores de cargas (*charge-carrier diffusion lengths*)[9],[14],[17]–[23]. Aun así, con todas sus propiedades óptimas para la aplicación en células solares hay dos importantes limitaciones para la aplicabilidad de estos materiales en la industria:

1. La alta toxicidad del Pb (el cual está presente en todas las células solares de altas eficiencias), lo que conlleva un alto riesgo para la salud y posibles daños medioambientales.

2. La baja estabilidad de dichos materiales, el cual es derivado de la degradación hacia los precursores, debido a la exposición a altas temperaturas (>100ºC), humedad y oxígeno.

Lo primero a tener en cuenta es la alta toxicidad del Pb. Para ello la sustitución de este elemento por otro menos toxico es fundamental desde el punto de vista de la seguridad sanitaria. La sustitución del Pb en una perovskita 3D requiere utilizar cationes divalentes (B^{2+}), como pueden ser cationes del grupo 14, metales alcalinotérreos, metales de transición o lantánidos (Figura 9). A priori se podrían utilizar una gran variedad de cationes que formen perovskitas híbridas sin plomo con estructura 3D (manteniendo el límite de tolerancia de Goldschmidt). Sin embargo, existen múltiples problemas al sustituir el Pb por estos elementos, que incluyen una mayor toxicidad (Cd^{2+} y Hg^{2+}), un band gap muy grande (Be^{2+}, Ca^{2+}, Sr^{2+}, Ba^{2+})[40] problemas de inestabilidad en el estado de oxidación, etc. El Germanio (Ge) es un elemento del grupo 14 que presenta estado de oxidación 2+ al igual que el Pb. La principal ventaja del Ge frente al Pb es

que presenta una baja toxicidad y las perovskitas basadas en Ge^{2+} presentan teóricamente propiedades ópticas y de transporte comparables a sus análogas basadas en Pb[41], [42].

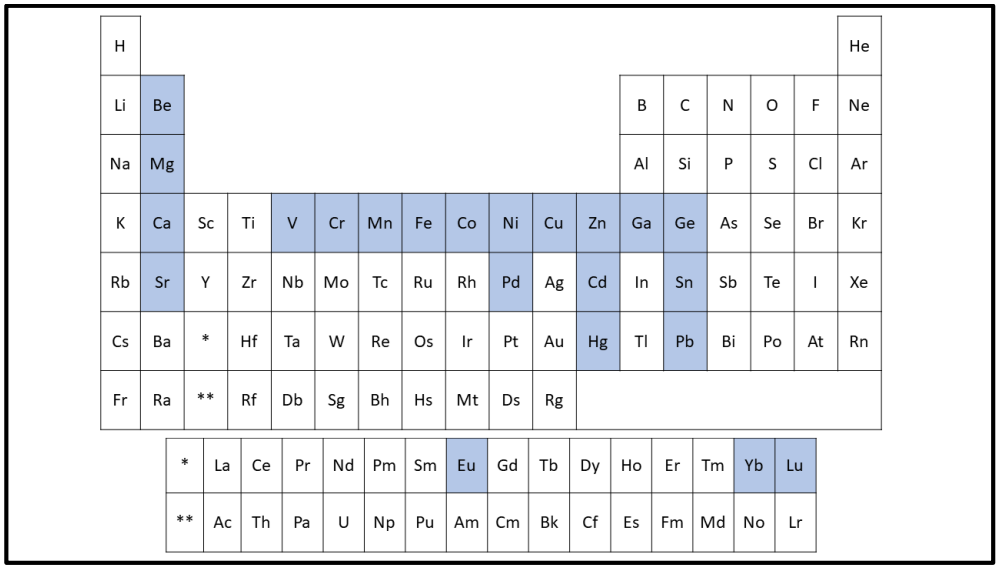

Figura 9. Tabla periódica donde se resaltan los elementos que se podrían usar como "B" en perovskitas 3D.

El Ge al tratarse de un compuesto menos electronegativo comparado con el Pb, presenta un enlace de carácter más covalente y un radio iónico más reducido (73 pm) comparado al Pb (119 pm)[43]. Un factor muy relevante es que el Ge^{2+} se oxida más fácilmente a Ge^{4+} en comparación con la oxidación del Pb^{2+} a Pb^{4+}, lo que se traduce en un efecto perjudicial sobre la estabilidad de la perovskita. Esto se debe al efecto menos intenso del par inerte ns^2.

Otro elemento del grupo 14 con radio iónico comparable es el estaño (Sn) el cual ha sido propuesto como el principal candidato para remplazar al Pb debido a que tienen similares band gaps las perovskitas tipo $ASnI_3$ siendo "A" los cationes cesio (Cs^+), metilamonio (MA,$CH_3NH_3^+$) o formamidinio (FA, $CH(NH_2)_2^+$). Tienen un band gap de 1.2-1.4 eV[43], inferior al band gap de sus análogas con Pb^{2+} y también presenta energías de unión del excitón similares (2-50 meV)[44]. El principal problema al remplazar el Pb por Sn es

la facilidad que tiene este último en oxidarse (Sn^{2+} a Sn^{4+}) en condiciones medioambientales[29],[30] lo cual destruye la electroneutralidad de la estructura de perovskita formándose óxidos / hidróxidos[31],[32].

Otra alternativa es la sustitución del Pb por un metal de transición o un metal alcalinotérreo debido a su abundancia en la tierra y la naturaleza mayoritariamente no tóxica de estos elementos. Todos los metales alcalinotérreos presentan un estado de oxidación 2+ y tanto el Sr^{2+} como el Ca^{2+} presentan un radio iónico efectivo adecuado (118 pm y 100 pm, respectivamente) para la síntesis de perovskitas tipo ABX_3[43]. Por otra parte, los metales de transición como el cobre (Cu), el hierro (Fe) y el paladio (Pd) presentan radios iónicos efectivos inferiores al del Pb (Cu^{2+}: 73 pm; Fe^{2+}: 78 pm; Pd^{2+}: 86 pm; Pb^{2+}: 119 pm) lo que conlleva la formación de perovskitas de más baja dimensionalidad como pueden ser las Ruddlesden-Popper. Además de esto último, los múltiples estados de oxidación de los metales de transición dificultan la estabilidad química de las perovskitas. Por todas estas dificultades, no se ha conseguido hasta la fecha la sustitución del Pb por otro elemento menos tóxico que consiga mantener los mismos rendimientos en células solares basadas en perovskitas.

Por otra parte, los únicos cationes monovalentes capaces de formar perovskitas 3D son el metilamonio, el formamidinio y el Cesio. Se ha propuesto y estudiado la sustitución parcial de estos cationes por otros alternativos como por ejemplo el catión Rubidio (Rb^+), el etilamonio ($CH_3CH_2NH_3^+$) o el guanidinio ($C(NH_2)_3^+$), los cuales no cumplen con el factor de tolerancia de Goldschmidt (Rb^+: 0.77; etilamonio: 1.03; guanidinio: ~1.04). Así, estos cationes por si solos no son capases de formar perovskitas 3D, al contrario, suelen formar estructuras no-perovskita como es el caso del Rb^+ el cual solo cristaliza en una fase no-perovskita ($RbPbI_3$) de color amarilla con poco interés en fotovoltaica.[49] Por lo tanto, la estrategia que se ha planteado hasta la fecha es la combinación de cationes

monovalentes en una misma estructura de perovskita. Este nuevo enfoque de sustituir parcialmente los cationes metilamonio, cesio y formamidinio por otros que por sí solos no forman estructuras perovskita proporcionan un abanico de combinaciones y de posibilidades incontables. Un ejemplo de ello es la mezcla de RbCsMAFA, la cual no solo potencia las eficiencias de la célula solar si no que da un paso hacia adelante en el problema de la estabilidad, logrando mantener un 95% su eficiencia inicial durante una prueba de resistencia durante 500 horas. Otro caso en el cual se utiliza esta estrategia es con el guanidinio (Gua, $C(NH_2)_3^+$), que se mezcla con metilamonio para formar una perovskita con la estequiometria $Ma_{1-x}Gua_xPbI_3$, dando excelentes resultados al incrementar el rendimiento de la célula solar y mostrando un aumento de estabilidad en un test de 1000 horas a iluminación constante. Este último ejemplo es uno de los artículos que conciernen a esta tesis.

Métodos de síntesis y deposición en capa fina.

Todas las diferentes estructuras químicas de las perovskitas pueden ser sintetizadas y depositadas por diferentes métodos sobre un sustrato para con ello fabricar una célula solar.

Comenzaremos hablando de un método de síntesis muy útil desde el punto de vista de la caracterización mediante difracción de rayos X, como es la síntesis de monocristales (*single crystal*). Este tipo de síntesis tiene múltiples enfoques y hay distintos métodos[50]–[54], siendo uno de ellos el "*antisolvent vapor-assisted crystallization"* (Figura 10) el cual consiste en una disolución con las sales precursoras (MAI/PbI_2) que se introduce en un recipiente que contiene el antisolvent (liquido en el cual no son solubles las sales precursoras). El recipiente se cierra para favorecer la difusión del antisolvent hacia la disolución que contiene los precursores, de esta manera empiezan a precipitar pequeños cristales de perovskita los cuales actúan como núcleos de recristalización que hacen que con el paso del tiempo vayan aumentando su tamaña hasta formar un monocristal de unos pocos milímetros de diámetro.

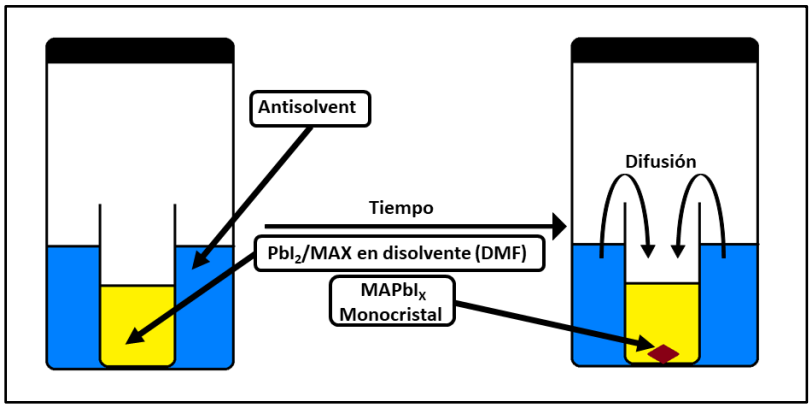

Figura 10. Esquema del proceso de antisolvent vapor-assisted crystallization.

Otro método empleado por su rapidez y simplicidad es el "*inverse temperature crystallization*"[55], [56] (Figura 11) el cual consiste en sumergir en un baño de aceite una disolución con las sales precursoras (MAI/PbI_2) a temperatura ambiente y calentar hasta una temperatura fija. El proceso de recristalización ocurre dentro de la disolución caliente que con el paso del tiempo va incrementando el tamaño del cristal. Este proceso es relativamente rápido (3-5 horas) en comparación al anterior.

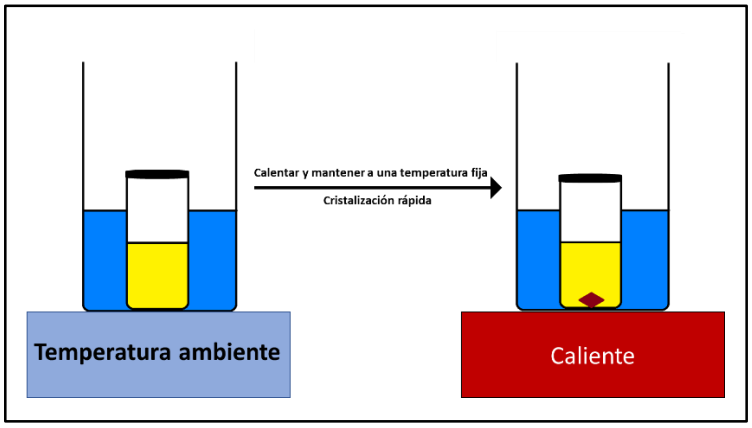

Figura 11. Esquema del proceso de inverse temperature crystallization

Desafortunadamente estos métodos de síntesis no son viables para la deposición de las perovskitas en un sustrato y la formación de una capa fina con aplicaciones en células solares. Por esta razón este método solo se utiliza para caracterización estructural mediante difracción de rayos X de monocristales, la cual da información muy importante desde el punto de vista estructural.

Por otra parte, existe otro método de síntesis en estado sólido también muy útil para caracterizar perovskitas hibridas orgánicas – inorgánicas: la mecanosíntesis[57]–[60]. (Este método fue empleado en esta tesis y se detalla más en el *Capítulo III*). Este método de síntesis se basa en la molienda de los precursores mediante un molino de bolas que consiste en un recipiente

de acero al que se le introducen unas bolas de acero junto con los precursores (por ejemplo, MAI/PbI_2). Este método permite sintetizar de manera rápida (10 min) y simple una gran cantidad de muestra lo que facilita la caracterización de este tipo de materiales, ya que en una sola síntesis es suficiente para realizar la caracterización completa del material.

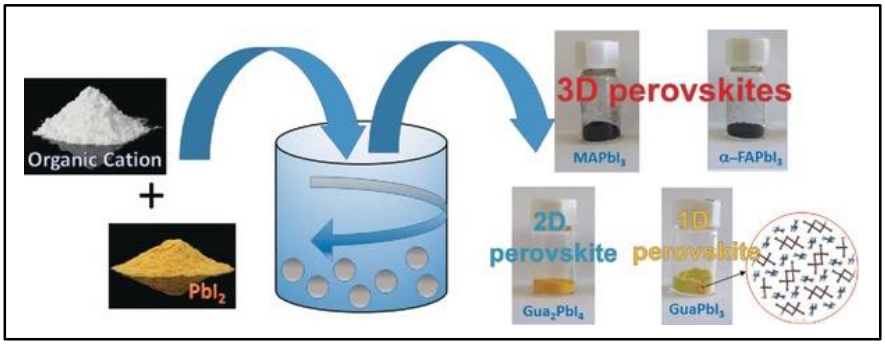

Figura 12. Representación del proceso de mecanosíntesis

A diferencia del caso anterior (monocristales), en este caso se sintetizan las perovskitas en forma de policristales de tamaños relativamente pequeños (50-500 nm). El tamaño se puede controlar modificando las revoluciones por minuto (rpm) que se aplican en el molino de bolas, aunque no es muy preciso ya que presenta mucha dispersión de tamaños.

El método más utilizado para depositar y sintetizar perovskitas directamente sobre un sustrato es el de *spincoating,* obteniéndose capas finas homogéneas. Este método es sumamente útil en la síntesis y deposición de perovskitas ya que permite la deposición directa sobre el sustrato que se utilizará para formar la célula solar, y por lo tanto, fue el usado en esta tesis ya que es el más utilizado con diferencia en el campo de las células solares basadas en perovskitas. La técnica de spincoating consiste en sujetar un sustrato mediante vacío o algún método de sujeción al equipo (spincoater),

a continuación se deposita una pequeña cantidad de la disolución que contiene los precursores sobre el sustrato y por último se hace dispersar la disolución sobre la superficie al hacer girar el sustrato con una velocidad angular constante.

Además de los nombrados anteriormente también existe el método de deposición química de vapor a ultra vacío (10^{-8} torr)[61]. Este método es muy utilizado sobre todo por la ventaja de poder incrementar considerablemente el área de deposición de la perovskita sobre el sustrato, lo cual es fundamental para escalar a nivel industrial. El principal inconveniente es el elevado precio de esta tecnología, lo cual sería un inconveniente a la hora de comercializar células solares de perovskita. Por esta razón existe otro método que cumple con las características de poder formar grandes superficies de perovskita en capa fina de manera aún más rápida que la deposición química de vapor a ultra vacío, como es la impresión de inyección de tinta (*inkjet printing*)[62]–[65] en la que se utiliza una "tinta" con los precursores disueltos o en algunos casos en suspensión. El proceso implica esencialmente la eyección de una cantidad fija de tinta desde una cámara, la cual se contrae en respuesta a la aplicación de un voltaje externo. Esta reducción repentina establece una onda de choque en el líquido, lo cual hace que una gota del líquido se expulse de la boquilla y se deposita sobre el sustrato. De esta manera se puede depositar en superficies sin inconvenientes del área a depositar.

Células solares: conceptos básicos, arquitectura y configuración

Una célula solar es un dispositivo electrónico que convierte la radiación proveniente del sol (UV-VIS-NIR) en energía eléctrica. Este proceso produce una corriente generada por la luz solar y consiste de dos pasos. El primero es la absorción de fotones incidentes para crear pares electrón – hueco (excitón). Estos se generarán siempre que la energía incidente sea igual o mayor al band gap del semiconductor (perovskita). Sin embargo, el excitón es metaestable y solo existirá, en promedio, durante un periodo de tiempo igual al tiempo de vida del portador minoritario (los portadores minoritarios son las partículas cuánticas encargadas del transporte de corriente eléctrica que se encuentra en menor proporción en un semiconductor tipo-n o tipo-p) antes de recombinarse. Si se recombinan, entonces el par electrón – hueco generado por la luz se pierde y no se puede generar corriente y por ende no hay potencia eléctrica. El segundo paso es la recolección de estos portadores de carga en la unión p-n para separar el electrón del hueco generado. Esta unión se basa en un material donde se mueven las cargas positivas (p) que serían los huecos y otro donde se mueven las cargas negativas (n) que serían los electrones (Figura 13). Los portadores de carga son separados por la acción del campo eléctrico existente en la unión p-n. Si el portador minoritario (por ejemplo, un hueco) alcanza la unión p-n, este es barrido a través de la unión debido al campo eléctrico, pasando del material tipo n al tipo p y convirtiéndose por consiguiente en un portador mayoritario (partículas cuánticas encargadas del transporte de corriente eléctrica que se encuentra en exceso en un semiconductor tipo-n o tipo-p). Por otra parte, el electrón que pasa por el circuito externo alcanza la base del contacto donde se encuentra con el hueco que pasó a través del material tipo p. En este caso cuando el emisor y la base de la célula solar están conectados entre sí, se denomina que la célula solar está en cortocircuito.

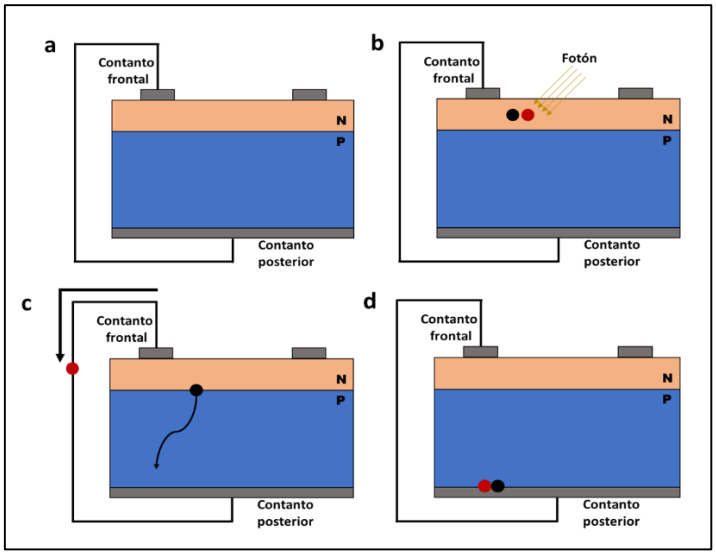

Figura 13. Esquema ideal del flujo en corto circuito de electrones y huecos en una unión p-n. **a)** Esquema de una célula solar con unión p-n. **b)** La absorción de un fotón genera un par electrón-hueco. **c**) Caso ideal el portador minoritario (en este caso, un hueco) atraviese la unión n-p y se convierta en un operador mayoritario. **d)** Después de atravesar el circuito externo, el electrón se encuentra con el hueco y completa el circuito

La recolección de portadores de carga generados por la luz no da lugar a la generación de energía por sí misma. Para generar energía eléctrica, se debe generar un voltaje y una corriente. El voltaje se genera en una célula solar mediante un proceso conocido como “efecto fotovoltaico”. La recolección de portadores por la unión p-n causa un movimiento de electrones hacia el lado tipo “n” y los huecos hacia el lado tipo “p” de la unión. En condiciones de cortocircuito, no existe acumulación de carga, ya que los portadores salen del dispositivo como corriente generada por la luz. Sin embargo, si se evita que los portadores generados salgan de la célula solar, la recolección de portadores causa un aumento en el número de electrones en el lado de tipo n de la unión p-n y un aumento similar en los huecos en el material de tipo p. Esta separación de carga crea un campo eléctrico en la unión que se opone a lo que ya existe en la unión, lo que reduce el campo eléctrico neto.

Dado que el campo eléctrico representa una barrera para el flujo de corriente, la reducción del campo eléctrico conlleva a un aumento de la corriente de difusión, en el cual se alcanza un nuevo equilibrio en el que existe un voltaje a través de la unión p-n.

En condiciones de circuito abierto, la polarización directa de la unión aumenta hasta un punto en el que la corriente generada por la luz alcanza un equilibrio con la corriente de difusión de polarización directa, y la corriente neta es cero. El voltaje requerido para hacer que estas dos corrientes se equilibren se llama voltaje de circuito abierto (V_{OC}).

Por otra parte, la corriente de cortocircuito es la corriente a través de la célula solar cuando el voltaje a través es cero (es decir, cuando la célula solar esta cortocircuitada). Usualmente se denota como I_{SC}. Esta corriente se debe a la generación y recolección de portadores. Para una célula solar ideal la mayoría de los mecanismos de perdida de corriente (debido a resistencias) son despreciables, entonces se considera que I_{SC} y la corriente generada por la luz son idénticas. Por lo tanto, I_{SC} es la corriente más grande que puede extraerse de una célula solar.

Por consiguiente, para medir el rendimiento de una célula solar son fundamentales conocer I_{SC} y V_{OC}. Para ello las medidas de voltaje frente a corriente, curva I-V, es el procedimiento habitual para obtener el rendimiento de una célula solar (Figura 14).

La curva I-V en una célula solar se define como la superposición de la curva I-V del diodo de la célula solar en la oscuridad con la corriente generada por efecto de la luz (fotocorriente). La luz tiene un efecto de desplazar la curva I-V hacia valores negativos de corriente lo que implica que se puede extraer energía del diodo. Al iluminar una célula solar a la fotocorriente se le agrega las corrientes en oscuridad lo cual deja la ley del diodo:

$$\mathbf{I} = \boldsymbol{I_L} - \boldsymbol{I_0}\left[\boldsymbol{exp}\left(\frac{\boldsymbol{qV}}{\boldsymbol{nkT}}\right)\right] \quad [1]$$

Donde:

I_0: Corriente de saturación.

I_L: Fotocorriente.

n: Factor de idealidad (normalmente con valores entre 1 y 2).

T: Temperatura.

V: voltaje.

k: Constante de Boltzmann.

q: Carga del electrón.

La eficiencia es el parámetro más utilizado para comparar rendimientos de una célula solar con otra. La eficiencia se define como la relación entre producción de energía de la célula solar y la entrada de energía proveniente de la luz solar. Además de reflejar el rendimiento de la célula solar en sí, la eficiencia depende del espectro y la intensidad de la luz solar incidente y la temperatura. Por lo tanto, las condiciones en las que se mide la curva I-V deben ser controladas cuidadosamente para poder comparar un dispositivo con otro. Para ello se recomienda medir las células solares a 25ºC y usando un espectro radiación AM1.5. Por lo tanto, se puede definir la eficiencia de una célula solar mediante la siguiente ecuación:

$$\mathbf{EFF} = \frac{V_{OC} I_{SC} FF}{P_i} \qquad [2]$$

Donde:

V_{OC}: Voltaje a circuito abierto.

I_{SC}: Corriente en cortocircuito.

FF: Factor de relleno.

P_i: Potencia de radiación incidente (normalmente 1 sol, 100mW/cm^2)

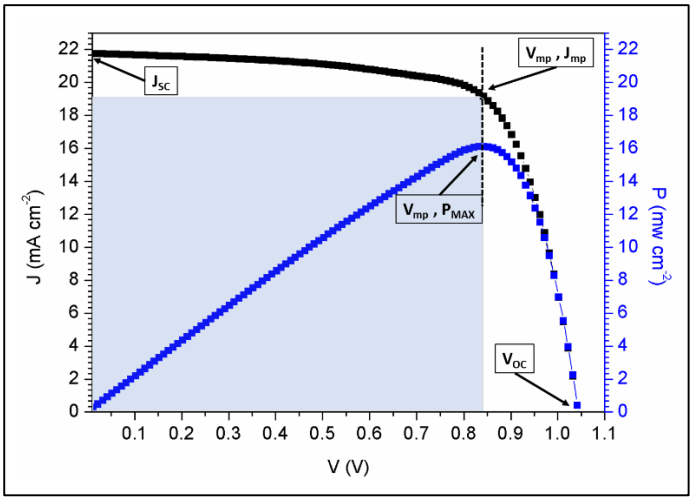

Figura 14. Grafica que muestra la curva I-V (negra) y curva de potencia (azul) donde se refleja los parámetros más importantes, densidad de corriente en corto circuito (J_{SC}), voltaje en circuito abierto (V_{OC}), voltaje en punto de máxima potencia (V_{mp}), densidad de corriente en el punto de máxima potencia (J_{mp}) y punto de máxima potencia (P_{MAX}).

Además de los diferentes métodos de síntesis y deposición mencionados anteriormente, hay que tener en cuenta el tipo de superficie sobre la que se deposita la perovskita, ya que se han usado diferentes tipos de arquitecturas, n-i-p y p-i-n (Figura 15) y con distintas configuraciones.

1. n-i-p con configuración mesoporosa-activa

Esta es la más utilizada por sus altas eficiencias. Se basa en depositar una capa de TiO_2 compacta (TiO_2-c) sobre un sustrato con FTO (óxido de estaño dopado con flúor) seguida de una capa de TiO_2 mesoporosa (TiO_2-m) que actúa de andamio y aumenta la superficie de contacto con la perovskita al mismo tiempo que aumenta el espesor de la capa de perovskita depositada. A continuación, se añade la capa de perovskita y encima de esta se deposita el material transportador de huecos (HTM), normalmente se utiliza Spiro-OMeTAD, y por último el contra electrodo (CE). Esta es la configuración que se utiliza en esta tesis para realizar los dispositivos.

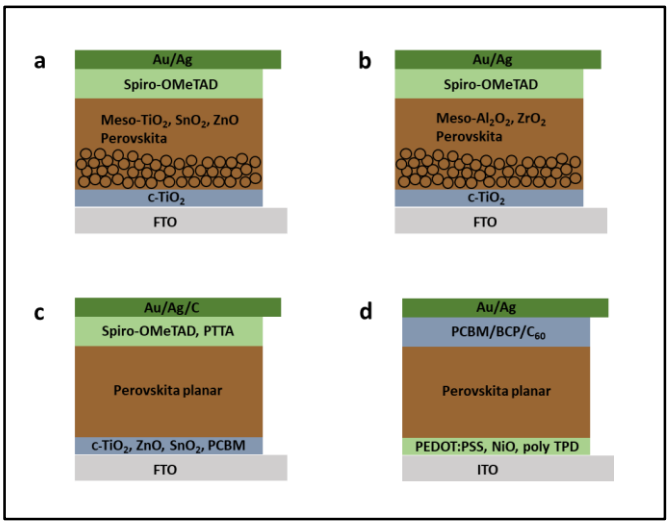

Figura 15. Esquema de las distintas configuraciones en la arquitectura de células solares. **a)** Configuración mesoporosa-activa n-i-p. **b)** Configuración mesoporosa-pasiva n-i-p. **c)** Configuración plana-regular n-i-p. **d)** Configuración plana-invertida p-i-n.

2. n-i-p con configuración mesoporosa-pasiva.

En este caso es exactamente como el anterior, pero en vez de utilizar TiO_2-m se utiliza un oxido de aluminio o de zirconio como capa mesoporosa (AlO_3-m ZrO_2-m), el resto de las capas son iguales.

3. n-i-p con configuración plana-regular.

En la configuración plana no se utiliza una capa mesoporosa, de ahí su nombre. Para esta configuración se utiliza también una capa compacta de TiO_2 y posteriormente se añade la capa de perovskita seguida del material transportador de huecos y por último el contra electrodo.

4. p-i-n con configuración plana-invertida.

En esta arquitectura, a diferencia de las tres anteriores, la primera capa a depositar es el transportador de huecos que puede ser PEDOT: PSS, NiO,

Poly-TPD (poli(biss-4-butilfenil-N,N-bisfenil) bencidina). Posteriormente se añade la capa de perovskita seguida del material transportador de electrones (ETM) el cual en este caso puede ser PCBM ([6,6] fenil-C_{61}-ácido butírico metil ester), BCP (2,9-dimetil-4,7-dimetil-1,10-fenantrolina) C_{60}.

En las tablas siguientes se muestran los rendimientos de las distintas arquitecturas y configuraciones nombradas anteriormente.

Tabla 2. Datos que destacan varias células solares de perovskita de alto rendimiento que utilizan capa mesoporosa-activa

mesoporosa-activa	**V_{OC} / (V)**	**I_{SC} / (mA/cm^2)**	**FF**	**PCE / (%)**	**Ref.**
ITO/c TiO_2/mesoTiO_2/MA FAPIBr/spiroOMeTAD/Au	1.16	24.60	0.73	20.80	[66]
ITO/c TiO_2/meso TiO_2/FAPI /PTAA/Au	1.06	24.70	0.775	20.10	[67]
FTO/c TiO_2/meso TiO_2/MAPI/spiroOMeTAD/Ag	1.09	23.83	0.76	19.71	[68]
FTO/c- TiO_2/meso TiO_2-MAPI/spiroOMeTAD/Au	1.09	21.21	0.78	18.36	[69]
FTO/c- TiO_2/mesoTiO_2/MAPI/spiroOMeTAD/Au	1.06	21.39	0.76	17.19	[70]
ITO/c- TiO_2/meso-TiO_2/MAPI/spiroOMeTAD/Au	1.06	21.64	0.74	17.01	[71]
FTO/c- TiO_2/meso TiO_2-MAPI/MAPI/V886/Au	1.08	21.38	0.73	16.91	[69]
FTO/c- TiO_2/meso TiO2-MAPI/spirom-mp/Au	1.02	21.20	0.78	16.70	[72]
FTO/c- TiO_2/meso TiO2-MAPI/azuleneHTM/Au	1.08	21.70	0.71	16.50	[73]
FTO/c- TiO_2/meso TiO2/MAPI-Br/PTAA/Au	1.09	19.50	0.76	16.22	[74]
FTO/meso-TiO_2/MAPICl/spiroOMeTAD/Au	1.03	21.68	0.72	16.08	[75]
FTO/c- TiO_2/FAPI-MAPI/spiroOMeTAD/Au	1.03	20.97	0.74	16.01	[76]
FTO/c- TiO_2/meso TiO_2-MAPI/spiroOMeTAD/Au	1.02	20.10	0.76	15.60	[77]
FTO/c- TiO_2/meso TiO_2-MAPI/OMeTAD/Au	1.00	20.40	0.74	15.20	[72]
FTO/c TiO_2/meso-TiO_2-MAPI/spiroOMeTAD/Au	0.99	20.00	0.73	15.00	[78]
FTO/c- TiO_2/mesoTiO_2-MAFAPI/spiroOMeTAD/Au	1.03	21.20	0.70	14.90	[79]
FTO/c-TiO2/mesoTiO2/MAPI/CuSCN/Au	1.02	19.70	0.62	12.40	[80]

Tabla 3. Datos que destacan varias células solares de perovskita de alto rendimiento que utilizan capa mesoporosa-pasiva

mesoporosa-pasiva	**V_{OC} / (V)**	**I_{SC} / (mA/cm^2)**	**FF**	**PCE / (%)**	**Ref.**
FTO/c-TiO2/mesoAl2O3/MAPICl/spiroOMeTAD/Ag	1.02	21.50	0.71	15.90	[81]
FTO/c-TiO2/mesoAl2O3-IPFB-perov/spiro+buffer/Au	1.03	20.62	0.62	13.07	[82]
FTO/c-TiO2/mesoAl2O3/MAPICl/spiroOMeTAD/Ag	1.02	18.00	0.67	12.30	[83]
FTO/c-TiO2/mesoZrO2/MAPI/spiroOMeTAD/Au	1.07	17.30	0.59	10.80	[84]

Tabla 4. Datos que destacan varias células solares de perovskita de alto rendimiento que utilizan configuración plana-invertida.

plana-invertida	**V_{OC} / (V)**	**I_{SC} / (mA/cm^2)**	**FF**	**PCE / (%)**	**Ref.**
ITO/PEDOT:PSS/Perov1/PC71BM/Ca-Al	1.03	20.60	0.85	18.0	[85]
ITO/PEDOT:PSS/MAPICl/PC61BM/PFN/al	1.05	20.30	0.80	17.1	[86]
ITO/PEDOT:PSS/MAPI-D/PC61BM/MUTAB/	1.03	20.06	0.80	16.5	[87]
ITO/PEDOT:PSS/MAPI/ZnO ALD/Ag	1.02	20.73	0.76	16.2	[87]
ITO/PEDOT:PSS/MAPICl/PC61BM/Al	0.87	22.31	0.80	15.6	[88]
ITO/Cu:NiOx/Perov/PC61BM/C60surf/Ag	1.11	19.01	0.73	15.4	[89]
ITO/polyTPD/MAPI/PCBM/C60/BCP/Ag	1.10	22.00	0.70	15.3	[90]
ITO/VB-DAAF/MAPI/C60/BCP/Al	1.02	18.92	0.78	15.2	[91]
ITO/PEDOT:PSS-GeO2/MAPICl/PCBM/Ag	0.96	20.57	0.74	15.2	[92]
ITO/PEDOT:PSS/MAPICl/PCBC fullerene/Al	0.98	22.08	0.7	15.1	[93]
ITO/PEDOT:PSS/MAPI/PCBM/BCP/Ag	0.99	20.80	0.73	15	[94]

Tabla 5. Datos que destacan varias células solares de perovskita de alto rendimiento que utilizan configuración plana-regular.

Dispositivo tipo: plana-regular	**V_{OC} / (V)**	**I_{SC} / (mA/cm^2)**	**FF**	**PCE / (%)**	**Ref.**
ITO-PEIE/Y-TiO2-MAPICl/spiroOMeTAD/Au	1.13	22.75	0.75	19.3	[95]
FTO/c-SnO2/MAPBr-FAPI/spiroOMeTAD/au	1.14	21.30	0.74	18.4	[96]
FTO/cTiO2/MAPI/spiroOMeTAD/Au	1.05	22.20	0.75	17.5	[97]
ITO/TiO2-PC60BM/MAPI/spiroOMeTAD/Au	1.11	21.00	0.77	17.6	[98]
FTO/cTiO2/MAPI/spiroOMeTAD/Ag	1.04	21.90	0.74	16.8	[99]
ITO/TiO2/PCBB-2CN-2C8/MAPI/spiroOMeTAD/Au	1.06	19.85	0.78	16.4	[100]
FTO/cTiO2/MAPICl/DERDTS-TBDT/MoO3/Ag	1.05	21.20	0.73	16.2	[84]
FTO/cSnO2/MAPI/spiroOMeTAD/Au	1.11	22.83	0.64	16.0	[101]
FTO/cZnO/MAPI/spiroOMeTAD/Ag	1.03	20.40	0.75	15.7	[102]
FTO/cTiO2/MAPICl/spiroOMeTAD/Ag	1.07	21.50	0.67	15.4	[103]
FTO/PEI/PCBM/MAPI/PTAA (polytriarylamine)/Au	0.98	21.80	0.72	15.3	[104]
FTO/cTiO2/MAPI/spiroOMeTAD/MoO3/Ag	1.00	22.70	0.67	15.2	[105]
FTO/ZnO/MAPI /spiroOMeTAD/Ag	1.08	20.04	0.70	15.0	[106]
FTO/TiO2-C60SAM/MAPI/spiroOMeTAD/Ag	1.01	20.00	0.73	14.8	[107]
FTO/ZnO/MAPI/spiroOMeTAD/Ag	1.06	19.44	0.79	14.4	[108]
FTO/ZnO-C3SAM/MAPI/spiroOMeTAD/MoO /Ag	1.07	22.51	0.65	14.3	[80]

De las tablas (2-5) se puede denotar que el rendimiento fotovoltaico de las células solares no solo depende de la composición química de la perovskita sino también de la arquitectura (n-i-p o p-i-n), configuración (meso-activa, meso-pasiva, plana-regular o plana-invertida) y distintos ETM y HTM, por lo

tanto se nos plantea un sinfín de combinaciones para poder alcanzar la combinación óptima para las células solares basadas en perovskitas.

Bibliografía

[1] P. Jackson *et al.*, “Properties of Cu(In,Ga)Se2solar cells with new record efficiencies up to 21.7%,” *Phys. Status Solidi - Rapid Res. Lett.*, vol. 9, no. 1, pp. 28–31, 2015.

[2] F. Kessler and D. Rudmann, “Technological aspects of flexible CIGS solar cells and modules,” *Sol. Energy*, vol. 77, no. 6, pp. 685–695, 2004.

[3] A. Romeo *et al.*, “Development of thin-film Cu(In,Ga)Se2 and CdTe solar cells,” *Prog. Photovoltaics Res. Appl.*, vol. 12, no. 23, pp. 93–111, 2004.

[4] M. Gloeckler, I. Sankin, and Z. Zhao, “CdTe solar cells at the threshold to 20% efficiency,” *IEEE J. Photovoltaics*, vol. 3, no. 4, pp. 1389–1393, 2013.

[5] A. Romeo, E. Artegiani, and D. Menossi, “Low substrate temperature CdTe solar cells: A review,” *Sol. Energy*, no. October 2017, pp. 0–1, 2018.

[6] M. Grätzel, “Dye-sensitized solar cells,” *J. Photochem. Photobiol. C Photochem. Rev.*, vol. 4, no. 2, pp. 145–153, 2003.

[7] Akihiro Kojima, K. Teshima, Y. Shirai, and T. Miyasaka, “Organometal Halide Perovskites as Visible- Light Sensitizers for Photovoltaic Cells,” *J Am Chem Soc*, vol. 131, no. October, pp. 6050–6051, 2009.

[8] J. H. Im, C. R. Lee, J. W. Lee, S. W. Park, and N. G. Park, “6.5% Efficient Perovskite Quantum-Dot-Sensitized Solar Cell,” *Nanoscale*, vol. 3, no. 10, pp. 4088–4093, 2011.

[9] H. S. Kim *et al.*, “Lead iodide perovskite sensitized all-solid-state submicron thin film mesoscopic solar cell with efficiency exceeding 9%,” *Sci. Rep.*, vol. 2, pp. 1–7, 2012.

[10] “Nickel-Strunz Classification.” [Online]. Available: http://webmineral.com/strunz.shtml#.WzpC69IzZPb. [Accessed: 02-

Jul-2018].

[11] J. K. Barton, *Progress in Inorganic Chemistry Advisory Board*, vol. 51. 2002.

[12] A. H. Janowicz and R. G. Bergman, “Activation of carbon-hydrogen bonds in saturated hydrocarbons on photolysis of (.eta.5-C5Me5)(PMe3)IrH2. Relative rates of reaction of the intermediate with different types of carbon-hydrogen bonds and functionalization of the metal-bound alkyl groups,” *J. Am. Chem. Soc.*, vol. 105, no. 12, pp. 3929–3939, 1983.

[13] S. N. Ruddlesden and P. Popper, “New compounds of the K_2NIF_4 type,” *Acta Crystallogr.*, vol. 10, no. 8, pp. 538–539, 1957.

[14] S. N. Ruddlesden and P. Popper, “The compound $Sr_3Ti_2O_7$ and its structure,” *Acta Crystallogr.*, vol. 11, no. 1, pp. 54–55, 1958.

[15] G. de Miguel, G. Garcia-Espejo, D. Rodriguez-Padron, M. Perez-Morales, R. Luque, and L. Camacho, “Mechanochemical synthesis of one-dimensional (1D) hybrid perovskites incorporating polycyclic aromatic spacers: highly fluorescent cation-based materials,” *J. Mater. Chem. C*, 2018.

[16] X. Xu, X. Zhang, W. Deng, J. Jie, and X. Zhang, “1D Organic-Inorganic Hybrid Perovskite Micro/Nanocrystals: Fabrication, Assembly, and Optoelectronic Applications,” *Small Methods*, vol. 1700340, p. 1700340, 2018.

[17] B. Inst and O. F. Tech, “The Benefit and Challenges of Zero-Dimensional Perovskites,” 2018.

[18] S. Rühle, “Tabulated values of the Shockley-Queisser limit for single junction solar cells,” *Sol. Energy*, vol. 130, pp. 139–147, 2016.

[19] C. H. Henry, “Limiting efficiencies of ideal single and multiple energy gap terrestrial solar cells,” *J. Appl. Phys.*, vol. 51, no. 8, pp. 4494–4500, 1980.

[20] W. Shockley and H. J. Queisser, “Detailed balance limit of efficiency of p-n junction solar cells,” *J. Appl. Phys.*, vol. 32, no. 3, pp. 510–519, 1961.

[21] A. A. Shah, P. Torres, R. Tscharner, N. Wyrsch, and H. Keppner, “Photovoltaic Technology : The Case for Thin-Film Solar Cells Published by : American Association for the Advancement of Science Photovoltaic Technology : The Case for Thin-Film Solar Cells,” vol. 285, no. 5428, pp. 692–698, 2016.

[22] S. K. Deb, “Thin-film solar cells: An overview,” *Renew. Energy*, vol. 8, no. 1–4, pp. 375–379, 1996.

[23] A. M. Askar and K. Shankar, “Exciton Binding Energy in Organic–Inorganic Tri-Halide Perovskites,” *J. Nanosci. Nanotechnol.*, vol. 16, no. 6, pp. 5890–5901, 2016.

[24] A. Miyata *et al.*, “Direct measurement of the exciton binding energy and effective masses for charge carriers in organic-inorganic tri-halide perovskites,” *Nat. Phys.*, vol. 11, no. 7, pp. 582–587, 2015.

[25] V. D’Innocenzo *et al.*, “Excitons versus free charges in organo-lead tri-halide perovskites,” *Nat. Commun.*, vol. 5, pp. 1–6, 2014.

[26] S. D. Stranks, V. M. Burlakov, T. Leijtens, J. M. Ball, A. Goriely, and H. J. Snaith, “Recombination Kinetics in Organic-Inorganic Perovskites: Excitons, Free Charge, and Subgap States,” *Phys. Rev. Appl.*, vol. 2, no. 3, pp. 1–8, 2014.

[27] K. Tanaka, T. Takahashi, T. Ban, T. Kondo, K. Uchida, and N. Miura, “Comparative study on the excitons in lead-halide-based perovskite-type crystals CH3NH3PbBr3CH3NH3PbI3,” *Solid State Commun.*, vol. 127, no. 9–10, pp. 619–623, 2003.

[28] M. Hirasawa, T. Ishihara, T. Goto, K. Uchida, and N. Miura, “compound (CH3NH3)PbI3,” vol. 201, pp. 427–430, 1994.

[29] S. Sun *et al.*, “The origin of high efficiency in low-temperature solution-

processable bilayer organometal halide hybrid solar cells," *Energy Environ. Sci.*, vol. 7, no. 1, pp. 399–407, 2014.

[30] C. Wehrenfennig, G. E. Eperon, M. B. Johnston, H. J. Snaith, and L. M. Herz, "High charge carrier mobilities and lifetimes in organolead trihalide perovskites," *Adv. Mater.*, vol. 26, no. 10, pp. 1584–1589, 2014.

[31] C. Wehrenfennig, M. Liu, H. J. Snaith, M. B. Johnston, and L. M. Herz, "Charge-carrier dynamics in vapour-deposited films of the organolead halide perovskite CH3NH3PbI3-xClx," *Energy Environ. Sci.*, vol. 7, no. 7, pp. 2269–2275, 2014.

[32] W. Rehman *et al.*, "Charge-Carrier Dynamics and Mobilities in Formamidinium Lead Mixed-Halide Perovskites," *Adv. Mater.*, vol. 27, no. 48, pp. 7938–7944, 2015.

[33] S. de Wolf *et al.*, "Organometallic Halide Perovskites: Sharp Optical Absorption Edge and," *J. Phys. Chem. C*, vol. 5, pp. 1035–139, 2014.

[34] S. D. Stranks *et al.*, "Electron-hole diffusion lengths exceeding 1 micrometer in an organometal trihalide perovskite absorber," *Science (80-.).*, vol. 342, no. 6156, pp. 341–344, 2013.

[35] R. E. Brandt, V. Stevanovi??, D. S. Ginley, and T. Buonassisi, "Identifying defect-tolerant semiconductors with high minority-carrier lifetimes: Beyond hybrid lead halide perovskites," *MRS Commun.*, vol. 5, no. 2, pp. 265–275, 2015.

[36] A. Walsh, D. O. Scanlon, S. Chen, X. G. Gong, and S. H. Wei, "Self-regulation mechanism for charged point defects in hybrid halide perovskites," *Angew. Chemie - Int. Ed.*, vol. 54, no. 6, pp. 1791–1794, 2015.

[37] Y. Deng, E. Peng, Y. Shao, Z. Xiao, Q. Dong, and J. Huang, "Scalable fabrication of efficient organolead trihalide perovskite solar cells with doctor-bladed active layers," *Energy Environ. Sci.*, vol. 8, no. 5, pp.

1544–1550, 2015.

[38] G. Xing *et al.*, “Long-range balanced electron-and hole-transport lengths in organic-inorganic CH3NH3PbI3,” *Science (80-.).*, vol. 342, no. 6156, pp. 344–347, 2013.

[39] A. M. Ganose, C. N. Savory, and D. O. Scanlon, “Beyond methylammonium lead iodide: prospects for the emergent field of ns2containing solar absorbers,” *Chem. Commun.*, vol. 53, no. 1, pp. 20–44, 2017.

[40] S. Chatterjee and A. J. Pal, “Influence of metal substitution on hybrid halide perovskites: Towards lead-free perovskite solar cells,” *J. Mater. Chem. A*, vol. 6, no. 9, pp. 3793–3823, 2018.

[41] J. Qian, B. Xu, and W. Tian, “A comprehensive theoretical study of halide perovskites ABX3,” *Org. Electron. physics, Mater. Appl.*, vol. 37, pp. 61–73, 2016.

[42] G. Settanni *et al.*, “Protein corona composition of PEGylated nanoparticles correlates strongly with amino acid composition of protein surface,” 2016.

[43] R. D. Shannon, “Revised effective ionic radii and systematic studies of interatomic distances in halides and chalcogenides,” *Acta Crystallogr. Sect. A*, vol. 32, no. 5, pp. 751–767, 1976.

[44] J. S. Manser, J. A. Christians, and P. V. Kamat, “Intriguing Optoelectronic Properties of Metal Halide Perovskites,” *Chem. Rev.*, vol. 116, no. 21, pp. 12956–13008, 2016.

[45] F. Hao, C. C. Stoumpos, D. H. Cao, R. P. H. Chang, and M. G. Kanatzidis, “Lead-free solid-state organic-inorganic halide perovskite solar cells,” *Nat. Photonics*, vol. 8, no. 6, pp. 489–494, 2014.

[46] N. K. Noel *et al.*, “Lead-free organic-inorganic tin halide perovskites for photovoltaic applications,” *Energy Environ. Sci.*, vol. 7, no. 9, pp. 3061–3068, 2014.

[47] T. Leijtens, R. Prasanna, A. Gold-Parker, M. F. Toney, and M. D. McGehee, “Mechanism of Tin Oxidation and Stabilization by Lead Substitution in Tin Halide Perovskites,” *ACS Energy Lett.*, vol. 2, no. 9, pp. 2159–2165, 2017.

[48] Y. Takahashi *et al.*, “Charge-transport in tin-iodide perovskite CH3NH3SnI3: Origin of high conductivity,” *Dalt. Trans.*, vol. 40, no. 20, pp. 5563–5568, 2011.

[49] M. Saliba *et al.*, “Incorporation of rubidium cations into perovskite solar cells improves photovoltaic performance,” *Science (80-.).*, vol. 354, no. 6309, pp. 206–209, 2016.

[50] Q. Dong *et al.*, “Solar cells. Electron-hole diffusion lengths > 175 μm in solution-grown CH3NH3PbI3 single crystals.,” *Science*, vol. 347, no. 6225, pp. 967–70, 2015.

[51] D. Shi *et al.*, “Low Trap-State Density and Long Carrier Diffusion in Organolead Trihalide Perovskite Single Crystals,” *Sci. (80-.).*, vol. 347, no. 6221, pp. 519–522, 2015.

[52] T. Baikie *et al.*, “Synthesis and crystal chemistry of the hybrid perovskite (CH3NH3)PbI3 for solid-state sensitised solar cell applications,” *J. Mater. Chem. A*, vol. 1, no. 18, p. 5628, 2013.

[53] Y. Dang *et al.*, “Bulk crystal growth of hybrid perovskite material CH3NH3PbI3,” *CrystEngComm*, vol. 17, no. 3, pp. 665–670, 2015.

[54] C. C. Stoumpos, C. D. Malliakas, and M. G. Kanatzidis, “Semiconducting tin and lead iodide perovskites with organic cations: Phase transitions, high mobilities, and near-infrared photoluminescent properties,” *Inorg. Chem.*, vol. 52, no. 15, pp. 9019–9038, 2013.

[55] M. I. Saidaminov *et al.*, “High-quality bulk hybrid perovskite single crystals within minutes by inverse temperature crystallization,” *Nat. Commun.*, vol. 6, no. May, pp. 1–6, 2015.

[56] G. Maculan *et al.*, “CH<inf>3</inf>NH<inf>3</inf>PbCl<inf>3</inf>

Single Crystals: Inverse Temperature Crystallization and Visible-Blind UV-Photodetector," *J. Phys. Chem. Lett.*, vol. 6, no. 19, pp. 3781–3786, 2015.

[57] Z. Y. Zhu *et al.*, "Solvent-Free Mechanosynthesis of Composition-Tunable Cesium Lead Halide Perovskite Quantum Dots," *J. Phys. Chem. Lett.*, vol. 8, no. 7, pp. 1610–1614, 2017.

[58] D. J. Kubicki *et al.*, "Formation of Stable Mixed Guanidinium-Methylammonium Phases with Exceptionally Long Carrier Lifetimes for High-Efficiency Lead Iodide-Based Perovskite Photovoltaics," *J. Am. Chem. Soc.*, vol. 140, no. 9, pp. 3345–3351, 2018.

[59] P. Sadhukhan *et al.*, "Solvent free Solid state Synthesis of High Yield Mixed Halide Perovskites for Easily Tunable Composition and Band gap," *Cryst. Growth Des.*, 2018.

[60] D. Prochowicz *et al.*, "Mechanosynthesis of pure phase mixed-cation $MA_xFA_{1-x}PbI_3$ hybrid perovskites: photovoltaic performance and electrochemical properties," *Sustain. Energy Fuels*, vol. 1, no. 4, pp. 689–693, 2017.

[61] J. Ávila, C. Momblona, P. P. Boix, M. Sessolo, and H. J. Bolink, "Vapor-Deposited Perovskites: The Route to High-Performance Solar Cell Production?," *Joule*, vol. 1, no. 3, pp. 431–442, 2017.

[62] E. Tekin, P. J. Smith, and U. S. Schubert, "Inkjet printing as a deposition and patterning tool for polymers and inorganic particles," *Soft Matter*, vol. 4, no. 4, pp. 703–713, 2008.

[63] M. Singh, H. M. Haverinen, P. Dhagat, and G. E. Jabbour, "Inkjet printing-process and its applications," *Adv. Mater.*, vol. 22, no. 6, pp. 673–685, 2010.

[64] Z. Wei, H. Chen, K. Yan, and S. Yang, "Inkjet printing and instant chemical transformation of a CH3NH3PbI3/nanocarbon electrode and interface for planar perovskite solar cells," *Angew. Chemie - Int. Ed.*,

vol. 53, no. 48, pp. 13239–13243, 2014.

[65] M.-R. Ahmadian-Yazdi, A. Rahimzadeh, Z. Chouqi, Y. Miao, and M. Eslamian, “Viscosity, surface tension, density and contact angle of selected PbI_2, $PbCl_2$ and methylammonium lead halide perovskite solutions used in perovskite solar cells,” *AIP Adv.*, vol. 8, no. 2, p. 025109, 2018.

[66] D. Bi *et al.*, “Efficient luminescent solar cells based on tailored mixed-cation perovskites,” *Sci. Adv.*, vol. 2, no. January, 2016.

[67] W. Van Schalkwijk and N. Mater, “High-performance photovoltaic perovskite layers fabricated through intramolecular exchange,” *Science (80-.).*, vol. 348, no. 6240, pp. 2013–2017, 2015.

[68] N. Park, “Highly Reproducible Perovskite Solar Cells with Average E ffi ciency of 18.3% and Best E ffi ciency of 19.7% Fabricated via Lewis Base Adduct of Lead(II) Iodide,” *J. Am. Chem. Soc.*, vol. 137, no. II, pp. 8696–8699, 2015.

[69] P. Gratia *et al.*, “A Methoxydiphenylamine-Substituted Carbazole Twin Derivative : An Efficient Hole-Transporting Material for Perovskite Solar Cells ** Angewandte,” *Angew. Chemie - Int. Ed.*, vol. 54, pp. 11409–11413, 2015.

[70] W. Li, J. Fan, J. Li, Y. Mai, and L. Wang, “Controllable Grain Morphology of Perovskite Absorber Film by Molecular Self-Assembly toward E ffi cient Solar Cell Exceeding 17%,” *J. Am. Chem. Soc.*, vol. 137, no. 32, pp. 10399–10405, 2015.

[71] J. Im, I. Jang, N. Pellet, and N. Park, “size for high-ef fi ciency perovskite solar cells,” *Nat. Nanotechnol.*, vol. 9, pp. 927–932, 2014.

[72] M.-H. Li *et al.*, “Novel spiro-based hole transporting materials for efficient perovskite solar cells,” *Chem. Commun.*, vol. 51, no. 85, pp. 15518–15521, 2015.

[73] H. Nishimura *et al.*, “Hole-Transporting Materials with a Two-

Dimensionally Expanded ??-System around an Azulene Core for Efficient Perovskite Solar Cells," *J. Am. Chem. Soc.*, vol. 137, no. 50, pp. 15656–15659, 2015.

[74] N. J. Jeon *et al.*, "o-Methoxy Substituents in Spiro – OMeTAD for Efficient Inorganic – Organic Hybrid Perovskite Solar Cells o -Methoxy Substituents in Spiro – OMeTAD for Efficient Inor- ganic – Organic Hybrid Perovskite Solar Cells," *J. Am. Chem. Soc.*, vol. 136, no. 22, pp. 7837–7840, 2014.

[75] A. Manuscript, "Energy & Environmental Science," *Energy Environ. Sci.*, vol. 8, pp. 3208–3214, 2015.

[76] J. W. Lee, D. J. Seol, A. N. Cho, and N. G. Park, "High-efficiency perovskite solar cells based on the black polymorph of HC(NH2)2PbI3," *Adv. Mater.*, vol. 26, no. 29, pp. 4991–4998, 2014.

[77] Q. Shen *et al.*, "Optical absorption, charge separation and recombination dynamics in Sn/Pb cocktail perovskite solar cells and their relationships to photovoltaic performances," *J. Mater. Chem. A*, vol. 3, no. 17, pp. 9308–9316, 2015.

[78] J. Burschka *et al.*, "Sequential deposition as a route to high-performance perovskite-sensitized solar cells," *Nature*, vol. 499, no. 7458, pp. 316–319, 2013.

[79] N. Pellet *et al.*, "Mixed-organic-cation perovskite photovoltaics for enhanced solar-light harvesting," *Angew. Chemie - Int. Ed.*, vol. 53, no. 12, pp. 3151–3157, 2014.

[80] L. Zuo *et al.*, "Enhanced Photovoltaic Performance of CH\n 3\n NH\n 3\n PbI\n 3\n Perovskite Solar Cells through Interfacial Engineering Using Self-Assembling Monolayer," *J. Am. Chem. Soc.*, vol. 137, no. 7, pp. 2674–2679, 2015.

[81] K. Wojciechowski, M. Saliba, T. Leijtens, A. Abate, and H. J. Snaith, "Sub-150 ??c processed meso-superstructured perovskite solar cells

with enhanced efficiency," *Energy Environ. Sci.*, vol. 7, no. 3, pp. 1142–1147, 2014.

[82] S. Guarnera *et al.*, "Improving the long-term stability of perovskite solar cells with a porous Al2O3 buffer layer," *J. Phys. Chem. Lett.*, vol. 6, no. 3, pp. 432–437, 2015.

[83] J. M. Ball, M. M. Lee, A. Hey, and H. J. Snaith, "Low-temperature processed meso-superstructured to thin-film perovskite solar cells," *Energy Environ. Sci.*, vol. 6, no. 6, pp. 1739–1743, 2013.

[84] D. Bi *et al.*, "Using a two-step deposition technique to prepare perovskite (CH3NH3PbI3) for thin film solar cells based on ZrO2 and TiO2 mesostructures," *RSC Adv.*, vol. 3, no. 41, p. 18762, 2013.

[85] C. G. Wu, C. H. Chiang, Z. L. Tseng, M. K. Nazeeruddin, A. Hagfeldt, and M. Grätzel, "High efficiency stable inverted perovskite solar cells without current hysteresis," *Energy Environ. Sci.*, vol. 8, no. 9, pp. 2725–2733, 2015.

[86] J. Dong, J. Shi, D. Li, Y. Luo, and Q. Meng, "Controlling the conduction band offset for highly efficient ZnO nanorods based perovskite solar cell," *Appl. Phys. Lett.*, vol. 107, no. 7, pp. 1–6, 2015.

[87] C. Chang *et al.*, "High-Performance , Air-Stable , Low-Temperature Processed Semitrans- parent Perovskite Solar Cells Enabled by Atomic Layer Deposition," *Chem. Mater.*, vol. 27, no. 14, pp. 5122–5130, 2015.

[88] H. Tsai *et al.*, "Optimizing Composition and Morphology for Large Grain Perovskite Solar Cell Efficiency via Controlling Chemical Reaction," *Chem. Mater.*, vol. 3, no. 110, p. 150729095517005, 2015.

[89] J. H. Kim *et al.*, "High-performance and environmentally stable planar heterojunction perovskite solar cells based on a solution-processed copper-doped nickel oxide hole-transporting layer," *Adv. Mater.*, vol. 27, no. 4, pp. 695–701, 2015.

[90] W. Chen, F. Z. Liu, X. Y. Feng, A. B. Djurišić, W. K. Chan, and Z. B. He, "Cesium Doped NiOxas an Efficient Hole Extraction Layer for Inverted Planar Perovskite Solar Cells," *Adv. Energy Mater.*, vol. 7, no. 19, pp. 1–8, 2017.

[91] T. Y. Chiang *et al.*, "Functional p-Type, Polymerized Organic Electrode Interlayer in CH3NH3PbI3 Perovskite/Fullerene Planar Heterojunction Hybrid Solar Cells," *ACS Appl. Mater. Interfaces*, vol. 7, no. 44, pp. 24973–24981, 2015.

[92] Z. K. Wang, M. Li, D. X. Yuan, X. B. Shi, H. Ma, and L. S. Liao, "Improved hole interfacial layer for planar perovskite solar cells with efficiency exceeding 15%," *ACS Appl. Mater. Interfaces*, vol. 7, no. 18, pp. 9645–9651, 2015.

[93] X. Liu, W. Jiao, M. Lei, Y. Zhou, B. Song, and Y. Li, "Crown-ether functionalized fullerene as a solution-processable cathode buffer layer for high performance perovskite and polymer solar cells," *J. Mater. Chem. A*, vol. 3, no. 17, pp. 9278–9284, 2015.

[94] J. Qing *et al.*, "Chlorine Incorporation for Enhanced Performance of Planar Perovskite Solar Cell Based on Lead Acetate Precursor," *ACS Appl. Mater. Interfaces*, vol. 7, no. 41, pp. 23110–23116, 2015.

[95] B. Nicholson, S. Verma, P. Med, and S. S, "R es e a rc h," *Science (80-.).*, vol. 345, no. 6196, pp. 542–546, 2014.

[96] J. P. Correa Baena *et al.*, "Highly efficient planar perovskite solar cells through band alignment engineering," *Energy Environ. Sci.*, vol. 8, no. 10, pp. 2928–2934, 2015.

[97] D. Song *et al.*, "Managing Carrier Lifetime and Doping Property of Lead Halide Perovskite by Postannealing Processes for Highly Efficient Perovskite Solar Cells," *J. Phys. Chem. C*, vol. 119, no. 40, pp. 22812–22819, 2015.

[98] C. Tao *et al.*, "17.6% Stabilized Efficiency in Low-Temperature

Processed Planar Perovskite Solar Cells," *Energy Environ. Sci.*, vol. 8, no. 8, pp. 2365–2370, 2015.

[99] B. Yang *et al.*, "Perovskite Solar Cells with Near 100% Internal Quantum Efficiency Based on Large Single Crystalline Grains and Vertical Bulk Heterojunctions," *J. Am. Chem. Soc.*, vol. 137, no. 29, pp. 9210–9213, 2015.

[100] Y. Li *et al.*, "Multifunctional Fullerene Derivative for Interface Engineering in Perovskite Solar Cells," *J. Am. Chem. Soc.*, vol. 137, no. 49, pp. 15540–15547, 2015.

[101] P. Vanelderen *et al.*, "Spectroscopic definition of the copper active sites in mordenite: Selective methane oxidation," *J. Am. Chem. Soc.*, vol. 137, no. 19, pp. 6383–6392, 2015.

[102] W. Ke *et al.*, "Lowerature solution-processed tin oxide as an alternative electron transporting layer for efficient perovskite solar cells," *J. Am. Chem. Soc.*, vol. 137, no. 21, pp. 6730–6733, 2015.

[103] D. Liu and T. L. Kelly, "Perovskite solar cells with a planar heterojunction structure prepared using room-temperature solution processing techniques," *Nat. Photonics*, vol. 8, no. 2, pp. 133–138, 2014.

[104] S. Ryu *et al.*, "Fabrication of metal-oxide-free CH3NH3PbI3perovskite solar cells processed at low temperature," *J. Mater. Chem. A*, vol. 3, no. 7, pp. 3271–3275, 2015.

[105] M. Liu, M. B. Johnston, and H. J. Snaith, "Efficient planar heterojunction perovskite solar cells by vapour deposition," *Nature*, vol. 501, no. 7467, pp. 395–398, 2013.

[106] L. Yang, J. Wang, and W. W. F. Leung, "Lead Iodide Thin Film Crystallization Control for High-Performance and Stable Solution-Processed Perovskite Solar Cells," *ACS Appl. Mater. Interfaces*, vol. 7, no. 27, pp. 14614–14619, 2015.

[107] K. Wojciechowski *et al.*, “Heterojunction Modification for Highly Efficient Organic - Inorganic Perovskite Solar Cells,” *ACS Nano*, vol. 8, no. 12, pp. 12701–12709, 2014.

[108] D.-Y. Son, J.-H. Im, H.-S. Kim, and N.-G. Park, “11% Efficient Perovskite Solar Cell Based on ZnO Nanorods: An Effective Charge Collection System,” *J. Phys. Chem. C*, vol. 118, no. 30, pp. 16567–16573, 2014.

Capítulo II

Experimental

Chapter II

Experimental

Experimentación

1. Espectroscopia absorción UV/Vis y de reflectancia difusa.

- *Reflectancia difusa.*

Los espectros de reflectancia difusa para los polvos sintetizados por el molino de bolas ($FAPbI_3$, $MAPbI_3$, Gua_2PbI_4 y $GuaPbI_3$) fueron medidos a temperatura ambiente usando un CARY 5000 con una esfera integradora, utilizando un detector inteligente NIR de Pb para extender el rango de detección (200-1000 nm). Como referencia de material no absorbente se utilizó $BaSO_4$.

Los polvos de perovskita se depositaron en unos portamuestras cilíndricos con una barrera de cuarzo para permitir el paso de la luz. Se comprimió ligeramente la muestra para crear una superficie homogénea en contacto con el cuarzo del portamuestra.

Al incidir la luz en la muestra, parte de la luz incidente se refleja en todas las direcciones. El fenómeno de reflexión, refracción, difracción y absorción por las partículas orientadas en todas las direcciones se denomina reflectancia difusa. Para el caso de reflectancia difusa ideal, la distribución angular de la luz reflejada es independiente del ángulo de incidencia y obedece la ley del coseno de Lambert:

$$\boldsymbol{I_\alpha = I_0 \cdot cos(\alpha)} \quad [1]$$

Donde:

I_α: intensidad según el ángulo de observación en candelas (cd)

I_0: intensidad según la normal en candelas (cd)

α: ángulo de incidencia.

Esta ley establece que la intensidad de la radiación sobre un plano decrece en forma proporcional al coseno del ángulo de incidencia en relación a la normal. No existe un reflector difuso ideal, pero el comportamiento cercano

a Lambert se observa normalmente en muestras de polvo fuertemente prensadas. Mediante la ecuación de Kubelka-Munk se analizan los espectros obtenidos por reflectancia difusa.

- *Teoría de Kubelka-Munk*

La teoría de Kubelka-Munk supone que una capa plana de espesor X es capaz de dispersar y absorber radiación, esta capa se irradia en la dirección -x con un flujo de radiación monocromático. El tamaño de la muestra es muy grande en relación con su espesor X y lo que se hace es dividirlo en capas infinitesimales de espesor dx. El flujo de radiación difusa en la dirección *x* tanto negativa como positiva se designa como I y J, respectivamente (Figura 1). Si, al pasar por dx, el flujo descendente I se reduce en una cantidad *KI*dx por absorción, y se incrementa en una cantidad *SI*dx por dispersión, y se hace un razonamiento similar para el flujo ascendente J, entonces se pueden derivar las siguientes ecuaciones diferenciales:

$$\frac{-dI}{dx} = -(K + S)I + SJ \quad \textbf{[2]}$$

$$\frac{-dJ}{dx} = -(K + S)J + SI \quad \textbf{[3]}$$

Donde K y S son los coeficientes de absorción y de dispersión respectivamente. Mediante un tratamiento matemático aplicando una solución hiperbólica explicita se obtiene la función de Kubelka-Munk:

$$\mathbf{K} = \frac{S\cdot(1-R_\infty)^2}{2\cdot R_\infty} = \mathbf{F}(R_\infty) \quad \textbf{[4]}$$

Donde R_∞ es la reflectancia de una capa lo suficientemente gruesa para que el aumento de la misma no cambia el valor de la reflectancia. La ecuación 4 relaciona la parte que corresponde a la dispersión (S) con la parte que corresponde a la absorbancia (K)[1].

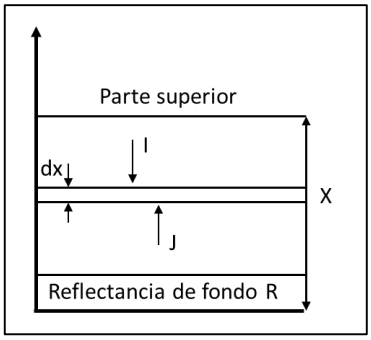

Figura 1. Diagrama de una sección trasversal en una lámina de muestra en polvo.

- *Espectroscopia de absorción.*

Las medidas de absorbancia de las distintas muestras de perovskita $MA_{1-x}Gua_xPbI_3$, $FAPbI_3$, $MAPbI_3$, Gua_2PbI_4 y $GuaPbI_3$ consistieron en el primer paso de la caracterización de estos materiales (junto con la reflectancia difusa). En el caso de la perovskita $MA_{1-x}Gua_xPbI_3$ se han comparado los espectros de las distintas muestras preparadas (para valores de $0 \leq x \leq 1$) y se midió la absorbancia depositándolas sobre un sustrato de vidrio en las mismas condiciones en que se prepararon las células solares. Las medidas fueron realizadas utilizando un espectrofotómetro UV/Vis/NIR PerkinElmer Lamda 1050.

En la espectroscopia de absorbancia UV/vis se estudia la interacción del espectro electromagnético con la materia en la región que abarca las longitudes de onda (λ) de 200 a 800 nm para obtener un espectro de absorbancia. A este rango de longitudes de onda le corresponden un valor de energía que se deduce según:

$$ƒ = \frac{c}{\lambda};\ ƒ = \frac{E}{h};\qquad \mathbf{E} = \frac{hc}{\lambda},$$ **[5]**, **[6]**, **[7]**

donde:

c = 299792458 m/s (velocidad de la luz en el vacío)

h = $6.62606896 \times 10^{-34}$ J·s = $4.13566733 \times 10^{-15}$ eV·s (constante de Planck)

Utilizando estas ecuaciones y pasando las longitudes de onda a energía (eV) estaríamos trabajando con radiación electromagnética con energía de 6.1-1.4 eV.

La absorción de un fotón resulta en la transición electrónica desde un estado basal a un estado excitado (Figura 2). En una molécula, la distancia energética entre un estado fundamental y uno excitado está determinado por la fuerza de unión entre los núcleos y los electrones. Por lo tanto, diferentes sustancias absorben a diferentes longitudes de onda. La longitud de onda de máxima absorción de una sustancia es una de las propiedades características de esa sustancia, por esta razón el espectro de absorbancia es fundamental para caracterizar distintos tipos de perovskitas.

La transición más probable a menudo ocurre desde el orbital molecular ocupado más alto (HOMO) hasta el orbital molecular desocupado más bajo (LUMO) como se ilustra en la Figura 2.

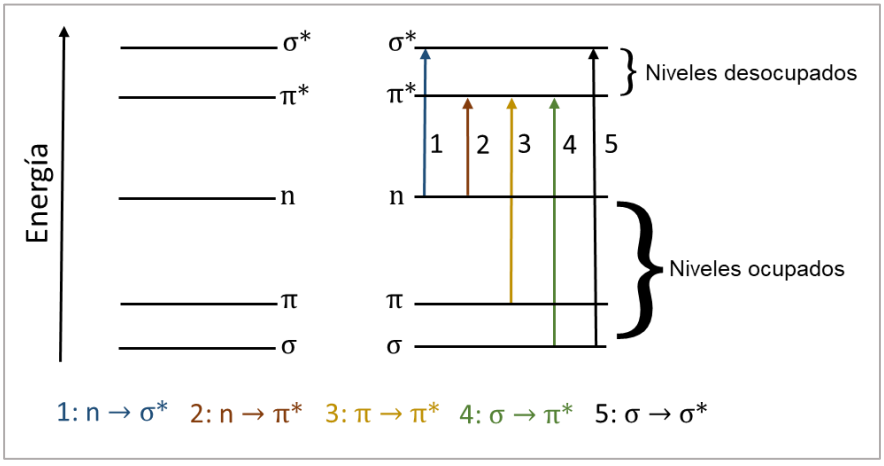

Figura 2. Diagrama de transiciones electrónicas.

La absorción de la luz se mide experimentalmente en términos de transmitancia (T) o absorbancia (A). La transmitancia se define como:

$$\mathbf{T} = \frac{I}{I_0}, \textbf{ [8]}$$

donde I es la intensidad de la luz después de que pasa a través de la muestra y I_0 es la intensidad de la luz que sale de la lámpara. La relación entre A y T es:

$$\mathbf{A} = -\log_{10} \boldsymbol{T} = -\log_{10}(\frac{\boldsymbol{I}}{\boldsymbol{I_0}}) \quad \textbf{[9]}$$

- *Espectrofotometro.*

Los instrumentos modernos de medición de la absorción, como los espectrofotómetros, generalmente pueden mostrar los datos como transmisión, %-transmisión o absorbancia. Un espectrofotómetro es un instrumento que hace incidir luz de una serie completa de longitudes de onda a través de una muestra y también a través de una referencia que solo tiene el disolvente (en caso de disoluciones) o el sustrato (en el caso de capas finas). En ambos casos se compara la intensidad de la luz que proviene de la fuente con la de la luz que sale de la muestra para producir el espectro adecuado.

De hecho, la atenuación de la luz en un experimento de absorbancia se produce a partir de muchos procesos, como la absorbancia del disolvente, los reflejos de la interface entre el aire y la muestra, la muestra y la cubeta, además del cromóforo. Estos factores a menudo se eliminan al definir I0, como la luz que pasa a través de la muestra "en blanco" (corrección de "línea base") o muestra de referencia (Figura 3).

2. Fotoluminiscencia.

Las medidas en estado estacionario de fotoluminiscencia (PL) fueron realizadas mediante un espectrofotómetro (Gilden Photonics) mientras que las medidas de micro-PL fueron obtenidas en un microscopio Raman Renishaw InVia con un objetivo L100X (con una abertura alrededor de 300 nm). El mapeo de fotoluminiscencia fue grabado utilizando un láser verde a 532 nm y con una intensidad de 100 μJ cm^{-2}. Las muestras para este análisis fueron preparadas depositando la perovskita mediante spincoating, para

posteriormente poner una capa de polimetilmetacrilato (PMMA) la cual se usaba de barrera para proteger la muestra de la humedad y oxígeno.

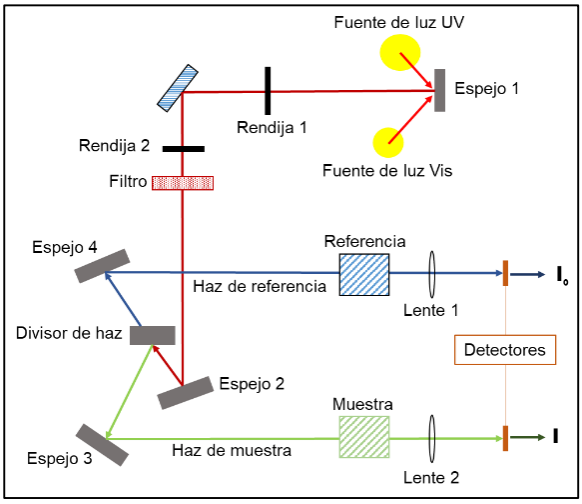

Figura 3. Esquema de un espectrofotómetro UV-visible. Un instrumento típico de doble haz consiste en una fuente de luz, un monocromador, dos detectores, un portamuestras y un portador de referencia. En un instrumento típico de doble haz, la luz que emana de la fuente de luz se divide en dos haces, el haz de muestra y el haz de referencia. La fuente de luz para la radiación electromagnética en la región ultravioleta del espectro es usualmente una lámpara de deuterio y para las longitudes de onda en la región visible del espectro se usa una segunda fuente de luz, una lámpara de tungsteno.

- *Fundamentos básicos de fluorescencia.*

Después de la fotoexcitación, las especies en el estado excitado regresan a sus estados basales, como se ilustra en la figura 4, liberándose el exceso de energía en forma de luz (proceso radiativo) o través de algún otro mecanismo (proceso no radiativo). La energía de la luz emitida (fotoluminiscencia) se relaciona con la diferencia en los niveles de energía entre dos estados electrónicos implicados en la transición entre el estado excitado y el estado de equilibrio[2].

En el proceso de desactivación del estado excitado también intervienen mecanismos de relajación vibracionales los cuales disipan la energía de manera no radiativa. Posteriormente el electrón decae a un estado

vibracional dentro del estado electrónico fundamental emitiendo de esta manera un fotón con una energía diferente al absorbido. Aprovechando este fenómeno se pudo comparar los diferentes espectros de fotoluminiscencia los cuales son característicos de cada material y de esta manera verificar haciendo un mapeo de fotoluminiscencia en un área de unos 36 μm^2 que no existía segregación de fases.

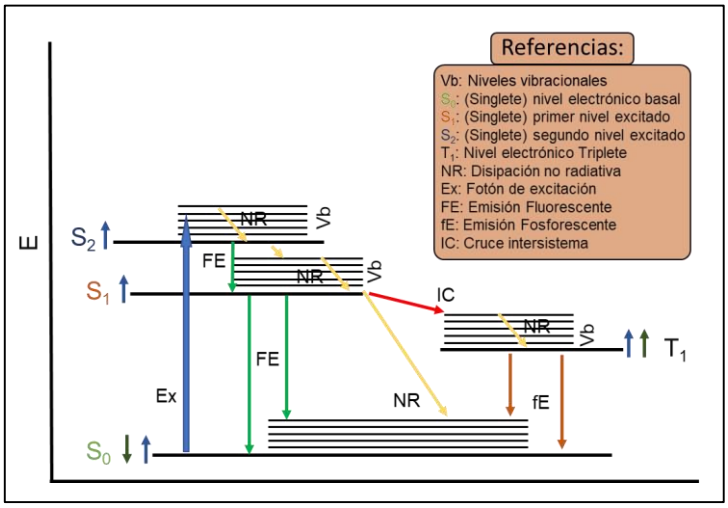

Figura 4. Diarama de Jablonski

3. Difracción de rayos X (DRX)

Las muestras de perovskita basada en guanidinio ($MA_{1-x}Gua_xPbI_3$) depositadas en capa fina fueron medidas en un difractómetro de rayos X Bruker D8 ADVANCE (geometría Bragg-Brentano, con una fuente de Cu, λ = 1.5406 Å). Se configuró el experimento para que registrara en el intervalo de 5-80º, pero solo se estudió el rango de 5-55º, el cual es el que contiene más información para obtener la estructura del cristal.

Las muestras en polvo de $MAPbI_3$ y $FAPbI_3$ que fueron preparadas mediante el molino de bolas se midieron en un difractómetro Bruker D8 ADVANCE operando a 40 kV y 40 mA usando como fuente de radiación Cu Kα (1.54060

Å) y Kβ (1.39222 Å). La medida se realizaron in-situ utilizando un horno HTK 1200N y la temperatura fue controlada mediante una unidad de control de temperatura TTCU 1000N. Para las muestras en polvo de $GuaPbI_4$ (2D) y $GuaPbI_3$ (1D) se utilizó un difractómetro de rayos X Bruker DISCOVERY operando a 40kV y 40mA utilizando como fuente de radiación Cu con Kα (1.54060 Å).

- *Estado cristalino*

Como los materiales cristalinos mantienen un ordenamiento de sus átomos e iones en su estructura, se define como celda unidad a la porción más simple de la estructura que al repetirse mediante traslación reproduce a todo el cristal (Figura 5).

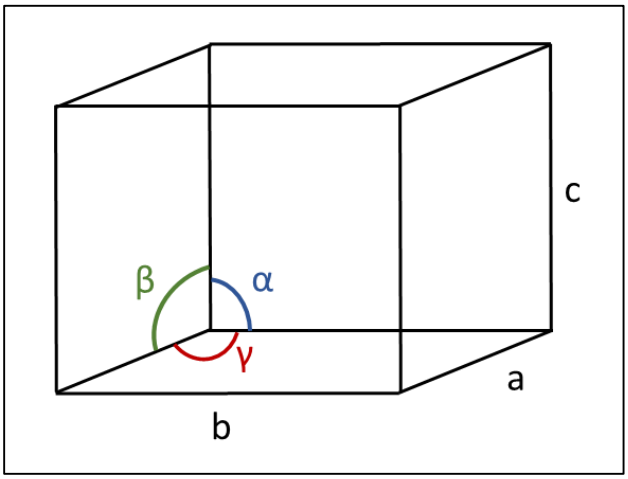

Figura 5. Ilustración de una celda unidad y sus parámetros.

La variación de los parámetros de la celda unidad da lugar a 7 sistemas cristalinos que se muestran en la tabla 1ex.

Tabla 1. Parámetros de la celda unidad para distintos sistemas cristalinos.

Parámetros de celda unidad	Sistema cristalino
$a \neq b \neq c, \alpha \neq \beta \neq \gamma$	Triclínico
$a \neq b \neq c, \alpha = \gamma = 90^o, \beta \neq 90^o$	Monoclínico
$a \neq b \neq c, \alpha = \beta = \gamma = 90^o$	Ortorrómbico
$a = b \neq c, \alpha = \beta = \gamma = 90^o$	Tetragonal
$a = b = c, \alpha = \beta = \gamma \neq 90^o$	Trigonal
$a = b \neq c, \alpha = \beta = 90^o, \gamma = 120^o$	Hexagonal
$a = b = c, \alpha = \beta = \gamma = 90^o$	Cúbico

Además de estos 7 sistemas cristalinos, dependiendo de la simetría traslacional de la estructura cristalina, se pueden caracterizar mediante la red de Bravais (14 redes de Bravais diferentes). Estas redes pueden ser:

- Tipo P. se denomina primitiva y tiene puntos de red en los vértices de la celda.
- Tipo I. Red centrada en el interior. Esta presenta puntos de red en los vértices de la celda y en el centro de la celda.
- Tipo F. Red centrada en todas las caras. Presenta puntos de red en los centros de todas las caras, así como en los vértices.
- Tipo C. red centrada en la base.

Además de la simetría traslacional en una red cristalina, existen también elementos de simetría. Los cuales son:

- Centro de inversión.
- Plano de reflexión.
- Ejes de rotación con diferentes órdenes (2, 3, 4 y 6).

- Ejes de rotación-inversión de orden 3, 4 y 6.

Estos elementos de simetría pueden coexistir en una estructura cristalina dando lugar a los grupos puntuales de simetría, habiendo un total de 32 grupos que cuando se combinan con los elementos de simetría traslacionales y las 14 redes de Bravais se obtienen los 230 grupos espaciales de simetría posibles. Estos grupos determinan todos los tipos y posiciones de los elementos de simetría que son posibles para una estructura cristalina dada.

Los puntos de red que muestran la simetría traslacional de una estructura pueden ser conectados mediante los planos de red. Cada plano pertenece a un conjunto de planos equidistantes que contienen todos los puntos de red, estos planos se nombran utilizando los índices de Miller. Estos índices se designan convencionalmente como h, k y l los cuales se escriben entre paréntesis (h,k,l) y son enteros, positivos, negativos o cero. La separación de los planos se conoce con el nombre de espaciado d_{hkl}. La relación entre el espaciado d y los parámetros de red pueden determinarse geométricamente y dependen de cada sistema cristalino. A medida que se disminuye la simetría del sistema cristalino aumenta la complejidad de la expresión para d_{hkl}.

Tabla 3. Expresión de d_{hkl} para distintos sistemas cristalinos.

Sistema Cristalino	Expresión para d_{hkl}
Cúbico	$\mathbf{1/d^2 = (h^2 + k^2 + l^2) / a^2}$
Tetragonal	$\mathbf{1/d^2 = ((h^2 + k^2) / a^2) + (l^2/c^2)}$
Ortorrómbico	$\mathbf{1/d^2 = (h^2/a^2) + (k^2/b^2) + (l^2/c^2)}$
Hexagonal	$\mathbf{1/d^2 = 4(h^2 + hk + k^2) / 3a^2 + (l^2/c^2)}$
Monoclínico	$\mathbf{1/d^2 = (1/sen^2(\beta))\cdot(h^2/a^2 + k^2 sen^2(\beta)/b^2 + l^2/c^2 - 2hlcos\beta/ac)}$
Triclínico	**Expresión compleja**

- *Interacción de los rayos X con la materia (Difracción).*

La interacción de los rayos X y la materia fundamentalmente ocurre mediante dos procesos. El primero de ellos es un proceso en el cual el haz incidente es desviado sin pérdida de energía (es el que origina el fenómeno de la difracción). En el segundo caso los fotones del haz incidente sufren una serie de choques inelásticos al incidir sobre un blanco y su energía causa un incremento de la temperatura de la muestra o da lugar al fenómeno de fluorescencia. Considerando el primer caso donde un rayo es difractado puede definirse como un rayo compuesto de un gran número de rayos dispersados que se refuerzan mutuamente. Por lo tanto, la difracción es básicamente un fenómeno de dispersión.

Los átomos dispersan la radiación que incide sobre ellos en todas las direcciones, y en algunas direcciones la radiación dispersada estará completamente en fase y por lo tanto se refuerzan mutuamente para formar rayos difractados (Figura 6).

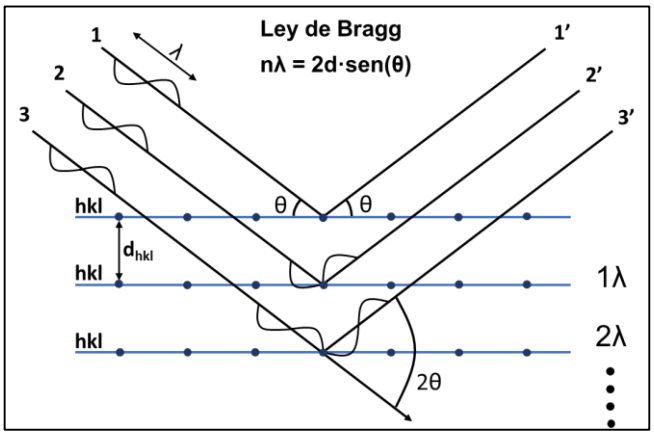

Figura 5. Esquema de la ley de Bragg.

Estos rayos dispersados estarán completamente en fase si la diferencia de fase es igual a nλ (siendo n un numero entero), siendo este valor:

$$\mathbf{n\lambda = 2d\,sen\theta} \quad \mathbf{[10]}$$

Esto se conoce como la Ley de Bragg (deducida por los físicos británicos William Henry Bragg y su hijo William Lawrence Bragg en 1913) y define las condiciones fundamentales que deben cumplirse para que ocurra la difracción. Por lo tanto, la difracción es esencialmente un fenómeno de dispersión en el que cooperan un gran número de átomos, ya que debido a que los átomos están dispuestos periódicamente en una red, los rayos X dispersados por estos tienen una relación de fase definida entre ellos; estas relaciones de fase derivan de tal manera que en la mayoría de las direcciones se produce una interferencia destructiva, pero en unas pocas direcciones se produce una interferencia constructiva formando así los rayos difractados. La difracción de rayos X de un átomo es la resultante de la dispersión por cada electrón por lo que cabe esperar que dependa directamente del número de electrones que posee cada átomo en la red cristalina. Consideran esto y teniendo los respectivos difractogramas de las distintas muestras de perovskita mediante un software (TOPAS o Materials Studio) se indexaron los distintos difractogramas para obtener sus respectivas celdas unidad, los cual se refinaron por el método de Rietveld[3],[4]

- **Diagrama de Difracción de Rayos X**

Un diagrama de difracción de rayos X (difractograma de rayos X) recoge las intensidades en función de los ángulos de difracción 2θ obteniéndose una serie de picos.

Del difractograma los datos más importantes que se pueden obtener a partir de él son:

- Posición de los picos expresados en valores normalmente 2θ, aunque también se pueden poner en función de θ, d, ó $1/d^2$.
- Intensidad de pico tomando la altura del pico o en casos de análisis más específicos se puede tomar el área.

- Perfiles de los picos. Aunque es menos utilizado es muy útil para sacar información sobre el tamaño de grano y tensiones.

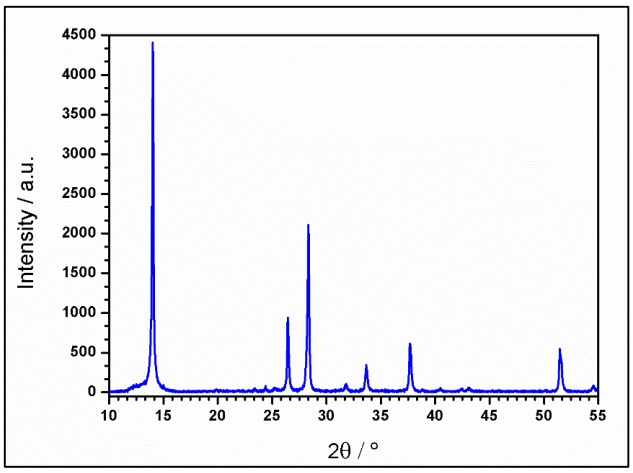

Figura 6. Difractograma de Rayos X.

El método Williamson-Hall es muy utilizado en cristalografía para determinar el tamaño de cristal y las micro-tensiones presentes en un cristal. Este método fue fundamental en esta Tesis, gracias a él se demostró que el cation guanidinio estaba dentro del cristal 3D en la perovskita $Ma_{1-x}Gua_xPbI_3$ ($x \leq 0.25$). Este método se basa en el principio de que las fórmulas para el ensanchamiento por el tamaño, B_L, y el ensanchamiento de micro-tensiones, B_e, varían de manera bastante diferente con respecto al ángulo de Bragg, θ. Estos ensanchamientos se definen según:

- $\boldsymbol{B_L(\theta) = \frac{K\lambda}{L\,cos(\theta)}}$ (ensanchamiento por el tamaño) [11]

- $\boldsymbol{B_e(\theta) = 4\varepsilon\frac{sen\,(\theta)}{cos(\theta)}}$ (ensanchamiento por las micro-tensiones) [12]

Donde:

B: Ancho del pico. L: tamaño del cristal

K: constante de Scherrer[5] ε: Micro-tensiones

Como la contribución $B_L(\theta)$ varía según 1/cos(θ) mientras que en el caso de $B_e(\theta)$ varía según sin(θ)/cos(θ) y considerando que ambas contribuciones están presentes en el cristal, la simplificación de Williamson-Hall supone que la convolución es una suma simple y utilizando esto como correcto obtenemos:

1. $\boldsymbol{B_{Muestra}(\theta) = B_L(\theta) + B_e(\theta) = \frac{K\lambda}{L\,cos(\theta)} + 4\varepsilon\frac{sen\,(\theta)}{cos\,(\theta)}}$, [13]

Despejando el cos(θ)

2. $\boldsymbol{B_{Muestra}(\theta)\,cos(\theta) = \frac{K\lambda}{L} + 4\varepsilon\,sen(\theta)}$ [14]

Haciendo una representación de $\boldsymbol{B_{Muestra}(\theta)\,cos(\theta)\ vs\ sin(\theta)}$, donde la pendiente es 4ε que corresponde a las micro-tensiones y el corte en el origen a $\boldsymbol{\frac{k\lambda}{L}}$.

4. Deposición mediante la técnica de Spincoating.

Las células solares fueron preparadas utilizando sustratos recubiertos de FTO (oxido de estaño dopado con flúor). Sobre estos sustratos fue depositado mediante spray pirolisis una fina capa de TiO_2. Posteriormente se deposita otra capa de TiO_2 mesoporosa y sobre esta las diferentes muestras de perovskita $MA_{1-x}Gua_xPbI_3$ para ello se utilizó la técnica de spincoating cuyo fundamento teórico fue descrito por primera vez en 1958 y está gobernada por las siguientes ecuaciones[6], [7]:

Balance de fuerzas:

$$-\eta\frac{\partial^2 v}{\partial z^2} = \boldsymbol{\rho\omega^2}\ [15]$$

y

$$\boldsymbol{\frac{\partial h}{\partial t} = -\frac{1}{r}\frac{\partial(rq)}{\partial r}}\ [16]$$

Donde el eje z es el eje de rotación, r es la dirección radial y se asume que tiene una simetría cilíndrica. La velocidad v(z) en la dirección r, η es la viscosidad, ρ es la densidad, la velocidad angular $\omega = 2\pi f$, y se define viscosidad cinética como $\nu = \eta/\rho$. El flujo total por unidad de la circunferencia esta dado por:

$$\mathbf{q} = \boldsymbol{\omega^2 r h^3 / 3\nu} \quad [17]$$

Las soluciones a dichas ecuaciones cuando se considera que no hay evaporación (no hay cambio de $\boldsymbol{\nu}$) manteniendo un perfil uniforme en el cual el espesor (h) decrece según:

$$\mathbf{h} = \boldsymbol{h_0}[\mathbf{1} + (\boldsymbol{4\omega^2/3\nu})\boldsymbol{h_0^2 t}]^{\mathbf{1/2}} \quad [18]$$

Esta sería la expresión que describiría el espesor en función de la viscosidad, densidad del disolvente, la velocidad angular y el tiempo empleado en el proceso. Esta información es fundamental ya que de esta manera se puede controlar el espesor de la perovskita depositada en el sustrato, la cual está directamente relacionado al rendimiento de la célula solar[8].

5. Medidas de Espectroscopia de fotoelectrones emitidos por rayos X (XPS) y espectroscopia fotoelectrónica ultravioleta (UPS).

Las medidas de XPS para el caso de las muestras compactadas en pastillas de $MAPbI_3$, $FAPbI_3$, Gua_2PbI_4 y $GuaPbI_3$ se realizaron en un espectrómetro SPECS Sage HR 100 con una fuente de rayos X no monocromático (Aluminio Kα $E_{fotón}$ = 1486.6 eV y 300W), colocado perpendicularmente al eje del analizador y calibrado utilizando la línea $3d_{5/2}$ de la Ag con una anchura a media altura de 1.1 eV. Todas las medidas fueron realizadas en alto vacío ($8 \cdot 10^{-8}$ mbar).

Las medidas para el caso del $MA_{1-x}Gua_xPbI_3$ se realizaron en capa fina depositando la perovskita sobre un sustrato de silicio para que fuera conductor. Para esta medida se realizó un ultra vacío ($2 \cdot 10^{-10}$ mbar)

utilizando una fuente de He (Omicron) con una energía de excitación de 21.1 eV para el UPS y una fuente de rayos X de Al (Kα con $E_{fotón}$ = 1486.6 eV) para XPS. Como referencia para el XPS se tomó el C 1s a 285 eV.

Las medidas de XPS se realizaron con el fin de obtener las relaciones Pb/I y el valor de la energía de unión del N-C en las distintas muestras (FA, MA y Gua).

- **Fundamentos básicos XPS y UPS.**

El XPS es una técnica espectroscópica cuantitativa sensible a la superficie[9] (penetra hasta una profundidad de unos 10 nm de la superficie) que mide la composición elemental en partes por mil, fórmula empírica, estado químico y estado electrónico de los elementos que existen en el material.

En esta técnica el material es irradiado con un haz de rayos X con una longitud de onda conocida (Al, $E_{fotón}$ = 1486.7 eV) produciéndose la emisión de electrones del material y lo que se mide es la energía cinética de los electrones emitidos. La energía de unión de cada electrón emitido se puede determinar usando la ecuación de Ernest Rutherford:

$$\boldsymbol{E_{Unión} = E_{Fotón} - (E_{Cinética} + \phi)} \quad [19]$$

Donde:

$E_{Unión}$: Energía de unión del electrón.

$E_{Fotón}$: Energía del fotón de rayos X.

$E_{cinética}$: Energía la energía cinética del electrón.

ϕ: Función de trabajo.

La función de trabajo depende tanto del instrumento como del material y también es un factor de corrección instrumental que representa la energía cinética que el fotoelectrón deja de absorber por el detector.

En el caso de UPS[10] opera usando los mismos principios que en XPS, la única diferencia es la energía ionizante ya que no se usa rayos X si no energía en el rango de ultravioleta. Como se utilizan fotones de menor energía, la fotoemisión de los niveles más cerca del núcleo no están

accesibles con UPS, por lo tanto, el espectro se limita a la región de la banda de valencia del material. Hay dos tipos de tipos de experimentos que se pueden realizar en UPS: adquisición de banda de valencia y medición de la función de trabajo.

Bibliografia

[1] J. Torrent and V. Barrón, “Diffuse reflectance spectroscopy,” *Methods Soil Anal. Part*, no. 5, pp. 367–385, 2008.

[2] T. Aoki, “Photoluminescence Spectroscopy,” *Charact. Mater.*, vol. 3, pp. 1–12, 2002.

[3] D. K. Smith, J. Fiala, and E. Ryba, “Book Reviews The Rietveld Method,” *B. Rev. Rietveld*, vol. 25, no. 6, pp. 252–254, 1994.

[4] H. M. Rietveld, “A profile refinement method for nuclear and magnetic structures,” *J. Appl. Crystallogr.*, vol. 2, no. 2, pp. 65–71, 1969.

[5] A. L. Patterson, “The scherrer formula for X-ray particle size determination,” *Phys. Rev.*, vol. 56, no. 10, pp. 978–982, 1939.

[6] A. G. Emslie, F. T. Bonner, and L. G. Peck, “Flow of a viscous liquid on a rotating disk,” *J. Appl. Phys.*, vol. 29, no. 5, pp. 858–862, 1958.

[7] D. Meyerhofer, “Characteristics of resist films produced by spinning,” *J. Appl. Phys.*, vol. 49, no. 7, pp. 3993–3997, 1978.

[8] M. Xiao *et al.*, “A fast deposition-crystallization procedure for highly efficient lead iodide perovskite thin-film solar cells,” *Angew. Chemie - Int. Ed.*, vol. 53, no. 37, pp. 9898–9903, 2014.

[9] N. Alov, “Fifty years of x-ray photoelectron spectroscopy,” *J. Anal. Chem.*, vol. 60, no. 3, pp. 331–334, 2005.

[10] S. Hufner, *Photoelectron Spectroscopy*, vol. 21, no. 1. 1970.

Capítulo III

Publicaciones

Chapter III

Publications

Angewandte International Edition Chemie

Impact Factor: 11.994

International Edition: DOI: 10.1002/anie.201607397
German Edition: DOI: 10.1002/ange.201607397

Benign-by-Design Solventless Mechanochemical Synthesis of Three-, Two-, and One-Dimensional Hybrid Perovskites.

*Alexander D. Jodlowski, Alfonso Yépez, Rafael Luque, * Luis Camacho, and Gustavo de Miguel**

A. D. Jodlowski, Prof. L. Camacho, Prof. G. de Miguel Institute of Fine Chemistry and Nanochemistry Department of Physical Chemistry and Applied Thermodynamics University of Cordoba, Campus Universitario de Rabanales Edificio Marie Curie, 14014 Córdoba (Spain)

Dr. A. Yépez, Prof. R. Luque Departamento de Química Orgánica, Universidad de Córdoba Edificio Marie Curie, Ctra Nnal IVa Km 396, 14014 Córdoba (Spain)

Abstract: *Organic–inorganic hybrid perovskites have attracted significant attention owing to their extraordinary optoelectronic properties with applications in the fields of solar energy, lighting, photodetectors, and lasers. The rational design of these hybrid materials is a key factor in the optimization of their performance in perovskite-based devices. Herein, a mechanochemical approach is proposed as a highly efficient, simple, and reproducible method for the preparation of four types of hybrid perovskites, which were obtained in large amounts as polycrystalline powders with high purity and excellent optoelectronics properties. Two archetypal three-dimensional (3D) perovskites ($MAPbI_3$ and $FAPbI_3$) were synthesized, together with a two-dimensional (2D) perovskite (Gua_2PbI_4) and a "double-chain" one-dimensional (1D) perovskite ($GuaPbI_3$), whose structure was elucidated by X-ray diffraction.*

Three-dimensional (3D) organic–inorganic hybrid perovskites recently emerged as a breakthrough in the field of photovoltaics owing to their potential to enable power conversion efficiencies (ca. 20%) in perovskite-based devices that are comparable to those reported for commercial silicon based solar cells.[1] This change of paradigm in photovoltaics prompted a renaissance of interest in the wider family of hybrid perovskites, including two-dimensional (2D), one-dimensional (1D), and zero-dimensional (0D) materials, with improved flexibility in the type of organic cations that can be employed.[2] The rediscovery of these new types of hybrid materials opened up a multitude of optoelectronics applications that remained unexplored for many years, including light-emitting diodes,[3] photodetectors,[4] and lasing.[5] However, the excellent optoelectronic properties of these materials and, more importantly, their impact on the performance of perovskite-based devices are highly sensitive to the adopted synthetic strategy. In general, the preparation of particular device architectures incorporating high-quality perovskite crystals is required for most applications. Traditional synthetic methods to prepare hybrid perovskites include 1) precipitation from solution and 2) gas-phase deposition.[6] In the solution-based method, stoichiometric mixtures of metal halides and organic ammonium halide precursors are normally dissolved in dimethylformamide (DMF) or dimethyl sulfoxide (DMSO). For the preparation of single perovskite crystals at the micrometer scale, the solvent is allowed to slowly evaporate at room temperature or under mild heating. However, the solution containing the precursors needs to be spread homogeneously over a substrate by different methods (spin coating, spray coating, screen printing, or dip coating) for the preparation of thin films and/or for particular applications.[7] The deposition can be carried out in a single step process or through a two-step process, in which the metal halide is first deposited on the substrate, followed by the subsequent incorporation of the organic cation into the film to form the perovskite. In the

vapor-phase method, the precursors are generally co-evaporated in a vacuum deposition chamber onto a substrate by the use of two separate sources to form uniform and controlled-thickness films.[8] Despite the remarkable advances in the development of simple and inexpensive methods to fabricate 3D hybrid perovskites, significant efforts are ongoing in the design of new strategies that allow the synthesis of high-quality crystals.

Mechanochemistry has emerged as an attractive alternative synthetic process featuring remarkable simplicity, swiftness, and reproducibility in line with unprecedented green credentials (e.g. solventless solid-state synthesis) for the design of a wide range of nanomaterials, including supported nanoparticles and MOFs.[9] The combination of the mechanical energy generated under ball-milling conditions and the inherent chemical modification of structures/surfaces make this methodology extremely promising for nanomaterials design, particularly for alternative greener perovskite syntheses.

We disclose herein a novel and efficient mechanochemical approach for the design of polycrystalline hybrid perovskites. The precursors used in this study, PbI_2 and methylammonium (MAI), formamidinium (FAI), or guanidinium iodide (GuaI), were mixed in a 1:1 molar ratio inside a ball mill under an ambient atmosphere to produce large amounts of polycrystalline powders. One of the main advantages of the proposed protocol is the solventless nature of the synthetic process for perovskite formation. Further advantages are the swiftness, simplicity, and reproducibility of the method as well as its significant potential for extension to the design of various structures. In this way, two 3D hybrid perovskites ($MAPbI_3$ and $FAPbI_3$), a 2D perovskite containing Gua, and a “double-chain” 1D perovskite with $GuaPbI_3$ stoichiometry were synthesized. In particular, the structure of 1D $GuaPbI_3$ perovskite was elucidated for the first time owing to the high purity

of the polycrystalline powder.[10] The different powders were characterized comprehensively by X-ray diffraction, diffuse reflectance spectroscopy, X-ray photoelectron spectroscopy, thermogravimetric analysis, differential scanning calorimetry, and scanning electron microscopy.

Figure 1 shows a photograph of the black powder synthesized with MAI (left), the light-yellow powder synthesized with FAI (center left), and the intense-yellow powder synthesized with GuaI (center). We annealed all powders up to approximately 170ºC in an oven and then cooled them down to room temperature to explore potential phase transitions or further chemical reactions that could potentially take place in the materials. The powder prepared with FAI turned black at approximately 150ºC and remained black upon cooling to 30ºC (Figure 1, center right). The black color of the powders prepared with MAI and FAI agrees well with those reported for the well-known 3D hybrid perovskites $MAPbI_3$ and α-$FAPbI_3$ prepared by other synthetic protocols. [11] Annealing gave a pale-yellow powder for material prepared with GuaI, and this color also remained unchanged after cooling to room temperature (Figure 1, right).

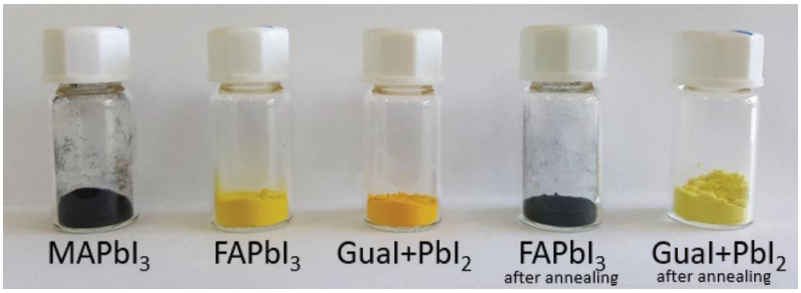

Figure 1. Photograph of the different as-prepared powders synthesized by ball milling. The black powder containing FAI (center-right vial) and the pale-yellow powder with GuaI (right vial) were obtained by heating the corresponding as-prepared powders at 170ºC, followed by cooling to room temperatur

To assess the existence of phase transitions and the stability of the as-prepared powders, we conducted thermogravimetric analysis (TGA) and

differential scanning calorimetry (DSC) for each sample (see Figure S1 in the Supporting Information). The TGA curves of powders prepared with MAI and FAI showed no significant weight loss up to 250–300ºC. In both cases, this behavior supports the good stability of the 3D hybrid perovskite particles, which started to degrade at 250ºC (usually associated with the loss of HI).[12] A closer examination of the TGA curves pointed to a slight drop in the signal (0.05–0.1%) around 55 and 130ºC. Welldefined endothermic peaks could be observed around 60 and 135ºC in the DSC curves for $MAPbI_3$ and $FAPbI_3$, respectively. These temperatures are in good agreement with reported phase transitions from tetragonal to cubic symmetry in $MAPbI_3$ and from a non-perovskite phase (d-phase) to trigonal symmetry (a-phase) in $FAPbI_3$.[11] Furthermore, the DSC curves also revealed additional endothermic peaks at 115 and 138ºC for $MAPbI_3$ and 87 and 173ºC for $FAPbI_3$.

These signals could be assigned to the elimination of water upon heating, since the same perovskites prepared by solvent-assisted methods also revealed a minor weight loss at approximately 100ºC associated with physisorbed water as well as another signal drop at 180ºC attributed to more strongly bound water.[13] No weight loss was observed in the studied temperature range (up to 200ºC) for powders prepared with GuaI before annealing (see Figure S1C), with the presence of an endothermic peak at 134ºC as observed by DSC analysis. Similarly, no weight loss was detected in the same sample after annealing (Figure S1D), with the DSC analysis showing an endothermic peak shifted to 160ºC, as reported for a perovskite with $GuaPbI_3$ stoichiometry.[14]

We subsequently characterized the crystalline powders obtained from the mechanosynthesis process by X-ray diffraction (XRD) studies to investigate the nature and purity of the perovskite materials. The experimental XRD pattern for the powder prepared with MAI (Figure 2A) revealed a tetragonal structure of the 3D hybrid $MAPbI_3$ perovskite upon comparison with the

previously reported simulated structure pattern (I4/mcm space group).[11] The lattice parameters derived from our crystallographic analysis (see Figure S2A) are a=b=8.879(3) Å and c=12.663(4) Å , highly consistent with those previously reported.[11] Clearly, no diffraction peaks of the precursors (typically present as characteristic diffraction peaks at 12.8º for PbI_2 and 20º for MAI) are visible in the experimental diffractogram. These findings demonstrate the high yields of the mechanochemical synthesis of $MAPbI_3$ with the absence of crystalline impurities. To investigate the phase transitions of $MAPbI_3$, we conducted variable-temperature powder XRD analysis of the as-prepared powders.

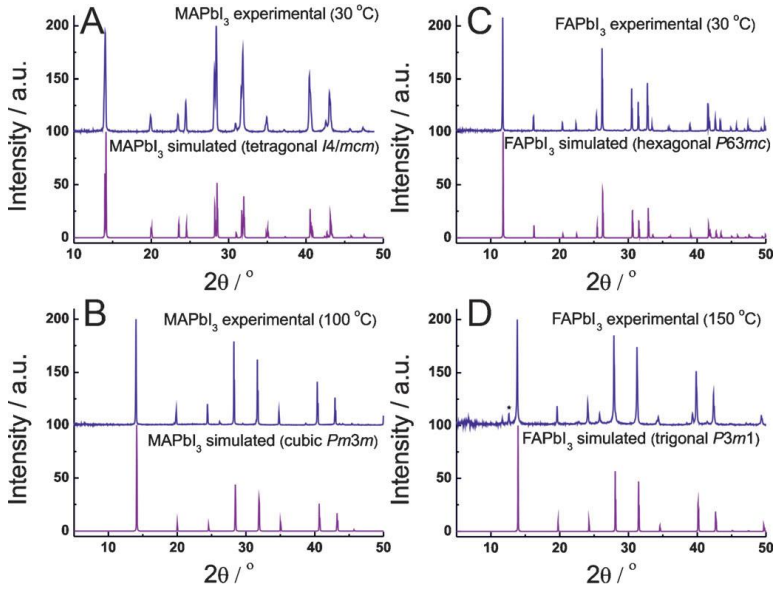

Figure 2. Blue lines: Experimental XRD patterns of the powders synthesized with MAI at 30º (A) and 100ºC (B), and with FAI at 30º (C) and 150ºC (D). Purple lines: Simulated XRD patterns for the 3D hybrid perovskites $MAPbI_3$, in the tetragonal (A) and cubic phase (B), and $FAPbI_3$, with hexagonal (C) and trigonal symmetry (D). The star in (D) indicates the reflection peak of PbI_2.

The XRD patterns (30–100ºC) showed an abrupt disappearance of reflections at 23.4 and 30.9º in the 55–60ºC temperature range (see Figure S3), thus matching the DSC results. This behavior was previously ascribed

definitively to a change in the crystallographic phase from tetragonal to cubic symmetry in $MAPbI_3$.[11] No changes were evident in the XRD patterns upon increasing the temperature up to 100ºC, thus confirming the high stability of the cubic phase in the studied temperature range. Figure 2B displays the experimental (at 100ºC) and simulated (Pm3m space group) XRD patterns for the cubic $MAPbI_3$ structure, with an excellent match between the two patterns. From a Pawley data fit, we obtained a lattice parameter of a=b=c= 6.3430(9) Å (see Figure S2B). Figure 2C shows XRD powder patterns for samples prepared with FAI and PbI_2 at room temperature as well as the simulated pattern for the d-phase of the $FAPbI_3$ structure.[11] Excellent agreement was observed between the two patterns, with no residual reflection peaks from any other concurrent structure, thus demonstrating the presence of a pure phase obtained under ball milling. The absence of impurities in this material can contribute to its rapid implementation in optoelectronics. A Pawley fit of the experimental XRD pattern (see Figure S2C) allowed us to obtain the lattice parameters of the unit cell: a=b=8.6838 (7) Å and c=7.9306(7) Å. δ-$FAPbI_3$ is a layered crystal structure with hexagonal symmetry (P63mc space group) and no straightforward applications in photovoltaics owing to its limited absorption in the visible range.[11] However, at higher temperature, δ-$FAPbI_3$ is transformed into the α-$FAPbI_3$ phase with excellent photophysical properties for electronic applications. The δ-$FAPbI_3$ powder was heated up to 160ºC, and XRD measurements were gradually recorded to determine phase changes. Figure 3A shows XRD patterns of $FAPbI_3$ from 30 to 160ºC and again at 30ºC after cooling of the sample.

There was a sharp change in the diffraction pattern between 140 and 150ºC, consistent with that reported previously (ca. 140ºC) for the corresponding phase transformation.[11] The α-$FAPbI_3$ structure possesses trigonal symmetry (P3m1 space group) with lattice parameters of a=b=9.049(2) Å

and c=11.069(2) Å, as obtained by crystallographic analysis of the XRD pattern at 160ºC (see Figure S2D). Even though the majority of the diffraction peaks were indexed to the α-$FAPbI_3$ structure at higher temperatures, a minor peak at 12.68 corresponding to PbI_2 was detected in the XRD pattern. This result has also been reported for $FAPbI_3$ structures prepared by solution methods.[11] The XRD patterns at 160ºC and 30ºC after cooling are identical, thus pointing to an irreversible or slow α-to-δ-$FAPbI_3$ phase transformation in this polycrystalline powder material. Figure 3B shows the XRD pattern for the as-prepared powder with GuaI (blue line), with no signal of unreacted GuaI and a moderate peak at 12.7º indicating the presence of some PbI_2. Interestingly, most of the remaining peaks in the XRD pattern can be reasonably assigned to a previously reported bidimensional (2D) hybrid perovskite (Gua_2PbI_4 stoichiometry) with orthorhombic symmetry.[15] Unlike the 3D hybrid perovskites synthesized with MAI and FAI, this 2D hybrid perovskite consists of corrugated sheets of the $(PbI_4)_n^{2-}$ polyanion, with the Gua cations enclosed in voids and channels between the neighboring sheets.[15] In the proposed mechanochemical synthesis, the 2D perovskite is not produced quantitatively, since some PbI_2 remained unreacted. Indeed, to induce the full reactivity of PbI_2 to obtain a pure phase, we carried out the annealing process at 170ºC for 300 min and thus obtained the previously described pale-yellow powder. XRD patterns revealed the complete disappearance of the PbI_2 reflection peak at 12.78º.

In principle, a reaction may take place within the 2D hybrid perovskite during annealing, as PbI_2 is thermally stable up to 300ºC. The loss of all reflection peaks assigned to the 2D hybrid perovskite upon heating proved the previous assumption. Simultaneously, new reflection peaks appeared in the final XRD pattern, which seemed to correspond to the product of the reaction PbI_2+Gua_2PbI_4. The powder obtained from the annealing process turned orange when heated to 170ºC. This behavior has been reported previously

for the formation of $GuaPbI_3$ perovskite phases, although no further information concerning its structure was provided to date.[14]

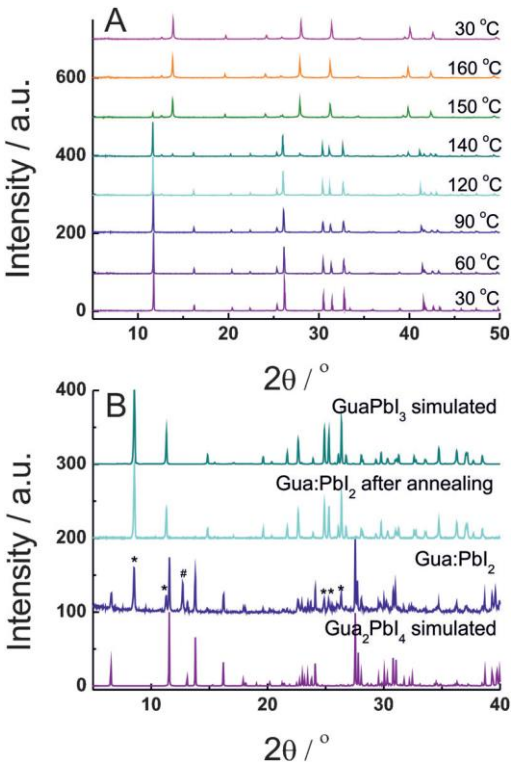

Figure 3. A) XRD patterns at different temperatures of the powder synthesized with FAI. B) XRD patterns of the as-prepared powder with GuaI:PbI_2 at 30ºC (blue line) and after the annealing process at 160ºC (light-blue line). The simulated XRD patterns of Gua_2PbI_4 and $GuaPbI_3$ are shown for comparison. The hash sign (#) in (B) indicates the reflection peak of PbI_2. The stars (B) indicate reflection peaks from the $GuaPbI_3$ structure.

We performed crystallographic analysis of the final XRD pattern after annealing to enable the complete assignment of all reflection peaks within the orthorhombic symmetry (Pna21 space group; Table 1). The elucidated structure corresponds to a 1D hybrid perovskite comprising a "double chain" of inorganic PbI_3^- separated by Gua cations stabilizing the negative charges through electrostatic interactions (Figure 4). Similar inorganic crystal structures were formed previously by the use of various organic cations, including MA and H_2O or DMF, benzidine, and 4,4'- methylenedianilinium.[16] The particular feature defining this crystal structure is the small value for one of the lattice parameters of approximately 4.5 Å.

The elucidation of the crystal structure of the perovskite containing the Gua cation ($GuaPbI_3$ stochiometry) could be particularly valuable in the field of photovoltaics owing to the increasing interest in using this symmetric cation, which could remove the hysteresis of the I–V curves.[17]

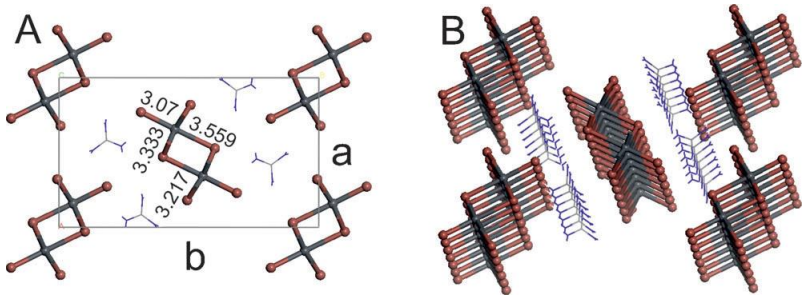

Figure 4. Crystal structure of GuaPbI3. A) Unit cell viewed down the c axis, showing the different Pb-I bond distances. B) Overview of the "double-chain" assembly in the GuaPbI3 1D hybrid perovskite.

We also performed theoretical calculations for insight into the band structure of 1D $GuaPbI_3$ (for full details, see the Supporting Information). The main contribution to the top valence band is from the I 5p state, with minor contributions from Pb 2s, Pb 5p and N 2p (see Figure S5). In the bottom conduction bands, the main component is Pb 6p, with minor contributions from I 6s and I 6p. These results indicate that I 5p electrons can be photoexcited to Pb 6p empty states (see Figure S5), in analogy with previous reports for $MAPbI_3$.[18] However, there is an additional contribution of the N 2p state at the valence band, unlike the behavior in $MAPbI_3$. The theoretical band-gap energy obtained from this calculation is 2.1 eV. The calculated band structure of 1D $GuaPbI_3$ shows a minimum band gap at the G symmetry point (see Figure S6). Both the top valence band and the bottom conduction band are broad, thus indicating the nonlocalized character of the states.

Table 1. Crystal data and structure refinement for $GuaPbI_3$ at 303 K.

Chemical formula	$PbI_3N_3H_6$
Wavelenght	1.540562 Å
Crystallographic system	Orthorhombic
Space group	Pna21
Unit-cell dimensions	a = 11.990(7) Å
	b = 20.880(9) Å
	c = 4.476(2) Å
Unit-cell volume	1120.68 $Å^3$
Z	4
Density	3.8406 g cm^{-3}
Absorption coefficient	23.259 mm^{-1}
2θ range for data collection	2-39.993°
Step size	0.016°
Time per step	288 s
Refinement method	Rietveld
R_{wp}	0.056
R_{wb}	0.056
R_p	0.099
CMACS	0.73%
DOF	23

X-ray photoelectron spectroscopy (XPS) measurements were also conducted and confirmed the stoichiometry of the crystal structures as determined by XRD (for full details, see the Supporting Information). In particular, XPS measurements revealed the absence of metallic Pb in our

mechanochemically synthesized perovskite materials, whereas metallic Pb is found in materials prepared by solvent-assisted methods.[19] Since the presence of metallic Pb is associated with iodide deficiencies, we conclude that our perovskite crystals lack these types of defects. The lack of these defects could have a beneficial impact on optoelectronic applications of these materials. We used scanning electron microscopy (SEM) to image the morphology and sizes of the synthesized materials and found particles with a distribution of sizes in the range of 10–200 mm for $MAPbI_3$ and $FAPbI_3$. The large size of the synthesized crystals originates from a lower concentration of surface states and bulk defects than in perovskite crystals prepared by solvent-assisted processes.[20] Extensive details of both investigations with additional discussion have been included in the Supporting Information.

The absorption capacity of each perovskite powder was investigated by diffuse reflectance UV/Vis spectroscopy. The optical absorption coefficient (a) can be calculated according to the Kubelka–Munk equation, $F(R)= \alpha =(1-R)^2/2R$, in which R is the reflectance of each sample.[21] Figure 5A shows the four absorption spectra for $MAPbI_3$ (black line), $FAPbI_3$ (green line), $GuaPbI_3$ (orange line), and Gua_2PbI_4 (brown line). The last spectrum resembles that of PbI_2 (the unreacted precursor of this synthesis), thus preventing the identification of the absorption features of the 2D perovskite. In the other perovskite materials, the absorption spectra are characterized by a broad and featureless absorption band typical of hybrid perovskites, with the absorption band edge shifted to the low-energy region when going from $GuaPbI_3$ (ca. 500 nm) to $MAPbI_3$ (ca. 800 nm) and $FAPbI_3$ (ca. 850 nm). The large blue shift of the absorption band in $GuaPbI_3$ as compared to that of $MAPbI_3$ and $FAPbI_3$ is associated with the disruption of the 3D network of PbI_6^{4-} octahedra owing to the bulky Gua cations in the 1D “doublechain” structure of $GuaPbI_3$. In particular for the $MAPbI_3$ and $FAPbI_3$ materials, the

extrapolation of the absorption of direct transitions at the edge gives a band gap (E_g) of 1.51 and 1.41 eV, respectively (Figure 5B).[11]

These values are in good agreement with those reported for single crystals or polycrystalline samples with large crystal sizes (>500 nm), thus strongly supporting the SEM results.[22] The small values of E_g in our $MAPbI_3$ and $FAPbI_3$ powders as compared to those found in thin films are a clear indication of the high quality of the crystals with decreased localized defect states.[11c] Regarding the band gap of $GuaPbI_3$, the extrapolation of the sharp absorption edge points to a band gap of 2.25 eV, which is fairly similar to the theoretical value and an experimental value (2.16 eV) reported for stripelike crystallites of $GuaPbI_3$ synthesized by cooling down an aqueous solution containing the precursors.[23] We conducted steady-state and time-resolved fluorescence measurements for all perovskite powders to investigate the optoeletronic properties of these materials. Clear emission spectra were observed for each powder with maxima (lmax) in the near-infrared region at 770 and 795 nm for $MAPbI_3$ and $FAPbI_3$ and at around 525 nm for both guanidinium-based perovskites, $GuaPbI_3$ and Gua_2PbI_4 (see Figure S10). The lmax values for both 3D perovskites are in close agreement with those reported for single crystals, whereby an increasing size of the crystals involves a redshift of the λ_{max} value.[11c]

The fluorescence lifetimes obtained from a biexponential fit of the data were 4.5 and 37.1 ns for $MAPbI_3$ and 3.0 and 25.2 ns for $FAPbI_3$ (see Table S4). The fluorescence lifetimes are considerably longer than those reported for small grains but not as long as those reported for single crystals.[24] The relatively long fluorescence lifetimes are also a strong indication of a reduced concentration of surface and bulk defects.[24]

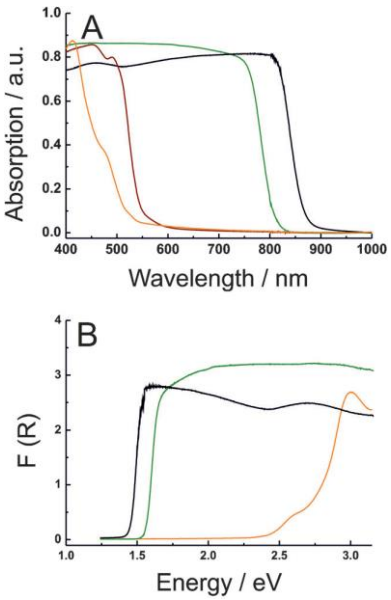

Figure 5. A) UV/Vis absorption spectra obtained in diffuse reflectance mode for the four synthesized powders: $MAPbI_3$ (green line), $FAPbI_3$ (black line), Gua_2PbI_4 (brown line), and $GuaPbI_3$ (orange line). B) Kubelka–Munk spectra of $MAPbI_3$ (green line), $FAPbI_3$ (black line), and $GuaPbI_3$

To evaluate the potential incorporation of designed perovskites in layered structures of optoelectronic devices, we prepared homogeneous thin films by spin coating on quartz substrates from DMF solutions. The fluorescence lifetimes measured for thin films (see Figure S11 for the steady-state absorption and emission spectra for all synthesized perovskites) were even longer than those observed for the powders (see Table S4). These results indicate that our 1D, 2D, and 3D hybrid perovskites synthesized by ball milling could potentially be used in the fabrication of optoelectronic devices.

In conclusion, the proposed mechanochemical synthesis offers a simple, efficient, and highly reproducible approach for the design of advanced hybrid perovskites, including 3D, 2D, and 1D materials. This solventless synthetic method is expected to pave the way for the further discovery and design of novel perovskite materials with useful properties, as currently under investigation by our research group. Additionally, the facile and cost-efficient preparation of large quantities of the perovskite materials (ca. 5–10 g per batch) remarkably simplifies their use in unexplored strategies for optoelectronics applications.

Acknowledgements

G.d.M. thanks the Ministry of Economy and Competitiveness for a “Ramón y Cajal” contract (RYC-2013-12772). G.d.M. and L.C. acknowledge the Ministry of Economy and Competitiveness for financial support (CTQ2014-56422-P). We are grateful to Prof. Carlos Pérez for his help with the XRD measurements and Prof. Vidal Barrón for his assistance with diffuse reflectance spectroscopy.

Keywords: ball milling · hybrid materials · optoelectronic properties · perovskite phases · powder X-ray diffraction

References

[1] a) M. M. Lee, J. Teuscher, T. Miyasaka, T. N. Murakami, H. J. Snaith, Science **2012**, 338, 643 – 647; b) J. Burschka, N. Pellet, S. J. Moon, R. Humphry-Baker, P. Gao, M. K. Nazeeruddin, M. Grätzel, Nature **2013**, 499, 316 – 319; c) H. Zhou, Q. Chen, G. Li, S. Luo, T.-b. Song, H.-S. Duan, Z. Hong, J. You, Y. Liu, Y. Yang, Science **2014**, 345, 542 – 546; d)W. S. Yang, J. H. Noh, N. J. Jeon, Y. C. Kim, S. Ryu, J. Seo, S. I. Seok, Science **2015**, 348, 1234 –1237.

[2] a) B. Sarapov, D. Mitzi, Chem. Rev. 2016, 116, 4558 – 4596; b) K. Meg, S. Gao, L. Wu, G. Wang, X. Liu, G. Chen, Z. Liu, G. Chen, Nano Lett. 2016, 16, 4166 – 4173.

[3] a) M. Yuan, L. N. Quan, R. Comin, G. Walters, R. Sabatini, O. Voznyy, S. Hoogland, Y. Zhao, E. M. Beauregard, P. Kanjanaboos, Z. Lu, D. H. Kim, E. H. Sargent, Nat. Nanotechnol. **2016**, 11, 872 – 877; b) S. D. Stranks, H. J. Snaith, Nat. Nanotechnol. **2015**, 10, 391 – 402; c) H. Cho, S.-H. Jeong, M.-H. Park, Y.-H. Kim, C. Wolf, C.-L. Lee, J. H. Heo, A. Sadhanala, N. Myoung, S. Yoo, S. H. Im, R. H. Friend, T.-W. Lee, Science **2015**, 350, 1222 – 1225; d) Y. Ling, Z. Yuan, Y. Tian, X. Wang, J. C. Wang, Y. Xin, K. Hanson, B. Ma, H. Gao, Adv. Mater. **2016**, 28, 305 – 311.

[4] a) Y. Fang, Q. Dong, Y. Shao, Y. Yuan, J. Huang, Nat. Photonics **2015**, 9, 679 – 686; b) B. R. Sutherland, A. K. Johnston, A. H. Ip, J. Xu, V. Adinolfi, P. Kanjanaboos, E. H. Sargent, ACS Photonics **2015**, 2, 1117 – 1123; c) L. Dou, Y. Yang, J. You, Z. Hong, W.-H. Chang, G. Li, Y. Yang, Nat. Commun. **2014**, 5, 5404.

[5] a) H. Zhu, Y. Fu, F. Meng, X. Wu, Z. Gong, Q. Ding, M. V. Gustafsson, M. T. Trinh, S. Jin, X.-Y. Zhu, Nat. Mater. **2015**, 14, 636 – 642; b) S. A. Veldhuis, P. P. Boix, N. Yantara, M. Li, T. C. Sum, N. Mathews, S. G.

Mhaisalkar, Adv. Mater. **2016**, 28, 6804 –6834; c) S. W. Eaton, M. Lai, N. A. Gibson, A. B. Wong, L. Dou, J. Ma, L.-W. Wang, S. R. Leone, P. Yang, Proc. Natl. Acad. Sci. USA **2016**, 113, 1993 – 1998; d) J. Xing, X. F. Liu, Q. Zhang, S. T. Ha, Y. W. Yuan, C. Shen, T. C. Sum, Q. Xiong, Nano Lett. **2015**, 15, 4571 – 4577.

[6] a) Y. Zhao, K. Zhu, Chem. Soc. Rev. **2016**, 45, 655 – 689; b) S. Brittman, G. W. P. Adhyaksa, E. C. Garnett, MRS Commun. **2015**, 5, 7 – 26.

[7] a) J. H. Heo, H. J. Han, D. Kim, T. K. Ahn, S. H. Im, Energy Environ. Sci. **2015**, 8, 1602 – 1608; b) A. T. Barrows, A. J. Pearson, C. K. Kwak, A. D. F. Dunbar, A. R. Buckley, D. G. Lidzey, Energy Environ. Sci. **2014**, 7, 2944 – 2950; c) S. Colella, E. Mosconi, P. Fedeli, A. Listorti, F. Gazza, F. Orlandi, P. Ferro, T. Besagni, A. Rizzo, G. Calestani, G. Gigli, F. De Angelis, R. Mosca, Chem. Mater. **2013**, 25, 4613 – 4618.

[8] a) O. Malinkiewicz, C. Roldán-Carmona, A. Soriano, E. Bandiello, L. Camacho, M. K. Nazeeruddin, H. J. Bolink, Adv. Energy Mater. **2014**, 4, 1400345; b) M. Liu, M. B. Johnston, H. J. Snaith, Nature **2013**, 501, 395.

[9] a) C. Xua, S. De, A. M. Balu, M. Ojeda, R. Luque, Chem. Commun. **2015**, 51, 6698 – 6713; b)W. Yuan, T. Friscic, D. Apperley, S. L. James, Angew. Chem. Int. Ed. **2010**, 49, 3916 – 3919; Angew. Chem. 2010, 122, 4008 – 4011; c) T. Friscic, Chem. Soc. Rev. 2012, 41, 3493 – 3510; d) S. L. James, C. J. Adams, C. Bolm, D. Braga, P. Collier, T. Friscic, F. Grepioni, K. D. M. Harris, G. Hyett, W. Jones, A. Krebs, J. Mack, L. Maini, A. G. Orpen, I. P. Parkin, W. C. Shearouse, J.W. Steed, D. C. Waddell, Chem. Soc. Rev. **2012**, 41, 413 – 447.

[10] a) X. Ma, G. K. Lim, K. D. M. Harris, D. C. Apperley, P. N. Horton, M. B. Hursthouse, S. L. James, Cryst. Growth Des. **2012**, 12, 5869 – 5872; b) V. André, A. Hardeman, I. Halasz, R. S. Stein, G. J. Jackson, D. G. Reid, M. J. Duer, C. Curfs, M. T. Duarte, T. Friscic, Angew. Chem. Int. Ed. **2011**, 50, 7858 – 7861; Angew. Chem. **2011**, 123, 8004 – 8007.

[11] a) T. Baikie, Y. Fang, J. M. Kadro, M. Schreyer, F. Wei, S. G. Mhaisalkar, M. Grätzel, T. J. White, J. Mater. Chem. A **2013**, 1, 5628 – 5641; b) M. T. Weller, O. J. Weber, P. F. Henry, A. M. Di Pumpo, T. C. Hansen, Chem. Commun. **2015**, 51, 4180 – 4183; c) Q. Han, S.-H. Bae, P. Sun, Y.-T. Hsieh, Y. Yang, Y. S. Rim, H. Zhao, Q. Chen, W. Shi, G. Li, Y. Yang, Adv. Mater. **2016**, 28, 2253 – 2258; d) M. T. Weller, O. J. Weber, J. M. Frost, A. Walsh, J. Phys. Chem. Lett. **2015**, 6, 3209 – 3212; e) N. J. Jeon, J. H. Noh, W. S. Yang, Y. C. Kim, S. Ryu, J. Seo, S. Seok, Nature **2015**, 517, 476 – 480.

[12] A. Dualeh, P. Gao, S. Seok, M. K. Nazeeruddin, M. Grätzel, Chem. Mater. **2014**, 26, 6160 – 6164.

[13] W. Xie, Z. Gao, W.-P. Pan, D. Hunter, A. Singh, R. Vaia, Chem. Mater. **2001**, 13, 2979 – 2990.

[14] M. Szafranski, Thermochim. Acta **1997**, 307, 177 – 183.

[15] M. Szafranski, A. Katrusiak, Phys. Rev. B **2000**, 61, 1026 – 1035.

[16] a) F. Hao, C. C. Stoumpos, Z. Liu, R. P. H. Chang,M. Kanatzidis, J. Am. Chem. Soc. 2014, 136, 16411 – 16419; b) G. H. Imler, X. Li, B. Xu, G. E. Dobereiner, H.-L. Dai, Y. Rao, B. B. Wayland, Chem. Commun. **2015**, 51, 11290 – 11292; c) A. Lemmerer, D. G. Billing, CrystEngComm **2012**, 14, 1954 – 1966; d) G.-E.Wang, G. Xu, M.-S. Wang, J. Sun, Z.-N. Xu, G.-C. Guo, J.-S. Huanga, J. Mater. Chem. **2012**, 22, 16742 – 16744.

[17] N. De Marco, H. Zhou, Q. Chen, P. Sun, Z. Liu, L. Meng, E.-P. Yao, Y. Liu, A. Schiffer, Y. Yang, Nano Lett. **2016**, 16, 1009 – 1016.

[18] Y. Wang, T. Gould, J. F. Dobson, H. Zhang, H. Yang, X. Yao, H. Zhao, Phys. Chem. Chem. Phys. **2014**, 16, 1424 – 1429.

[19] a) R. Lindblad, D. Bi, B.-W. Park, J. Oscarsson, M. Gorgoi, H. Siegbahn, M. Odelius, E. M. J. Johansson, H. Rensmo, J. Phys. Chem. Lett. **2014**, 5, 648 – 653; b) B. Conings, L. Baeten, C. De Dobbelaere, J. DHaen, J. Manca, H. G. Boyen, Adv. Mater. 2014, 26, 2041 – 2046.

[20] B. Wang, K. Y. Wong, S. Yang, T. Chen, J. Mater. Chem. A **2016**, 4, 3806 – 3812.

[21] J. Torrent, V. Barr_n in Encyclopedia of Surface and Colloid Science (Ed.: P. Somasundaran), Marcel Dekker, New York, **2002**.

[22] V. D'Innocenzo, G. Grancini, M. J. P. Alcocer, A. R. S. Kandada, S. D. Stranks, M. M. Lee, G. Lanzani, H. J. Snaith, A. Petrozza, Nat. Commun. **2014**, 5, 3586.

[23] L. Dimesso, A. Quintilla, Y.-M. Kima, U. Lemmer, W. Jaegermann, Mater. Sci. Eng. B **2016**, 204, 27 – 33.

[24] Y. Li, W. Yan, Y. Li, S. Wang, W. Wang, Z. Bian, L. Xiao, Q. Gong, Sci. Rep. **2015**, 5, 14485.

Supporting Information

Benign-by-Design Solventless Mechanochemical Synthesis of Three-,Two-, and One-Dimensional Hybrid Perovskites

Alexander D. Jodlowski, Alfonso Yépez, Rafael Luque,* Luis Camacho, and Gustavo de Miguel*

Experimental Section

Materials. All materials were purchased from Sigma-Aldrich and stored in a glovebox. Only CH_3NH_3I was synthesized by neutralizing equimolar amounts of HI and CH_3NH_2 in 33% absolute ethanol solution. The product was then crystallized by removing the solvent in an oven at 100 ºC for 24 hours.

General Procedure. All the perovskite powders were synthesized by grinding an organic salt (MAI, FAI and GuaI) and PbI_2 (stoichiometric ratio 1:1) in an electric ball mill (Retsch, model: Planetary Ball Mill PM-100, stainless steel grinding jar with a volume of 125 ml and 16 stainless steel balls, diameter size 10 mm) for 10 min at 350 rpm. 0.340 g of MAI and 1.004 g of PbI_2 were mixed to prepare the $MAPbI_3$ powder. 0.375 g of FAI and 1.003 g of PbI2 were mixed to prepare the $FAPbI_3$ powder. 0.611 g of GuaI and 1.506 g of PbI2 were mixed to prepare the Gua_2PbI_4 powder. The resulting powders were stored in a vacuum desiccator chamber and are stable during months.

Powder X-ray diffraction (XRD). XRD experiments for $MAPbI_3$ and $FAPbI_3$ were performed using Bruker D8 ADVANCE diffractometer operating at 40 kV and 40 mA and using Cu Kα (1.54060 Å) and Kβ (1.39222 Å). The measurements were carried out in-situ using HTK 1200N oven-chamber and the temperature was controlled with TTCU 1000N temperature control unit.

Powder X-ray diffraction experiments for Gua_2PbI_4 and $GuaPbI_3$ (2D and 1D) were performed using a Bruker D8 DISCOVER diffractometer operating at 40 kV and 40 mA and using Cu Kα radiation (1.54060 Å). Rietveld and Pawley refinements were performed using the program Topas for all samples. The $GuaPbI_3$ structure was obtained with PowderSolve package.

X-ray photoelectron spectroscopy (XPS). XPS experiments were performed in a SPECS Sage HR 100 spectrometer with a non-monochromatic X ray source (Aluminum Kα line of 1486.6 eV energy and 300 W), placed perpendicular to the analyzer axis and calibrated using the 3d5/2 line of Ag with a full width at half maximum (FWHM) of 1.1 eV. The selected resolution for the spectra was 10 eV of Pass Energy and 0.15 eV/step. All measurements were made in an ultra-high vacuum (UHV) chamber at a pressure below 8·10-8 mbar. An electron flood gun was used to neutralize for charging. In the fittings asymmetric and Gaussian Lorentzian functions were used (after a Shirley background correction) where the FWHM of all the peaks were constrained while the peak positions and areas were set free.

Scanning electron microscope (SEM) analysis. The SEM images were acquired using a JEOL JSM 6300.

Thermal analysis. Thermal analysis was performed by simultaneous TG-DSC measurements using a System Setaram Setsys 12 TGA instrument. Samples were heated at a rate of 5 °C min^{-1} in N2 (40 mL min^{-1}) at the temperature range 30–300 °C.

UV-vis diffuse-reflectance spectroscopy. Diffuse-reflectance measurements were performed at room temperature using a CARY 5000,

using a Pb Smart NIR detector for extended photometric range (200 to 1000 nm). $BaSO_4$ was used as a non-absorbing reflectance reference.

Computational details. Periodic DFT-GGA calculations using the PBE exchangecorrelation functional were performed.[1] Electron-ion interactions were described by ultrasoft pseudopotentials. In case of the Pb atom we used a scalar relativistic pseudopotential. A 6×6×6 Monkhorst–Pack grid was chosen for sampling the Brillouin zone.[2] A geometry optimization (without cell optimization) was previously performed for the structure obtained after the Rietveld refinement. Standard DFT-GGA calculations in perovskites are usually shown to provide geometrical structures and relative stabilities in good agreement with experimental data.[3-6] Given these compounds are essentially ionic in nature, electrostatic interactions well described by DFT-GGA are expected to represent the main contribution in the interaction. This is indirectly confirmed by the usually good agreement between experimental and calculated structural parameters for this type of materials.[3]

X-Ray Photoelectron Spectroscopy (XPS)

To investigate the elemental composition and chemical environments of Pb, I and N atoms at the perovskite structures, X-ray photoelectron spectroscopy (XPS) measurements were performed in the powders prepared with MAI, FAI (after annealing at 170 ºC) and GuaI (before and after annealing at 170 ºC). Interestingly, we do not observe any difference in peak positions and relative areas in the powders with GuaI before and after annealing. Figure S7 shows the Pb 4f core level photoemission peaks, with the 4f7/2 component at a binding energy of ~138.3 eV corresponding to Pb^{2+} (Pb-I bonds) in all samples. In $MAPbI_3$ perovskites fabricated with other synthetic methods, a photoemission peak around 136.3 eV is frequently observed being related to unsaturated Pb recently ascribed to metallic Pb (Pb^0).[7] The presence of

metallic Pb species is associated with iodide deficiencies in the perovskite structure which has been proved to have a detrimental impact upon photovoltaic performance in this perovskite.[8] Interestingly, the absence of metallic Pb in our samples reflects the high quality of the perovskite material prepared via the mechanical synthesis with no apparent side reactions. In Figure S7, the I 3d photoemission peak shows only one component denoting only one type of I atoms and with the position of the I 3d5/2 peak at around 619.1 eV for all four samples which is attributed to Pb-I bonds. In case of the N atom, Figure S8 shows the N 1s photoemission peaks for each sample where only one component is clearly derived from the theoretical fit of the experimental data. However, the position of the N 1s peak varies considerably within the three samples, 402.1, 400.7 and 400.1 eV for MA, FA and Gua (same position before and after the thermal annealing), respectively. This significant shift of the N 1s peak clearly indicates a different chemical environment of the N atom in each perovskite. In particular, the position of the N 1s peak with MA is assigned to the NH_3^+ group with the positive charge located at the only N atom. However, the presence of resonance structures within FA and Gua allocates the charge in the different NH2 groups reducing the partial positive charge in each N to 1/2 and 1/3, respectively. The consequence of this charge distribution is the displacement to the N 1s peak to lower binding energies while decreasing the partial charge on the N atoms. The stoichiometry of the four samples was also estimated from the signals of Pb 4f, I 3d and N 1s. For the sample with MA, I/Pb and N/Pb ratio are 3.60 and 1.05, respectively. In case of FA, I/Pb and N/Pb ratio are slightly different, 2.65 and 0.87, respectively. It is expected that both I/Pb and N/Pb ratio with FAI are underestimated since the presence of some PbI_2 confirmed in the XRD experiments overvalues the amount of Pb^{2+} in the $FAPbI_3$ structure. Thus, if we compare these experimental values with those expected for 3D hybrid perovskites (I/Pb = 3 and N/Pb = 1 and 2

for MA and FA, respectively), the errors in both ratio can be explained as a consequence of the use of different core levels for each element. In the powders prepared with GuaI, the I/Pb and N/Pb ratio are nearly the same 3.2 and 3.3 and 2.9 and 2.7, before and after the annealing, respectively. This result is anticipated since no weight loss was detected in the TGA analysis upon heating the sample to 200 ºC. In the as-prepared powder with GuaI, the estimated I/Pb = 4 and N/Pb = 6 ratio deduced from the stoichiometry of the 2D hybrid perovskite (GA_2PbI_4) is not obtained due to the presence of PbI_2. However, in the structure obtained after the annealing both ratio reveal the $GAPbI_3$ stoichiometry, in agreement with that of the proposed hybrid perovskite derived from the XRD measurements.

Scanning Electron Microscopy (SEM)

The morphology of the powders was studied by using scanning electron microscopy (SEM). In case of $MAPbI_3$ and $FAPbI_3$, large structures are observed with a wide distribution of sizes in the range of 10-200 μm (Fig. S9A and S9C). In $MAPbI_3$, the large domains are formed by clusters of particles with a crystal size of around 0.5-1.5 μm (Fig. S9B). The morphology of these particles is quite irregular with no clear hints of the tetragonal lattice of this perovskite. In $FAPbI_3$, the surface of the large domains is quite smooth and no individual particles can be detected (Fig. S9D). Finally, in $GuaPbI_3$, Fig. S9E and S9F show an agglomeration of cylindrical-shaped particles with a size of 2-4 μm. These particles resembles to those reported for a perovskite containing Gua cations and synthesized by a self-organization process.[9]

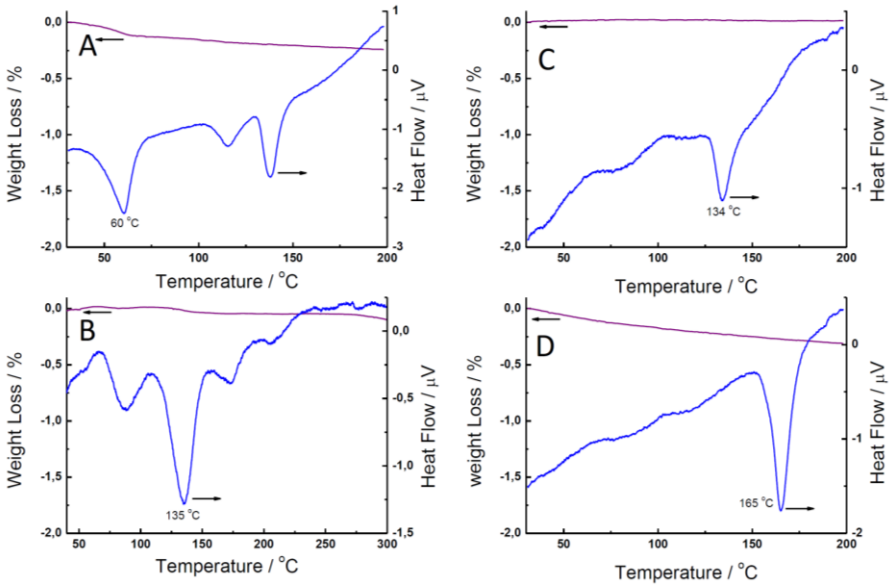

Figure S1. TGA (purple line) and DSC (blue line) curves of the synthesized powders with MAI (A), FAI (B) and GuaI, before (C) and after (D) annealing.

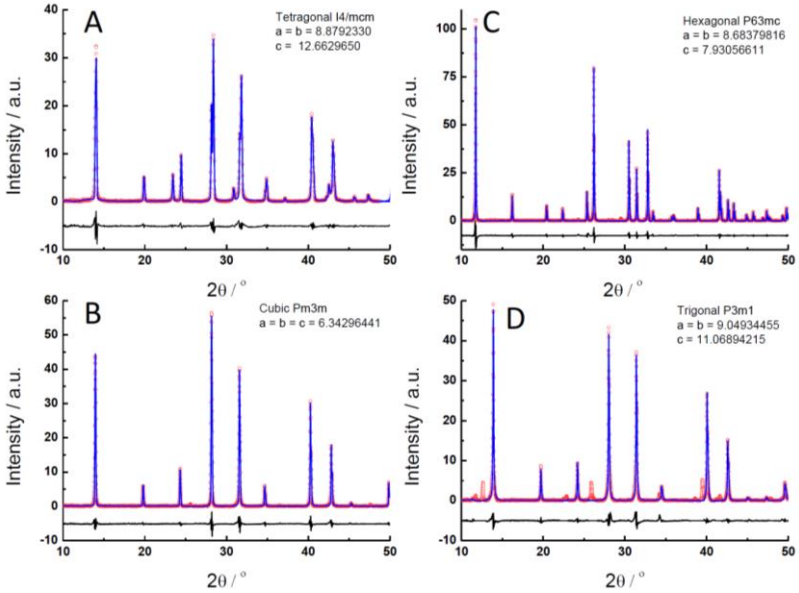

Figure S2. Pawley fits of the XRD patterns of $MAPbI_3$ at 30 ºC (A) and 100 ºC (B) and of $FAPbI_3$ at 30 ºC (C) and 160 ºC (D).

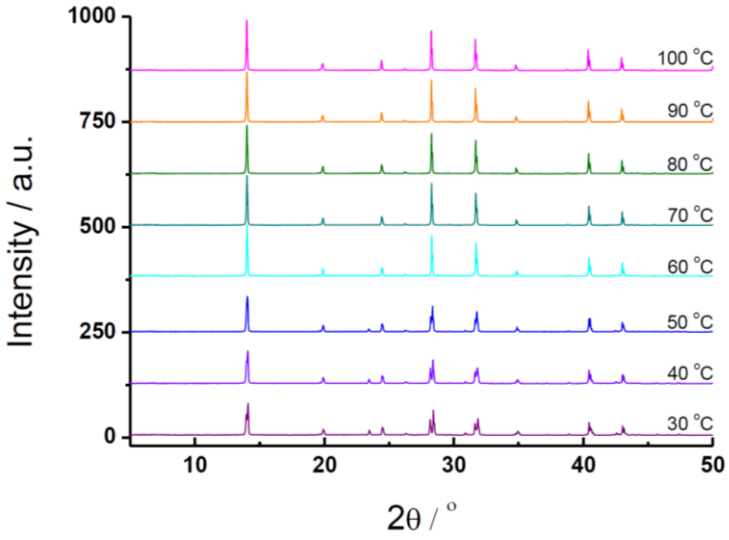

Figure S3. XRD patterns at different temperatures for the powder synthesized with MAI.

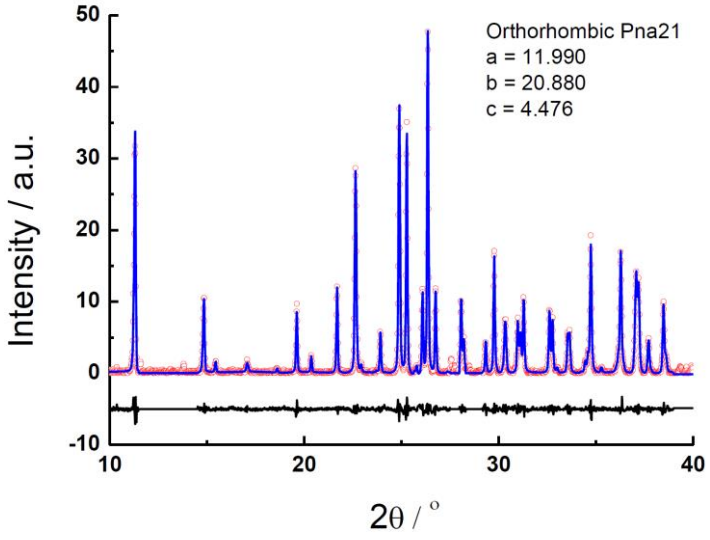

Figure S4. Pawley fit of the XRD pattern of $GuaPbI_3$ at 30 ºC.

Table S1. Refined atomic position and atomic displacement parameter for orthorhombic (Pna21) $GuaPbI_3$ at 30 ºC.

Fractional Coordinates				
	u	v	w	U_{eq}
Pb	0.6577(2)	0.5536(1)	0.653(2)	0.018
I1	0.7716(3)	0.6842(2)	0.730(1)	0.010
I2	0.4714(3)	0.5998(2)	0.144(1)	0.014
I3	0.8203(4)	0.4938(2)	0.154(1)	0.010
C	0.5828(14)	0.8171(6)	0.221(1)	0.050
N1	0.543(2)	0.7603(6)	0.116(2)	0.0143
N2	0.515(1)	0.8695(6)	0.229(2)	0.058
N3	0.690(1)	0.8215(7)	0.3188(9)	0.015
H1	0.461(1)	0.753(2)	0.096(35)	0.039
H2	0.595(2)	0.725(2)	0.056(35)	0.158
H3	0.502(8)	0.895(4)	0.047(2)	0.027
H4	0.477(8)	0.882(3)	0.417(21)	0.029
H5	0.754(2)	0.816(4)	0.177(9)	0.189
H6	0.707(2)	0.830(3)	0.531(13)	0.022

Table S2. Anisotropic atomic displacement parameters (Å^2) for $GuaPbI_3$ at 30 ºC.

Name	U_{11}	U_{22}	U_{33}	U_{12}	U_{23}	U_{13}
Pb	0.00949 ± *0.00222*	0.04194 ± *0.00330*	0.00123 ± *0.00086*	-0.00662 ± *0.00196*	-0.00200 ± *0.00117*	0.00066 ± *0.00096*
I	0.00728 ± *0.00243*	0.02209 ± *0.00293*	0.00110 ± *0.00112*	0.00000 ± *0.00162*	0.00001 ± *0.00068*	0.00000 ± *0.00093*
I	0.01636 ± *0.00479*	0.02222 ± *0.00327*	0.00237 ± *0.00186*	0.00108 ± *0.00223*	0.00040 ± *0.00096*	0.00343 ± *0.00247*
I	0.00729 ± *0.00219*	0.02209 ± *0.00395*	0.00118 ± *0.00122*	0.00000 ± *0.00201*	-0.00001 ± *0.00097*	-0.00002 ± *0.00085*
C	0.07291 ± *0.05576*	0.06649 ± *0.04222*	0.01178 ± *0.00000*	0.05135 ± *0.03922*	0.01270 ± *0.01449*	0.01752 ± *0.02338*
N	0.01718 ± *0.00000*	0.02260 ± *0.01209*	0.00320 ± *0.00742*	0.00206 ± *0.00848*	-0.00028 ± *0.00360*	0.00038 ± *0.00000*
N	0.08495 ± *0.03367*	0.08494 ± *0.03420*	0.00535 ± *0.01537*	-0.06972 ± *0.02510*	0.00294 ± *0.01000*	-0.00424 ± *0.01212*
N	0.01053 ± *0.01418*	0.02218 ± *0.01476*	0.01204 ± *0.00000*	-0.00034 ± *0.00869*	-0.00102 ± *0.00598*	0.00418 ± *0.00918*
H	0.07836 ± *0.26254*	0.02670 ± *0.03145*	0.01109 ± *0.05402*	-0.00563 ± *0.03567*	-0.00011 ± *0.01317*	0.00725 ± *0.09033*
H	0.37179 ± *0.00000*	0.08867 ± *0.06131*	0.01444 ± *0.04668*	-0.14896 ± *0.00000*	0.01861 ± *0.00000*	-0.04645 ± *0.00000*
H	0.02922 ± *0.04983*	0.04148 ± *0.06573*	0.01055 ± *0.04563*	-0.01415 ± *0.04123*	0.00387 ± *0.02339*	-0.00564 ± *0.02522*
H	0.03098 ± *0.05947*	0.04186 ± *0.08122*	0.01301 ± *0.00000*	-0.00101 ± *0.05239*	-0.00609 ± *0.00000*	0.00174 ± *0.02998*
H	0.29042 ± *0.00000*	0.26380 ± *0.00000*	0.01354 ± *0.00000*	-0.25630 ± *0.00000*	0.00741 ± *0.00000*	-0.00703 ± *0.00000*
H	0.02490 ± *0.06171*	0.02923 ± *0.03611*	0.01156 ± *0.05997*	-0.00492 ± *0.02722*	-0.00182 ± *0.01535*	0.00125 ± *0.03125*

Table S3. Bond length (Å) for $GuaPbI_3$ at 30 ºC.

Bond lengths (Å)	
Pb-I1	3.068
Pb-I2	3.333
Pb-I3	3.217
Pb#1-I2	3.559

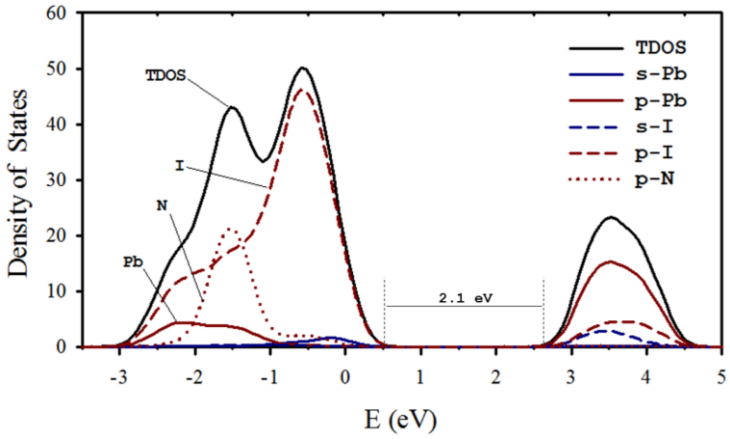

Figure S5. Calculated density states of the 1D $GuaPbI_3$ perovskite. Total (solid black line), s-Pb (blue solid line), p-Pb (red solid line), s-I (blue dashed line), p-I (red dashed line) and p-N (red dotted line).

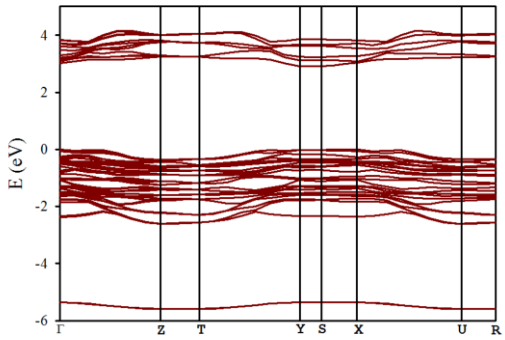

Figure S6. Calculated band structure of the 1D $GuaPbI_3$ perovskite.

nature energy

Impact Factor: 46.859

DOI: 10.1038/s41560-017-0054-3

Large guanidinium cation mixed with methylammonium in lead iodide perovskites for 19% efficient solar cells.

Alexander D. Jodlowski[1,2], Cristina Roldán-Carmona[1*], Giulia Grancini[1], Manuel Salado[1,3], Maryline Ralaiarisoa[4,5], Shahzada Ahmad[3], Norbert Koch[4,5], Luis Camacho[2], Gustavo de Miguel[2*] and Mohammad Khaja Nazeeruddin[1*]

[1] Group for Molecular Engineering of Functional Materials, Institute of Chemical Sciences and Engineering, Ecole Polytechnique Fédérale de Lausanne (EPFL), Sion, Switzerland.

[2] Departamento de Química Física y Termodinámica Aplicada, Instituto Universitario de Investigación en Química Fina y Nanoquímica IUQFN, Universidad de Córdoba, Campus de Rabanales, Edificio Marie Curie, Córdoba, Spain.

[3] Abengoa Research, Abengoa, C/ Energía Solar no. 1, Campus Palmas Altas, Sevilla, Spain.

[4] Humboldt-Universität zu Berlin, Institut für Physik & IRIS Adlershof, Berlin, Germany.

[5] Helmholtz-Zentrum Berlin für Materialien und Energie, Devision Renewable Energies, Berlin, Germany.

Abstract: Organic–inorganic lead halide perovskites have shown photovoltaic performances above 20% in a range of solar cell architectures while offering simple and low-cost processability. Despite the multiple ionic compositions that have been reported so far, the presence of organic constituents is an essential element in all of the high-efficiency formulations, with the methylammonium and formamidinium cations being the sole efficient options available to date. In this study, we demonstrate improved material stability after the incorporation of a large organic cation, guanidinium, into the $MAPbI_3$ crystal structure, which delivers average power conversion efficiencies over 19%, and stabilized performance for 1,000 h under continuous light illumination, a fundamental step within the perovskite field.

Hybrid perovskites have recently emerged as outstanding materials for efficient and low-cost solar technology. Unique properties, including high absorption coefficient[1], large charge-carrier diffusion length[2], small exciton binding energy[3] and low trap density[4], pushed their performances to a record efficiency beyond 22%[5]. The most common perovskite arranges into $APbX_3$, (A = CH_3NH_3 + (methylammonium, MA) or $CH_3(NH_2)_2$ + (formamidinium, FA); X = Cl^-, Br^-or I^-), which crystallizes in a three-dimensional (3D) network[3]. Among different candidates, mixed ionic compositions of MA and FA cations6 and Br^-/I^- halides have recently led to superior performance, with efficiencies close to 21% for $(FAPbI_3)_{0.85}(MAPbBr_3)_{0.15}$ (ref. 7). Nevertheless, these improvements in the efficiency of perovskite materials come with stability concerns, due to decomposition to the initial precursors[8], and intrinsic halide segregation[9,10] with ambiguous long-term consequences.

To overcome the stability issue, a few strategies have been proposed[11– 14], including the exploration of alternative cations. Recent reports have shown promising results with the introduction of Cs^+ and Rb^+ mixtures into the hybrid $(FAPbI_3)_{0.85}(MAPbBr_3)_{0.15}$ structure, leading to a complex triple[15] and quadruple[16] composition with efficiency over 20%. Nevertheless, organic alternatives with a proper ionic radius (R), such as hydrazinium $[H_3N–NH_2]^+$ or azetidinium $[(CH_2)_3NH_2]^+$ (ref. 17), that can fit into the inorganic Pb–I framework while maintaining an adequate Goldschmidt tolerance factor ($\mathbf{t} = (\boldsymbol{R_A} + \boldsymbol{R_I}) / \sqrt{\mathbf{2}}\,(\boldsymbol{R_{Pb}} + \boldsymbol{R_I})$ to ensure a cubic structure (t = 0.8–1)[17,18] are not available. On the other hand, obtaining good perovskite films with alternative cations has been experimentally challenging, and no results comparable to the state-of-the-art perovskites have been reported so far.

Here we introduce a perovskite based on the organic cation guanidinium (CH_6N^+, Gua) as a more stable and efficient alternative to the state-of-the-art $MAPbI_3$. Gua features an ionic radius of ~278 pm (ref. 17), slightly above the upper limit of the tolerance factor (t ~1.03), forming low-dimensional

perovskites (LDPs) when mixed with PbI_2 (refs 19,20). In this work, we demonstrate that when combined with methylammonium in a mixed $MA_{1-x}Gua_xPbI_3$ composition ($0 < x < 0.25$) the Gua cation inserts in the crystal unit, forming a 3D perovskite with enhanced thermal and environmental stability. Our results widen the exploration of cations with a radius beyond the tolerance limit, while preserving a 3D structure and high photovoltaic performance. With this approach, solar cells display an average photoconversion efficiency (PCE) of 19.2 ± 0.4% at enhanced stability.

Structural characterization of $MA_{1-x}Gua_xPbI_3$ perovskites

To gain insight into the arrangement of the Gua cations in the $MA_{1-x}Gua_xPbI_3$ crystal structure, X-ray diffraction (XRD) measurements of the thin films were performed (see Methods for details). Figure 1a shows the diffractograms of the perovskite films containing MA/Gua mixtures, where $0 < x_{Gua} < 1$ (x_{Gua} represents the Gua molar ratio), compared with $MAPbI_3$. The incorporation of Gua cations yields a gradual decrease of the reflection peak intensity but retaining the $MAPbI_3$ tetragonal phase even for $x_{Gua} = 0.25$. Larger Gua percentages significantly decrease the diffraction signal, while the appearance of new diffraction peaks at 8.54° and 11.31° indicates the formation of a 1D $GuaPbI_3$ phase, as previously reported[21]. Interestingly, a closer inspection of the reflection peaks reveals a notable shift to lower angles, as shown in the zoom of Fig. 1b corresponding to the (110) and (220) lattice planes. On increasing the Gua content, a gradual shift of the peaks occurs, as reported for the $FAPbI_3$ α-phase after sequential substitution of FA cations for Cs[22] or in the recently reported $MA_xEA_{1-x}PbBr_3$ perovskite (EA = ethylammonium) at increasing EA contents[23]. In our case, this phenomenon denotes a gradual expansion of the unit-cell volume, indicating the incorporation of the larger Gua cation by direct substitution of MA, forming a mixed $MA_{1-x}Gua_xPbI_3$. The lattice parameters, a and c, calculated

from the experimental XRD patterns, indicate that the c value remains constant for all percentages, 12.625 Å, while a gradually changes from 8.838 Å to 8.902 Å, remaining invariable for Gua contents larger than 25% (Fig. 1c). Thus, a distortion of the crystal prevalently affecting the a and b lattice parameters takes place for $x_{Gua} < 0.25$.

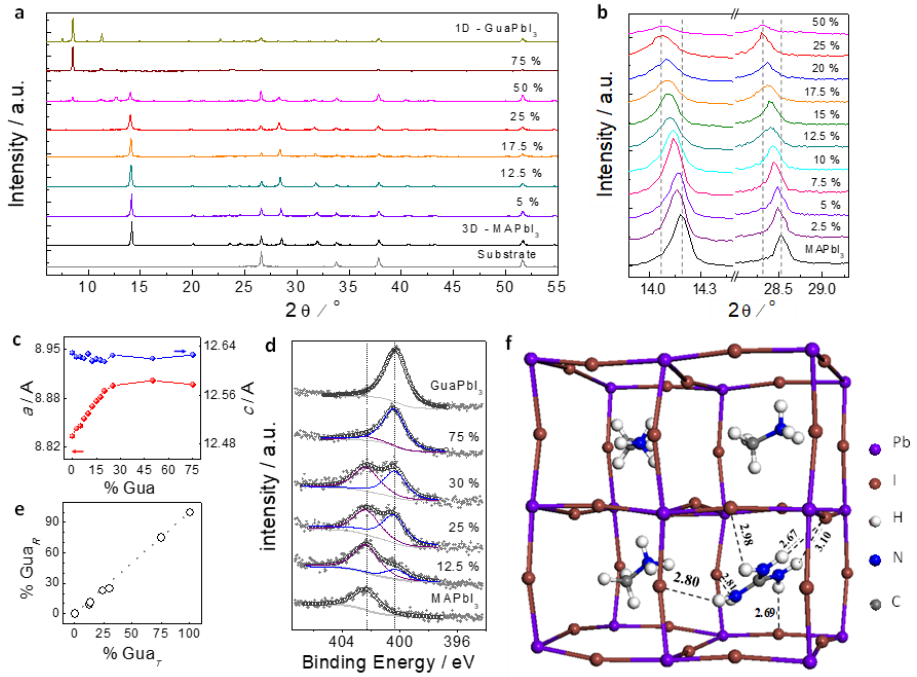

Fig. 1 | XRD and XPS characterization of Gua-based perovskites. a, Normalized XRD data for the mixed MA/Gua perovskite films containing different percentages of Gua. **b**, Magnification of the XRD peaks at (110) (left) and (220) (right) on variation of the Gua content (indicated in per cent). **c**, Lattice parameter variation (a and c) of the $MA_{1-x}Gua_xPbI_3$ unit cell obtained from the crystallographic analysis of the experimental XRD patterns. **d**, XPS spectra of N 1s for thin films of typical $MA_{1-x}Gua_xPbI_3$ perovskite mixtures (x = 0, 12.5, 25, 30, 50, 100) (for clarity, traces are shifted vertically). **e**, Quantification of the percentage of Gua obtained from the XPS analysis (Gua_R corresponds to the measured values; Gua_T corresponds to theoretical values, initially incorporated into the precursor solution). **f**, Optimized simulated structure of the unit cell of $Ma_{0.75}Gua_{0.25}PbI_3$ including the six H-bond distances with respect to I atoms.

Due to the mismatch in size with respect to the MA cation, the incorporation of Gua entails local distortions in the crystal, which manifest as a broadening

of the peaks. The crystal strains in the structure are evaluated using the Williamson–Hall method (Supplementary Fig. 1). The results demonstrate an increased number of micro-strains and distortions of the $MAPbI_3$ lattice at larger percentages of Gua, supporting its inclusion in the crystal. However, further increments do not incorporate into the crystalline network and lead to a phase-separated 1D $GuaPbI_3$, as suggested by the XRD. It is worth noting that these results are in contradiction to those of previous reports, where Gua has been proposed as a passivating agent that does not incorporate into the perovskite structure due to its larger size[24]. Nevertheless, significant variations in the preparation method could account for the different crystallization dynamics. Here, we incorporate Gua within the precursor solution, ensuring the desired stoichiometry during crystallization.

The relative composition and chemical environment of the constituents in the perovskite materials have been analysed by X-ray photoelectron spectroscopy (XPS). Measurements performed for the pure MA and Gua phases and four representative mixtures (x_{Gua} = 12.5%, 25% 30% and 50%) reveal the formation of Pb–I bonds and a relative Pb/I ratio of ~3.0, consistent with the theoretical stoichiometry present in the 3D $MA_{1-x}Gua_xPbI_3$ and 1D $GuaPbI_3$ structures (Supplementary Fig. 2a).

In addition, the photoemission spectra of the N 1s region reveals the two peaks attributed to the NH_3^+ group in MA (402.3 eV) and the NH_2^+ group in Gua (400.3 eV), which changes gradually in intensity on increasing the Gua content (Fig. 1d). The initial experimental MA/Gua ratio is preserved within the final structure, as presented in Fig. 1e (corroborated by NMR measurements, Supplementary Fig. 2b, c), which is particularly valuable in the determination of the crystalline structure. To analyse the role of Gua in the crystalline material and examine the stability of the $MA_{1-x}Gua_xPbI_3$ structures, density functional theory with generalized gradient approximation (DFT–GGA) calculations using the Perdew–Burke–Ernzerhof (PBE)

exchange correlation functional were conducted. An estimation of the formation enthalpies at zero temperature, ΔH_f, for the pure MA and Gua phases, as well as for that containing $x_{Gua} = 0.25$ was performed (Supplementary Note 1). A remarkable difference for the three perovskite structures was found, with a clear tendency when increasing the Gua content: $\Delta H_{f(MA\_pure)} = -0.149$ eV $\gg \Delta H_{f(MA0.75\_Gua0.25)} = -1.484$ eV $> \Delta H_{f(Gua\_pure)} = -2.045$ eV. Compared with the pure $MAPbI_3$ phase, which exhibits a value close to zero, consistent with previous reports[25,26], 1D $GuaPbI_3$ points to enhanced stability, as expected for LDP[27]. However, a striking result appears for the mixed $Ma_{0.75}Gua_{0.25}PbI_3$ perovskite, which also exhibits a highly negative formation enthalpy, close to that of the 1D $GuaPbI_3$, while maintaining its 3D structure. Note that such a behaviour has important implications for the performance of the solar cell, as the substitution of Gua for ¼ of MA in the $MAPbI_3$ structure results in a significant increase of the system stability. Besides, a phase separation of the $MA_{0.75}Gua_{0.25}PbI_3$ into the pure MA and Gua systems was found to be thermodynamically less favoured ($\Delta H_f = -0.622$ eV), and it is foreseen that it does not occur at a lower percentage of Gua. Only at additions higher than 25%, both $Ma_{0.75}Gua_{0.25}PbI_3$ and $GuaPbI_3$ crystalline phases appear, given the impossibility of the 3D octahedral [PbI_6] network to accommodate additional Gua cations. Figure 1f shows the optimized unit cell for $Ma_{0.75}Gua_{0.25}PbI_3$, where the main H–I interactions with the Gua cation can be identified.

Note that the formation of hydrogen bonds plays a key role in the structural stabilization. Compared with the 1–2 H bonds per MA molecule[28], the introduction of Gua increases the number of interactions to six H bonds while reducing the H–I distance, which seems to be the ultimate cause for the superior $Ma_{0.75}Gua_{0.25}PbI_3$ stability. Importantly, our results suggest that the crystal distortions produced by the larger cation could be compensated at the

expense of the neighbouring cavities where the small MA cation localizes, preserving its 3D structure.

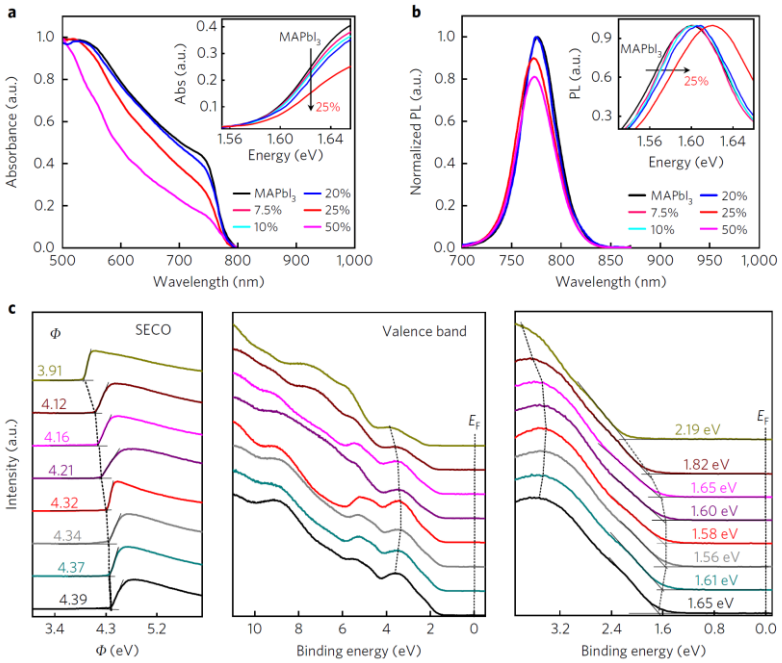

Fig. 2 | UPS and optical characterization. a, Ultraviolet–visible–near-infrared absorption spectra of typical $MA_{1-x}Gua_xPbI_3$ films containing x ≤ 0.5 shown in Fig. 1. Inset: magnification of the band edge for mixed films containing x ≤ 0.25 of Gua. **b**, Photoluminescence (PL) spectra of the perovskite films shown in **a. c**, Secondary-electron cutoffs for workfunction determination (left), and wide (centre) and narrow (right) binding energy range valence spectra of the samples with different Gua/MA ratios.

Optical and electronic properties

The effect of the lattice expansion on the optoelectronic properties was also analysed by DFT–GGA calculations. The electronic band structures and density of states for $MAPbI_3$ and two representative mixtures (12.5% and 25% of Gua content) show no appreciable difference, with I 5p states mainly contributing to the top valence band and Pb 6p states dominating the lowest conduction band (Supplementary Fig. 3). Nevertheless, there is a small but gradual increase in the bandgap energy with the insertion of Gua, showing

values equal to 1.77 eV, 1.79 eV and 1.82 eV for $MAPbI_3$, 12.5% and 25% of Gua, respectively. The direct character of the $MAPbI_3$ bandgap is also conserved in the two mixtures, with the minimum bandgap occurring at the Γ symmetry point. Moreover, the three samples display a similar dispersion of the valence and conduction bands, which ensures low carrier effective masses.

Consequently, the incorporation of Gua preserves the optical properties of the material. Figure 2a shows the normalized absorption spectra for four typical $Ma_{1-x}Gua_xPbI_3$ thin films with $x_{Gua} < 0.5$. In agreement with the theoretical calculations, no significant changes in the shape of the spectrum are observed for mixtures containing $x_{Gua} < 0.2$, except a tiny but continuous shift in the absorption band edge, as illustrated in the inset of Fig. 2a. Yet, $x_{Gua} > 0.2$ produces an appreciable lowering of the absorption capacity along with a blueshift of the band edge (~ 0.02 eV), indicative of a widening of the bandgap. This can be related to the different organic–inorganic interactions mediated by the new hydrogen bonds, which lead to crystal unit. Results for higher Gua percentages are also reported in Supplementary Fig. 4a. A sharp band edge at ~500 nm, with a remarkable excitonic peak at 390 nm appears for pure 1D $GuaPbI_3$ (ref. 21). This is also detected for $x_{Gua} > 0.5$, which, together with the absorption band edge of $Ma_{0.75}Gua_{0.25}PbI_3$ at ~775 nm, confirms the preservation of both individual phases.

Accordingly, the photoluminescence (PL) spectra shown in Fig. 2b (Supplementary Fig. 4b–d) manifest a gradual shift towards higher energy for samples with $x_{Gua} < 0.2$ (see inset to Fig. 2b), which becomes more apparent for $x_{Gua} = 0.25$, and is preserved for larger Gua amounts, consistent with the results observed in Fig. 2a. These findings provide compelling evidence that the substitution of Gua for MA efficiently stabilizes a 3D perovskite phase while retaining extended and efficient absorption similar to $MAPbI_3$.

In addition, the electronic structure was also investigated by ultraviolet photoelectron spectroscopy (UPS). The results reveal a slight gradual shift of the valence band onset (by 0.04–0.09 eV) towards the Fermi level from $MAPbI_3$ to $MA_{1-x}Gua_xPbI_3$ samples containing up to 25% Gua, while retaining the main valence band features of $MAPbI_3$, as depicted in Fig. 2c.

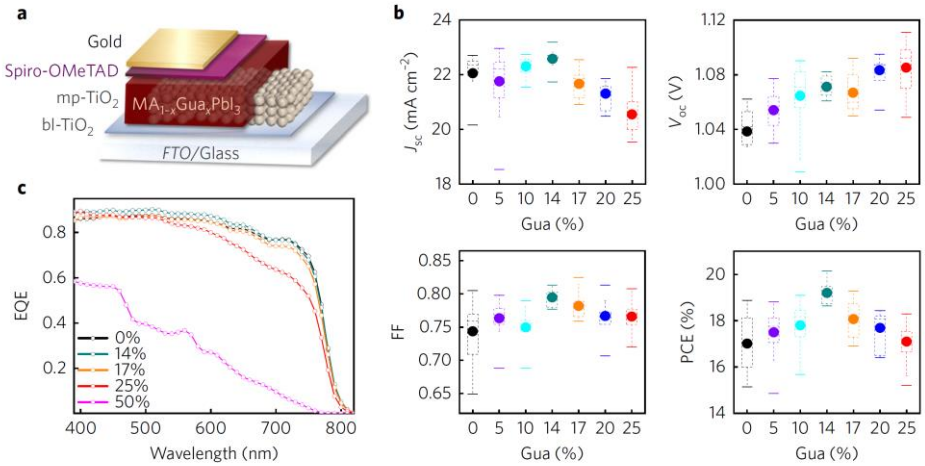

Fig. 3 | Device architecture and photovoltaic performance. **a**, Device architecture of the perovskite solar cells incorporating Gua cations (glass/FTO/ c-TiO_2/mp-TiO_2/perovskite/spiro-OMeTAD/Au). **b**, Statistical data for J_{sc}, V_{oc}, FF and PCE obtained from more than 120 cells (at least 17 cells per condition) prepared with $MA_{1-x}Gua_xPbI_3$ as a function of *x*. The top bar shows the maximum value, the bottom bar shows the minimum value, the circle shows the mean value and the dashed rectangle shows the region containing 25–75% of the data, obtained for each condition. **c**, EQE spectra of mixed $MA_{1-x}Gua_xPbI_3$ (x = 0.14, 0.17 and 0.25) and that incorporating 50% Gua. The result for $MAPbI_3$ (0%) is also included as a reference.

Concomitantly, the ionization energy becomes slightly reduced (by up to 0.14 eV). However, larger amounts of Gua (> 25%) result in a shift of the valence band onset away from the Fermi level. A solid change in the valence band features, increasingly resembling those corresponding to pure $GuaPbI_3$ (binding energy region between 5.5 eV and 8.7 eV), suggests the coexistence of $GuaPbI_3$ at the surface above 25% Gua content, which is corroborated also by scanning electron microscopy (SEM; as discussed

below). As $GuaPbI_3$ contains an increased number of Pb^0- related surface states, which tend to pin the Fermi level close to the conduction band minimum29 (Supplementary Fig. 2a), the wider gap of $GuaPbI_3$ as compared with $MAPbI_3$ results in the shift of the valence band onset towards higher binding energy for $x_{Gua} > 0.3$.

Photovoltaic performance

To demonstrate the applicability of Gua-containing perovskites, we embodied the $Ma_{1-x}Gua_xPbI_3$ ($0 < x < 0.25$) into solar cells sandwiched in between the mesoporous (mp)-TiO2, used as the electron-transporting material, and 2,2′ ,7,7′ -tetrakis(N,N′ -di-p-methoxyphenylamine)- 9,9′ -spirobifluorene (spiro-OMeTAD), as the hole-transporting material (Fig. 3a and Supplementary Fig. 5). The average photovoltaic parameters obtained from the cells are shown in Fig. 3b and listed in Table 1, which also includes the champion cells obtained for each condition (see also Supplementary Table 1). The short-circuit current density (Jsc) hardly changes for Gua fractions up to 20%, but gradually lowers for increased Gua contents, with 14% of Gua outstanding among the others. This behaviour can be related to the decreased absorption detected for $x_{Gua} > 0.2$, as supported by the external quantum efficiency (EQE) spectra shown in Fig. 3c (photographs of the as-prepared $MA_{1-x}Gua_xPbI_3$ solar cells are provided in Supplementary Fig. 6).

In addition, the average open-circuit voltage (Voc) increases progressively with the Gua incorporation, from 1.04 ± 0.02 V for x = 0 to 1.085 ± 0.02 V for x = 0.25 (see Table 1), as expected from the optical bandgap observations. Notably, the fill factor (FF) remains almost unaltered, with high average values over 0.75 (and maxima close to 0.80). As a result, the PCE of the prepared cells increases from 17 ± 1% for $MAPbI_3$ to 19.2 ± 0.4% for the Gua/MA mixed system containing 14% Gua, with a champion cell efficiency

of 20.15%. Moreover, even for perovskites containing 25% Gua, the photovoltaic performance remains similar to that of the $MAPbI_3$, with an average PCE of 17.1 ± 0.8% and a record efficiency of 18.30% (Supplementary Fig. 7). The current density versus voltage (J−V) curve and EQE obtained for the champion device are presented in Fig. 4a, b, respectively.

Table 1 | Photovoltaic performance

Gua (%)	J_{sc} (mA cm^{-2})	V_{oc} (V)	FF	PCE (%)
0	22.50 (22.0 ± 0.8)	1.050 (1.04 ± 0.02)	0.80 (0.74 ± 0.04)	18.88 (17 ± 1)
5.00	22.49 (22 ± 1)	1.070 (1.054 ± 0.01)	0.782 (0.76 ± 0.02)	18.81 (17 ± 1)
10.0	22.53 (22.3 ± 0.3)	1.090 (1.07 ± 0.02)	0.777 (0.75 ± 0.03)	19.09 (17.8 ± 0.9)
14.0	23.19 (22.8 ± 0.3)	1.082 (1.07 ± 0.01)	0.803 (0.79 ± 0.01)	20.15 (19.2 ± 0.4)
17.0	22.54 (21.7 ± 0.5)	1.091 (1.08 ± 0.02)	0.785 (0.78 ± 0.02)	19.29 (18.1 ± 0.7)
20.0	21.31 (21.3 ± 0.5)	1.095 (1.08 ± 0.01)	0.790 (0.77 ± 0.03)	18.43 (17.7 ± 0.8)
25.0	20.85 (20.6 ± 0.7)	1.107 (1.09 ± 0.02)	0.790 (0.77 ± 0.02)	18.30 (17.1 ± 0.8)

Photovoltaic parameters obtained for the best performing cells containing MA/Gua perovskite systems measured under AM1.5G Sun illumination. In brackets are indicated the averaged values for each condition (scan rate: 0.01 V s^{-1}; stabilization time: 5 s).

The EQE demonstrates high photon-to-current conversion over 80% throughout the entire ultraviolet–visible spectrum, leading to an integrated current density of 22.09 mA cm−2. J–V hysteresis measurements are reported in Supplementary Fig. 8. We also analysed the charge dynamics by electro-chemical impedance spectroscopy (Supplementary Figs. 9 and 10), which suggest an increased recombination resistance and longer electron

lifetime with Gua incorporation, possibly related to a more efficient charge extraction and better crystal formation.

Device stability and phase segregation analysis

The device stability has been tested under AM1.5 G Sun illumination at maximum power point (MPP) tracking, for more than 1,000 hours, at 60 °C and under an Ar atmosphere. The results (Fig. 4d) reveal an enhanced stability for higher Gua contents, providing evidence of the beneficial effect on the material stability, as predicted by the simulations. Despite the initial decrease, recently associated with the inter-penetration of spiro-OMeTAD and gold electrode[30], a gradual stabilization and recuperation of the performance is observed, which is reproducible (Supplementary Fig. 11a) and clearly correlated with the Gua content. Alternatively, we have performed an initial light stress test at 85 °C using polytriarylamine polymer, a more stable hole-transporting material, under 300 h of illumination, which further confirms the enhanced stability compared with $MAPbI_3$, for the mixed MA/Gua perovskite (Supplementary Fig. 11b). As presented in the figure, the $MAPbI_3$ film has a grainy-like morphology with large crystal domains of around 1 μm diameter (see orange line). On the contrary, $GuaPbI_3$ presents an elongated rod-like morphology with crystals of several micrometres in length, typical for the 1D aggregation.

Notably, samples containing $x_{Gua} < 0.25$ do not show any similar phase, resembling the $MAPbI_3$ as emphasized by the orange line in the picture. A relation between the amount of Gua and the size of the crystal domains is also observed for all samples, in which the domains remain like islands of several micrometres within the capping layer (Supplementary Figs. 12 and 13). The 1D-like morphology is detected only for samples containing higher amounts of Gua (> 25%), as also appreciated in Fig. 5, at which phase segregation occurs.

These results are confirmed by the micro-Raman and micro-PL analysis (Fig. 5e, f). Averaged over a diffraction-limited spot size of 300 nm, this technique can provide further information about local heterogeneities within the film[31]. The emission of four different samples was investigated, with a focus on the distribution of the PL peak position.

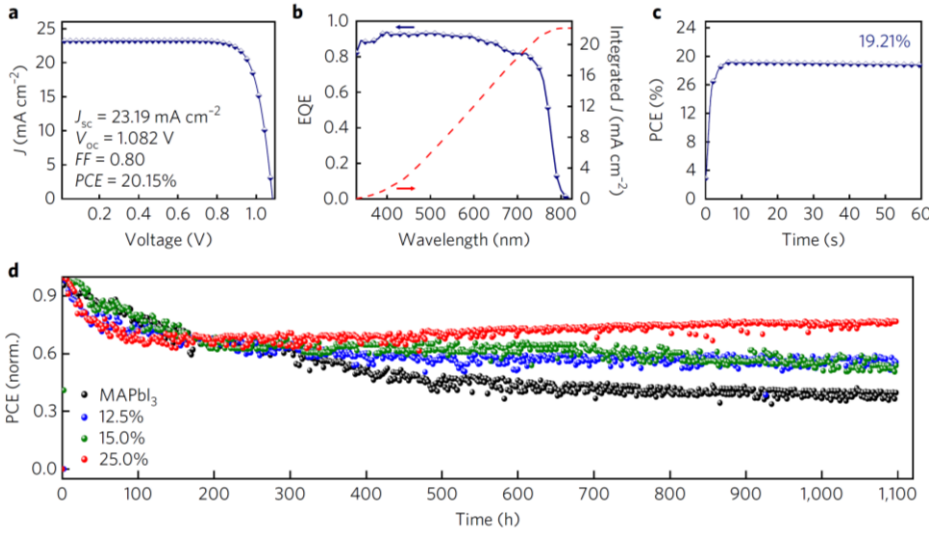

Fig. 4 | Champion device and thermal stability test. a,b, J–V curve (**a**) and EQE spectrum (**b**) of the champion cell prepared with mixed MA/Gua perovskite containing 14% Gua. **c**, MPP tracking under 1 Sun AM1.5G illumination measured in air, for a typical high-efficiency cell ($MA_{1-x}Gua_xPbI_3$ (x = 0.14)). **d**, Thermal stability test of $MA_{1-x}Gua_xPbI_3$ perovskite solar cells (x = 0, 0.125, 0.15, 0.25) at 60 °C under continuous light illumination and MPP tracking in an argon atmosphere. The initial PCE for each cell was 18.77%, 18.97%, 18.11%, and 17.14%, respectively.

The latter is intimately linked to the material bandgap, which changes with composition9 and/or local disorder[32] over microscopic areas of the samples. Fig. 5e shows the map of the PL peak position over 6 × 6 μm^2 regions. In the wavelength emission range between 710 nm and 780 nm, no appreciable change in the PL peak is observed for $x_{Gua} < 0.25$, remaining around 770 nm, as for the pure $MAPbI_3$ (Supplementary Fig. 14). On the contrary, the addition of 75% Gua leads to the appearance of a contrasted PL map with regions extending up to a few micrometres, with a remarkable PL shift down to 710

nm. This behaviour indicates a phase segregation in the material, resulting in a distribution of different bandgaps across the film. On the same areas, micro-Raman spectra were recorded (Fig. 5f).

For Gua contents up to 25%, the Raman spectra closely resemble that for the pure $MAPbI_3$. Characteristic broad peaks in the region below 200 cm^{-1} are observed related to the Pb–I stretching and bending modes33,34, along with a broad feature around 250 cm^{-1} related to the vibrations of the organic cation. Remarkably, as recently observed with FA incorporation to the $MAPbI_3$, a gradual shift of the peak to lower wavenumber appears, suggesting a shrinking of the mode due to the incorporation of the distinct Gua cation in the unit cell

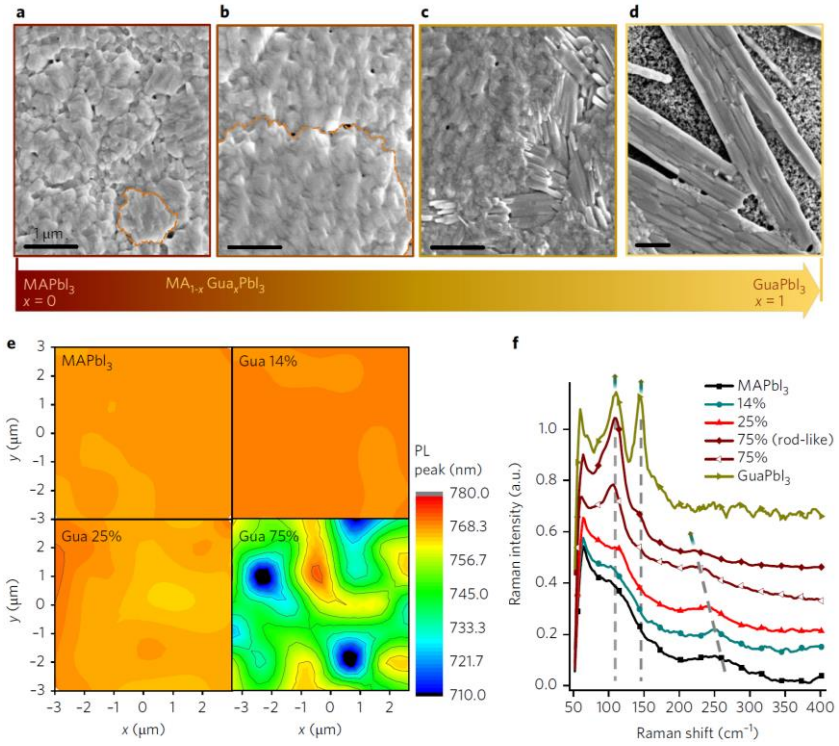

Fig. 5 | Morphology and phase segregation analysis. **a**–**d**, Top-surface SEM images of four representative samples, including pure $MAPbI_3$ (**a**), mixed $MA_{1-x}Gua_xPbI_3$ with $x = 0.14$ (**b**), with $x = 0.30$ (**c**), and pure $GuaPbI_3$ (**d**). Scale bars, 1 µ m. **e**,**f**, Micro-PL wavelength peak shift map (**e**) and micro-Raman spectra (**f**) of the perovskite surface obtained for Gua contents equal to 0, 15, 25 and 75%. The traces are shifted vertically for clarity.

For Gua content above 25%, we could identify a position-dependent signal that changes in line with the PL variation. Some regions show a similar spectrum as for the lower Gua content, while on the regions presenting the 'rod-like' morphology, a redistribution of the relative peak intensity happens with a dominant peak at 120 cm^{-1} and an additional peak at 135 cm^{-1}, both with a reduced broadening of the signal. This peak shift is usually attributed to isolated Pb–I planes, similarly to the case of PbI_2 intercalated with large organic molecules[35], which suggest the formation of a LDP as for the pure $GuaPbI_3$ arranging into the 1D phase. As corroborated in the figure, $GuaPbI_3$ shows apparent peaks at 120 cm^{-1} and 135 cm^{-1} as previously asserted for the 75 % sample. These results further confirm the phase homogeneity of the mixed $MA_{1-x}Gua_xPbI_3$ for Gua < 25%, which, on the contrary, reveals a severe phase segregation into a 3D/1D mixture for larger Gua amounts, while retaining the individual features of the single constituents. No visible degradation signs are observed during the PL measurements, as shown in Supplementary Fig. 14b.

Conclusions

We present a perovskite composition based on a combination of Gua/MA cations that exhibits superior photovoltaic performance and material stability compared with $MAPbI_3$. We demonstrate that the incorporation of large Gua cations unexpectedly forms a highly stable 3D crystalline structure, plausibly mediated by the increased number of H bonds within the inorganic framework. The prepared $MA_{1-x}Gua_xPbI_3$ perovskite preserved the good optoelectronic properties associated with the organic lead halide materials, leading to a high PCE surpassing 20% for a Gua content of 14%. Our results emphasize the versatility of organic– inorganic lead halide perovskites, and invite further exploration of organic cations including those that are beyond the limit of the tolerance factor.

Methods

Solar cell fabrication. Perovskite solar cells were fabricated on F-doped SnO_2 (NSG10) substrates previously cleaned by a sequential sonication treatment in a 2% Hellmanex solution, acetone and isopropanol, followed by ultraviolet–ozone treatment for 15 min. A compact blocking layer of TiO_2 (bl-TiO2, 30 nm in thickness) was then deposited onto the fluorine-doped tin oxide (FTO) glass substrate by spray pyrolysis, using a titanium diisopropoxide bis(acetylacetonate) solution in ethanol (60% v/v), and then sintered at 450 °C for 30 min. A 200-nmthick layer of mesoporous TiO_2 (mp-TiO_2, 30 NR-D titania paste from Dyesol) was prepared by spin-coating a diluted TiO_2 dispersion in ethanol, ratio 1:8 by weight, at 2,000 r.p.m. for 15 s followed by a sintering step at 500 °C for 30 min. Afterwards, the substrates were lithium-treated by spin-coating 40 μ l of tris (bis (trifluoromethylsulfonyl)imide) (Li-TFS) (14.67 mg ml–1 in acetonitrile) onto the mesoporous layer, followed by a sintering step at 500 °C for 30 min. Stoichiometric precursor solutions were prepared by mixing MAI, GuaI (Dyesol) and PbI_2 (TCI) in N,N′ -dimethylsulfoxide (DMSO) with MAI/GuaI gradually changing from 1:0 to 0:1, while keeping the PbI2 molarity equal to 1.25. The perovskite layers were then fabricated by using a two-step spin-coating process reported previously[36] (first step 1,000 r.p.m. for 10 s; second step 4,000 r.p.m for 30 s), and 15 s before the end of the programme, 100 μ l of chlorobenzene was poured onto the films, and then the substrates were annealed at 100 °C for 45 min. After this time, spiro-OMeTAD was spin-coated at 4,000 r.p.m., for 30 s from a chlorobenzene solution (28.9 mg in 400 μ l, 60 mmol) containing Li-TFSI (7.0 μ l from a 520 mg ml–1 stock solution in acetonitrile), TBP (11.5 μ l) and Co(II)TFSI (10 mol%, 8.8 μ l from a 40 mg ml–1 stock solution) as dopants. Finally, a 70 nm gold electrode was evaporated.

Thin-film characterization. The XRD patterns of the prepared films were measured using a D8 Advance diffractometer from Bruker (Bragg–Brentano geometry, with an X-ray tube Cu Kα , λ = 1.5406 Å). The absorption spectra were registered with an ultraviolet–visible–infrared spectrophotometer (PerkinElmer Instrument). Photoluminescence (PL) steady-state measurements were recorded with a spectrophotometer (Gilden Photonics). The micro-PL and micro-Raman measurements were performed on a Renishaw InVia Raman microscope with an L100× objective (spot size of about 300 nm). The PL map was recorded using 0.0005% laser intensity (corresponding to 100 μ J cm^{-2}), using a 532 nm green laser diode. The spectra were registered in the 710–820 nm region. Raman spectra were obtained using the same excitation monitoring the 50–250 cm^{-1} range, particularly sensitive to the Pb–I modes. The final data were averaged over 50 accumulations to maximize the signal-to-noise ratio. To prevent sample degradation or thermal effects, the laser power intensity was kept below (excitation density of around 3 mW cm^{-2} (0.005%)) and the light exposure time per measurement was 0.1 s. Photoelectron spectroscopy measurements were performed in an ultrahighvacuum system (base pressure of 2 × 10−10 mbar) using a He-discharge ultraviolet source (Omicron) with an excitation energy of 21.2 eV for UPS and an Al Kα X-ray source (excitation energy: 1486.6 eV) for XPS. The photoelectron spectra were recorded using a Phoibos 100 (Specs) hemispherical energy analyser at a pass energy of 5 eV for the valence band and a pass energy of 20 eV for the core levels. For workfunction determination, the secondary-electron cutoff was recorded by applying a − 10 V sample bias to clear the analyser workfunction. The reported valence band spectra were background subtracted. The binding energies for all of the photoemission spectra are referenced to the Fermi level. For a comparison of the XPS core-level spectra, the binding energy values were all adjusted to the C 1s carbon at

lower binding energy that was here referenced to 285 eV. A mixed Gaussian/Lorentzian peak shape and a Shirley-type background were employed for XPS peak fitting with the XPS Peak 4.1 software. NMR measurements were performed for samples containing up to 30% Gua. Mixed $MA_{1-x}Gua_xPbI_3$ perovskite films were prepared on conductive FTO substrates in the same conditions as for the photovoltaic devices. Once the perovskite layers were crystallized, the solid films were re-dissolved in deuterated DMSO (DMSO-d6) and directly analysed in liquid-state 1H-NMR 800 MHz instruments equipped with a 5 mm triple-channel 1H/13C/15N cryoprobe and a AVII console. The method used was a single pulse with 16 scans, a delay of 5 s and a pulse length of 7.8 μ s.

Device characterization. The photovoltaic device performance was analysed using a VeraSol LED solar simulator (Newport) producing 1 Sun AM 1.5 (1,000 W m^{-2}) sunlight. Current–voltage curves were measured in air with a potentiostat (Keithley 2604). The light intensity was calibrated with a NREL-certified KG5-filtered Si reference diode. The solar cells were masked with a metal aperture of 0.16 cm^2 to define the active area. The cells were measured in air, at room temperature and without encapsulation, at a constant rate 10 mV s^{-1} for both forward and reverse bias. No special pre-conditioning protocol was used apart from 5 s of stabilization time before the measurement. No anti-reflective coating was used during the measurement. The stability test was performed in a sealed cell holder flushed with a flow of argon (30 ml min^{-1}) and I–V curves were characterized by an electronic system using a 22-bit delta–sigma analog-to-digital converter, performed every 2 h. For I–V curve measurement, a scan rate of 25 mV s^{-1} with a step of 5 mV was used, maintaining the temperature of the cells at around 60 °C. Cells were maintained at the maximum power point using a MPP tracking algorithm under 100 mW cm^{-2}. A reference Si photodiode was placed in the

holder to verify the stability of the light. EQE was measured with the IQE200B (Oriel) without bias light.

Computational calculations. Geometrical structures of PbI_2 (ref. 37), GuaI (ref. 38), MAI (refs 39,40), tetragonal $MAPbI_3$ (ref. 41) and 1D $GuaPbI_3$ (ref. 21), from the bibliography, were optimized, without cell optimization. For the different perovskites, $MA_{1-x}Gua_xPbI_3$, where x = 0, 0.25 and 1, only the organic material position was optimized, restricting the Pb and I position to those obtained from the diffractogram. We proceed in this way because the MA geometric arrangement is not known in detail from the information obtained from the diffractograms[42,43]. Periodic DFT–GGA calculations using the PBE exchange correlation functional were performed[44]. Electron–ion interactions were described by ultrasoft pseudopotentials. In the case of the Pb atom, we used a scalar relativistic pseudopotential. A 4 × 4 × 4 Monkhorst—Pack grid was chosen for sampling the Brillouin zone45. Given that these compounds are essentially ionic in nature, electrostatic interactions well described by DFT–GGA are expected to represent the main contribution in the interaction. This is indirectly confirmed by the usually good agreement between experimental and calculated structural parameters for this type of material[46].

References

1. De Wolf, S. et al. Organometallic halide perovskites: sharp optical absorption edge and its relation to photovoltaic performance. J. Phys. Chem. Lett. 5, 1035–1039 (2014).

2. Stranks, S. D. et al. Electron–hole diffusion lengths exceeding 1 micrometer in an organometal trihalide perovskite absorber. Science 342, 341–344 (2013).

3. Xing, G. et al. Long-range balanced electron- and hole-transport lengths in organic–inorganic $CH_3NH_3PbI_3$. Science 342, 344–347 (2013).

4. Shi, D. et al. Low trap-state density and long carrier diffusion in organo lead trihalide perovskite single crystals. Science 347, 519–522 (2015).

5. Yang., W. S. et al. Iodide management in formamidinium-lead-halide-based perovskite layers for efficient solar cells. Science 356, 1376–1379 (2017).

6. Zhang, Y. et al. Optimization of stable quasi-cubic $FA_xMA_{1-x}PbI_3$ perovskite structure for solar cells with efficiency beyond 20%. ACS Energy Lett. 2, 802–806 (2017).

7. Bi, D. et al. Efficient luminescent solar cells based on tailored mixed-cation perovskites. Sci. Adv. 2, e1501170 (2016).

8. Conings, B. et al. Intrinsic thermal instability of methylammonium lead trihalide perovskite. Adv. Energy Mater. 5, 1500477 (2015).

9. Gratia, P. et al. Intrinsic halide segregation at nanometer scale determines the high efficiency of mixed cation/mixed halide perovskite solar cells. J. Am. Chem. Soc. 138, 15821–15824 (2016).

10. Hoke, E. T. et al. Reversible photo-induced trap formation in mixed-halide hybrid perovskites for photovoltaics. Chem. Sci. 6, 613–617 (2015).

11. Li, X. et al. Improved performance and stability of perovskite solar cells by crystal crosslinking with alkylphosphonic acid ω -ammonium chlorides. Nat. Chem. 7, 703–711 (2015).

12. You, J. et al. Improved air stability of perovskite solar cells via solutionprocessed metal oxide transport layers. Nat. Nanotech. 11, 75–81 (2016).

13. Kaltenbrunner, M. et al. Flexible high power-per-weight perovskite solar cells with chromium oxide-metal contacts for improved stability in air. Nat. Mater. 14, 1032–1039 (2015).

14. Tsai, H. et al. High-efficiency two-dimensional Ruddlesden–Popper perovskite solar cells. Nature 536, 312–316 (2016).

15. Saliba, M. et al. Cesium-containing triple cation perovskite solar cells: improved stability, reproducibility and high efficiency. Energy Environ. Sci. 9, 1989–1997 (2016).

16. Saliba, M. et al. Incorporation of rubidium cations into perovskite solar cells improves photovoltaic performance. Science 354, 206–209 (2016).

17. Kieslich, G., Sun, S. & Cheetham, A. K. Solid-state principles applied to organic-inorganic perovskites: new tricks for an old dog. Chem. Sci. 5, 4712-4715 (2014).

18. Goldschmidt, V. M. Die Gesetze der Krystallochemie. Naturwissenschaften 14, 477–485 (1926).

19. Szafrański, M. Investigation of phase instabilities in guanidinium halogenoplumbates(II). Thermochim. Acta 307, 177–183 (1997).

20. Szafrański, M. & Katrusiak, A. Phase transitions in the layered structure of diguanidinium tetraiodoplumbate. Phys. Rev. B 61, 1026–1035 (2000).

21. Jodlowski, A. D., Yépez, A., Luque, R., Camacho, L. & de Miguel, G. Benign-by-design solventless mechanochemical synthesis of three-, two-, and one-dimensional hybrid perovskites. Angew. Chem. 55, 14972–14977 (2016).

22. Huang, J., Xu, P., Liu, J. & You, X.-Z. C. Sequential introduction of cations deriving large-grain $Cs_xFA_{1-x}PbI_3$ thin film for planar hybrid solar cells: insight into phase-segregation and thermal-healing behavior. Small 13,

1603225 (2016).

23. Gholipour, S. et al. Globularity-selected large molecules for a new generation of multication perovskites. Adv. Mater. 29, 1702005 (2017).

24. Marco, N. D. et al. Guanidinium: a route to enhanced carrier lifetime and open-circuit voltage in hybrid perovskite solar cells. Nano Lett. 16, 1009–1016 (2016).

25. Buin, A., Comin, R., Xu, J., Ip, A. H. & Sargent, E. H. Halide-dependent electronic structure of organolead perovskite materials. Chem. Mater. 27, 4405–4412 (2015).

26. Nagabhushana, G. P., Shivaramaiah, R. & Navrotsky, A. Direct calorimetric verification of thermodynamic instability of lead halide hybrid perovskites. Proc. Natl Acad. Sci. USA 113, 7717–7721 (2016).

27. Quan, L. N. et al. Ligand-stabilized reduced-dimensionality perovskites. J. Am. Chem. Soc. 138, 2649–2655 (2016).

28. Lee, J. H., Lee, J.-H., Kong, E.-H. & Jang, H. M. The nature of hydrogenbonding interaction in the prototypic hybrid halide perovskite, tetragonal $CH_3NH_3PbI_3$. Sci. Rep. 6, 21687 (2016).

29. Zu, F.-S. et al. Impact of white light illumination on the electronic and chemical structures of mixed halide and single crystal perovskites. Adv. Opt. Mater. 5, 1700139 (2017).

30. Domanski, K. et al. Not all that glitters is gold: metal-migration-induced degradation in perovskite solar cells. ACS Nano 10, 6306–6314 (2016).

31. Draguta, S. et al. Spatially non-uniform trap state densities in solutionprocessed hybrid perovskite thin films. J. Phys. Chem. Lett. 7, 715–721 (2016).

32. Grancini, G. et al. The impact of the crystallization processes on the structural and optical properties of hybrid perovskite films for photovoltaics. J. Phys. Chem. Lett. 5, 3836–3842 (2014).

33. Quarti, C. et al. The Raman spectrum of the $CH_3NH_3PbI_3$ hybrid perovskite: interplay of theory and experiment. J. Phys. Chem. Lett. 5, 279–284 (2014).

34. Grancini, G. et al. $CH_3NH_3PbI_3$ perovskite single crystals: surface photophysics and their interaction with the environment. Chem. Sci. 6, 7305–7310 (2015).

35. Preda, N. et al. Raman and photoluminescence studies on intercalated lead iodide with pyridine and iodine. J. Optoelectron. Adv. Mater. 10, 319–322 (2008).

36. Jeon, N. J. et al. Solvent engineering for high-performance inorganic–organic hybrid perovskite solar cells. Nat. Mater. 13, 897–903 (2014).

37. Wyckoff, R. W. G. Crystal Structures 2nd edn, Vol. 1 239–444 (John Wiley, New York, 1963).

38. Szafranski, M. & Jarek, M. Origin of spontaneous polarization and reconstructive phase transition in guanidinium iodide. CrystEngComm 15, 4617–4623 (2013).

39. Yamamuro, O. et al. Neutron diffraction and calorimetric studies of methylammonium iodide. Acta Cryst. B48, 329–336 (1992).

40. Ishida, H. et al. EXAFS study on the phase-transition (phase-α ′ -δ) in CH3NH3I. Z. Naturforsch. A 50, 876–880 (1995).

41. Stoumpos, C. C., Malliakas, C. D. & Kanatzidis, M. G. Semiconducting tin and lead iodide perovskites with organic cations: phase transitions, high mobilities, and near-infrared photoluminescent properties. Inorg. Chem. 52, 9019–9038 (2013).

42. Motta, C. et al. Revealing the role of organic cations in hybrid halide perovskite $CH_3NH_3PbI_3$. Nat. Commun. 6, 7026–7033 (2015).

43. Ong, K. P., Goh, T. W., Xu, Q. & Huan, A. Structural evolution in methylammonium lead iodide $CH_3NH_3PbI_3$. J. Phys. Chem. A 119, 11033–11038 (2015).

44. Perdew, J. P., Burke, K. & Ernzerhof, M. Generalized gradient approximation made simple. Phys. Rev. Lett. 77, 3865–3868 (1996).

45. Monkhorst, H. J. & Pack, J. D. Special points for Brillouin-zone integrations. Phys. Rev. B 13, 5188–5192 (1976).

46. Lv, H., Gao, H., Yang, Y. & Liu, L. Density functional theory (DFT) investigation on the structure and electronic properties of the cubic perovskite $PbTiO_3$. Appl. Catal. A 404, 54–58 (2011).

Acknowledgements

We thank the European Commission H2020-ICT-2014-1, SOLEDLIGHT project, grant agreement no. 643791, the Swiss State Secretariat for Education, Research and Innovation (SERI) and Toyota Motor Europe Technical Center, Advanced Technology division, Home Wei 33, B-1930 Zaventem-Belgium for financial support. G.G. acknowledges the co-funded Marie Skłodowska Curie fellowship, H2020 grant agreement no. 665667, fund number 588072, and the SNSF Ambizione Energy grant SNF project PZENP2_173641. G.M. thanks the Ministry of Economy and Competitiveness for a 'Ramón y Cajal' contract (RYC-2013-12772). G.M. and L.C. acknowledge the Ministry of Economy and Competitiveness for financial support (CTQ2014-56422-P). A.D.J. thanks COSTSTSM-MP1307 for financial support. Work in Berlin was supported by the SFB951 (DFG). We thank E. Oveisi and E. Baudat for the helpful discussions, L. Wen for his support during the XPS measurement and M. Tschumi for providing the instrument required for the stability measurements.

Author contributions

A.D.J. planned the experiments and prepared and characterized the cells; M.S. performed the impedance measurements and analysis; S.A. supervised M.S.; G.M. performed the XPS, XRD and absorption analysis; G.G. carried out the Raman and PL characterization; C.R.-C. designed the experiments, carried out the SEM analysis and wrote the manuscript; L.C. performed the theoretical simulations; M.R. and N.K. performed UPS and XPS analysis; C.R.-C., G.M., L.C. and M.K.N. conceived the idea, and supervised the research project.

Supplementary Figures

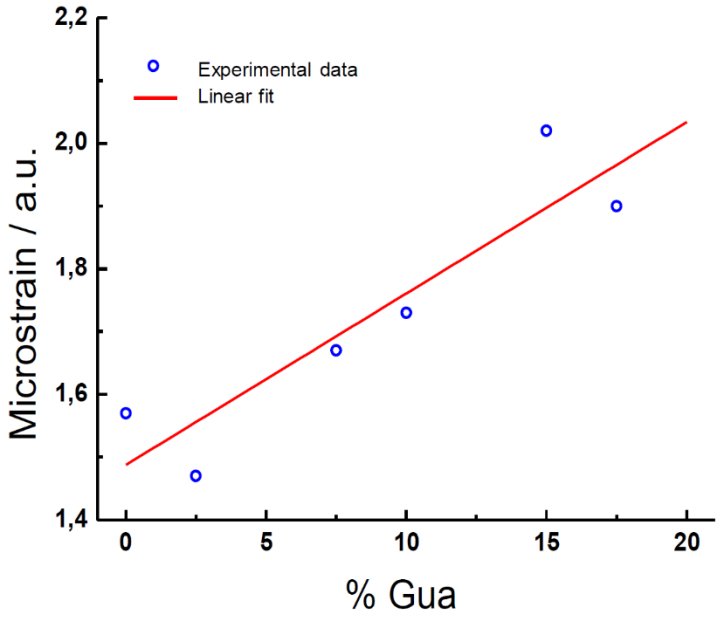

Supplementary Figure 1. Micro-strain (ε) variations in MAPbI3 structure upon increasing Gua content. The ε values are estimated by using the Williamson-Hall equation, $\beta = 1/D + 2\varepsilon/d$, where β is the width of the reflection peaks, D is the crystallite size and d is the position of the reflections peaks.

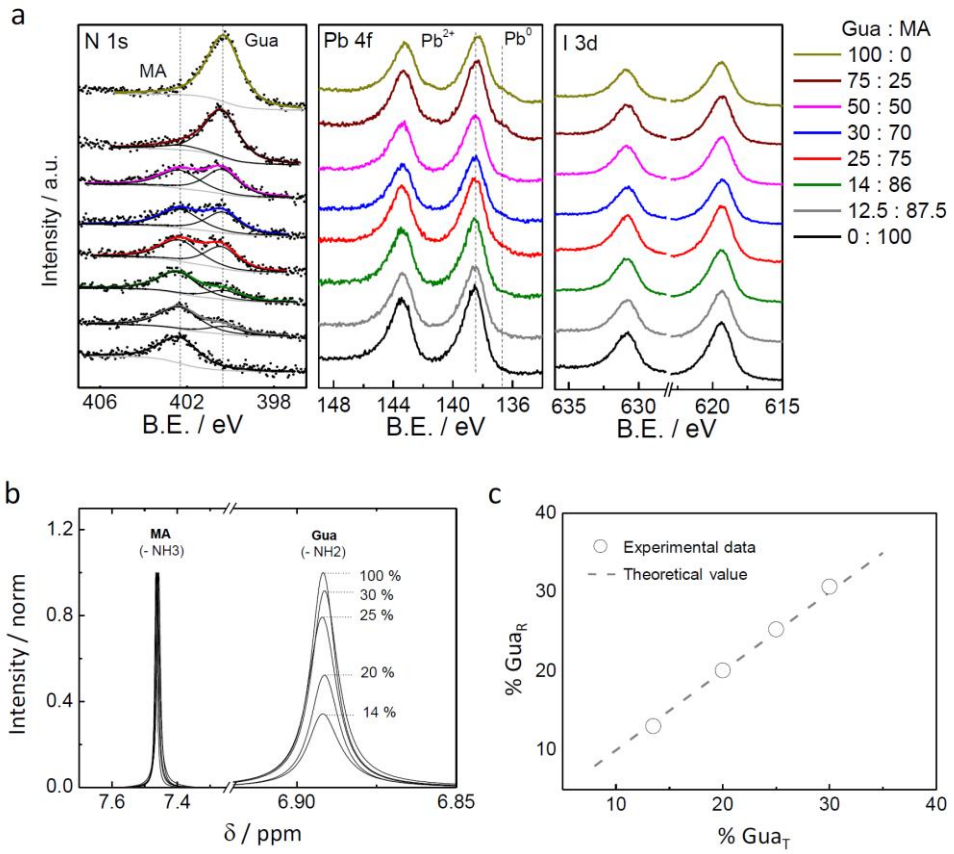

Supplementary Figure 2. a. XPS spectra of N 1s (left), Pb 4f (center) and I 3d (right) core level photoemission peaks1 obtained from thin films of $MAPbI_3$ and mixed $MA_{1-x}Gua_xPbI_3$ systems (with x = 0.125, 0.25, 0.50, and 1.0). Traces have been shifted vertically for clarity. b, Liquid 1H-NMR spectra obtained from $MA_{1-x}Gua_xPbI_3$ perovskite samples dissolved in d-DMSO, containing x = 0.14; 0.20; 0.25 and 0.30 (as indicated in the label). The relative ratio for $-NH_3$ and NH_2 groups (corresponding to MA and Gua respectively) is gradually decreasing with the increased incorporation of Gua. c, Quantification of MA:Gua ratio obtained from the 1HNMR spectra shown in (c) (Gua_R, value calculated from NMR spectra; Gua_T, theoretical value initially incorporated to the precursor solutions).

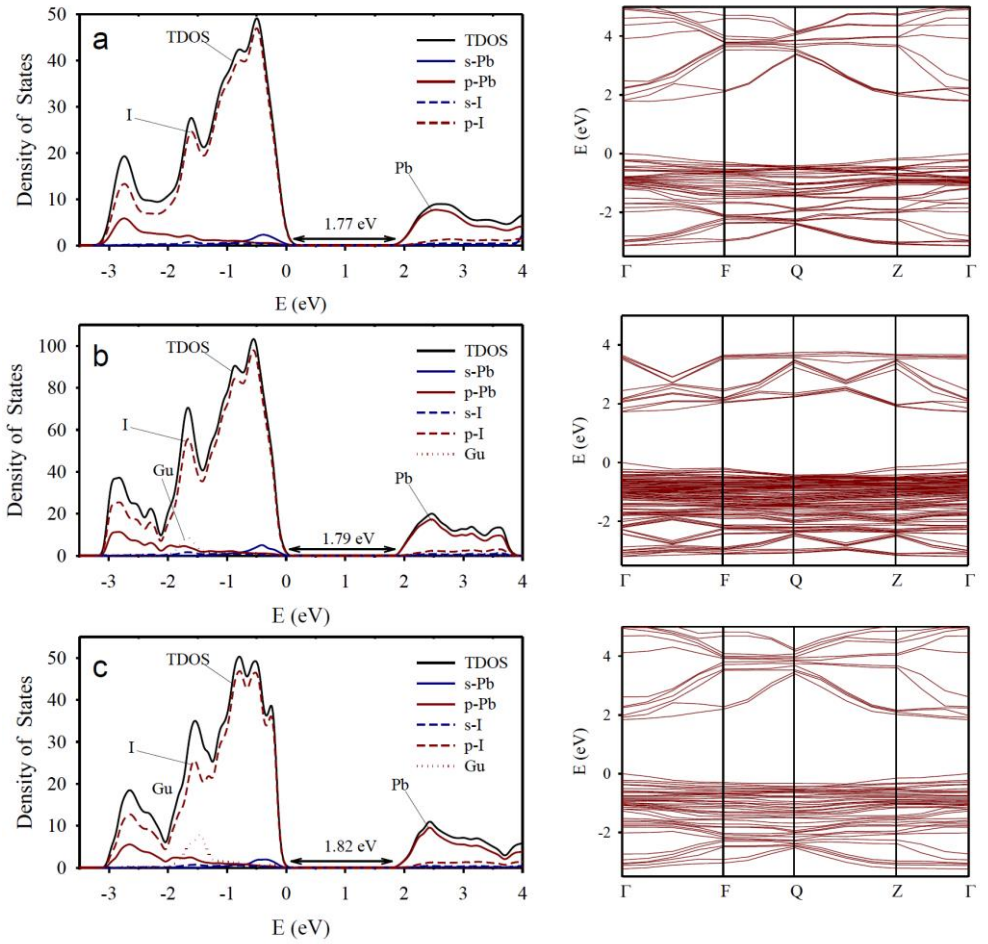

Supplementary Figure 3. Calculated band structure (left) and density of states (right) of a, $MAPbI_3$; b, $MA_{0.875}Gua_{0.125}PbI_3$ and c, $MA_{0.75}Gua_{0.25}PbI_3$. Inset: total (solid black line), s-Pb (blue solid line), p-Pb (red solid line), s-I (blue dashed line), p-I (red dashed line) and p-Gua (red dotted line) density of states.

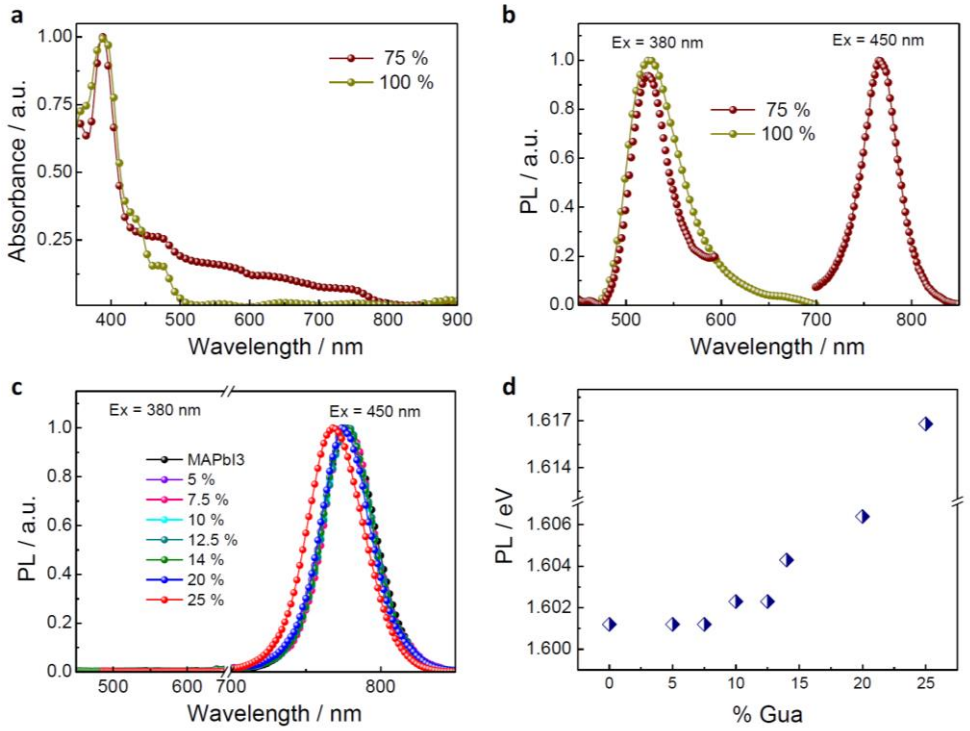

Supplementary Figure 4. a, UV-visible absorption spectra registered for MA:Gua mixed perovskite containing 75 % of Gua, as well as the pure 1D-GuaPbI$_3$ perovskite. b, Photoluminescence (PL) spectra registered for the systems presented in (a), excited at 380 nm (region below 700 nm) and 450 nm. The 75% sample exhibits emissions corresponding to the two coexisting phases (1D-GuaPbI$_3$, and MA$_{1-x}$Gua$_x$PbI$_3$). c, Photoluminescence (PL) spectra registered for MA$_{1-x}$Gua$_x$PbI$_3$ mixed perovskites containing x ≤ 0.25, excited at both 380 nm (region below 700nm) and 450 nm. d, Evolution of the PL maximum (in eV) with % of Gua.

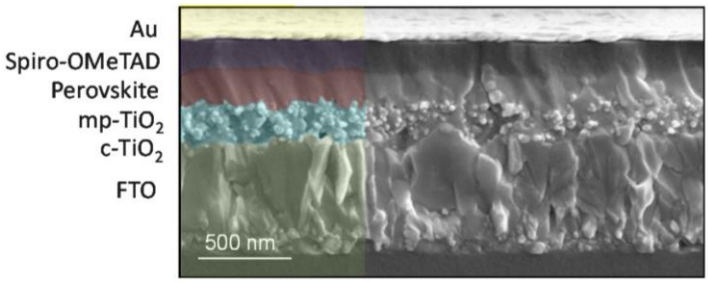

Supplementary Figure 5. Cross-sectional SEM image of a typical mixed MA:Gua PSC containing 14 % of Gua. Device architecture: Glass/FTO/c-TiO_2/ mp-TiO_2/ Perovskite/ Spiro-OMeTAD/ Au.

Supplementary Figure 6. Photographs of the MA:Gua mixed perovskite devices containing increased % of Gua, as indicated in the labels.

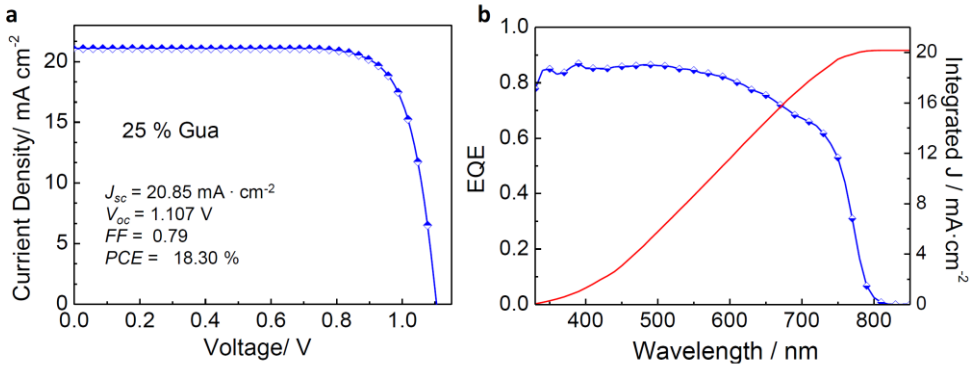

Supplementary Figure 7. Photovoltaic parameters obtained for the record cell containing $MA_{1-x}Gua_xPbI_3$ (x=0.25). a, Current density versus voltage ($J-V$) curve measured under AM1.5G sun illumination, at room temperature. b, EQE spectrum and integrated current density curve obtained for $MA_{1-x}Gua_xPbI_3$ solar cell (x=0.25).

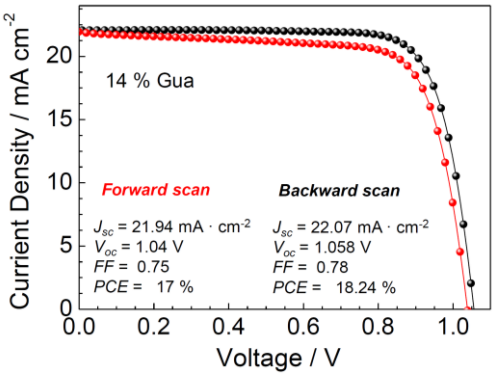

Supplementary Figure 8. $J-V$ curve measured for $MA_{1-x}Gua_xPbI_3$ (x=0.14) perovskite solar cell under forward (V_{oc} to J_{sc}) and reverse (J_{sc} to V_{oc}) bias conditions at AM1.5G sun illumination.

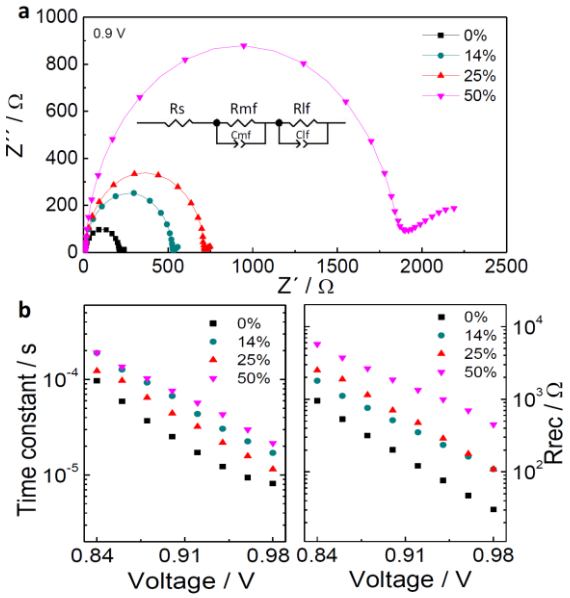

Supplementary Figure 9. a, Nyquist plot of PSCs prepared with MA:Gua systems containing increasing Gua content, as indicated in the label (the photovoltaic performance is presented in Supplementary Table 2). The equivalent circuit, shown in the inset, contains the series resistance (R_s), recombination resistance (R_{mf}, R_{lf}) and capacitance (C_{mf}, C_{lf}) at medium and low frequency. b, Recombination resistance at medium frequencies (Rmf) versus applied voltage for the PSC analyzed in (a), left panel, and charge recombination time-constant calculated for perovskite devices shown in (a), right panel. See Supplementary Note 2.

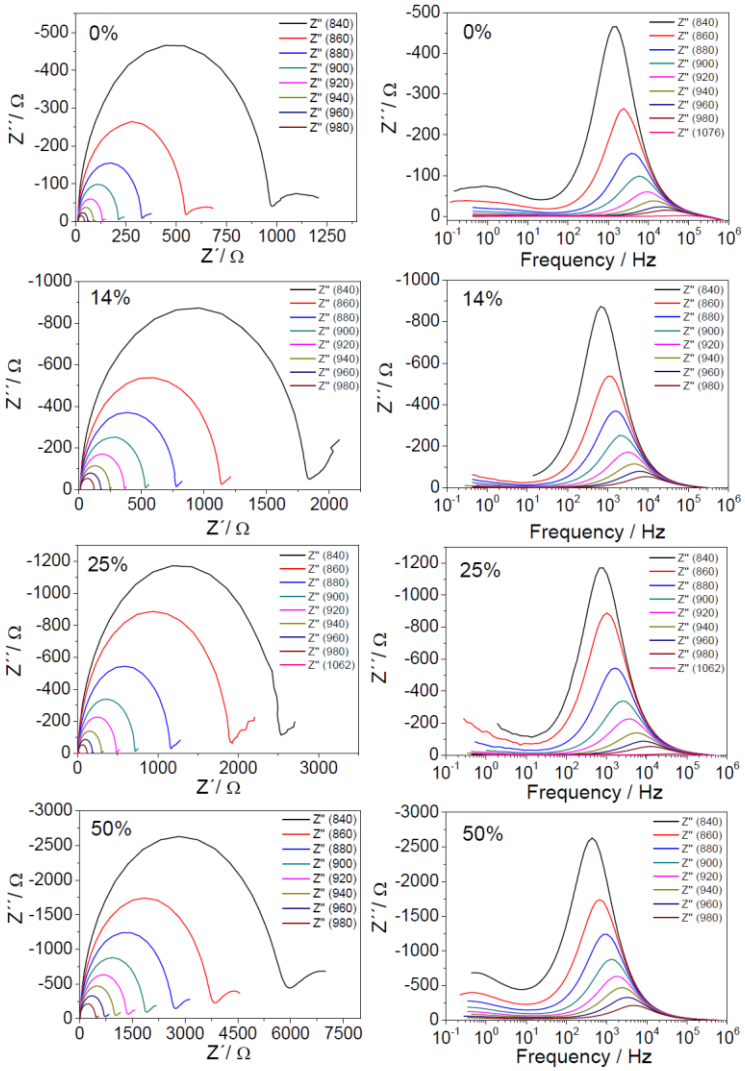

Supplementary Figure 10. Frequency plot of the imaginary part of the impedance response corresponding to the cells shown in Supplementary Table 2.

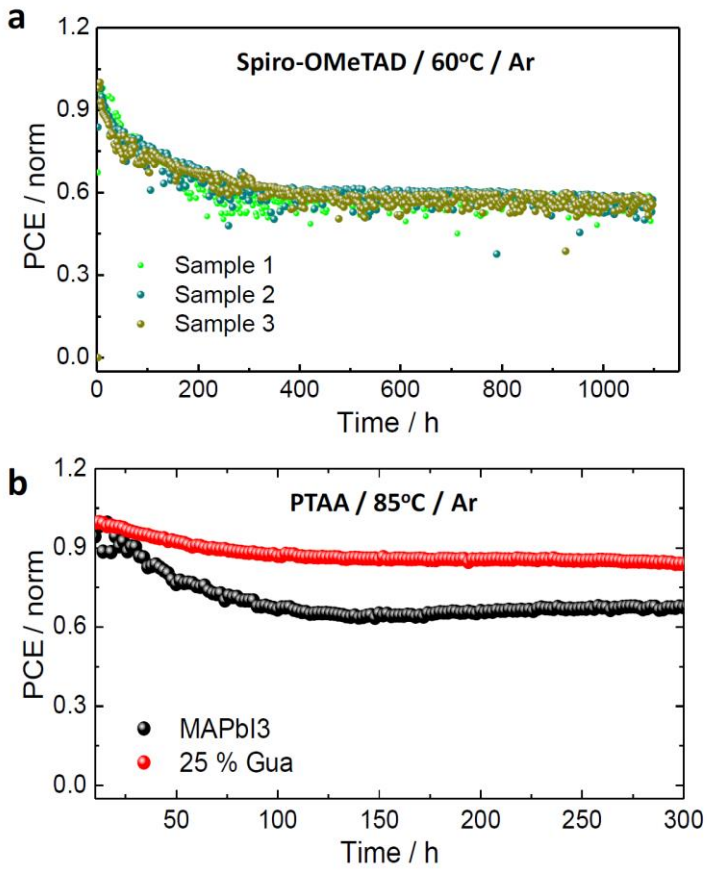

Supplementary Figure 11. Thermal stability test performed at maximum power point tracking (MPPT) under continuous light illumination of a, three different $MA_{1-x}Gua_xPbI_3$ (x = 0.125) perovskite solar cells containing Spiro-OMeTAD as HTM. Measurements performed at 60 ºC. b, $MA_{1-x}Gua_xPbI_3$ (x = 0.25) perovskite solar cell containing PTAA as HTM, $MAPbI_3$ is included as reference. Measurements performed at 85 ºC.

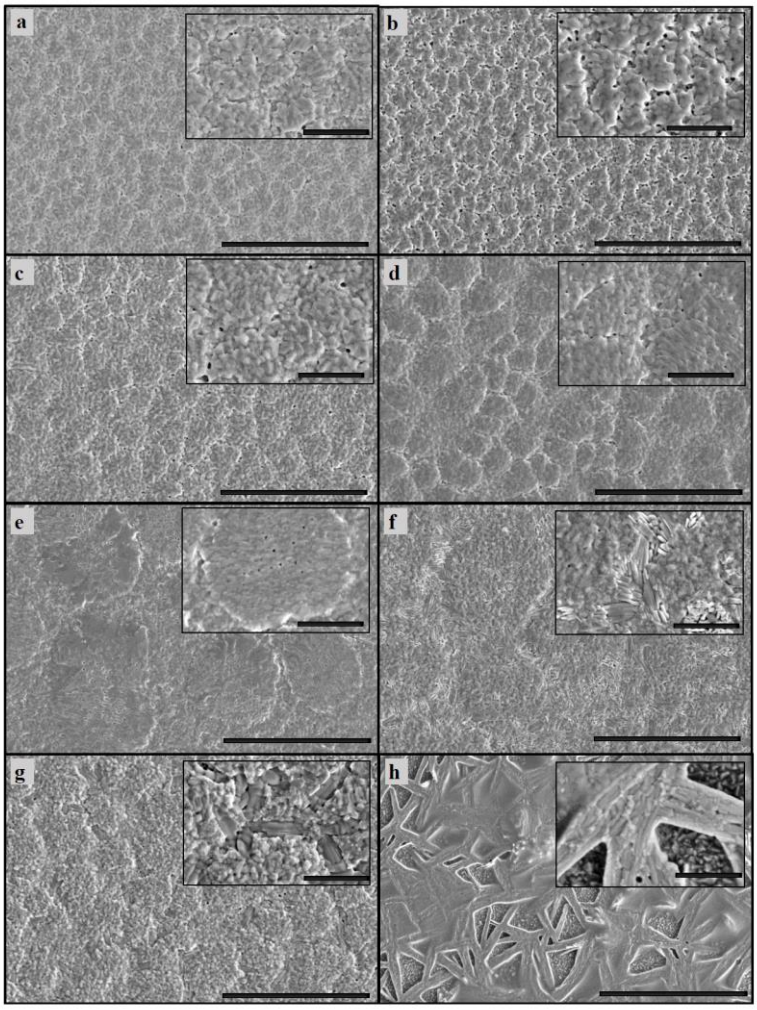

Supplementary Figure 12. Top view SEM images of a MA:Gua mixed systems at two different magnifications. The percentage of Gua incorporated into the system is (a) 0% ($MAPbI_3$), (b) 2.5 %, (c) 5 %, (d) 15 %, (e) 25 %, (f) 30 %, (g) 50 % and (h) 75 %. Large scale bar: 10 μm. Short scale bar (inset): 2 μm.

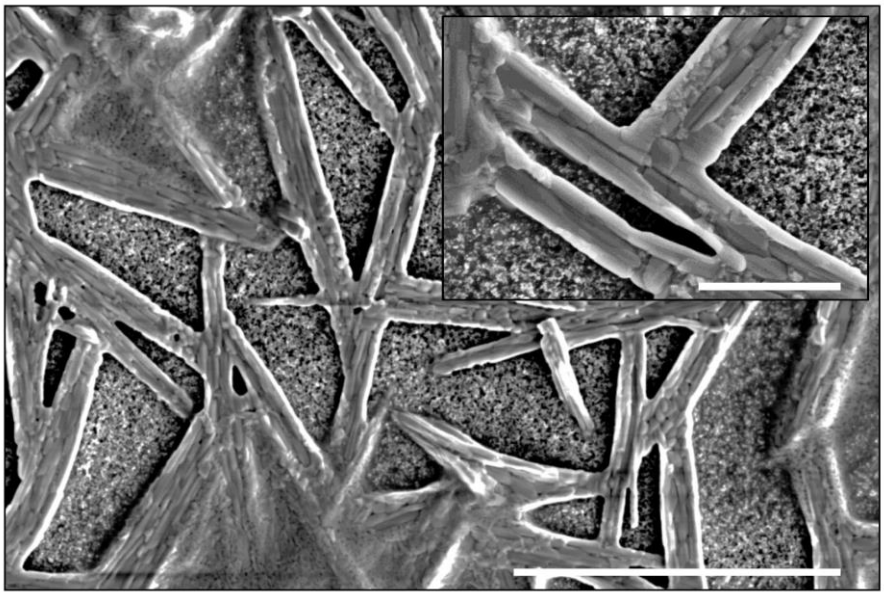

Supplementary Figure 13. Top view SEM image of a pure 1D-GuaPbI$_3$ perovskite sample on mp-TiO$_2$ substrate. Large scale bar: 10 μm. Short scale bar (inset): 2 μm.

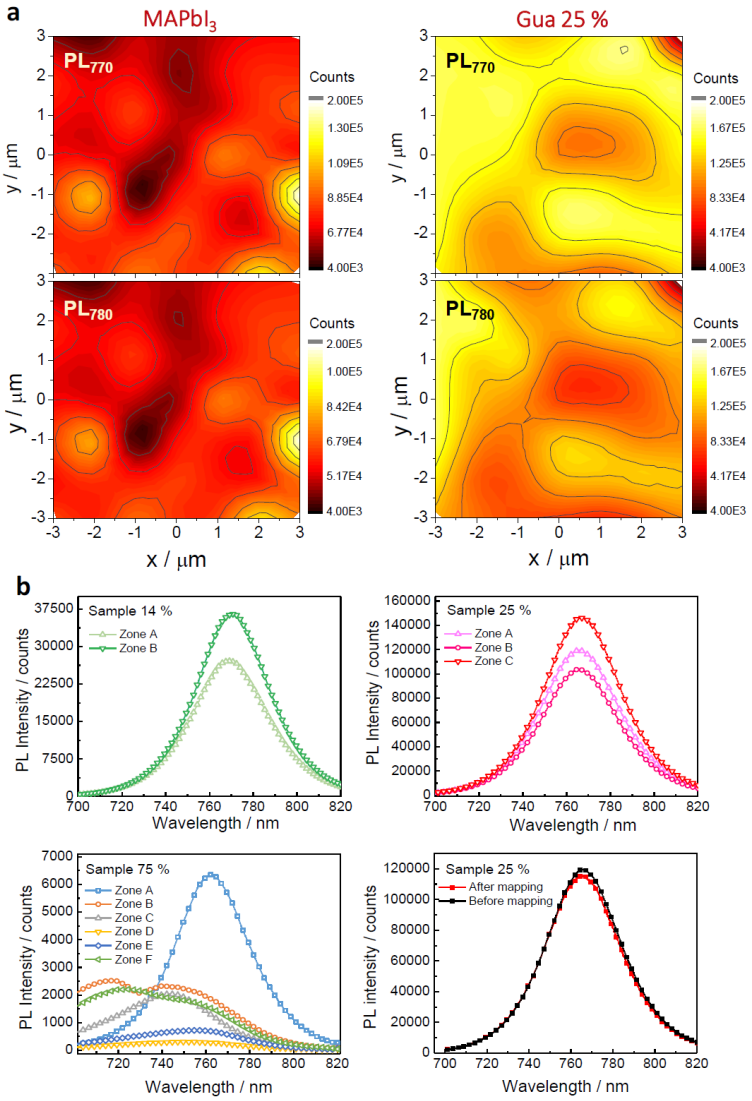

Supplementary Figure 14. a, Micro-PL intensity map of the perovskite surface obtained for $MAPbI_3$ and 25% Gua content (PL_{max} of 770nm (top) and 780nm (bottom)). The scalebar indicates the PL peak intensity in counts. **b,** PL emission peaks obtain from different zones in mixed $MA_{1-x}Gua_xPbI_3$ films (x = 0, 0.14 and 0.25). For comparison, the PL spectrum before and after the mapping has been recorded.

Supplementary Tables

Supplementary Table 1. Photovoltaic parameters obtained for the best performing cells containing MA:Gua perovskite systems measured under AM1.5G sun illumination. In brackets are indicated the averaged values for each condition from more than 190 devices (scan rate: 0.01 $V \cdot s^{-1}$; stabilization time: 5 s).

% Gua	*J_{sc} ($mA \cdot cm^{-2}$)*	*V_{oc} (V)*	*FF*	*PCE (%)*
0	22.50 (22.0 ± 0.8)	1.050 (1.04 ± 0.02)	0.80 (0.74 ± 0.04)	18.88 (17 ± 1)
2.50	22.28 (21.99 ± 0.7)	1.060 (1.058 ± 0.009)	0.76 (0.75 ± 0.04)	18.14 (17 ± 1)
5.00	22.49 (22 ± 1)	1.070 (1.054 ± 0.01)	0.782 (0.76 ± 0.02)	18.81 (17 ± 1)
7.50	22.49 (22.0 ± 0.4)	1.061 (1.05 ± 0.01)	0.786 (0.77 ± 0.03)	18.75 (17.8 ± 0.9)
10.0	22.53 (22.3 ± 0.3)	1.090 (1.07 ± 0.02)	0.777 (0.75 ± 0.03)	19.09 (17.8 ± 0.9)
12.5	22.79 (22.4 ± 0.5)	1.094 (1.07 ± 0.02)	0.785 (0.77 ± 0.03)	19.58 (18.3 ± 0.7)
14.0	23.19 (22.8 ± 0.3)	1.082 (1.07 ± 0.01)	0.803 (0.79 ± 0.01)	20.15 (19.2 ± 0.4)
15.0	22.34 (22.3 ± 0.4)	1.070 (1.07 ± 0.01)	0.795 (0.77 ± 0.02)	18.99 (18.4 ± 0.4)
17.0	22.54 (21.7 ± 0.5)	1.091 (1.08 ± 0.02)	0.785 (0.78 ± 0.02)	19.29 (18.1 ± 0.7)
20.0	21.31 (21.3 ± 0.5)	1.095 (1.08 ± 0.01)	0.790 (0.77 ± 0.03)	18.43 (17.7 ± 0.8)
25.0	20.85 (20.6 ± 0.7)	1.107 (1.09 ± 0.02)	0.790 (0.77 ± 0.02)	18.30 (17.1 ± 0.8)
50.0	12.79 (11 ± 2)	1.080 (1.09 ± 0.03)	0.667 (0.66 ± 0.02)	9.21 (8 ± 1)
75.0	0.59 (0.56 ± 0.08)	0.920 (0.88 ± 0.04)	0.600 (0.61 ± 0.04)	0.33 (0.30 ± 0.04)
100	0.50 (0.3 ± 0.3)	0.857 (0.882 ± 1)	0.394 (0.42 ± 0.04)	0.17 (0.12 ± 0.08)

Supplementary Table 2. Photovoltaic parameters measured for the four different samples employed for electro-chemical impedance spectroscopy (EIS) characterization.

Gua %	V_{oc} (V)	J_{sc} ($mA \cdot cm^{-2}$)	FF	PCE (%)
0	1.06	22.56	0.77	18.41
14	1.09	22.79	0.78	19.45
25	1.11	20.94	0.77	17.89
50	1.13	11.56	0.70	9.20

Supplementary Notes

Supplementary Note 1. To evaluate the stability of the proposed mixed $MA_{1-x}Gua_xPbI_3$ structures, the formation enthalpies, ΔH_f, of the pure MA or Gua perovskite phases and that containing 25% Gua were theoretically estimated by means of periodic DFT-GGA calculations using the PBE exchange correlation functional. To estimate the ΔH_f for each perovskite, we used the total energy per solid unit corresponding to each chemical specie depicted in eq. (1), which are obtained from the DFT-GGA calculations. The obtained values are a good approximation to the ΔH_f at zero temperature despite the zero-point vibrational energy and, less importantly, the standard pressure effects on the total energy are not considered[2]. Since the entropy contribution can be neglected at room temperature, ΔH_f can be utilized as a criterion for the stability of the different perovskites.

$$PbI_2 + (1 - x)MAI + xGua \rightarrow MA_{1-x}Gua_xPbI_3 \qquad \text{eq (1)}$$

The estimated formation enthalpies for the three studied materials are the following: for the $MAPbI_3$ material it is close to zero, -0.149 eV, which is very similar to that reported in a recent article (ΔH_f = -0.1 eV) by using similar DFT calculations3. Direct calorimetric measurements of ΔH_f have also revealed a positive value of 0.36 eV for $MAPbI_3$[4]. Thus, both experimental and theoretical values of ΔH_f indicate the low stability of the $MAPbI_3$ perovskite with the chemical equilibrium in eq. (1) shifted to the initial precursors. This is clearly the origin of the poor stability of the solar cells prepared with this material. In the case of the 1D-$GuaPbI_3$ perovskite, the estimated value of ΔH_f is -2.045 eV, which indicates that eq. (1) is highly exothermic implying a great stability of the perovskite product[5].

Regarding the mixture with 25% Gua, $Ma_{0.75}Gua_{0.25}PbI_3$, the calculated ΔH_f is -1.484 eV, a highly negative value close to that of the 1D $GuaPbI_3$. The more negative value of ΔH_f in $Ma_{0.75}Gua_{0.25}PbI_3$ with respect to the $MAPbI_3$ perovskite indicates that the mixed phase is thermodynamically more stable than the pure phase. In addition, the optimization of the crystalline structure reveals the formation of hydrogen bonding, which plays a key role in the structural stabilization, revealing close distances in between the H atoms of the Gua cations and the I atoms. Although an evaluation of the H-bonds formation requires a more extensive theoretical investigation, these preliminary results indicates that the increased number of H atoms in the Gua results in larger number of H-bonds, which may be the ultimate responsible for the extended stability of the mixed $Ma_{0.75}Gua_{0.25}PbI_3$ systems compared to the archetypal $MAPbI_3$ perovskite.

Finally, to demonstrate that the addition of 25% Gua instead of MA leads to the formation of the mixed $Ma_{0.75}Gua_{0.25}PbI_3$ perovskite (eq. (1)) and not to a phase separation with 75% $MAPbI_3$ and 25% $GuaPbI_3$ (eq. (2)), the ΔH_f for the latter reaction was calculated.

$$PbI_2 + 0.75\mathrm{MAI} + 0.25\mathrm{GuaI} \rightarrow 0.75\mathrm{MAPb}I_3 + 0.25GuaPbI_3 \qquad eq\ (2)$$

The ΔH_f value for the formation of both perovskites, $MAPbI_3$ and $GuaPbI_3$, is -0.622 eV, less negative than that of the mixed phase formation, -1.484 eV. Thus, the formation of the mixed $Ma_{0.75}Gua_{0.25}PbI_3$ is thermodynamically favored with respect to the phase separation, which supports our experimental XRD results.

Supplementary Note 2. Supplementary Figure 10 presents the complex impedance plot obtained for cells containing various Gua % under illumination. Two arcs with different characteristic frequencies can be distinguished: one on the low frequency region 0,1-10 Hz, usually related to slow processes such as ionic motion or charge accumulation at the interfaces 6-8, and one in the mid-frequency region, 102-105 Hz, related with the recombination kinetics within the cell, as shown in Supplementary Fig. 11. Gua based solar cells exhibit better recombination resistance (it increases over 100 mV) and larger electron lifetime recombination compared with the $MAPbI_3$ reference.

Supplementary References

1. Wagner, C. D.; Riggs, W. M.; Davis, L. E., Handbook of X-ray photoelectron spectroscopy. Muilenberg, G.E., Ed. Minnesota (1979).

2. Huang, J. et al. Sequential Introduction of Cations Deriving Large-Grain $Cs_xFA_{1-x}PbI_3$ Thin Film for Planar Hybrid Solar Cells: Insight into Phase-Segregation and Thermal-Healing Behavior. Small 13, 1603225, (2016).

3. Buin, A et al. Halide-Dependent Electronic Structure of Organolead Perovskite Materials. Chemistry of Materials 27, 4405-4412, (2015).

4. Nagabhushana, G. P.et. al. Direct calorimetric verification of thermodynamic instability of lead halide hybrid perovskites. Proceedings of the National Academy of Sciences 113, 7717-7721, (2016).

5. Quan, L. N. et al. Ligand-Stabilized Reduced-Dimensionality Perovskites. Journal of the American Chemical Society 138, 2649-2655, (2016).

6. Bisquert, J.et al. Theory of Impedance and Capacitance Spectroscopy of Solar Cells with Dielectric Relaxation, Drift-Diffusion Transport, and Recombination. The Journal of Physical Chemistry C 118, 18983-18991, (2014).

7. Guillén, E. et al. Elucidating Transport-Recombination Mechanisms in Perovskite Solar Cells by Small-Perturbation Techniques. The Journal of Physical Chemistry C 118, 22913-22922, (2014).

8. Xiao, Z. et al. Giant switchable photovoltaic effect in organometal trihalide perovskite devices. Nature Materials 14, 193-198, (2015).

ADVANCED ENERGY MATERIALS

Impact Factor: 21.875

DOI: 10.1002/aenm.201703120

Alternative Perovskites for Photovoltaics

Alexander Davis Jodlowski, Daily Rodríguez-Padrón, Rafael Luque, and Gustavo de Miguel*

Abstract: The discovery of unique optoelectronic properties of 3D ABX_3 perovskites has produced a great impact on the field of photovoltaics. In the initial years after the breakthrough, interest has focused on a limited number of 3D ABX_3 perovskite materials, including the archetypal $CH_3NH_3PbI_3$ and its counterparts. Undoubtedly, the main limitation of perovskite devices is their low stability due the fast degradation of the perovskite layer; however, the high toxicity of Pb also poses a concern. Herein, the recent increasing number of articles reporting the theoretical modeling, synthesis, optoelectronic characterization, and implementation of alternative perovskite materials in solar devices is summarized. The extensive variety of perovskite derivatives is classified according to the material dimensionality and the crystal structure. The particular strengths and weaknesses for each novel material are discussed, and the device performance and potential stability enhancements are also highlighted.

1. Introduction

Since their first publication in 2009, the emergence of perovskite materials has revolutionized the field of photovoltaics.[1] The initial perovskite-based device was fabricated using the $CH_3NH_3PbI_3$ ($MAPbI_3$) perovskite, which delivered a power conversion efficiency (PCE) of 3.8%. This PCE has been surpassed to a maximum value of 22.7%.[1–10] In the following years, many researchers from many disciplines have been attracted to the fascinating field of perovskites to shed more light into the nature of the extraordinary properties of these materials. The key optoelectronic features that make the 3D $MAPbI_3$ perovskite an excellent active material for photovoltaics include an optimal band gap energy of ≈1.55 eV, high absorption coefficient (104–105 cm^{-1}) due to the direct band gap transition, reduced exciton binding energy (10–30 meV) enabling free carrier generation, high charge-carrier mobilities due to low charge effective masses (m_h^* or $m_e^* \approx 0.1m_0$) derived from the large band dispersion, good defect tolerance that avoids the formation of deep trap states and long charge-carrier diffusion lengths.[11–19] Additionally, 3D $MAPbI_3$ is a solution processable material constituted by earth abundant raw materials, which minimizes fabrication costs.[20–25] However, there are two important limitations for the further industrial application of these solar devices: the high toxicity of Pb, which poses a risk to humans and causes environmental contamination, and the low stabilities of perovskite materials, which is derived from degradation to its initial precursors due to thermal, moisture and operational effects.[26–35]

Conventional perovskites utilized in photovoltaics exhibit a stoichiometric formula of ABX_3, where A is a monovalent cation, B is a divalent cation, and X is a halide anion. The perovskite structure is comprised of corner-sharing BX_6 octahedra with in between voids occupied by A cations to achieve charge neutrality (see Figure 1). The perovskite crystal lattice is formed by a 3D network of inorganic octahedra that are primarily responsible for the

outstanding optoelectronic properties of this material, including the low binding energy and isotropic charge transport.[12–14,36] The size of the A cation suitable for the octahedral voids is experimentally defined by the Goldschmidt tolerance factor $t = [R_A + R_x]/[\sqrt{2}(R_B + R_x)]$, where R_A, R_B, and R_X are the ionic radii for each component. Only A cations with tolerance factors between $0.8 < t < 1.0$ give rise to valuable 3D perovskite materials. [37–40]

The main architecture of solar devices fabricated with perovskites is a mesoporous scaffold configuration; however, a planar arrangement offers rivaling PCE values.[36,41] The mesoporous layer is predominately formed by TiO_2 acting as an electrontransport layer (ETL), while the typical solid-state hole-transport layer (HTL) is the organic compound, 2,2′,7,7′ tetrakis(N,N′-di-pmethoxyphenylamine)-9,9′-spirobifluorene (Spiro-OMeTAD).[2,3] In the planar configuration, the ETL layer is usually formed by compact, thin layers of TiO_2 or SnO_2 deposited through different methods. The deposition of the perovskite layer is usually performed by a spin-coating technique from a solution containing the precursors (PbI_2 + MAI for the $MAPbI_3$ perovskite) and further annealing at ≈120 °C.[5,42] The use of the so-called “antisolvent” method consisting of the addition of a nonpolar solvent during the spin-coating process has been found to provide optimum solar efficiencies.[43,44] The typical layer configuration is FTO/ETL/perovskite/HTL/metal contact, where FTO is fluorinedoped tin oxide as the transparent conductive electrode, and gold serves as the standard metal counter electrode (see Figure 1).

The short-circuit photocurrents (J_{sc}) in a perovskite-based solar cell are usually in the range of 20–22 mA cm^{-2}, with a reduced loss of photocurrent linked to absorption from different layers, detrimental reflections and transmissions or the morphology of the perovskite material.[4,7,45,46] The open-circuit voltage (V_{oc}) is normally above 1.0 eV (can reach 1.2 eV when using

mixed halide anions). [5,41,47,48] The high V_{oc} values are related to the sharp absorption onset and low nonradiative recombination. [11] The fill factor (FF) values normally approach 80%, with the grain boundaries seemingly limiting the achievement of the theoretical limit of 91% in $MAPbI_3$.[49]

A significant operational feature of perovskite-based solar cells has been current–voltage hysteresis, which has attracted significant interest in early years.[50,51] The J–V curves differ considerably depending on the scan rate, and hysteresis occurs when the forward and backward scans do not overlap at the same scan rate.[52] The migration of ionic defects in perovskites during J–V measurements seems to be the responsible mechanism for the hysteresis phenomenon.[53–55] Some efforts have focused on reducing hysteresis via interfacial layer engineering.[56] However, the principal limitation that hampers the commercialization of perovskite cells is the restrained stability of these devices.[57] Thus far, an established protocol to determine the stability of the devices does not exist, and each research group performs stability tests under different conditions. Among different aging factors, humidity and high temperatures can degrade perovskite materials.[26] Another important factor is gold migration through the HTL layer, which can also influence the perovskite structure.[58] Perovskite solar cells degrade by 50% in only a few hours in the absence of proper encapsulation under UV illumination in ambient atmosphere.[59] Initial efficiencies have been reported to be maintained over 90 days at 85 °C with appropriate encapsulation and using carbon electrodes and ZrO_2 as the HTLs.[60]

In addition to the archetypal perovskite, $CH_3NH_3PbI_3$, that has delivered efficiencies near 20%, other innovative perovskite materials based on modifications of the $MAPbI_3$ structure have been implemented in solar devices to optimize the photovoltaic performance.

Modifications of the halide substitution were the first strategy to design novel materials with optimized optoelectronic properties.[61] The incorporation of

bromide or chloride instead of iodide rendered $MAPbBr_3$ and $MAPbCl_3$ perovskites with band gap energies (2.24 and 2.97 eV, respectively) higher than that of $MAPbI_3$ (1.53 eV). [62] The large band gaps make these two perovskites unsuitable for single-junction solar cells, but $MAPbBr_3$ may have potential in tandem devices.

The replacement of Pb has also been proposed as an approach due to the high toxicity of this element, which may cause important legal restrictions to the commercialization of solar devices. [63–65] A widespread approach has been the employment of Sn instead of Pb to obtain $CH_3NH_3SnI_3$ perovskites that possess a promising low band gap energy (1.23 eV).[66] However, only unexpectedly low PCEs near 6% have been reported due to the rapid degradation of $CH_3NH_3SnI_3$ resulting from the rapid oxidation of Sn^{2+} to Sn^{4+} (see Figure 2). [66,67] Last but not least, formamidinium $CH(NH_2)^{2+}$ (FA) and Cs^+ cations besides methyl ammonium $CH_3NH_3^+$ (MA) have been incorporated into perovskites for photovoltaics.[68–71]

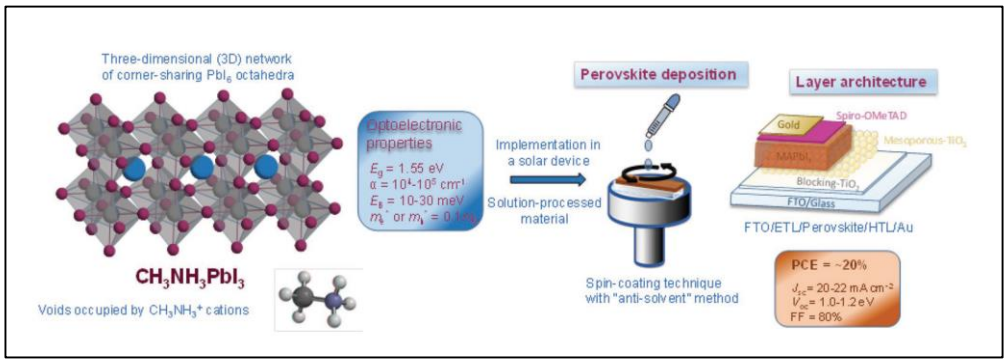

Figure 1. Structure, optoelectronic properties and implementation in solar devices of the $MAPbI_3$ perovskite.

The three mentioned cations are the only monovalent cations possessing Goldschmidt tolerance factors between 0.8 and 1.0, which entail the formation of the 3D “black” phase with optimum optoelectronic properties for

photovoltaic applications.[36] The black phases formed with Cs and FA ($CsPbI_3$ and $FAPbI_3$) are only stable at high temperature, but these phases can be stabilized at ambient temperature by partially mixing with the archetypal MA cation in different combinations, i.e., MA/FA, Cs/MA, Cs/FA, and Cs/ MA/FA in the so-called multiple cation approach.[8,70–72] The best PCEs have been obtained with mixed cation as well as mixed halides perovskites, such as $FA_xMA_{1-x}Pb(Br_yI_{1-y})_3$ offering a PCE of 22% and $Cs_x(FA_{0.17}MA_{0.83})_{1-x}Pb(Br_yI_{1-y})_3$ giving a PCE of 21% (see Figure 2).[7,8,47,72] Despite the enhanced stabilities obtained using mixed cation and halide perovskites compared to $MAPbI_3$, further improvements are needed to achieve a lifetime suitable for industrial applications.

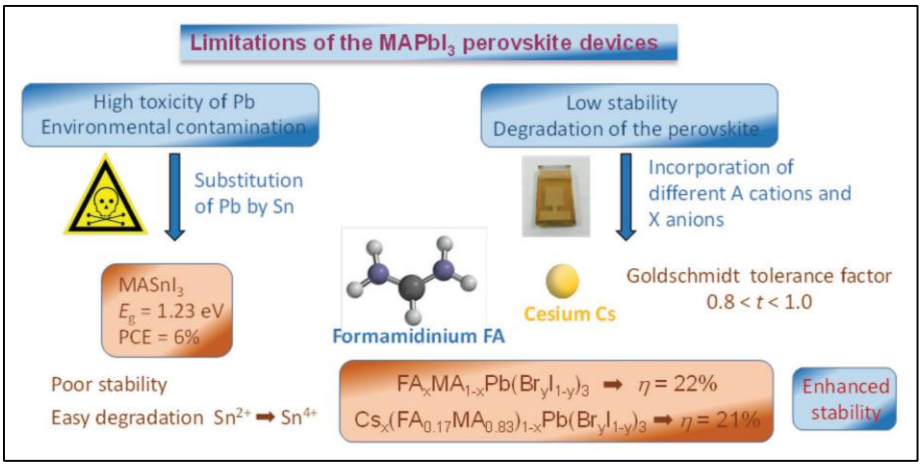

Figure 2. Main limitations of $MAPbI_3$ perovskite devices for industrial applications. Strategies to overcome these issues include lead-free perovskites and the incorporation of novel A cations, such as formamidinium $CH(NH_2)_2^+$ (FA) and cesium Cs^+.

In this contribution, recent approaches conducted to explore the implementation of innovative perovskite materials in solar devices are presented. A large variety of alternative perovskites have been reported that are expected to overcome the principal limitations of conventional perovskites, including the stability and toxicity. We classified the novel

materials according to their crystal structure, closely related to the stoichiometric formula. The particular arrangement of the inorganic octahedra BX_6 in perovskites defines the dimensionality of the material, covering 3D, 2D and 1D systems. Despite the atoms composing each perovskite being important for the nature of the material, the dimensionality of each perovskite imposes the main optoelectronic properties and dictates the further optimal implementation in photovoltaic devices.

2. 3D Perovskites with ABX_3 Formula

Preservation of the 3D network containing corner-sharing BX_6 octahedra in alternative perovskite materials is a critical factor to retain the excellent properties of $MAPbI_3$ perovskites in high-performance solar cells. Based on this assumption, the potential substitution of atoms in the archetypal $MAPbI_3$ structure includes three main options: 1) replacement of toxic Pb^{2+} with other divalent cations; 2) incorporation of other types of organic/inorganic cations into the structure, i.e., partial or complete substitution of MA; and 3) insertion of relatively small monovalent anions instead of halide atoms. The versatility of these three approaches is very limited due to the important restrictions imposed by charge neutrality, the stability of the AB_6 octahedra and the complementary ionic radii of the A, B, and X species through the Goldschmidt tolerance factor t.

2.1. Pb Substitution

The straightforward motivation to eliminate Pb from the $MAPbI_3$ structure corresponds to the high toxicity of this element, which certainly imposes certain limitations on the commercialization of these devices by demanding high cost encapsulation or due to the complete banning of these materials.
The equivalent substitution of Pb in a 3D perovskite requires the utilization of divalent cations, such as group-14 cations, alkaline-earth metals,

transition metals or lanthanides. A priori, a large variety of cations could be incorporated into the 3D network instead of Pb. However, multiple detrimental issues of potential lead-free 3D perovskites, including higher toxicity, poor chemical stability, or unsuitable band gaps, prevent the incorporation of all these materials into photovoltaic devices. Thus far, the only viable replacement of Pb^{2+} involves the utilization of germanium halide perovskites.

Germanium is a group-14 element that can be employed in the preparation of 3D perovskites, but thus far, little attention has been paid to this alternative metal replacement. The main advantage of Ge with respect to Pb is its low toxicity, which, together with its moderate earth-abundance, justify attempts to incorporate Ge instead of Pb in the archetypal $MAPbI_3$. Regarding its chemical properties, Ge is comparatively less electronegative than Pb, with a more covalent character and a reduced ionic radius (73 pm) compared to Pb (119 pm).[73] Importantly, the 2+ oxidation state is less stable in Ge than in Pb due to the less-intense inert pair effect of the ns^2 electrons within the group-14 atoms. The straightforward consequence is that Ge^{2+} can be more easily oxidized to Ge^{4+} compared to the oxidation of Pb^{2+} to Pb^{4+}, providing a detrimental effect on the perovskite stability.

To date, only one contribution has reported solar cells fabricated with Ge-based perovskites, which exhibited moderate efficiencies of 0.11% and 0.20% for $CsGeI_3$ and $MAGeI_3$, respectively.[74] While the photocurrent densities are promisingly high, i.e., ≈5.0 mA cm^{-2}, the open-circuit voltage and FF are extremely deficient (≈100 mV and 30%, respectively). The authors attributed the poor performance to a double effect: the low quality of the perovskite layer and the oxidation of Ge^{2+} to Ge^{4+} during the fabrication process (see Figure 3).[74] The solution employed in the spin-coating deposition is semi-transparent, also indicating the poor solubility of the precursors in the polar solvent, which accounts for the deficient morphology

of the synthesized perovskite films. The rapid oxidation of Ge^{2+} in ambient atmosphere further confirms that the stability issues are more significant in Ge-based perovskites than in Sn- or Pb-based perovskites. Additionally, a patent published in 2014 claimed efficiencies of 3.2% in a solar cell fabricated with $CsGeI_3$; however, few details of the device were reported.[75]

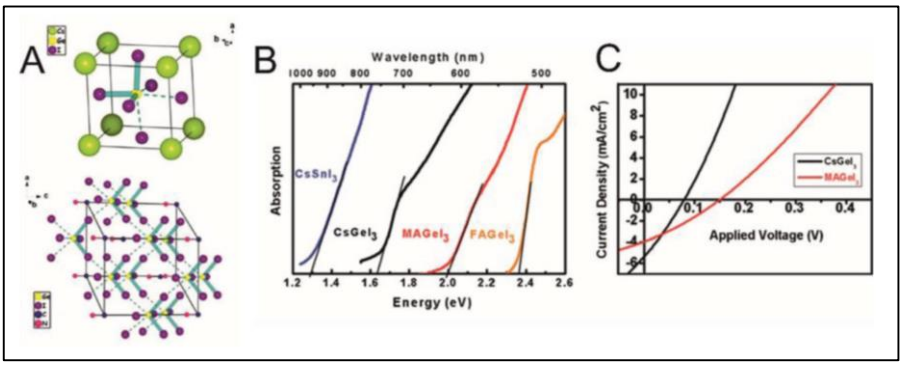

Figure 3. A) Unit cells of $CsGeI_3$ in rhombohedral symmetry (top) and $CH_3NH_3GeI_3$ in hexagonal symmetry (bottom). Reproduced with permission.[76] Copyright 2015, American Chemical Society. B) Optical absorption spectra of $CsGeI_3$ (black line), $CH_3NH_3GeI_3$ (red line), $CH(NH_2)_2GeI_3$ (orange line), and $CsSnI_3$ (blue line). Reproduced with permission.[74] Copyright 2015, Royal Society of Chemistry. C) J–V curves of solar cells fabricated with $CsGeI_3$ (black line) and $CH_3NH_3GeI_3$ (red line). Adapted with permission.[74] Copyright 2015, The Royal Society of Chemistry.

In addition to the $CsGeI_3$ and $MAGeI_3$ structures, other Gebased 3D halides perovskites ($AGeX_3$) have been synthesized or theoretically simulated that could be potentially suitable for photovoltaics (see Figure 3).[76–78] These novel perovskites have been basically obtained by exchanging the A cation with Cs, Rb, MA, or FA, by combining X halide atoms Cl, Br or I and utilizing possible combinations among these exchanges. Different X-ray diffraction (XRD) studies have confirmed that the Ge-based 3D perovskites crystallize within the trigonal crystal system with $[GeI_6]^{4-}$ corner-sharing octahedra possessing two types of nonequivalent bonds, in contrast to the equivalent Pb-I bond in tetragonal $MAPbI_3$. The theoretically calculated band structures

and density of states (DOS) indicate that $AGeX_3$ perovskites are direct band gap semiconductors with the valence band maximum (VBM) dominated by I 5p and Ge 4 s orbitals, whereas the conduction band minimum (CBM) is contributed by Ge 4p orbitals. $CsGeI_3$ and $MAGeI_3$ exhibit band gap values ideal for solar cells, i.e., 1.53–1.63 and 1.9–2.0 eV, respectively.[76] The effect of the type of X atom on the band gap is similar to that in the Pb counterparts, where larger band gap values are obtained when converting from I^- to Cl^-. The substitution of the previously reported A atoms in the $AGeX_3$ formula by larger organic cations, for example, guanidinium (Gua), has invariably led to low-dimensionality systems with modified properties, for example, indirect band gap semiconductors. Due to the limited number of articles reporting the fabrication of Ge-based perovskite solar cells, the extremely low efficiency values and poor stability of the devices cannot be deemed a definitive result for these devices but should rather be deemed a starting point for further improvements. The morphology optimization of perovskite films emerged as a key factor to enhance the V_{oc} and FF of the devices. Identifying specific precursor materials, solvents and deposition conditions that facilitate the formation of homogeneous crystalline films is necessary. Additionally, Ge^{2+} oxidation issues require careful control over the synthesis conditions under inert atmosphere. Regarding the long-term stability of Ge based solar devices, appropriate encapsulation is certainly a critical issue, but the current developments of new encapsulation strategies for Pb-based devices can alleviate this issue for Ge-based perovskites.

2.2. Other Organic/Inorganic A Cations

Among all the monovalent organic/inorganic cations, only MA, FA, and Cs possess Goldschmidt tolerance factors between 0.8 and 1.0 to ensure the formation of 3D “black” phases with optimal optoelectronic properties for photovoltaics. However, the partial incorporation of smaller and larger

monovalent cations together with MA, FA or Cs into the ABX_3 structure has emerged as an innovative strategy to optimize the performances of perovskite-based solar cells. In particular, the multication approach can lead to enhanced stabilities for the solar devices due to the decreased formation enthalpy in the perovskites upon the insertion of inorganic cations or the formation of additional hydrogen bonds. The small addition of alternative monovalent cations might have a beneficial impact on the optoelectronic properties through the optimization of the band gap energy and better perovskite processability.

2.2.1. Rubidium Mixed Perovskites

The first cation employed in the multication approach was rubidium Rb, with a Goldschmidt tolerance factor of 0.77, which is very close to the tolerance factor of 0.80 that limits the formation of the photoactive black phase.[79,80] $RbPbI_3$ crystallizes in a photoinactive yellow nonperovskite phase at ambient temperature without turning to the black phase upon heating.[79] The multication approach was applied to four combinations of cations and PbI_2, varying the Rb content for each case: RbFA, RbCsFA, RbMAFA, and RbCsMAFA (see Figure 4).[79]

The addition of Rb has resulted in several beneficial effects to perovskite materials: 1) stabilization of the black phase of the FA based perovskite; 2) excellent reproducibility of the RbCsMAFA based perovskites due to improved homogeneous crystallization conditions, 3) suppression of the yellow-phase of the MAFA-based perovskite and residual PbI_2 precursors; and 4) formation of large crystallite sizes in RbCsMAFA-based perovskite (see Figure 4).[79–81]

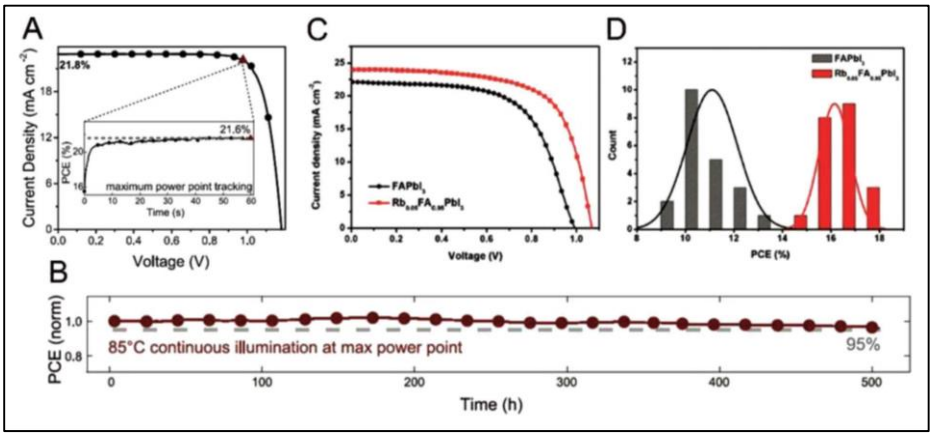

Figure 4. A) J–V curve taken at a scan rate of 10 mV s^{-1} of a solar cell containing the RbCsMAFA-based perovskite with a 21.8% efficiency (V_{oc} = 1180 mV, J_{sc} = 22.8 mA cm^{-1}, and FF = 0.81). The inset shows the scan-rate-independent maximum power point (MPP) tracking for 60 s, resulting in a stabilized efficiency of 21.6% at 977 mV and 22.1 mA cm^{-1} (displayed as triangles in the J–V and MPP scans). Reproduced with permission.[79] Copyright 2016, American Association for the Advance of Science. B) Thermal stability test of the RbCsMAFA-based perovskite. The device was aged for 500 h at 85 °C under continuous full illumination and MPP tracking in a nitrogen atmosphere (red curve, circles). Reproduced with permission.[79] Copyright 2016, American Association for the Advance of Science. C) J–V curves of $FAPbI_3$ and $Rb_{0.05}FA_{0.95}PbI_3$ based solar cells. Reproduced with permission.[81] Copyright 2017, Wiley-VCH. D) Histogram representing the distribution of PCEs for $FAPbI_3$- and $Rb_{0.05}FA_{0.95}PbI_3$-based solar cells. Adapted with permission.[81] Copyright 2017, Wiley-VCH.

Interestingly, the incorporation of Rb into the perovskite structure has not been fully demonstrated, and further studies are needed.[82] Solar cells incorporating these mixed A-cation perovskites were fabricated using mesoporous TiO_2 and spiro-OMeTAD layers as electron- and hole-transport materials and deposited by the spin-coating method.[79,80] The Rb content in each mixture was varied between 5% and 10% to obtain overall performance efficiencies of 14% (RbFA), 19.3% (RbCsFA), 19.2% (RbMAFA), and 21.6% (RbCsMAFA).[79] The device fabricated with RbCs-MAFA exhibited increases in the average V_{oc} (1158 vs 1120 mV) and FF (0.78 vs 0.75) with respect to the device fabricated with CsMAFA. Regarding the stability of the devices, 95% of the initial performance was maintained at 85 °C under nitrogen

atmosphere after 500 h, demonstrating the potential viability of these devices for industrial applications (see Figure 4). A gasquenching method was also employed to incorporate Rb in FAbased and MAFA-based perovskites to obtain overall solar device performances of 16.2% and 19.6%, respectively.[82]

The addition of small percentages of Rb to mixed-cation perovskites seems to improve the optoelectronic properties of these materials, resulting in enhanced stabilities and efficiencies in the solar devices. However, the mechanisms responsible for this optimization are not clear, and therefore, obtaining a deeper understanding of these processes is necessary to propose other potential cations.

2.2.2. Ethylammonium Mixed Perovskites

Ethylammonium $[(C_2H_5)NH_3]^+$ (EA) is another cation with a Goldschmidt tolerance factor (t = 1.03) slightly out of the 0.8-1.0 range for the formation of the photoactive black phase.[83] The proximity of the t value of EA to the established optimum range has stimulated researchers to employ EA in the multication approach together with MA ($MA_{(1-x)}EA_xPb(I_{(1-y)}Br_y)_3$).[83] The reflection peaks in XRD studies have shown a shift to lower diffraction angles upon increasing the quantity of EA; this induced unit cell expansion provided definitive proof for the replacement of MA by EA cations in the crystal lattice. EA cations can incorporate into the lattice up to ca. 30% EA. Increasing quantities of EA (above 30%) lead to a number of new reflections peaks corresponding to phase segregation (see Figure 5).[83]

The incorporation of large monovalent cations into the 3D perovskite structure is tolerated up to a certain percentage, as the crystal lattice can be potentially expanded. Thus, the potential of this approach to afford multimixed-cation 3D perovskites is impressive, promising novel materials with enhanced optoelectronic properties for photovoltaics applications.

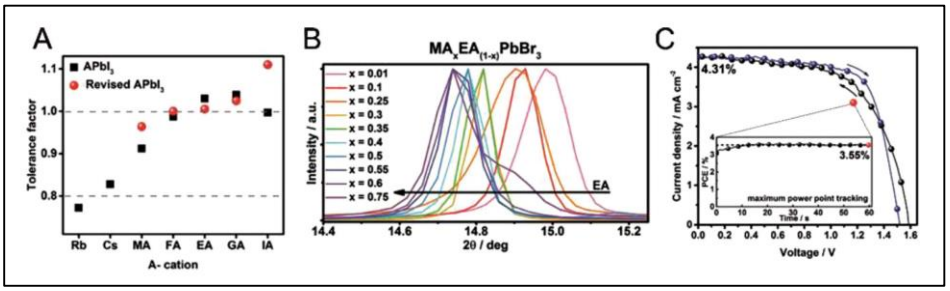

Figure 5. A) Tolerance factors of $APbI_3$ (squares) and revised tolerance factors for the same structures (circles). Reproduced with permission.[83] Copyright 2017, Wiley-VCH. B) The (001) XRD peak as a function of the EA content for $MA_{(1-x)}EA_xPbBr_3$. Reproduced with permission.[83] Copyright 2017, Wiley-VCH. C) J–V curve, taken at a scan rate of 10 mV s^{-1}, of the solar cell containing the $MA_{0.5}EA_{0.5}PbBr_3$ perovskite from forward bias to the short-circuit condition and the reverse scan. The inset shows the scan-rate-independent MPP tracking for 60 s, resulting in a stabilized efficiency of 3.55% at 1.17 V and 3.1 mA cm^{-1} (displayed as red circles in the J–V and MPP scans). Reproduced with permission.[83] Copyright 2017, Wiley-VCH.

2.2.3. Guanidinium Mixed Perovskites

The guanidinium cation (Gua) has a Goldschmidt tolerance factor of ≈1.04, and indeed, $GuaPbI_3$ is a 1D system with no suitable properties for photovoltaics.[84] However, the partial incorporation of Gua into $MAPbI_3$ has been demonstrated using XRD studies (see Figure 6).[85] The reflection peaks from XRD suffer a gradual shift to lower angles upon increasing the Gua percentage, indicating an expansion of the crystal lattice tolerated up to 25% Gua. After this percentage, phase segregation occurs between $MAPbI_3$ and $GuaPbI_3$. Importantly, theoretical calculations have demonstrated that the formation enthalpy (ΔH_f) is more negative for mixed Gua/MA perovskites, which is a promising result to achieve enhanced stability. The increased number of hydrogen bonds between Gua, compared to MA, with the iodine atoms is likely responsible for the more-negative formation enthalpy.

The optoelectronic properties of mixed $MA_{1-x}Gua_xPbI_3$ perovskite materials are only slightly affected due to the incorporation of Gua, compared to the

properties of $MAPbI_3$, demonstrating an increase in the band gap energy of 0.01–0.04 eV.

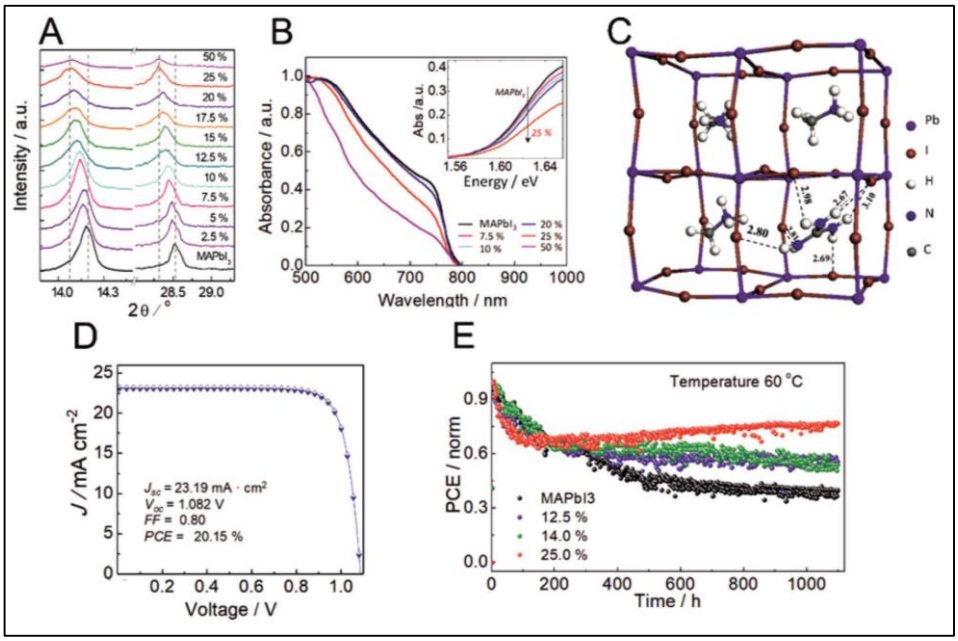

Figure 6. A) Magnification of the (220) (left) and (440) (right) XRD peaks upon variation of the Gua content (indicated in %). Reproduced with permission.[85] Copyright 2017, Macmillan Publishers Ltd: Nature. B) UV–vis–NIR absorption spectra of typical $MA_{1-x}Gua_xPbI_3$ films containing $x \leq 0.5$ and magnification of the band edges (inset) for mixed films containing $x \leq 0.25$ Gua. Reproduced with permission.[85] Copyright 2017, Macmillan Publishers Ltd: Nature. C) Optimized simulated structure of the unit cell of $Ma_{0.75}Gua_{0.25}PbI_3$, indicating the H-bonding distances with respect to the I atoms. Reproduced with permission.[85] Copyright 2017, Macmillan Publishers Ltd: Nature. D) J–V curve of the champion cell prepared with a mixed MA:Gua perovskite containing 14% Gua. Reproduced with permission.[85] Copyright 2017, Macmillan Publishers Ltd: Nature. E) Thermal stability tests of $MA_{1-x}GuaxPbI_3$ perovskite solar cells (x = 0, 0.125, 0.15, and 0.25) at 60 °C under continuous light illumination and MPP tracking in argon atmosphere. The initial PCEs for each cell were 18.77%, 18.97%, 18.11%, and 17.14%. Reproduced with permission.[85] Copyright 2017, Macmillan Publishers Ltd: Nature.

Photovoltaic devices fabricated with mixed $MA_{1-x}Gua_xPbI_3$ perovskites exhibited an impressive improvement in cell performance. A PCE of 20.1% was reached with perovskites containing 14% Gua ($MA_{0.86}Gua_{0.14}PbI_3$), whereas a PCE of 18.9% was obtained for the device exclusively employing

$MAPbI_3$. Moreover, the reproducibility of the PCE was largely improved due to the better crystallization of the mixed perovskites. However, a better result was the clear enhancement of the stability, retaining 75% of the initial PCE value after 1000 h at 60 °C under continuous light illumination and maximum power point (MPP) tracking under an argon atmosphere. This result was obtained for a mixed perovskite containing 25% Gua, but similar stability enhancements have been reported for other mixed perovskites.

The multication approach applied for Gua/MA mixtures resulted in a real improvement of the photovoltaic device properties. Moreover, the understanding of the improved stability due to the larger number of hydrogen bonds and the enhanced PCE resulting from the larger band gap energy is critical for the design of novel potential mixed-cation perovskites. In particular, the combination of Gua with FA and Cs is expected to deliver larger PCE values.

2.3. Nonhalide X Anions

The utilization of halide anions, in particular bromide (Br^-) and iodide (I^-), in ABX_3 systems is widespread in perovskite materials employed for solar devices with virtually no alternatives. The high electronegativities of halogen atoms impose a certain ionic character to the B–X bond that may be the origin of the low stability of these materials.[86] The motivation for the development of novel perovskites using nonhalide X anions is to achieve a B–X bond with more covalent character with the aim of enhancing the stability of these materials with a larger formation enthalpy. Not many monovalent anions exist with the appropriate size to fulfill the Goldschmidt tolerance factor. Only the thiocyanate anion (SCN) has been incorporated into a 2D layered perovskite ($A_2B(SCN)_2X_2$).[87]

More recently, divalent anions have emerged as alternatives to substitute X halide anions in ABX_3 structures. In particular, chalcogenide anions (Ch = S,

Se, and Te) have appeared as potential candidates to partially or fully replace halides, which requires the use of trivalent or tetravalent B cations to maintain charge neutrality in the $AB(Ch,X)_3$ or $ABCh_3$ structures, respectively. The mandatory substitution of Pb entails an additional beneficial impact: a decreased toxicity of the perovskite assuming the new B cation is less toxic than Pb.

2.3.1. Mixed Halide–Chalcogenide Perovskites

The partial substitution of halides with chalcogenides anions (Ch = S, Se, and Te) in the so-called split-anion approach was the first strategy to enhance the perovskite stability under ambient atmosphere (see Figure 7).[88] The substitution of one or two halides with a chalcogenide anion (and Pb^{2+} by B^{3+} or B^{4+} cations) in $MAPbI_3$ is expected to not significantly alter the optoelectronic properties of these materials.

To date, the only attempt to synthesize mixed halide–chalcogenide perovskites using solid-state reactions has been unsuccessful, leading to separate binary and ternary compounds.[89] Although theoretical density functional theory (DFT) calculations have estimated negative values for the formation enthalpy, the decomposition energies to form other secondary phases for $CsSbSX_2$, $CsSbS_2X$, $CsBiSX_2$, and $CsBiS_2X$ are all negative. These results point to the difficulty to synthesize these compounds under thermal equilibrium conditions.

Despite such synthetic failures, DFT calculations have shown certain intriguing optoelectronic properties of mixed halide–chalcogenide perovskites in photovoltaics. In particular, two of the evaluated compounds, $CH_3NH_3BiSeI_2$ and $CH_3NH_3BiSI_2$, exhibited optimum band gaps (1.3–1.4 eV) for single junction solar cells, with effective very low masses of electrons and holes (0.32 and 0.40m0, respectively).[88] Both compounds exhibited direct

electron transitions resulting in strong optical absorbers with similar distributions of orbitals in the band structures, similar to $CH_3NH_3PbI_3$.

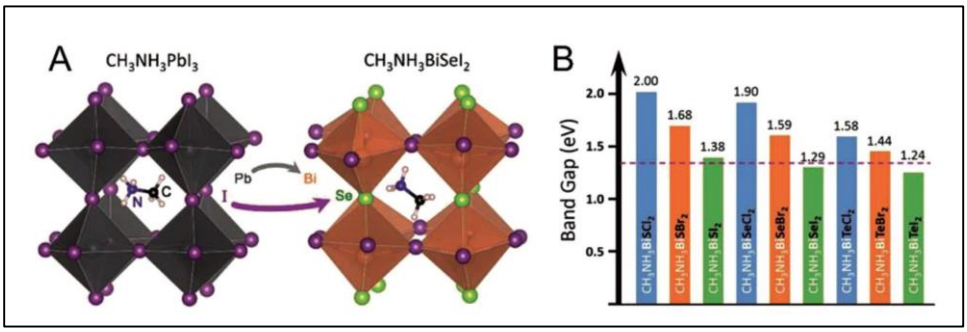

Figure 7. A) Atomic structures of $CH_3NH_3PbI_3$ and $CH_3NH_3BiSeI_2$ and a schematic illustrating the split-anion approach to replace Pb in $CH_3NH_3PbI_3$. Reproduced with permission.[88] Copyright 2016, The Royal Society of Chemistry. B) Calculated band gaps of $CH_3NH_3BiXY_2$ compounds (with X = S, Se, or Te and Y = Cl, Br, or I) using the HSE functional with spin–orbit coupling. The dashed line marks the optimal band gap for a single-junction solar cell according to the Shockley–Queisser theory. Reproduced with permission.[88] Copyright 2016, The Royal Society of Chemistry.

Finally, theoretical studies of dichalcogenide perovskites using Sn^{4+} as the B cation were also performed, obtaining a direct band gap of 1.1 eV for $CsSnS_2Cl$ (see Figure 7).[88] The critical point of this approach is the need to develop alternative synthetic methods that can stabilize the desired compounds by kinetic factors, as all expectations are based on theoretical calculations. Another approach might be a slight structural modification by including a low percentage of other atoms to thermodynamically stabilize the mixed halide–chalcogenide perovskites.

2.3.2. Chalcogenide Perovskites

In an attempt to overcome the stability issues of mixed halide– chalcogenide perovskites, the total substitution of halides with chalcogenide anions is an alternative strategy, returning to the topic of metal chalcogenide perovskite

($ABCh_3$) semiconductors previously synthesized in the 1950s as potential solar absorber for photovoltaics.[90] In the $ABCh_3$ formula, A and B species correspond to di- and tetravalent cations due to the required charge neutrality, with transition metals Ti, Zr or Hf or group 14 elements Sn or Ge as the B-site species and group 2 elements as the A-site species.[91] Here, the Goldschmidt's tolerance factor (t) is also a very reliable tool to predict the structures of the different metal chalcogenide perovskites. For Sn-based materials, t varies between 0.75 and 0.90, corresponding to a distorted perovskite structure. In Ge-based materials, t is slightly higher (0.85–1.0), consistent with a perfect cubic perovskite structure.[92]

Metal chalcogenide perovskites including transition metals exhibit a larger variability in the tolerance factor with t <0.71 or t >1, which represents a corner-sharing octahedra network structure, also known as the needle-like phase (see Figure 8).[90]

To date, the only synthesized metal chalcogenide perovskites with potential applications in photovoltaics are $BaZrS_3$, $CaZrS_3$, $SrTiS_3$ as well as the distorted (β-SZS) and needle-like (α-SZS) phases of $SrZrS_3$.[91,93,94] The d-orbital character of the conduction band increases this band energy in these chalcogenide- based perovskites with respect to ABX_3. Nevertheless, the insertion of chalcogenides cations also shifts the valence band to higher energy, maintaining the band gap in the visible–IR region.

$BaZrS_3$ is the most studied metal chalcogenide perovskite and crystallizes in a distorted $GdFeO_3$-type phase with an orthorhombic structure (space group Pnma).[93] The employed synthetic methods involve conventional solid-state reactions at high temperatures (>600 °C): the sulfurization of $BaZrO_3$ with CS2 via multiple heating and purification steps,[91] the reaction of BaS and ZrS_2 with repeated annealing steps[93] and reacting BaS with Zr and S elements using iodine as a catalyst.[94] The optical band gap energy (E_g) was estimated to be in the range of 1.73–1.85 eV with an absorption

coefficient of 105 cm^{-1} at 2.0 eV. (see Figure 8).[91,93,94] E_g is in excellent agreement with that theoretically calculated with DFT (1.70–1.82 eV), slightly larger than the optimum value for single-junction solar cells.[91,93]

Theoretical calculations showed the direct character of the band gap with the VBM mainly formed by S 3p and Zr 4d states and the CBM derived from Zr 4d and S 3p antibonding coupling.[93] Both bands are very dispersive, indicating small carrier effective masses. $BaZrS_3$ metal chalcogenide perovskites seem to be highly stable against degradation, as a sample stored in air for seven months did not exhibit any changes in the XRD pattern or UV–vis absorption spectrum even after washing with deionized water.[91]

$CaZrS_3$ and $SrTiS_3$ metal chalcogenide perovskites were also synthesized by sulfurization of $CaZrO_3$ and $SrTiO_3$ with CS_2 via multiple heating steps at 800–1000 °C.[91] The crystal structure of $CaZrS_3$ is a distorted perovskite with a band gap of 1.90 eV, while SrTiS3 crystallizes in the needle-like phase. The distorted (β-SZS) and needle-like (α-SZS) phases of $SrZrS_3$ were synthesized via solid-state reactions of SrS with elemental Zr and S using iodine as a catalyst and heating for 60 h at 850 °C (α-SZS phase) and 1100 °C (β-SZS phase) (see Figure 8).[94] The optical band gaps from diffuse-reflectance measurements were estimated to be 1.52 and 2.05 eV for the α-SZS and β-SZS phases, respectively. Theoretical calculations indicate a direct band gap character; however, the absorption coefficient is much larger for the distorted structure.[94]

In an attempt to reduce the band gap energy of $BaZrS_3$ to a value closer to that of $MAPbI_3$, Ti doping was theoretically estimated to linearly decrease the band gap energy to 1.47 eV with 10% Zr substitution.[93] However, the synthetic reactions to obtain $BaZr_{1-x}TixS_3$ chalcogenide perovskites were all unsuccessful, producing mixtures of $BaZrS_3$ and $BaTiS_3$ compounds.[93]

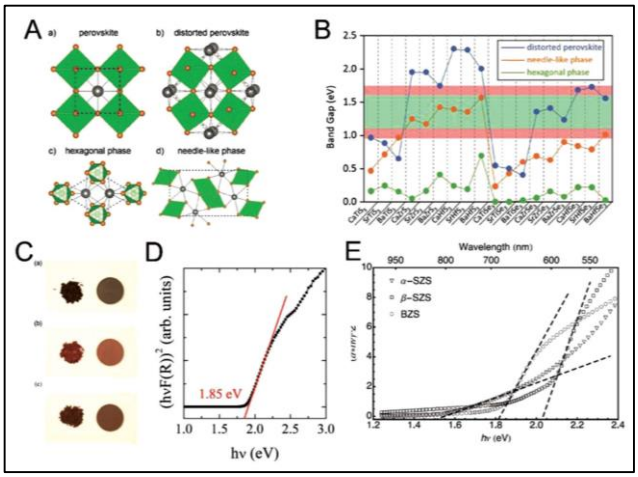

Figure 8. A) Different phases of $ABCh_3$ compounds: (a) ideal perovskite phase without distortion, (b) distorted perovskite phase with the Pnma space group, (c) hexagonal phase with the P63/mmc space group, and (d) needle-like phase also with the Pnma space group. Gray and brown spheres represent the A cations and Ch anions, respectively. The B cations are located at the centers of the green-colored octahedrons. Reproduced with permission.[90] Copyright 2014, American Chemical Society. B) Band gaps of 18 $ABCh_3$ compounds in the distorted perovskite, needle-like and hexagonal phases calculated with the HSE06 functional. The optimal band gap region for solar cell materials is highlighted in light green. An extended region with theoretical efficiency above 28% is highlighted in light red. Reproduced with permission.[90] Copyright 2014, American Chemical Society. C) Optical images of synthesized powders and pelletized samples for (a) α-$SrZrS_3$, (b) β-$SrZrS_3$, and (c) $BaZrS_3$. Reproduced with permission.[94] Copyright 2016, Wiley-VCH. D) Diffuse-reflectance data of dark-brown $BaZrS_3$ displaying a band gap of 1.85 eV. Reproduced with permission.[93] Copyright 2016, American Chemical Society. E) Band gap determinations with the absorbance values obtained from the diffuse-reflectance and transmittance measurements on translucent powder layers using the Kubelka–Munk theory. The deduced band gap values are 1.52 eV for α-$SrZrS_3$ (triangles), 2.05 eV for β-$SrZrS_3$ (squares), and 1.83 eV for $BaZrS_3$ (circles). Reproduced with permission.[94] Copyright 2016, Wiley-VCH.

First principles calculations also demonstrated the potential of Sn and Ge as B cations in metal chalcogenide perovskites for solar absorbing materials.[92] In particular, $SrSnSe_3$ and $SrSnS_3$ were predicted to fulfill most photovoltaic requirements due to the direct characters of their electronic transitions, optimum band gap energies (1.56 eV for $SrSnS_3$ and 1.00 for $SrSnSe_3$), high absorption coefficients (105 cm^{-1} at 2 eV for $SrSnSe_3$) and good carrier mobilities due to their low effective masses ($m_e = 0.20m_0$ and $m_h \approx 0.21m_0$ in

the distorted structure of the $SrSnSe_3$ material).[92] The computed band structure and DOS show that the VBM is derived from Se 4p orbitals in $SrSnSe_3$, while the CBM is composed of Se 4p orbitals and Sn 5s orbitals.

Metal chalcogenide perovskites possess optimum optoelectronic properties and good stability under ambient atmosphere. However, the need to employ very high temperatures in the synthesis process might prevent their widespread utilization as solar absorbing materials due to the high cost of this processing step. Thus far, no solution-processable methods have been reported to yield homogeneous thin films of these materials, hindering their incorporation in the layered structure of solar cells. The utilization of thermal evaporation in vacuum conditions to fabricate thin films of these materials might be an alternative strategy to overcome the aforementioned synthetic issues.

3. 3D Perovskites with $A_2BB'X_6$ Formula

The halide double perovskites or elpasolites are a group of compounds that have recently attracted increasing interest in the photovoltaic community despite being known for the last century.[95] The double perovskite structure is composed of corner-sharing BX_6 and $B'X_6^-$ alternating octahedra with two different cations (B and B′) forming a 3D superstructure typically denoted as rock-salt ordering.[96] The neutrality criterion requires that the total charge of the two B and B′ cations is +4, opening the door to combinations of 1+/3+ cations.

The two fundamental motivations for research on $A_2BB'X_6$ perovskites for photovoltaics relate to a preservation of the advantageous 3D network of inorganic corner-sharing octahedra and the possibility to substitute Pb with other less toxic species. This approach intends to retain the properties of 3D $APbX_3$ materials, such as the low band gap (≈1.6 eV), strong light absorption, long-lived photogenerated electron and holes and balanced carrier effective

masses, which can be added to the capacity of double perovskites to expand the type of atoms that can be incorporated into the B sites.

Thus far, only one article has reported the fabrication of solar cell device based on halide double perovskites, but the promising optoelectronic properties of these materials enables the prediction of their further implementation in photovoltaics.[97,98] Thus, the reports disclosing optoelectronic properties of halide double perovskites $A_2BB'X_6$ demonstrate the excellent features of these materials, similar to those of their 3D $APbX_3$ counterparts. However, their characterization always has been performed on relatively large crystals synthesized by solid-state chemistries, hydrothermal synthesis or solvent evaporation from supersaturated solutions containing the appropriate precursors.[99] Clearly, the limiting factor for the fabrication of solar cell devices based on these materials is the preparation of high-quality films due to the insolubility of some of the necessary precursors or the inability to prepare pure phases (mixtures with other lower dimensional phases that are more thermodynamically stable).

The most employed trivalent cation in double perovskites is Bi^{3+} due to its isoelectronic configuration with Pb^{2+} ($6s^26p^0$) and remarkably reduced toxicity. Regarding the B site, Ag^+, K^+ or Tl^+ are the only monovalent cations that have been utilized thus far, owing to their appropriate sizes to allow octahedral coordination.

The first halide double perovskite with potential applications in photovoltaics, i.e., $Cs_2AgBiBr_6$, was simultaneously synthesized by two different groups in 2016, crystallizing with Fm3m cubic space group symmetry.[100,101] This material possesses an E_g of 1.95/2.19 eV (semitransparent red solid), which is much reduced compared to that of the corresponding Pb-based counterpart, $CsPbBr_3$ (Eg = 2.25 eV).[100,101] The emission lifetime measured for $Cs_2AgBiBr_6$ is remarkably high (≈660 ns), with a similar value for single crystals or powdered samples, which suggests that the formation of defects

or surface sites in the less-crystalline phases is not expected to influence carrier transport in the devices (see Figure 9).[100]

Two synthetic methods have been conducted to prepare the $Cs_2AgBiBr_6$ material: 1) a solution process by mixing the corresponding bromide precursors with HBr and 2) a solid-state reaction with stoichiometric amounts of the precursors with grinding and heating to 210 °C. Light and moisture stability tests have demonstrated that $Cs_2AgBiBr_6$ shows superior stability compared to $APbX_3$ perovskites, which is an extra stimulus for solar cell applications.[100]

Theoretical DFT calculations of the $Cs_2AgBiBr_6$ band structure noted that the VBM shifts from the (111) Brillouin zone boundary (L point in a face centered cubic cell) in the ABX_3 materials (e.g., $CsPbBr_3$ or $MAPbI_3$) to the X point in the halide double perovskite $Cs_2AgBiBr_6$ and that the CBM remains at the L point of the Brillouin zone.[101,102] The participation of the Ag 4d states in the valence band is deemed to play a key role in such a VBM shift.[101,102] As a result, $Cs_2AgBiBr_6$ present an indirect band gap unlike the direct transition of its Pb-based counterparts.

$Cs_2AgBiBr_6$ is the only halide double perovskite that has been successfully incorporated into a solar cell device, providing a PCE of nearly 2.5% with J_{sc} = 3.93 mA cm^{-2}, V_{oc} = 0.98 V, and FF = 0.63.[97] High annealing temperatures of 250 °C were required to obtain a quantitative conversion of the precursors into the $Cs_2AgBiBr_6$ double perovskite. Interestingly, an initial test demonstrated enhanced stability against degradation under constant illumination under ambient conditions compared to $MAPbI_3$, with almost no degradation after 25 days (see Figure 9).[97]

In a recent work, Tl was incorporated into $Cs_2AgBiBr_6$ as a dilute impurity, resulting in the formation of opaque black crystals corresponding to the $Cs_2(Ag_{1-a}Bi_{1-b})Tl_xBr_6$ structure.[103] The Tl content was varied between 0.03% and 0.75%, and theoretical and experimental studies demonstrated that

these Tl contents could substitute both the Ag^+ (Tl^+) and Bi^{3+} (Tl^{3+}) sites, where substitution of Bi^{3+} was preferred at low doping levels, and substitution of Ag^+ was preferred at higher concentrations. Reflectance measurements clearly displayed a reduction in the experimental band gaps upon increasing the Tl content, with a minimum value of 1.57 eV at x = 0.075. DFT calculations revealed that replacing Bi^{3+} with Tl^{3+} reduces the band gap energy due to the formation of a new lower-energy conduction band with Tl 6s and Ag 4d character, which evolves into an indirect transition. For the replacement of Ag^+ with Tl^+, Tl 6p states together with Br 4p and Bi 6p states form a new conduction band with lower energy that generates a direct transition (see Figure 9).[103]

Hybrid inorganic–organic double perovskites have also been synthesized using $CH_3NH_3^+$ (MA) as the organic cation.[104] The first hybrid double perovskite material was prepared using K^+ and Bi^{3+} for the B^- and B′-site species, obtaining $(MA)_2KBiCl_6$ that crystallizes in rhombohedral R3m symmetry containing alternating KCl_6 and $BiCl_6$ octahedra.[104] $(MA)_2KBiCl_6$ crystals were synthesized using the hydrothermal, solvent evaporation or solution cooling methods; however, no thin films of this novel material have been prepared to date.[104] The experimentally calculated band gaps from reflectance measurements are 3.04 and 3.37 eV, associated with indirect and direct transitions, respectively.

The large E_g for $(MA)_2KBiCl_6$ precludes its utilization in photovoltaics but certainly serves as a proof of concept for the preparation of hybrid double perovskites. Interestingly, the energy states of K do not contribute to the valence band in these materials, as opposed to $Cs_2AgBiBr_6$, in which the Ag 4d orbitals contribute to the valence band.[104] The straightforward consequence is that the $(MA)_2KBiCl_6$ double perovskite preserves the direct character of the electronic transitions as in $APbX_3$ materials.

Two more hybrid double perovskites have been recently synthesized, $(MA)_2TlBiBr_6$ and $(MA)_2AgBiBr_6$, indicating the large possibilities for this family of materials.[105,106] Both hybrid perovskites were prepared using a hydrothermal method, crystallizing in the same cubic space group Fm3m. The experimental band gap of $(MA)_2TlBiBr_6$ was 2.16 eV, corresponding to a direct transition according to DFT calculations.[105] Similarly to the K atom in $(MA)_2KBiCl_6$, Tl does not alter the crystal momentum of the valence and conduction bands, preserving the strong absorption ability of $APbX_3$ materials.[105] However, $(MA)_2TlBiBr_6$ contains Tl, a seriously toxic element that may restrict the utilization of this material as an alternative in photovoltaics. For $(MA)_2AgBiBr_6$, the optical band gap is 2.02 eV, but theoretical calculations indicated an indirect character of the transition, similar to $Cs_2AgBiBr_6$.[106]

All previously described double perovskites have been based on the utilization of Bi^{3+} as the trivalent species, but lately, two novel compounds have been prepared employing alternative cations (see Figure 9).[107,108] The substitution of Bi^{3+} with In^{3+} rendered a new chloride double perovskite, $Cs_2AgInCl_6$.[107]

DFT calculations reflected the direct character of the band gap, as In s orbitals do not participate in the valence band, which could hypothetically interact with Ag 4d orbitals to push the VBM to the X point, as in $Cs_2AgBiCl_6$. This compound was synthesized by precipitation from an acidic solution containing all the chloride precursors and crystallized in the cubic space group Fm3m. The band gap obtained from diffuse-reflectance measurements was 3.3 eV, in agreement with those obtained for other chloride double perovskites.[107] A later report introduced Sb^{3+} as a trivalent cation to generate $Cs_2AgSbCl_6$.[108] This compound exhibited an indirect band gap of 2.54 eV due to mismatch in the crystal momentum between the valence and the conduction bands.[108]

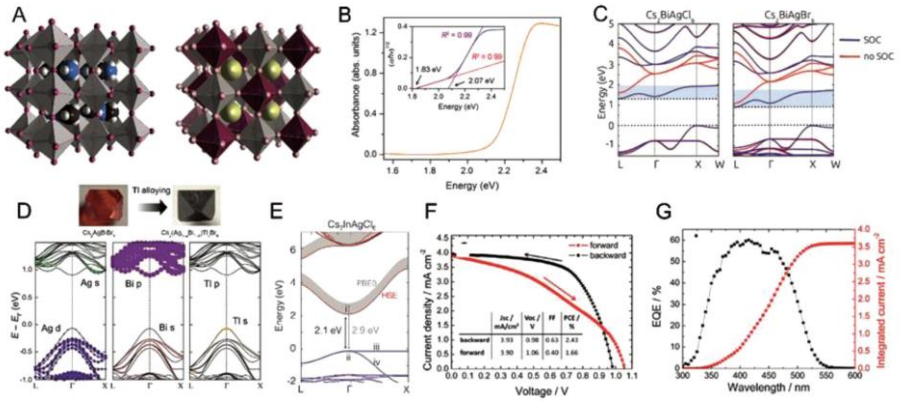

Figure 9. A) Atomic structures of $MAPbI_3$ (left) and $Cs_2BiAgBr_6$ (right) displayed with polyhedral models in the low-temperature orthorhombic and cubic phases, respectively. PbI_6 octahedra are shown in gray; the I anions are shown in brown; the large spheres in the cavities represent the $CH_3NH_3^+$ cations (N is blue, C is black); Cs is shown in yellow, Br is shown in pink; and the $BiBr_6$ and $AgBr_6$ octahedra are in shown in dark red and gray, respectively. Reproduced with permission.[65] Copyright 2016, American Chemical Society. B) Absorption spectrum of $Cs_2BiAgBr_6$ powder obtained from diffuse- reflectance measurements. Inset: Tauc plot showing the characteristics of an indirect band gap. Reproduced with permission.[100] Copyright 2016, American Chemical Society. C) DFT-LDA band structures of $Cs_2BiAgCl_6$ (left) and $Cs_2BiAgBr_6$ (right). The calculations were performed with (blue lines) and without (red lines) spin–orbit coupling. The light blue shading highlights the width of the lowest conduction band, as calculated from DFT+SOC: 0.6 eV for $Cs_2BiAgCl_6$ and 0.9 eV for $Cs_2BiAgBr_6$. Reproduced with permission.[102] Copyright 2016, American Chemical Society. D) Photographs of $Cs_2AgBiBr_6$ and $Cs_2(Ag_{1-a}Bi_{1-b})Tl_xBr_6$ (x = a + b = 0.075) single crystals and the band structures of $Cs_2(Ag_{1-a}Bi_{1-b})Tl_xBr_6$ (x = 0.06) for substitution of Tl^+ for Ag^+. Metal orbital characters of the bands are shown in color. Reproduced with permission.[103] Copyright 2017, American Chemical Society. E) Band structures and band gaps of $Cs_2InAgCl_6$, as calculated using the HSE hybrid functional (blue and red lines) or the PBE0 functional (shaded area). The zero of the energy scale is set to the VBM. Reproduced with permission.[107] Copyright 2017, American Chemical Society. F) J–V curve of the best-performing solar device assembled with $Cs_2AgBiBr_6$ films preheated at 75 °C. Reproduced with permission.[97] Copyright 2017, Royal Society of Chemisttry. G) EQE spectrum (black) and integrated predicted current (red) of a solar device assembled with $Cs_2AgBiBr_6$ films, demonstrating a Jsc of 3.7 mA cm^{-2}. Reproduced with permission.[97] Copyright 2017, Royal Society of Chemisttry.

Additionally, the ability to substitute trivalent metals, such as In^{3+} or Sb^{3+}, into $Cs_2AgBiBr_6$ has demonstrated band gap engineering to obtain a smallest value of 1.86 eV for $Cs_2Ag(Bi_{0.625}Sb_{0.375})Br_6$.[109]

The progress in the field of double perovskites has been remarkable in the past two years, with the synthesis of several new compounds together with the description of their optoelectronic properties. The complete characterization of each double perovskite has raised some significant restrictions for the implementation of these materials in stable and high-efficient solar cells.

The first important limitation relates to their large band gap energy (2.0–3.0 eV) compared to $MAPbI_3$. Theoretical calculations predicted lower band gaps for the iodide counterparts, similar to the ABX_3 systems, but efforts to synthesize iodide double perovskites have been unsuccessful to date.[109,110] The decomposition enthalpies (ΔH_d) for the hypothetical Cs_2AgBiI_6 and $(MA)_2AgBiI_6$ materials to generate the corresponding Cs_3Bi2I_9 and $(MA)_3Bi_2I_9$ bilayer perovskites have been estimated to be negative, indicating the possible instability of iodide double perovskites.[111]

The second important drawback of the studied double perovskites is the low absorption coefficient resulting from the indirect character of the electronic transitions. The interplay of the orbital states of monovalent B and trivalent B′ species at the band edges generally involves a shift of the CBM and VBM, leading to an indirect gap. Band gap engineering is a definitive tool to manipulate the character of the valence and conduction bands, turning indirect semiconductors into direct semiconductors via chemical adjustment of the relative proportions of the two types of trivalent B′ cations.[108]

The reduced electronic dimensionality of these materials, that is, the lack of connectivity of the atomic orbitals that comprises the lower conduction band (LCB) and the upper valence band (UVB), can be considered as an additional disadvantage of double perovskites with respect to 3D ABX_3 materials.[112] Two B and B′ cations must contribute to the LCB and UVB to allow 3D connectivity of the atomic orbitals, ensuring low effective masses in all three directions.[112]

In addition to the synthesized double perovskites, other monovalent and trivalent cations have been proposed as B- and B′-site species to create stable and nontoxic perovskites with improved optoelectronic properties. Suggested monovalent cations include Na^+, Rb^+, Cu^+, Au^+, In^+, and NH_4^+ as well as trivalent Tl^{3+}, Ga^{3+}, and Al^{3+} and most first-row transition metals and lanthanides.[65,113,114] The extensive combination of all these potential cations, including those previously described (K^+, Ag^+, Tl^+, Bi^{3+}, Sb^{3+}, and In^{3+}), may pave way for further developments of a future series of promising double perovskites. Among all potential estimates, theoretical simulations have indicated that most suitable combinations fulfilling the requirements for photovoltaics are those incorporating monovalent cations Cu^+, Ag^+, and Au^+ in conjunction with trivalent cations Bi^{3+}, Sb^{3+} or In^{3+}.[113,114] Another reported combination of B and B′ cations employs In+ and Bi^{3+} or Sb^{3+}, with the unstable In+ cation being stabilized through the utilization of organic A cations MA and FA.[115] However, the attempts to synthesize these materials through solid-state reactions via hydrothermal methods have been unsuccessful.

The rapid advancements in the synthesis of novel double perovskites with improved properties related to photovoltaic performance have not been accompanied with their subsequent implementation in solar devices, with the exception of $Cs_2AgBiBr_6$ as a proof-of-concept for these materials.[97] Thus, the major weakness of this approach seems to be related to the difficulty of fabricating crystalline thin films using solution processing methods. The poor solubility of the precursors has emerged as a critical factor to achieve suitable films, and more comprehensive studies reporting details of the deposition are required. An alternative strategy to deposit double perovskite thin films might be thermal evaporation under vacuum conditions using powders or single crystals of the corresponding compound as a starting material.

4. 0D Perovskites with A2BX6 Formula

Based on the rock-salt ordering of $A_2BB'X_6$ double perovskites, the substitution of one B-site cation for a vacancy yields $A_2\square BX_6$ perovskites (A_2BX_6), known as vacancy-ordered double perovskites, where □ is a vacancy.[116] To maintain the charge neutrality of the structure, B must accommodate a tetravalent cation, which extends the type of cations for employment. This material adopts an antifluorite structure as in K_2PtCl_6, where isolated BX_6^{2-} octahedra are bridged by A^+ cations.[116] Since the BX_6^{2-} octahedra are not connected to each other, the vacancy-ordered double perovskite can be referred as a 0D material.[113] A priori, the absence of connectivity between the inorganic octahedra might correlate to opposite optoelectronic properties in 0D A_2BX_6 materials with respect to 3D $APbX_3$ perovskites, preventing their potential application in photovoltaics. However, some interesting similarities are apparent that may potentially open a pathway to implement these materials in solar cells.

First, the isolated BX_6^{2-} octahedra lie in very close proximity to each other, resulting in a compact anionic lattice, comparable to that existing in $APbX_3$ perovskites. Second, the vacancy-ordered double perovskites experience the same loss of symmetry in phase transitions upon cooling as that occurring in ABX_3. This behavior is associated with a cooperative octahedral tilting and rotation directed by the mismatch in the ionic radii of the constituent atoms.[117] Unpredicted similarities with ABX_3 perovskites, together with a low structural dimensionality linked to a higher stability as well as the incorporation of nontoxic cations replacing Pb, can stimulate the future utilization of these materials in solar cells.

A_2BX_6 materials have been scarcely reported in the literature, and only the Cs_2SnI_6 vacancy-ordered double perovskite has been implemented in solar devices.[118] The devices were prepared in an n–i–p configuration using compact TiO_2 and poly-3-hexyl-thiophene (P3HT) as the ETL and HTL,

respectively. ACs_2SnI_6 light absorbing layer was deposited through a two-step sequential deposition method from CsI and SnI_2 precursors by thermal evaporation.[119] Initially, $CsSnI_3$ was synthesized under an inert atmosphere, but a phase change in air promotes the oxidation of Sn^{2+} to Sn^{4+} resulting in Cs_2SnI_6.

The PCEs of Cs_2SnI_6-based devices have barely reached 1% with Jsc = 5.41 mA cm^{-2}, V_{oc} = 0.51 V, and FF = 0.35 (see Figure 10).[118] Ultraviolet photoelectron spectroscopy (UPS) measurements of the valence band energy of this material have reported numbers varying from −5.40 to −6.10 eV, relatively more negative than that of the archetypal $MAPbI_3$ perovskite.[116,120,121] Indeed, the mismatch between the energy levels in Cs_2SnI_6 and the employed ETL and HTL can partially account for the observed low efficiency. Specific types of ETL and HTL therefore must be selected to optimize the PCE. The stability tests of Cs_2SnI_6-based devices demonstrated a decrease in efficiency after several hours that might originate from Cs_2SnI_6 degradation due to the interplay of the materials at the interfaces.[118]

The optoelectronic properties of Cs_2SnI_6 have been extensively studied in recent years to shed light onto such a low reported efficiency.[116,120–122] Cs_2SnI_6 crystallizes in a cubic structure (Fm3m space group) with SnI_6^{2-} octahedra presenting certain rotational disorder (see Figure 10). The tetravalent character of the Sn^{4+} cation implies a higher stability against oxidation in air with respect to its $CsSnI_3$ counterpart. In particular, thin films of this material exhibited enhanced stability in moist air compared to $MAPbI_3$ films. The optical band gap measured from diffuse-reflectance measurements for a solid sample was reported to be 1.25–1.30 eV, while a value of 1.60 eV was found for thin films of this material. DFT calculations demonstrated the direct character of the transition (Γ point), but the reported

band gap energy significantly differs (0.97 or 1.3 eV) probably due to the use of different exchange potentials.

The VBM is comprised of I 5p orbitals, while the CBM encompasses empty hybrid I 6p/Sn 5s orbitals. Although some controversy exists on this topic in the literature, the conduction band is apparently more dispersive than the valence band, leading to low electron effective masses (m_e^* = 0.5–1.0 eV) and relatively high hole effective masses (1.0–3.0 eV), indicating the n-type character of this semiconductor, in contrast to the balanced charge-transport properties in $MAPbI_3$ and $MASnI_3$ materials. In addition, the good electron conductivity of Cs_2SnI_6 also accounts for the high tolerance of this material to iodine vacancy defects that act as shallow electron donors.

Recently, the synthesis of a mixed Sn/Te vacancy-ordered double perovskite, $Cs_2Sn_{1-x}TexI_6$, was achieved from a solution-phase process using an appropriate ratio of SnI_4/TeI_4 precursors.[116] The incorporation of increasing amounts of Te into the Cs_2SnI_6 structure did not affect the crystal symmetry, retaining the cubic arrangement, but increases the unit cell parameters that is not sufficient to account for the disparity in the ionic radii (rSn = 0.69 to rTe = 0.97). Te^{4+} is incorporated into the Cs_2SnI_6 structure, expanding the BI_6^{2-} octahedra at the expense of reducing the separation between neighboring BI_6^{2-} octahedra. From this close-packed configuration, a higher carrier mobility is expected due to better overlap of the I orbitals. However, the electrical resistivity of the $Cs_2Sn_{1-x}Te_xI_6$ materials increases at higher Te^{4+} concentrations. DFT calculations of $Cs_2Sn_{1-x}Te_xI_6$ showed highly dispersive conduction band states with electron and hole effective masses comparable to those in Cs_2SnI_6.[116] The insulating behavior of $Cs_2Sn_{1-x}Te_xI_6$ was eventually explained from the larger formation energy of the iodine vacancies with respect to Cs_2SnI_6, which reduces the defect concentration. In addition to this significant limitation of $Cs_2Sn_{1-x}Te_xI_6$ for photovoltaics, the measured optical band gap was ≈1.59 eV, much larger than that measured

for Cs_2SnI_6. Finally, band structure calculations demonstrated the indirect character of the transition, which reduces the absorption coefficient. In conclusion, $Cs_2Sn_{1-x}Te_xI_6$ materials are not suitable for photovoltaics due the combination of several detrimental properties.

The last reported vacancy-ordered double perovskite is Cs_2PdBr_6, which exhibits optimum optoelectronic properties for photovoltaics (see Figure 10).[123] Cs_2PdBr_6 single crystals were synthesized from a solution process, crystallizing in the space group Fm3m. In the synthetic process, Pd was introduced in its 2+ oxidation state (using $PdBr_2$ as a precursor material) even though Pd is in its 4+ oxidation state in Cs_2PdBr_6. The in situ formation of the oxidizing agent, HBr:dimethyl sulfoxide (DMSO), was proposed to account for the Pd oxidation.[123] The optical band gap for the Cs_2PdBr_6 single crystals calculated from absorption measurements was 1.58 eV, while the band gap for the spin-coated thin films was 1.60 eV. The measured lifetimes of the emission signal for single crystals and thin films are very long (1.85 and 79 ns, respectively). Although the lowest direct transition appears at 1.59 eV, DFT calculations indicated an indirect fundamental band gap at 1.56 eV, in excellent agreement with the measured experimental optical band gaps. However, further calculations are required to assign the indirect/direct character of the transition. The electron and hole effective masses were also theoretically calculated ($m_e^* = 0.53m_0$ vs $m_h^* = 0.85m_0$), indicating the n-type character of this semiconductor.

The large dispersive profile of the band structure despite the lack of connectivity of the $PdBr_6^{2-}$ octahedra was explained based on the redistribution of charge between the Cs cations and the $PdBr_6^{2-}$ octahedra, in a similar fashion to $MAPbI_3$. Finally, the Cs_2PdBr_6 perovskite was shown to be chemical and phase stable upon immersion in water, corresponding to higher stability than that of $MAPbI_3$.

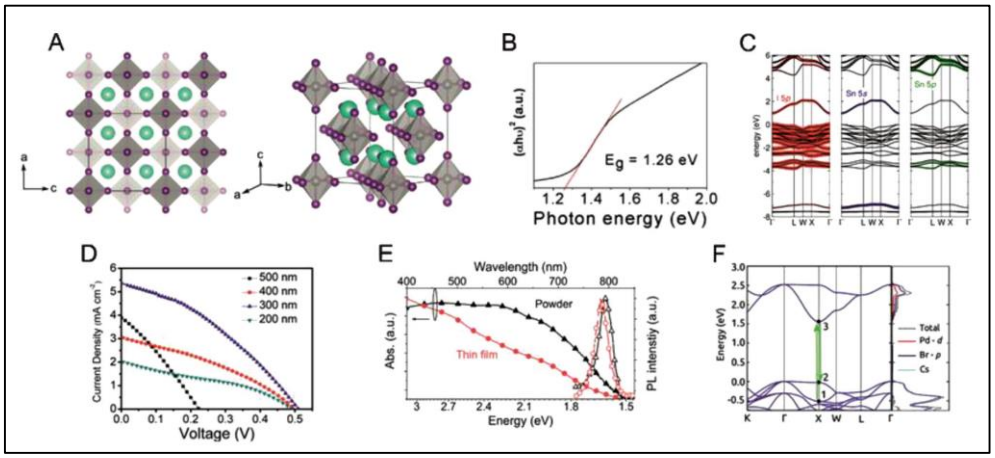

Figure 10. A) Crystal structure of the vacancy-ordered double perovskite Cs_2SnI_6 (left) and reorientation of the unit cell (right) revealing the isolated octahedra. Reproduced with permission.[116] Copyright 2016, American Chemical Society. B) Tauc plot of the Cs_2SnI_6 vacancy-ordered double perovskite, indicating a direct Eg of ≈1.3 eV. Reproduced with permission.[120] Copyright 2014, American Chemical Society. C) Band structures, including orbital projection analysis, of Cs_2SnI_6, showing the contributions of the I p states in red, the B 5s states in blue, and the B 5p states in green. Reproduced with permission.[116] Copyright 2016, American Chemical Society. D) J–V curves of perovskite solar cells fabricated with Cs_2SnI_6 of different thicknesses. Reproduced with permission.[118] Copyright 2016, Elsevier. E) UV–vis absorption and steady-state photoluminescence spectra of the Cs_2PdBr_6 double perovskite. Reproduced with permission.[123] Copyright 2017, American Chemical Society. F) Electronic band structure (left) and projected DOS (right) of Cs_2PdBr_6. The black dots mark the second highest (1) and highest (2) occupied state and the lowest unoccupied state (3) at the X point. Reproduced with permission.[123] Copyright 2017, American Chemical Society.

The reported vacancy-ordered double perovskites possess comparable optoelectronic properties to those of $MAPbI_3$, in addition to their higher stability and nontoxicity. Overall, A_2BX_6 materials are highly promising for future-generation photovoltaics owing to their low band gap energies, the direct character of their electronic transitions, high electron mobilities with reduced effective masses and solution-processable simplicity.

The unbalanced charge transport due to high hole effective masses is likely the principal detrimental feature of these materials, but appropriate doping or band engineering might solve this issue. Additionally, the large energy variation of the valence and conduction bands with respect to typical 3D

ABX_3 perovskites requires the employment of specific HTLs and ETLs to optimize the band alignment.

Regarding possible novel vacancy-ordered materials, A_2BX_6 compounds incorporating an organic A cation (MA, FA, or NH_4^+) are expected to generate hybrid A_2BX_6 perovskites with improved solution-processable properties. The range of tetravalent cations can also be extended (Mn^{4+}, Zr^{4+}, Cr^{4+}, and Ti^{4+}), or a combination between these cations can be utilized. These options, along with the already reported cations (Sn4+, Te^{4+}, and Pd^{4+}), broaden the family of vacancy-ordered double perovskites.

5. 0D Perovskites with $A_3B_2X_9$ Formula

This 0D family of materials is composed of isolated $B_2X_9^{3-}$ bioctahedra separated by A cations with hexagonal symmetry within the space group P63/mmc.[124] The crystal arrangement in this material family has been identified as a dimer structure formed by a pair of face-sharing octahedra (see Figure 11).[125] The $A_3B_2X_9$ stoichiometry possesses another polymorph, a layered structure formed by corner-sharing octahedra, 2D $A_3B_2X_9$, which will be described in the next section. Charge neutrality in the $A_3B_2X_9$ perovskites imposes a 3+ oxidation state for the B cation. To date, Bi^{3+} and Sb^{3+} have been exclusively employed in $A_3B_2X_9$. Both of these species exhibit reduced toxicity compared to Pb^{2+}, which is a considerable advantage. Additionally, the reduced dimensionality of 0D $A_3B_2X_9$ systems with respect to 3D ABX_3 materials can deliver better stability against phase degradation. Despite this family of perovskites being known from a long time, the photovoltaic community has only recently focused on these materials to take advantage of their optoelectronic properties.[126]

Solar cells based on the use of 0D $A_3B_2X_9$ have barely surpassed PCEs of 1% (see Figure 11).[127–129] The highest efficiency was obtained for a device fabricated with $Cs_3Bi_2I_9$ featuring J_{sc} = 2.15 mA cm^{-2}, V_{oc} = 0.85 V, FF = 0.60,

and η = 1.09%.[127] A $Cs_3Bi_2I_9$ layer was spin-coated between mesoporous TiO_2 and spiro-OMeTAD layers. The PCE of this solar cell measured one month after fabrication stored in dry air showed a stable value
indicating its high stability. The band gap energy of $Cs_3Bi_2I_9$ was calculated to be 1.9–2.2 eV (indirect transition) with an exciton absorption peak at ≈2.85 eV.[127] The exciton binding energy of $Cs_3Bi_2I_9$ was measured to be 270 meV for a grain size of 30.8nm, which may account for the low efficiency due to poor charge generation. Moreover, nonradiative recombination due to defect states in the band gap, a rough surface and the presence of pinholes in the perovskite films were also suggested to explain the low photovoltaic performance of this material. Another Bi-based material, $MA_3Bi_2I_9$, was also implemented in solar devices, yielding a PCE of 0.42% in a mesoscopic architecture by employing the appropriate concentration of MAI and BI_3 precursors.[128,130,131] The band gap energy for this material was 2.1 eV, with an exciton binding energy of 70 meV lower than that for $Cs_3Bi_2I_9$.[128]
Regarding Sb-based 0D $A_3B_2X_9$ materials, solar devices fabricated with $MA_3Sb_2I_9$ exhibited PCEs of ≈0.5% with J_{sc} = 1.0 mA cm^{-2}, V_{oc} = 0.88 V, and FF = 0.52 (see Figure 11).[129]
These devices were fabricated in an inverted configuration with PEDOT:PSS and PCBM as the HTL and ETL, respectively. $MA_3Sb_2I_9$ was deposited using a spin-coating method from a solution containing SbI_3 and CH_3NH_3I precursors and then further annealed at 100–120 °C under a N_2 atmosphere.[129] The experimentally calculated band gap energy of 2.14 eV and high absorption coefficient of α > 105 cm^{-1} theoretically implied a larger efficiency than 0.5%. The weak photoluminescence that was largely shifted to lower energies (1.58 eV) compared to the band gap edge (2.14 eV) was an indication of radiative recombination through subgap states, which might account for the observed low efficiency. A few more works have reported the optoelectronic properties of other 0D $A_3B_2X_9$ perovskites. $Cs_3Sb_2I_9$ has been

synthesized from a polar solution phase containing the appropriate CsI and SbI_3 precursors.[126,132] Orange colored crystals were obtained with an indirect band gap energy of 2.4 eV.

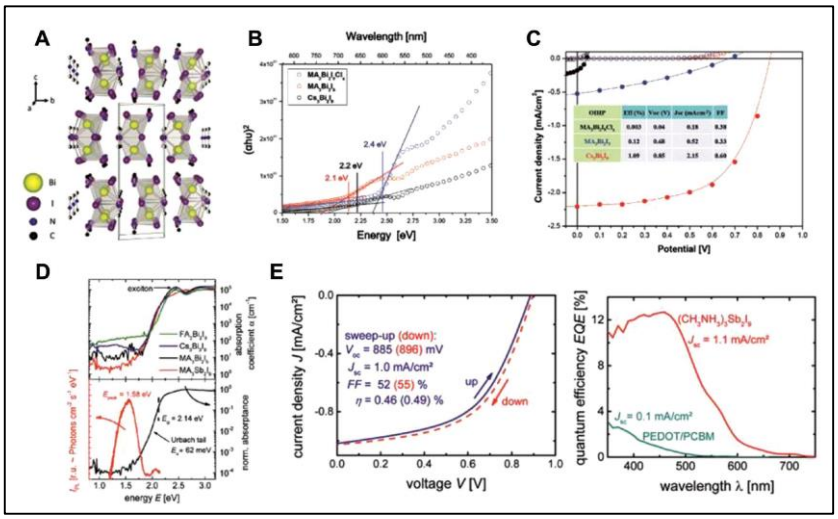

Figure 11. A) Representation of the layered structure of $(CH_3NH_3)_3Bi_2I_9$, characterized by isolated $[Bi_2I_9]^{3-}$ anions and two crystallographic inequivalent $CH_3NH_3^+$ cations. Reproduced with permission.[125] Copyright 2016, The Royal Society of Chemistry. B) Tauc plots for $MA_3Bi_2I_9Cl_x$, $MA_3Bi_2I_9$, and $Cs_3Bi_2I_9$ thin films. Reproduced with permission.[127] Copyright 2015, American Chemical Society. C) J–V curves for solar cells using the three different materials: $MA_3Bi_2I_9Cl_x$ (black line), $MA_3Bi_2I_9$ (blue line), and $Cs_3Bi_2I_9$ (red line). Reproduced with permission.[127] Copyright 2015, American Chemical Society. D) Comparison of the absorption coefficients of various Bi-based perovskites and $(CH_3NH_3)_3Sb_2I_9$ determined by photothermal deflection spectroscopy measurements (upper panel). Normalized absorptance of $(CH_3NH_3)_3Sb_2I_9$ with a calculated Urbach tail energy and corresponding room-temperature PL spectrum (lower panel). Reproduced with permission.[129] Copyright 2016, American Chemical Society. E) Illuminated J–V curve of a $(CH_3NH_3)_3Sb_2I_9$ solar cell measured with "up" and "down" sweep rates of 0.1 V s^{-1} (left) and EQE measurement of the $(CH_3NH_3)_3Sb_2I_9$ solar cell compared to a reference device (ITO (120 nm)/PEDOT/PCBM/ZnO-NP/Al) (right). Reproduced with permission.[129] Copyright 2016, American Chemical Society.

DFT calculations showed that the VBM is composed of I p and Sb s states, while the CBM is formed by Sb p states, similar to the situation in $MAPbI_3$.

A sulfur-doped $MA_3Bi_2I_9$ perovskite was also synthesized with a reduced band gap energy of 1.45 eV compared to the E_g = 2.1 eV for $MA_3Bi_2I_9$.[133]

Sulfur doping was performed through the utilization of bismuth ethyl xanthate ($Bixt_3$) as a soluble precursor, providing the insertion of S atoms at the interstitial sites. Interestingly, the high carrier concentration of 2.3 × 1021 cm^{-3} together with a high carrier mobility of 2.28 $cm^2\ V^{-1}\ s^{-1}$ exceeded the values for $MAPbI_3$ by several orders of magnitude, which noted the promising potential of this material for photovoltaics.

DFT theoretical studies reported the substitution effects of Bi atoms by trivalent cations in $Cs_3Bi_2I_9$ on the optoelectronic properties.[134] The incorporation of In or Ga in Cs_3BiInI_9 or Cs_3BiGaI_9 resulted in a reduced band gap energy yielding values of 1.9 and 1.6 eV, respectively. The reduced band gap energy was associated with the smaller lattice constant and volume.

$A_3B_2X_9$ perovskites are another example of 0D materials that have delivered relatively high efficiencies in yet nonoptimized solar cell devices. The formation of highly crystalline and homogeneous layers of these materials, in addition to the selection of the proper ETL and HTL, are required for the optimization of these devices to increase their efficiency. Moreover, extended the absorption range and reducing the recombination losses via defect states are other critical issues that must be addressed.

Another polymorph with $A_3B_2X_9$ stoichiometry is a layered defect perovskite comprising corrugated layers of corner-sharing BX_6 octahedra. The preferential formation of this 2D $A_3B_2X_9$ perovskite with respect to the 0D structure is governed by the synthesis method or the A cation size (see Figure 12).[135,136] The crystal structure of 2D $A_3B_2X_9$ perovskites originate from the 3D ABX_3 system, in which 1/3 of the octahedral B sites along one crystallographic direction are removed ($AB_{2/3}\square_{1/3}X_3$). The symmetry space group for each $A_3B_2X_9$ perovskite is dependent on the B vacancy direction. The reported optoelectronic properties have demonstrated promising prospects for the 2D polymorphs compared to the 0D structures; however,

the ability to form homogeneous thin layers using solution-processing methods is limited.[137]

Solar cells prepared using these materials have only been fabricated with Sb as a trivalent cation. The layered polymorph of $Cs_3Sb_2I_9$ has been incorporated into a solar device offering an efficiency of <1% with a very low Voc of 0.25−0.3 eV.[137] The device was fabricated by sandwiching the perovskite layer between a compact TiO_2 layer and a layer of poly-triarylamine, taking into account the deep VBM (−5.6 eV) calculated using UPS measurements.[137] The layered $Cs_3Sb_2I_9$ perovskite was deposited via coevaporation of CsI and SbI_3 precursors, obtaining oriented films with $Cs_3Sb_2I_9$ layers parallel to the substrate surface. The stability of the $Cs_3Sb_2I_9$ thin films was measured by XRD as the sample aged in air. Nearly no changes in the XRD patterns were observed after 60 d, compared to nearly full degradation for $MAPbI_3$ over the same period. The calculated band gap energy for the prepared thin film was 2.05 eV lower than that measured for the dimer form of the same $Cs_3Sb_2I_9$ perovskite (2.4 eV) (see Figure 12). Comparatively, the band gap of the bulk powder of layered $Cs_3Sb_2I_9$ obtained from solid-state reactions was 1.95 eV.[137] DFT calculations indicated the direct character of the transition with the top valence band composed of mixed I p and Sb s states and the conduction band formed by Sb p states, in a similar fashion to the 3D $MAPbI_3$ perovskite. The optical absorption coefficient calculated by DFT was very large (>105 cm^{-1} at 2.25 eV), similar to that of $MAPbI_3$. These results were explained based on the same p-orbital character of both the valence and conduction bands. In addition, both bands were apparently very dispersive, resulting in low charge effective masses, which were slightly larger perpendicular to the layers.

The second photovoltaic device fabricated with a layered polymorph employed $Rb_3Sb_2I_9$ deposited via a spin-coating method (see Figure 12).[136] An efficiency of 0.66% was measured with J_{sc} = 2.11 mA cm^{-2}, V_{oc} = 0.55 V,

and FF = 0.66 in a device that uses a mesoporous TiO_2 layer and poly-TPD as the ETL and HTL, respectively. In contrast to $Cs_3Sb_2I_9$, layered $Rb_3Sb_2I_9$ can be formed via a solution process, which is related to the more-negative formation energy for the layered polymorph with respect to the dimer structure.[136] The smaller ionic radius of Rb compared to that of Cs seems to play a key role in the preferential formation of the layered structure. $Rb_3Sb_2I_9$ powder was also synthesized by heating a DMF solution containing the precursors. Excess SbI_3 precursor was utilized to obtain thin films with ideal stoichiometry, with better coverage and without a preferred orientation. The crystal structure of $Rb_3Sb_2I_9$ belongs to the P1c1 space group and is thermally stable up to 250 °C. The band gap energy assuming a direct transition was 2.24 eV, as measured from Tauc plots, and the absorption coefficient was very high (105 cm^{-1} at 2.5 eV), very similar to that of $MAPbI_3$.[136] The high absorption ability of $Rb_3Sb_2I_9$ is linked to the p–p character of the electronic transition, as the VBM is composed of I p and Sb s states, and the conduction band is formed by I p and Sb p states. The variation in the V_{oc} value with the illumination intensity was studied to derive the nature of recombination in the material, indicating that a Shockley–Read–Hall mechanism via defect levels was the preferential process reducing the efficiency.

An additional layered structure with slightly different stoichiometry was recently synthesized and incorporated into a solar device.[138] $CsBi_3I_{10}$ possesses a similar structure compared to that of layered BiI_3 crystals but with certain similarities to 0D $Cs_3Bi_2I_9$. The estimated band gap energy for the $CsBi_3I_{10}$ thin film prepared via spin-coating was 1.77 eV, which is smaller than that of $Cs_3Bi_2I_9$ (2.03 eV). These films were incorporated into a device with a mesoscopic (TiO_2) architecture and P3HT as the HTL. The obtained PCE (η) was 0.4% with a J_{sc} of 3.4 mA cm^{-2}, which is higher than that reported for $Cs_3Bi_2I_9$ (2.2 mA cm^{-2}), attributing to the extended light

absorption capacity. However, the low V_{oc} value (0.31 V) and FF (0.38) preclude the achievement of larger η values. The energy levels of each material in the device were not aligned, and the $CsBi_3I_{10}$ layers contained pinholes and likely defect states, which accounted for the low V_{oc} and FF.

Single crystals and bulk powders of $K_3Bi_2I_9$ and $Rb_3Bi_2I_9$ layered perovskites have also been synthesized via solvothermal reactions at 120 °C or high-energy ball milling, respectively.[139] Thin films of these materials have also been prepared by spin-coating. The band gap energies derived from Tauc plots for the $K_3Bi_2I_9$ and $Rb_3Bi_2I_9$ powders are practically the same (≈2.1 eV), assuming direct transitions (see Figure 12). The VBM calculated from UPS measurements was estimated to be between −6.1 and −6.3 eV for both materials, in excellent agreement with the value of −6.1 eV derived from DFT calculations. The considerable energy difference compared to the VBM of $MAPbI_3$ (−5.4 eV) imposes the utilization of novel HTLs with appropriate energy alignments to optimize the V_{oc}.[139] DFT calculations also revealed a relatively flat VBM and CBM with poor dispersion, indicating high charge effective masses.

These 2D perovskites with an $A_3B_2X_9$ stoichiometry have been scarcely studied compared to 2D materials with an A_2BX_4 formula. The initial reports on these materials disclose their excellent optoelectronic properties for photovoltaics; however, the preliminary obtained efficiencies of the solar devices have been very poor. Therefore, developing strategies to achieve homogeneous and defect-free films is necessary, and appropriate types of ETL and HTL are required to optimize the device efficiency. Finally, a combination of different A and B cations within the same structure or doping with alternative monovalent A cations can create novel 2D $A_3B_2X_9$ materials with optimized photovoltaic properties.

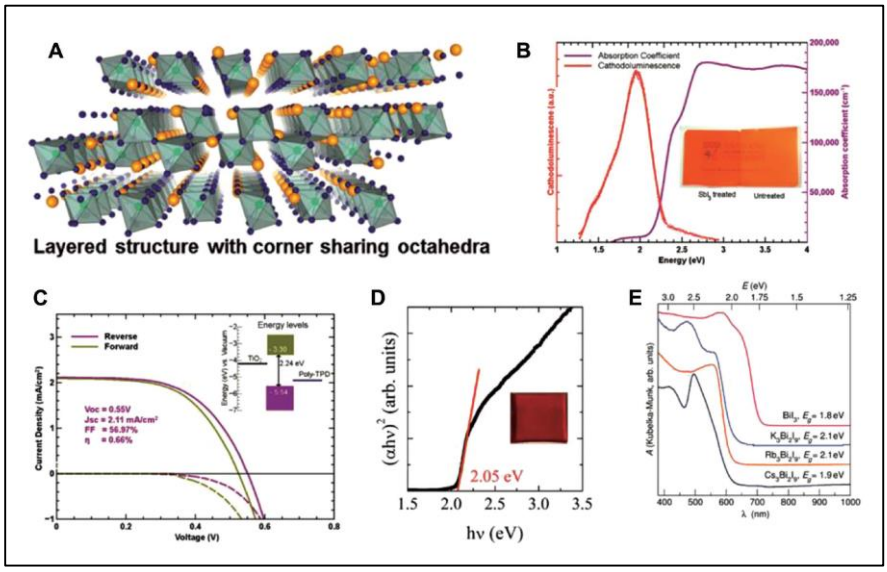

Figure 12. A) Crystal structure of the layered $Rb_3Sb_2I_9$ perovskite showing corner-sharing octahedral. Reproduced with permission.[136] Copyright 2016, American Chemical Society. B) Absorption coefficient and cathodoluminescence of SbI_3-treated $Rb_3Sb_2I_9$. Reproduced with permission.[136] Copyright 2016, American Chemical Society. C) J–V curve under forward and reverse scans of the best-performing $Rb_3Sb_2I_9$ solar device with the energy levels of $Rb_3Sb_2I_9$ shown in the inset. Reproduced with permission.[136] Copyright 2016, American Chemical Society. D) Band gap of layer-modified $Cs_3Sb_2I_9$ (inset shows a thin film) was calculated to be 2.05 eV from the absorbance data using the Tauc plot. Reproduced with permission.[137] Copyright 2015, American Chemical Society. E) UV–vis diffuse-reflectance spectra recorded on powder samples of $A_3Bi_2I_9$ and BiI_3 transformed into absorbance. Band gaps were obtained using Tauc plots assuming direct gaps for A = K and Rb and indirect gaps for the remaining phases. Reproduced with permission.[139] Copyright 2015, American Chemical Society.

7. Quasi-2D Ruddlesden–Popper Perovskites with $A'_2A_{n-1}BX_{3n+1}$ Formula

The quasi-2D homologous of the 3D ABX_3 perovskites has been known since the 1990s.[140,141] The general stoichiometric formula of these compounds is denoted as $A'_2A_{n-1}B_nX_{3n+1}$ (n is an integer number), where A = RNH_3 is a primary aliphatic or aromatic alkylammonium cation, A′ is a small alkylammonium cation (e.g., $CH_3NH_3^+$), B is a metallic cation (typically Pb), and X corresponds to halide anions (X = Cl^-, Br^- or I^-). The large A organic

cations act as spacers, separating the perovskite layers composed of corner-sharing BX_6 octahedra and resulting in the formation of alternating organic and inorganic layers that stack along the c direction to form oriented composites (see Figure 13). Thus, different layers maintain structural integrity, which is held together by a combination of hydrophobic and Coulombic forces.[141]

The characteristic property of these quasi-2D perovskites is electronic confinement in the sub-nanometer inorganic layers that originates from the formation of stable excitons with extended Bohr radii and high binding energies.[141] Thus, quasi- 2D perovskites can be considered natural multiple-quantumwells, in which the inorganic and organic layers act as potential "wells" and potential "barriers," respectively.[142,143] Importantly, the exciton stability does not seem to derive solely from the dimensional confinement but is also derives from the large organic cations that can modulate the dielectric properties of the material.[144,145]

The principal motivation to employ Ruddlesden–Popper perovskites in photovoltaics is the improved water resistance of these materials compared to their 3D ABX_3 analogs. Moreover, high-quality smooth films of these quasi-2D perovskites with good surface coverage were more easily prepared under ambient conditions without annealing compared to 3D ABX_3 materials. Ruddlesden–Popper perovskites offer more flexible arrangements due to the relaxed steric limitation of the organic cations. Thus, a large variety of organic cations can be incorporated into the 2D framework, while 3D domains have a more restrained capacity for structural engineering.

The quasi-2D Ruddlesden–Popper perovskites have been incorporated into solar devices as light-harvesting materials, delivering remarkable PCEs and exceptional performances in stability tests. Thus far, only six large organic cations, i.e., phenylethylammonium (PEA),[146] iodoethylammonium (IET),[147] butylammonium (BA),[148] polyethylenimine (PEI),[149] isobutylammonium (iso-

BA),[150] and anilinium (Any),[151] have been utilized in the preparation of Ruddlesden–Popper perovskites together with methylammonium (MA) as a small organic cation.

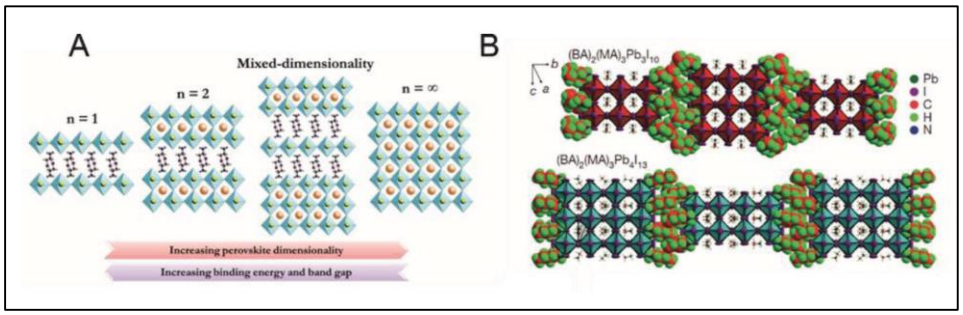

Figure 13. A) Schematic illustration showing the crystalline structures of 2D perovskites (n = 1 and 2, where n represents the metal halide lattices), mixed dimensionality Ruddlesden–Popper perovskites and 3D perovskites (n = ∞). Reproduced with permission.[147] Copyright 2016, Wiley-VCH. B) Crystal structures of the Ruddlesden–Popper $(BA)_2(MA)_2Pb_3I_{10}$ and $(BA)_2(MA)_3Pb_4I_{13}$ layered perovskites, depicted as n polyhedral blocks, where n refers to the number of layers; the BA spacer layers are depicted as space-filling models to illustrate the termination of the perovskite layers. Reproduced with permission.[154] Copyright 2016, Macmillan Publishers Ltd: Nature.

The first quasi-2D perovskite, $(PEA)_2(MA)_2Pb_3I_{10}$ with n = 3, was reported in 2014 and included the PEA cation ($C_6H_5(CH_2)_2NH_3^+$).[146] The band gap energy of $(PEA)_2(MA)_2Pb_3I_{10}$ was 2.06 eV, much larger than that of 3D $MAPbI_3$ (1.57 eV). Solar cells were fabricated utilizing a one-step spin-coating technique in a planar configuration with TiO_2 and spiro-OMeTAD as the ETL and HTL, respectively. The device showed a PCE of 4.73%, V_{oc} = 1.18 V, J_{sc} = 6.72 mA cm^{-2}, and FF = 0.60. The remarkably high V_{oc} was due to the increased band gap energy. The device displayed greater moisture resistance compared to those fabricated with 3D $MAPbI_3$.[146]

In a later work, the I^- anion was subsequently substituted by Br^-, and the influence of varying n from 1 to 60 in $(PEA)_2(MA)_{n-1}Pb_nBr_{3n-1}$ was studied (see Figure 14).[152] An increased band gap energy was reported compared to the iodide counterparts. The solar devices prepared using quasi-2D

perovskites with n = 60 and without an HTL delivered a PCE of 6.3%, V_{oc} = 1.25 V, J_{sc} = 8.2 mA cm^{-2}, and FF = 0.62. Additionally, with n = 50 and spiro-OMeTAD as the HTL, a comparable PCE of 8.5% was obtained with V_{oc} = 1.46 V, J_{sc} = 9.0 mA cm^{-2}, and FF = 0.65.[152] The PEA cation has also been employed to stabilize the α-phase of $FAPbI_3$, obtaining the quasi-3D perovskite with an $FA_xPE_{x-1}PbI_3$ formula. The solar cells were fabricated utilizing an inverted p–i–n planar configuration with NiO_x and PCBM as the HTL and ETL, respectively. The PCE reached 17.71% with V_{oc} = 1.04 V, J_{sc} = 22.08 mA cm^{-2}, and FF = 0.77.[153]

Iodoethylammonium has also been employed as a large organic cation to fabricate $(IET)_2(MA)_{n-1}Pb_nI_{3n+1}$ materials.[147] The dimensionality of each structure (n number) was defined by controlling the dipping time in a two-step spincoating deposition. Solar cells were prepared with an FTO/blocking-TiO_2/meso-TiO_2/$(IET)_2(MA)_{n-1}Pb_nI_{3n+1}$/Spiro/Au architecture, resulting in a PCE of 9.03% with V_{oc} = 0.883 V, J_{sc} = 14.88 mA cm^{-2}, and FF = 0.69.[147]

For the first time in 2015, BA was also employed as a cation to form quasi-2D perovskites with the formula $BA_2(MA)_{n-1}Pb_nI_{3n+1}$ (n = 1–4).[148] The most remarkable feature of these 2D Ruddlesden–Popper perovskites is their perpendicular growth, which facilitates charge extraction in solar cells. The device was prepared in both p–i–n planar and mesoporous configurations using a simple one-step spin-coating technique. The best PCE was 4.02% (n = 3) with the mesoporous configuration, along with V_{oc} = 0.929 V, J_{sc} = 9.42 mA cm^{-2}, and FF = 0.46.[148] In 2016, the same materials with n = 3 ($BA_2(MA)_2Pb_3I_{10}$) and n = 4 ($BA_2(MA)_3Pb_4I_{13}$) were deposited using a hot-casting method, resulting in superior crystallinity compared to those fabricated at room temperature and at 110 °C (see Figure 14).[154]

The solar cells were fabricated utilizing a planar-inverted configuration with an FTO/PEDOT:PSS/$BA_2(MA)_{n-1}Pb_nI_{3n+1}$/PCBM/Al architecture, offering the best efficiency with n = 4 (PCE = 12.51%, V_{oc} = 1.01 V, J_{sc} = 16.76 mA cm^{-2},

and FF = 0.74). The devices showed high moisture stability, retaining 65% of the efficiency under constant illumination after 2500 h and with no hysteresis.[154]

NH_4SCN was also utilized as an additive through a one-step spin-coating process for $BA_2(MA)_2Pb_3I_{10}$, obtaining perovskite films with fine crystallinity and perpendicular orientation with a planar-inverted configuration.[155] The energy levels of $BA_2(MA)_2Pb_3I_{10}$ decreased by 0.2 eV after the addition of SCN, which benefited the charge-carrier separation in PCBM (electrons) and PEDOT:PSS (holes). The solar cells demonstrated a PCE of 6.89% with V_{oc} = 0.97 V, J_{sc} = 12.79 mA cm^{-2}, and FF = 0.55.[155] Recently, quasi-2D $(BA)_2(MA)_3Pb_4I_{13}$ perovskites doped with cesium cations (Cs^+) provided the highest PCE among this type of materials (13.7%).[156] A hot-casting method was used for the deposition with DMSO functioning as a ligand to form a complex structure with the PbI_2 precursor, growing high-quality $(BA)_2Cs_{3n}(MA)_{3-3n}Pb_4I_{13}$ (n = 0, 0.05, 0.1, and 0.15) crystals. Cs^+ doping was observed to alter the phase transition. All the doped films exhibited better crystal orientation, with a band gap of 1.62–1.63 eV, which is very similar to that of $MAPbI_3$ (1.57eV), indicating that this material is a good absorber for photovoltaics. The solar cells were prepared with a FTO/blocking-TiO_2/blocking-TiO_2/$(BA)_2Cs_{3x}(MA)_{3-3x}Pb_4I_{13}$/Spiro/Au architecture, and the champion device with 5%-Cs doping demonstrated a PCE of 13.68% with V_{oc} = 1.08 V, J_{sc} = 19.95 mA cm^{-2}, and FF = 0.63.[156] Remarkably, due to the good moisture resistance, the device retained 89% of their initial PCE after 1400 h of exposure under ambient condition with 30% relative humidity.

The PEI cation was employed to fabricate $(PEI)_2(MA)_{n-1}Pb_nI_{3n-1}$ perovskites with n = 3, 5, and 7 to facilitate the electronic interactions between the separated inorganic layers, resulting in an enhancement of the charge-transport characteristics.[149] The solar cells prepared with n = 5 and 7

showed high moisture stability, retaining over 90% of the initial PCE value after 500 h of light illumination. The most remarkable achievement related to the preparation of large-area solar cells (2.32 cm^2) with a very high efficiency up to 8.77%.[149]

x

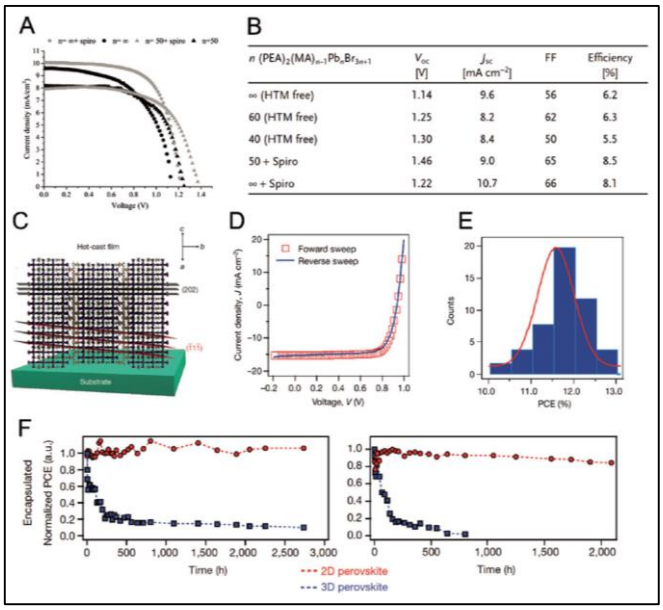

Figure 14. A) J–V curves of the best-performing cells for quasi-2D $(PEA)_2(MA)_{n-1}Pb_nBr_{3n+1}$ and 3D perovskites with and without an HTL. Reproduced with permission.[152] Copyright 2016, Wiley-VCH. B) Best-performing cells observed for quasi-2D $(PEA)_2(MA)_{n-1}Pb_nBr_{3n+1}$ and 3D perovskites with an HTL-free configuration and with Spiro as the HTL. Reproduced with permission.[152] Copyright 2016, Wiley-VCH. C) Schematic representation of the (101) orientation, along with the (111) and (202) planes of a near single-crystalline $(BA)_2(MA)_3Pb_4I_{13}$ perovskite film. Reproduced with permission.[154] Copyright 2016, Macmillan Publishers Ltd: Nature. D) J–V curves for hysteresis tests under AM1.5G illumination for planar devices using the 2D $(BA)_2(MA)_3Pb_4I_{13}$ perovskite as the absorbing layer measured by scanning the voltage in opposite directions. Reproduced with permission.[154] Copyright 2016, Macmillan Publishers Ltd: Nature. E) Histogram of the $(BA)_2(MA)_3Pb_4I_{13}$ device PCE over 50 measured devices, fitted with a Gaussian distribution (red line). Reproduced with permission.[154] Copyright 2016, Macmillan Publishers Ltd: Nature. F) Photostability tests under constant AM1.5G illumination for 2D ($(BA)_2(MA)_3Pb_4I_{13}$; red) and 3D ($MAPbI_3$; blue) perovskite devices without (upper-left panel) and with (lowerleft panel) encapsulation. Humidity stability tests under 65% relative humidity in a humid chamber for 2D ($(BA)_2(MA)_3Pb_4I_{13}$; red) and 3D ($MAPbI_3$; blue) perovskite devices without (upper-right panel) and with (lower-right panel)) encapsulation. Reproduced with permission.[154] Copyright 2016, Macmillan Publishers Ltd: Nature.

The devices were prepared with an ITO/PEDOT:PSS/ $(PEI)_2(MA)_{n-1}Pb_nI_{3n-1}$/$PC_{61}BM$/LiF/Ag architecture, showing an average PCE of 10.08% with V_{oc} = 1.10 V, J_{sc} = 13.12 mA cm^{-2}, and FF = 0.65 for the small-area devices (0.04 cm^{-2} and n = 7) and an average PCE of 8.06% with V_{oc} = 1.08 V, J_{sc} = 11.74 mA cm^{-2}, and FF = 0.63 for the large-area devices.[149]

Isobutylammonium (iso-BA), which is much shorter than the conventional linear n-BA cation, has also been employed as a spacer cation.[150] Thus, thin films of the quasi-2D $(iso\text{-}BA)_2(MA)_3Pb_4I_{13}$ Ruddlesden–Popper perovskite have displayed an increased optical absorption and crystallinity with respect to those of n-BA Ruddlesden–Popper perovskites. The highest

PCE for the $(iso\text{-}BA)_2(MA)_3Pb_4I_{13}$ solar devices was 10.33% with J_{sc} = 16.54 mA cm^{-2}, V_{oc} = 1.20 V and FF = 0.54, due to the preferential out-of-plane orientation; however, a significant hysteresis phenomenon was also observed.[150]

Finally, the conjugated anilinium cation (Any) has been incorporated into the quasi-2D perovskite structure to obtain $(Any)_2(CH_3NH_3)_{n-1}(PbI_2)_n$ perovskites with n = 1−5.[151] The implementation of these materials in solar devices has delivered an enhanced PCE value up to 5.94% (n = 5) compared to the PCE of 3.02% obtained for the devices with $(BA)_2(CH_3NH_3)_{n-1}(PbI_2)_n$.[151]

The main two drawbacks of quasi-2D Ruddlesden–Popper perovskites for photovoltaic applications include: 1) the large E_g and 2) the anisotropic reduction of the charge-carrier mobility upon decreasing the dimensionality of the inorganic BX_6 network. The limited absorption ability in Ruddlesden–Popper perovskites with low n values results from a quantum confinement effect and entails a reduced short-circuit current density (J_{sc}), while the reduced out-of-plane charge transport is originates from the presence of large organic cations that act as an insulating layer. Additionally, an increase

in the exciton binding energy (EB) at low n values is observed, which is associated with enhanced charge-carrier recombination rates.

Several approaches have been explored to circumvent the limitations of quasi-2D perovskites. Thus, the implementation of Ruddlesden–Popper phases with intermediate n values has been very successful, as the Eg and EB values are reasonably low, similar to those of $MAPbI_3$. An additional strategy involves the vertical growth of quasi-2D perovskite layers to take advantage of the good charge-transport characteristics of 2D $\{(MA)_{n-1}\ Pb_nI_{3n+1}\}^{2-}$ slabs avoiding electron transport through the insulating spacer layers.

Quasi-2D Ruddlesden–Popper perovskites can be considered as materials with intermediate optoelectronic properties between 3D ABX_3 and 2D A_2BX_4 perovskites. Thus, the selection of the most appropriate dimensionality of the quasi-2D phase (the n integer number) must be a compromise to retain the best attributes from each material. As the number of large organic cations employed in quasi-2D Ruddlesden–Popper perovskites is very limited, the incorporation of innovative cations, i.e., π-conjugated compounds, could optimize the performance of these materials in solar devices. An alternative approach for the implementation of quasi-2D perovskites in photovoltaics is the deposition of two sequential layers of an ABX_3 material and a quasi-2D Ruddlesden–Popper perovskite to combine the outstanding properties of each material.

8. 2D Perovskites with A_2BX_4 Formula

$A'_2A_{n-1}B_nX_{3n+1}$ Ruddlesden–Popper materials with n = 1 are a strict 2D family of perovskites with an A_2BX_4 formula,[157] whose particular optoelectronic properties have been frequently employed in optical and electronic devices, including field effect transistors,[158] and light-emitting diodes,[159] but their photovoltaic applications are still in their infancy.[160] These materials

comprise BX_6 octahedra interconnected through four halide bridges forming inorganic perovskite sheets separated from each other by organic cations to ensure charge neutrality.[157] These layered 2D perovskites accommodate different types of divalent cations, resulting in Pb-free materials that can overcome the toxicity issues of Pb-based perovskites. Moreover, the absence of the particular size limitations in 3D structures allows the introduction of a larger variety of available A cations that can provide unique properties. Additionally, these 2D materials possess enhanced moisture resistance that can significantly improve the stability of solar devices.

The first 2D A_2BX_4 material implemented as a light harvester in a solar device was $(CH_3NH_3)_2CuCl_xBr_{4-x}$ (see Figure 15).[160] In particular, $(CH_3NH_3)_2CuCl_2Br_2$ was infiltrated into a mesoporous TiO_2 layer via a spin-coating technique using spiro-OMeTAD as the hole conductor. A PCE of 0.017% was obtained with J_{sc} = 216 μA cm^{-2}, V_{oc} = 256 mV, and FF = 0.32.[160] Interestingly, photocurrent was generated over the entire UV–vis–NIR region (300–900 nm), which is optimum for a solar absorber. However, the low absorption coefficient as well as reduced charge mobility in $(CH_3NH_3)_2CuCl_xBr_{4-x}$ perovskites prevents the achievement of competitive PCE values compared to those of ABX_3 materials. Ligand-to-metal charge transfer (CT) transitions and d–d transitions of Cu are responsible for the observed absorption in $(CH_3NH_3)_2CuCl_xBr_{4-x}$ perovskites. Theoretical calculations showed a low DOS close to the band gap, which explained the low absorption coefficients. Moreover, charge transport was strongly anisotropic with large effective masses in the perpendicular direction of the inorganic planes.[160]

An improved PCE value with 2D A_2BX_4 were achieved employing $HAPbI_4$, where HA is the doubly charged histammonium cation (see Figure 15).[161] $HAPbI_4$ was inserted in a planar device with PEDOT:PSS and PCBM as the HTL and ETL, respectively. The device delivered a PCE value of 1.13%, with

J_{sc} = 2.65 mA cm^{-2}, V_{oc} = 0.91 V, and FF = 46.7%.[161] The large band gap energy of the $HAPbI_4$ perovskite limits the absorption range of this material and thus the device photocurrent. Interestingly, solution-deposited thin films of $HAPbI_4$ in the device adopted a perpendicular orientation with respect to the substrate, which is highly beneficial to optimize charge transport in the solar cell. This behavior was attributed to the dicationic nature of HA, as the 2D perovskite formed with benzylammonium cations, i.e., $(BZA)_2PbI_4$, possessed a similar structure as that with the HA cations and grew in a parallel orientation.[161]

Other 2D A_2BX_4 perovskites, including $(FC_2H_4NH_3)_2$ $PbCl_4$,[162] $(C(NH_2)_3)_2SnI_4$,[163] $(CH_3(CH_2)_3NH_3)_2SnI_4$,[163] $(C_8H_9NH_3)_2PbBr_xI_{3-x}$,[164] and $(CH_3NH_3)_2PdCl_4$,[165] have been recently proposed for photovoltaics applications. The hydrophobic nature of the fluorinated organic linkers used in $(FC_2H_4NH_3)_2PbCl_4$ may enhance the water resistance of these materials.[162] Additionally, two Sn-based perovskites, $(C(NH_2)_3)_2SnI_4$ and $(CH_3(CH_2)_3NH_3)_2SnI_4$, possess band gap energies of 2.10 and 1.80 eV, respectively, which are relatively low for 2D materials.[163] The employment of different solvents in the crystallization process of $(C_8H_9NH_3)_2PbBr_xI_{3-x}$ has a strong impact on the lateral sizes of these perovskite nanosheets, which subsequently tunes their optoelectronic properties.[164] $(CH_3NH_3)_2PdCl_4$ exhibits a band gap energy of 2.2 eV, with an absorption coefficient of ≈10−4 cm^{-1}, and is moderately stable in air.[165] $(CH_3NH_3)_2Pb(SCN)_2I_2$ with the thiocyanate (SCN) anion partially substituting the iodide anions is a particular interesting material.[166]

Despite some initial contradictory reports on this material, an indirect (2.04 eV) and direct band gap (2.11 eV) have been demonstrated with carriers confined within 2D layers.[87,166] Additionally, 2D halide perovskites can also be formed with other transition-metal ions, such as Cu(II),[167,168] Cr(II),[169]

Mn(II),[170] and Fe(II).[171,172] In this sense, the family of 2D hybrid perovskites $(C_6H_{13}NH_3)_2BCl_4$ (B = Cu^{2+}, Mn^{2+}, Cd^{2+}) has been synthesized.[173]

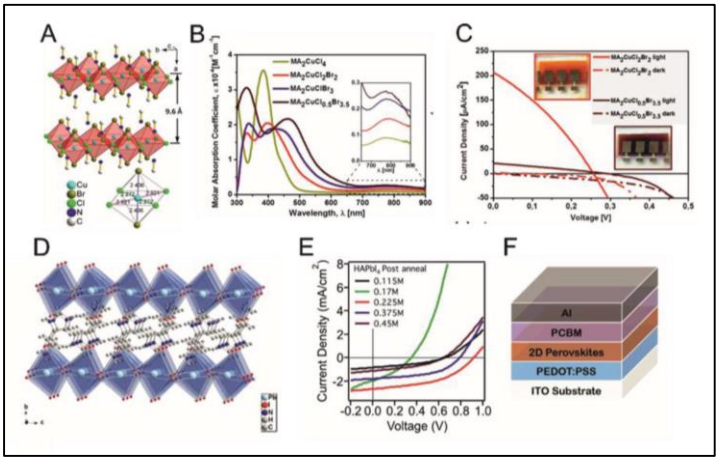

Figure 15. A) Crystal structure of $MA_2CuCl_2Br_2$, showing alternating organic and inorganic layers and the Cu−X bond lengths in the inorganic framework. Reproduced with permission.[160] Copyright 2016, American Chemical Society. B) Absorption coefficients for perovskites in the $MA_2CuCl_xBr_{4-x}$ series, showing strong CT bands below 650 nm and broad d–d transitions between 700 and 900 nm (inset). Reproduced with permission.[160] Copyright 2016, American Chemical Society. C) J–V curves of solar cells sensitized with $MA_2CuCl_2Br_2$ (red) and $MA_2CuCl_{0.5}Br_{3.5}$ (brown) under 1 sun light illumination. The dashed red and brown lines represent the dark current. Reproduced with permission.[160] Copyright 2016, American Chemical Society. D) Crystal structure of the 2D $(HA)PbI_4$ perovskite. Reproduced with permission.[161] Copyright 2016, American Chemical Society. E) J–V curves of $(HA)PbI_4$ using a postannealing method with various (0.115 to 0.45 m) concentrations. Reproduced with permission.[161] Copyright 2016, American Chemical Society. F) Device architecture of the fabricated 2D $(HA)PbI_4$ solar cell. Reproduced with permission.[161] Copyright 2016, American Chemical Society.

$(CH_3NH_3)_2CuCl_xBr_{4-x}$ and $HAPbI_4$ hybrid perovskites represent an early example of 2D A_2BX_4 materials with demonstrated potential for photovoltaics. Despite the low performance, the incorporation of other transition-metal divalent cations, such as Zn^{2+} or Fe^{2+}, or the insertion of π-conjugated organic cations makes this approach a promising alternative to provide a large avenue of research.

9. Conclusions and Outlook

The widespread family of perovskite materials includes a nearly countless number of compounds due to the large structural flexibility and the ease to incorporate different types of atoms. Thus, the main two factors that determine the suitability of different perovskites for photovoltaics are the material dimensionality and the type of B cation. The material dimensionality is not only a structural feature related to the connectivity between the inorganic octahedra but also, and more importantly, the interaction between the atomic orbitals that comprise the LCB and UVB to ensure good charge transport in all three directions. Regarding the B cation, substitution of Pb with Ge, Bi, Sb, or Sn has been realized to obtain lower PCE values that those reported with $MAPbI_3$. The employed B cation governs the type of perovskite crystal structure and the optoelectronic properties of the material due to the particular electronic configuration of each B cation. Finally, subtle modifications of the MAPbI3 structure have provided excellent results for the performance of solar devices. Thus, the partial substitution of MA by Rb^+, ethylammonium or guanidinium has provided further optimized efficiencies and device stabilities. The most recent approach is to employ chalcogenide perovskites that confer more covalent character to the B–X bonds, thus enhancing the perovskite stability.

The plethora of perovskite materials is an inspirational source for potential advances in state-of-the-art perovskite devices. The comparable low efficiencies obtained with alternative perovskites are mainly ascribed to the poor device optimization, especially the perovskite film quality and the employment of HTLs and ETLs with unsuitable energy levels. We believe that the knowledge attained with the characterization of these novel materials will be fundamental to the development of strategies to overcome the actual limitations of perovskite devices in future commercialization.

References

[1] A. Kojima, K. Teshima, Y. Shirai, T. Miyasaka, J. Am. Chem. Soc. 2009, 131, 6050.

[2] M. M. Lee, J. Teuscher, T. Miyasaka, T. N. Murakami, H. J. Snaith, Science 2012, 338, 643.

[3] H.-S. Kim, C.-R. Lee, J.-H. Im, K.-B. Lee, T. Moehl, A. Marchioro, S.-J. Moon, R. Humphry-Baker, J.-H. Yum, J. E. Moser, M. Grätzel, N.-G. Park, Sci. Rep. 2012, 2, 591.

[4] M. Liu, M. B. Johnston, H. J. Snaith, Nature 2013, 501, 395.

[5] J. Burschka, N. Pellet, S. J. Moon, R. Humphry-Baker, P. Gao, M. K. Nazeeruddin, M. Grätzel, Nature 2013, 499, 316.

[6] H. Zhou, Q. Chen, G. Li, S. Luo, T.-b. Song, H.-S. Duan, Z. Hong, J. You, Y. Liu, Y. Yang, Science 2014, 345, 542.

[7] N. J. Jeon, J. H. Noh, W. S. Yang, Y. C. Kim, S. Ryu, J. Seo, S. I. Seok, Nature 2015, 517, 476.

[8] M. Saliba, T. Matsui, J.-Y. Seo, K. Domanski, J.-P. Correa-Baena, M. K. Nazeeruddin, S. M. Zakeeruddin, W. Tress, A. Abate, A. Hagfeldt, M. Grätzel, Energy Environ. Sci. 2016, 9, 1989.

[9] W. S. Yang, B.-W. Park, E. H. Jung, N. J. Jeon, Y. C. Kim, D. U. Lee, S. S. Shin, J. Seo, E. K. Kim, J. H. Noh, S. Il Seok, Science 2017, 356, 1376.

[10] NREL, Best Research-Cell Efficiencies, http://www.nrel.gov (accessed: December 2017).

[11] S. De Wolf, J. Holovsky, S.-J. Moon, P. Löper, B. Niesen, M. Ledinsky, F.-J. Haug, J.-H. Yum, C. Ballif, J. Phys. Chem. Lett. 2014, 5, 1035.

[12] V. D'Innocenzo, G. Grancini, M. J. P. Alcocer, A. R. S. Kandada, S. D. Stranks, M. M. Lee, G. Lanzani, H. J. Snaith, A. Petrozza, Nature Commun. 2014, 5, 3586.

[13] C. Wehrenfennig, G. E. Eperon, M. B. Johnston, H. J. Snaith, L. M. Herz, Adv. Mater. 2014, 26, 1584.

[14] S. D. Stranks, G. E. Eperon, G. Grancini, C. Menelaou, M. J. P. Alcocer, T. Leijtens, L. M. Herz, A. Petrozza, H. J. Snaith, Science 2013, 342, 341.

[15] R. E. Brandt, V. Stevanovic, D. S. Ginley, T. Buonassisi, MRS Commun. 2015, 5, 265.

[16] A. Walsh, D. O. Scanlon, S. Chen, X. G. Gong, S.-H. Wei, Angew. Chem., Int. Ed. 2015, 127, 1811.

[17] Y. Deng, E. Peng, Y. Shao, Z. Xiao, Q. Dong, J. Huang, Energy Environ. Sci. 2015, 8, 1544.

[18] G. Xing, N. Mathews, S. Sun, S. S. Lim, Y. M. Lam, M. Grätzel, S. Mhaisalkar, T. C. Sum, Science 2013, 342, 344.

[19] A. M. Ganose, C. N. Savory, D. O. Scanlon, Chem. Commun. 2017, 53, 20.

[20] A. T. Barrows, A. J. Pearson, C. K. Kwak, A. D. F. Dunbar, A. R. Buckley, D. G. Lidzey, Energy Environ. Sci. 2014, 7, 2944.

[21] D. S. Bhachu, D. O. Scanlon, E. J. Saban, H. Bronstein, I. P. Parkin, C. J. Carmalt, R. G. Palgrave, J. Mater. Chem. A 2015, 3, 9071.

[22] G. Hodes, D. Cahen, Nat. Photonics 2014, 8, 87.

[23] S. Yang, W. Fu, Z. Zhang, H. Chen, C.-Z. Li, J. Mater. Chem. A 2017, 5, 11462.

[24] J. Xu, Y. Chen, L. Dai, Nat. Commun. 2015, 6, 8103.

[25] M. Lyu, J.-H. Yun, P. Chen, M. Hao, L. Wang, Adv. Energy Mater. 2017, 7, 1602512.

[26] Z. Song, A. Abate, S. C. Watthage, G. K. Liyanage, A. B. Phillips, U. Steiner, M. Grätzel, M. J. Heben, Adv. Energy Mater. 2016, 6, 1600846.

[27] G. Nagabhushana, R. Shivaramaiah, A. Navrotsky, Proc. Natl. Acad. Sci. USA 2016, 113, 7717.

[28] B. Hailegnaw, S. Kirmayer, E. Edri, G. Hodes, D. Cahen, J. Phys. Chem. Lett. 2015, 6, 1543.

[29] K. K. Bass, R. E. McAnally, S. Zhou, P. I. Djurovich, M. E. Thompson, B. C. Melot, Chem. Commun. 2014, 50, 15819.

[30] E. Mosconi, J. M. Azpiroz, F. De Angelis, Chem. Mater. 2015, 27, 4885.

[31] D. Bryant, N. Aristidou, S. Pont, I. Sanchez-Molina, T. Chotchuna ngatchaval, S. Wheeler, J. R. Durrant, S. A. Haque, Energy Environ. Sci. 2016, 9, 1655.

[32] B. Conings, J. Drijkoningen, N. Gauquelin, A. Babayigit, J. D'Haen, L. D'Olieslaeger, A. Ethirajan, J. Verbeeck, J. Manca, E. Mosconi, F. D. Angelis, H.-G. Boyen, Adv. Energy Mater. 2015, 5, 1500477.

[33] E. J. Juarez-Perez, Z. Hawash, S. R. Raga, L. K. Ono, Y. Qi, Energy Environ. Sci. 2016, 9, 3406.

[34] Z. Wang, Z. Shi, T. Li, Y. Chen, W. Huang, Angew. Chem., Int. Ed. 2017, 56, 1190.

[35] Z. Shi, J. Guo, Y. Chen, Q. Li, Y. Pan, H. Zhang, Y. Xia, W. Huang, Adv. Mater. 2017, 29, 1605005.

[36] J.-P. Correa-Baena, A. Abate, M. Saliba, W. Tress, T. J. Jacobsson, M. Grätzel, A. Hagfeldt, Energy Environ. Sci. 2017, 10, 710.

[37] V. M. Goldschmidt, Naturwissenschaften 1926, 14, 477.

[38] G. Kieslich, S. Sun, A. Cheetham, Chem. Sci. 2014, 5, 4712.

[39] G. Kieslich, S. Sun, A. Cheetham, Chem. Sci. 2015, 6, 3430.

[40] W. Travis, E. Glover, H. Bronstein, D. Scanlon, R. Palgrave, Chem. Sci. 2016, 7, 4548.

[41] O. Malinkiewicz, A. Yella, Y. H. Lee, G. M. Espallargas, M. Grätzel, M. K. Nazeeruddin, H. J. Bolink, Nat. Photonics 2014, 8, 128.

[42] J. S. Manser, M. I. Saidaminov, J. A. Christians, O. M. Bakr, P. V. Kamat, Acc. Chem. Res. 2016, 49, 330.

[43] N. J. Jeon, J. H. Noh, Y. C. Kim, W. S. Yang, S. Ryu, S. Il Seok, Nat. Mater. 2014, 13, 897.

[44] Y. Zhao, K. Zhu, J. Phys. Chem. Lett. 2014, 5, 4175.

[45] J.-P. Correa-Baena, M. Anaya, G. Lozano, W. Tress, K. Domanski, M. Saliba, T. Matsui, T. J. Jacobsson, M. E. Calvo, A. Abate, M. Grätzel, H. Míguez, A. Hagfeldt, Adv. Mater. 2016, 28, 5031.

[46] J. M. Ball, S. D. Stranks, M. T. Horantner, S. Huttner, W. Zhang, E. J. W. Crossland, I. Ramirez, M. Riede, M. B. Johnston, R. H. Friend, H. J. Snaith, Energy Environ. Sci. 2015, 8, 602.

[47] D. Bi, W. Tress, M. I. Dar, P. Gao, J. Luo, C. Renevier, K. Schenk, A. Abate, F. Giordano, J.-P. Correa Baena, J.-D. Decoppet, S. M. Zakeeruddin, M. K. Nazeeruddin, M. Grätzel, A. Hagfeldt, Sci. Adv. 2016, 2, e1501170.

[48] T. J. Jacobsson, J.-P. Correa-Baena, E. Halvani Anaraki, B. Philippe, S. D. Stranks, M. E. F. Bouduban, W. Tress, K. Schenk, J. Teuscher, J.-E. Moser, H. Rensmo, A. Hagfeldt, J. Am. Chem. Soc. 2016, 138, 10331.

[49] N. Marinova, W. Tress, R. Humphry-Baker, M. I. Dar, V. Bojinov, S. M. Zakeeruddin, M. K. Nazeeruddin, M. Grätzel, ACS Nano 2015, 9, 4200.

[50] E. L. Unger, E. T. Hoke, C. D. Bailie, W. H. Nguyen, A. R. Bowring, T. Heumuller, M. G. Christoforo, M. D. McGehee, Energy Environ. Sci. 2014, 7, 3690.

[51] H.-S. Kim, N.-G. Park, J. Phys. Chem. Lett. 2014, 5, 2927.

[52] W. Tress, N. Marinova, T. Moehl, S. M. Zakeeruddin, M. K. Nazeeruddin, M. Gratzel, Energy Environ. Sci. 2015, 8, 995.

[53] S. Yang, Y. C. Zheng, Y. Hou, X. Chen, Y. Chen, Y. Wang, H. J. Zhao, H. G. Yang, Chem. Mater. 2014, 26, 6705.

[54] S. Meloni, T. Moehl, W. Tress, M. Franckevicius, M. Saliba, Y. H. Lee, P. Gao, M. K. Nazeeruddin, S. M. Zakeeruddin, U. Rothlisberger, M. Grätzel, Nat. Commun. 2016, 7, 10334.

[55] T.-Y. Yang, G. Gregori, N. Pellet, M. Grätzel, J. Maier, Angew. Chem., Int. Ed. 2015, 54, 7905.

[56] J. P. Correa Baena, L. Steier, W. Tress, M. Saliba, S. Neutzner, T. Matsui, F. Giordano, T. J. Jacobsson, A. R. Srimath Kandada, S. M. Zakeeruddin, A. Petrozza, A. Abate, M. K. Nazeeruddin, M. Grätzel, A. Hagfeldt, Energy Environ. Sci. 2015, 8, 2928.

[57] Z. Wang, Z. Shi, T. Li, Y. Chen, W. HuangAngew. Chem., Int. Ed. 2016, 55, 2.

[58] K. Domanski, J.-P. Correa-Baena, N. Mine, M. K. Nazeeruddin, A. Abate, M. Saliba, W. Tress, A. Hagfeldt, M. Grätzel, ACS Nano 2016, 10, 6306.

[59] F. Bella, G. Griffini, J.-P. Correa-Baena, G. Saracco, M. Grätzel, A. Hagfeldt, S. Turri, C. Gerbaldi, Science 2016, 354, 203.

[60] X. Li, M. Tschumi, H. Han, S. S. Babkair, R. A. Alzubaydi, A. A. Ansari, S. S. Habib, M. K. Nazeeruddin, S. M. Zakeeruddin, M. Grätzel, Energy Technol. 2015, 3, 551.

[61] A. Sadhanala, S. Ahmad, B. D. Zhao, N. Giesbrecht, P. M. Pearce, F. Deschler, R. L. Z. Hoye, K. C. Godel, T. Bein, P. Docampo, S. E. Dutton, M. F. L. De Volderand, R. H. Friend, Nano Lett. 2015, 15, 6095.

[62] Y. C. Liu, Z. Yang, D. Cui, X. D. Ren, J. K. Sun, X. J. Liu, J. R. Zhang, Q. B. Wei, H. B. Fan, F. Y. Yu, X. Zhang, C. M. Zhao, S. Z. Liu, Adv. Mater. 2015, 27, 5176.

[63] T. J. Jacobsson, M. Pazoki, A. Hagfeldt, T. Edvinsson, J. Phys. Chem. C 2015, 119, 25673.

[64] P. P. Boix, S. Agarwala, T. M. Koh, N. Mathews, S. G. Mhaisalkar, J. Phys. Chem. Lett. 2015, 6, 898.

[65] F. Giustino, H. J. Snaith, ACS Energy Lett. 2016, 1, 1233.

[66] N. K. Noel, S. D. Stranks, A. Abate, C. Wehrenfennig, S. Guarnera, A. A. Haghighirad, A. Sadhanala, G. E. Eperon, S. K. Pathak, M. B. Johnston, A. Petrozza, L. M. Herz, H. J. Snaith, Energy Environ. Sci. 2014, 7, 3061.

[67] F. Hao, C. C. Stoumpos, D. H. Cao, R. P. H. Chang, M. G. Kanatzidis, Nat. Photonics 2014, 8, 489.

[68] W. S. Yang, J. H. Noh, N. J. Jeon, Y. C. Kim, S. Ryu, J. Seo, S. I. Seok, Science 2015, 348, 1234.

[69] J. W. Lee, D. J. Seol, A. N. Cho, N. G. Park, Adv. Mater. 2014, 26, 4991.

[70] C. Yi, J. Luo, S. Meloni, A. Boziki, N. Ashari-Astani, C. Gratzel, S. M. Zakeeruddin, U. Rothlisberger, M. Gratzel, Energy Environ. Sci. 2016, 9, 656.

[71] J.-W. Lee, D.-H. Kim, H.-S. Kim, S.-W. Seo, S. M. Cho, N.-G. Park, Adv. Energy Mater. 2015, 5, 1501310.

[72] T. J. Jacobsson, J.-P. Correa-Baena, M. Pazoki, M. Saliba, K. Schenk, M. Grätzel, A. Hagfeldt, Energy Environ. Sci. 2016, 9, 1706.

[73] R. D. Shannon, Acta Crystallogr., A 1973, 32, 751.

[74] T. Krishnamoorthy, H. Ding, C. Yan, W. L. Leong, T. Baikie, Z. Zhang, M. Sherburne, S. Li, M. Asta, N. Mathews, S. G. Mhaisalkar, J. Mater. Chem. A 2015, 3, 23829.

[75] C. Huang, X. C. Yan, G. Cui, Z. Liu, S. Pang, H. Xu, CN Patent App. CN 201, 410, 173, 750, 2014.

[76] C. C. Stoumpos, L. Frazer, D. J. Clark, Y. S. Kim, S. H. Rhim, A. J. Freeman, J. B. Ketterson, J. I. Jang, M. G. Kanatzidis, J. Am. Chem. Soc. 2015, 137, 6804.

[77] P.-P. Sun, Q.-S. Li, L.-N. Yang, Z.-S. Li, Nanoscale 2016, 8, 1503.

[78] X. Lu, Z. Zhao, K. Li, Z. Han, S. Wei, C. Guo, S. Zhou, Z. Wu, W. Guo, C.-m. L. Wu, RSC Adv. 2016, 6, 86976.

[79] M. Saliba, T. Matsui, K. Domanski, J.-Y. Seo, A. Ummadisingu, S. M. Zakeeruddin, J.-P. Correa-Baena, W. R. Tress, A. Abate, A. Hagfeldt, M. Grätzel. Science 2016, 354, 206.

[80] T. Duong, H. K. Mulmudi, H. Shen, Y. Wu, C. Barugkin, Y. O. Mayon, H. T. Nguyen, D. Macdonald, J. Peng, M. Lockrey, W. Li, Y.-B. Cheng, T. P. White, K. Weber, K. Catchpole, Nano Energy 2016, 30, 330.

[81] Y. H. Park, I. Jeong, S. Bae, H. J. Son, P. Lee, J. Lee, C.-H. Lee, M. J. Ko, Adv. Funct. Mater. 2017, 27, 1605988.

[82] M. Zhang, J. S. Yun, Q. Ma, J. Zheng, C. F. J. Lau, X. Deng, J. Kim, D. Kim, J. Seidel, M. A. Green, S. Huang, A. W. Y. Ho-Baillie, ACS Energy Lett. 2017, 2, 438.

[83] S. Gholipour, A. M. Ali, J.-P. Correa-Baena, S.-H. Turren-Cruz, F. Tajabadi, W. Tress, N. Taghavinia, M. Grätzel, A. Abate, F. De Angelis, C. Alberto Gaggioli, E. Mosconi, A. Hagfeldt, M. Saliba, Adv. Mater. 2017, 29, 1702005.

[84] A. D. Jodlowski, A. Yépez, R. Luque, L. Camacho, G. de Miguel, Angew. Chem., Int. Ed. 2016, 55, 14972.

[85] A. D. Jodlowski, C. Roldán-Carmona, G. Grancini, M. Salado, M. Ralaiarisoa, S. Ahmad, N. Koch, L. Camacho, G. de Miguel, M. K. Nazeeruddin, Nat. Energy 2017, 2, 972.

[86] X. Li, M. I. Dar, C. Yi, J. Luo, M. Tschumi, S. M. Zakeeruddin, M. K. Nazeeruddin, H. Han, M. Grätzel, Nat. Chem. 2015, 7, 703.

[87] A. M. Ganose, C. N. Savory, D. O. Scanlon, J. Mater. Chem. A 2017, 5, 7845.

[88] Y.-Y. Sun, J. Shi, J. Lian, W. Gao, M. L. Agiorgousis, P. Zhang, S. Zhang, Nanoscale 2016, 8, 6284.

[89] F. Hong, B. Saparov, W. Meng, Z. Xiao, D. B. Mitzi, Y. Yan, J. Phys. Chem. C 2016, 120, 6435.

[90] Y.-Y. Sun, M. L. Agiorgousis, P. Zhang, S. Zhang, Nano Lett. 2015, 15, 581.

[91] S. Perera, H. Hui, C. Zhao, H. Xue, F. Sun, C. Deng, N. Gross, C. Milleville, X. Xu, D. F. Watson, B. Weinstein, Y.-Y. Sun, S. Zhang, H. Zeng, Nano Energy 2016, 22, 129.

[92] M.-G. Ju, J. Dai, L. Ma, X. Cheng Zeng, Adv. Energy Mater. 2017, 7, 1700216.

[93] W. Meng, B. Saparov, F. Hong, J. Wang, D. B. Mitzi, Y. Yan, Chem. Mater. 2016, 28, 821.

[94] S. Niu, H. Huyan, Y. Liu, M. Yeung, K. Ye, L. Blankemeier, T. Orvis, D. Sarkar, D. J. Singh, R. Kapadia, J. Ravichandran, Adv. Mater. 2017, 29, 1604733.

[95] G. Meyer, Prog. Solid State Chem. 1982, 14, 141.

[96] A. H. Slavney, R. W. Smaha, I. C. Smith, A. Jaffe, D. Umeyama, H. I. Karunadasa, Inorg. Chem. 2017, 56, 46.

[97] E. Greul, M. L. Petrus, A. Binek, P. Docampo, T. Bein, J. Mater. Chem. A 2017, 5, 19972.

[98] C. N. Savory, A. Walsh, D. O. Scanlon, ACS Energy Lett. 2016, 1, 949.

[99] S. F. Hoefler, G. Trimmel, T. Rath, Monatsh. Chem. 2017, 148, 795.

[100] A. H. Slavney, T. Hu, A. M. Lindenberg, H. I. Karunadasa, J. Am. Chem. Soc. 2016, 138, 2138.

[101] E. T. McClure, M. R. Ball, W. Windl, P. M. Woodward, Chem. Mater. 2016, 28, 1348.

[102] M. R. Filip, S. Hillman, A.-A. Haghighirad, H. J. Snaith, F. Giustino, J. Phys. Chem. Lett. 2016, 7, 2579.

[103] A. H. Slavney, L. Leppert, D. Bartesaghi, A. Gold-Parker, M. F. Toney, T. J. Savenije, J. B. Neaton, H. I. Karunadasa, J. Am. Chem. Soc. 2017, 139, 5015.

[104] F. Wei, Z. Deng, S. Sun, F. Xie, G. Kieslich, D. M. Evans, M. A. Carpenter, P. D. Bristowe, A. K. Cheetham, Mater. Horiz. 2016, 3, 328.

[105] Z. Deng, F. Wei, S. Sun, G. Kieslich, A. K. Cheetham, P. D. Bristowe, J. Mater. Chem. A 2016, 4, 12025.

[106] F. Wei, Z. Deng, S. Sun, F. Zhang, D. M. Evans, G. Kieslich, S. Tominaka, M. A. Carpenter, J. Zhang, P. D. Bristowe, A. K. Cheetham, Chem. Mater. 2017, 29, 1089.

[107] G. Volonakis, A. A. Haghighirad, R. L. Milot, W. H. Sio, M. R. Filip, B. Wenger, M. B. Johnston, L. M. Herz, H. J. Snaith, F. Giustino, J. Phys. Chem. Lett. 2017, 8, 772.

[108] T. T. Tran, J. R. Panella, J. R. Chamorro, J. R. Morey, T. M. McQueen, Mater. Horiz. 2017, 4, 688.

[109] K.-Z. Du, W. Meng, X. Wang, Y. Yan, D. B. Mitzi, Angew. Chem., Int. Ed. 2017, 56, 8158.

[110] G. Volonakis, M. R. Filip, A. A. Haghighirad, N. Sakai, B. Wenger, H. J. Snaith, F. Giustino, J. Phys. Chem. Lett. 2016, 7, 1254.

[111] X.-G. Zhao, J. Yang, Y. Fu, D. Yang, Q. Xu, L. Yu, S.-H. Wei, L. Zhang, J. Am. Chem. Soc. 2017, 139, 2630.

[112] Z. Xiao, W. Meng, J. Wang, Y. Yan, ChemSusChem 2016, 9, 1.

[113] Z. Xiao, W. Meng, J. Wang, D. B. Mitzi, Y. Yan, Mater. Horiz. 2017, 4, 206.

[114] X.-G. Zhao, D. Yang, Y. Sun, T. Li, L. Zhang, L. Yu, A. Zunger, J. Am. Chem. Soc. 2017, 139, 6718.

[115] G. Volonakis, A. A. Haghighirad, H. J. Snaith, F. Giustino, J. Phys. Chem. Lett. 2017, 8, 3917.

[116] A. E. Maughan, A. M. Ganose, M. M. Bordelon, E. M. Miller, D. O. Scanlon, J. R. Neilson, J. Am. Chem. Soc. 2016, 138, 8453.

[117] S. Abrahams, J. Ihringer, P. Marsh, Acta Crystallogr., Sect. B: Struct. Sci. 1989, 45, 26.

[118] X. Qiu, B. Cao, S. Yuan, X. Chen, Z. Qiu, Y. Jiang, Q. Ye, H. Wang, H. Zeng, J. Liu, M. G. Kanatzidis, Sol. Energy Mater. Sol. Cells 2017, 159, 227.

[119] K. Shum, Z. Chen, J. Qureshi, C. L. Yu, J. J. Wang, W. Fenninger, P. N. Vockic, J. Midgley, J. T. Kennedy, Appl. Phys. Lett. 2010, 9, 221903.

[120] B. Lee, C. C. Stoumpos, N. Zhou, F. Hao, C. Malliakas, C.-Y. Yeh, T. J. Marks, M. G. Kanatzidis, R. P. Chang, J. Am. Chem. Soc. 2014, 136, 15379.

[121] B. Saparov, J.-P. Sun, W. Meng, Z. Xiao, H.-S. Duan, O. Gunawan, D. Shin, I. G. Hill, Y. Yan, D. B. Mitzi, Chem. Mater. 2016, 28, 2315.

[122] Z. Xiao, Y. Zhou, H. Hosono, T. Kamiya, Phys. Chem. Chem. Phys. 2015, 17, 18900.

[123] N. Sakai, A. A. Haghighirad, M. R. Filip, P. K. Nayak, S. Nayak, A. Ramadan, Z. Wang, F. Giustino, H. J. Snaith, J. Am. Chem. Soc. 2017, 139, 6030.

[124] K. Eckhardt, V. Bon, J. Getzschmann, J. Grothe, F. M. Wisser, S. Kaskel, Chem. Commun. 2016, 52, 3058.

[125] M. Abulikemu, S. Ould-Chikh, X. Miao, E. Alarousu, M. Banavoth, G. O. N. Ndjawa, J. Barbe, A. El Labban, A. Amassian, S. Del Gobbo, J. Mater. Chem. A 2016, 4, 12504.

[126] Y. N. Ivanov, A. A. Sukhovskii, V. V. Lisin, I. P. Aleksandrova, Inorg. Mater. 2001, 37, 623.

[127] B.-W. Park, B. Philippe, X. Zhang, H. Rensmo, G. Boschloo, E. M. J. Johansson, Adv. Mater. 2015, 27, 6806.

[128] X. Zhang, G. Wu, Z. Gu, B. Guo, W. Liu, S. Yang, T. Ye, C. Chen, W. Tu, H. Chen, Nano Res. 2016, 9, 2921.

[129] J.-C. Hebig, I. Kühn, J. Flohre, T. Kirchartz, ACS Energy Lett. 2016, 1, 309.

[130] S. Öz, J.-C. Hebig, E. Jung, T. Singh, A. Lepcha, S. Olthof, J. Flohre, Y. Gao, R. German, P. H. M. van Loosdrecht, K. Meerholz, T. Kirchartz, S. Mathur, Solar Energy Mater. Solar Cells 2016, 158, 195.

[131] M. Lyu, J.-H. Yun, M. Cai, Y. Jiao, P. V. Bernhardt, M. Zhang, Q. Wang, A. Du, H. Wang, G. Liu, L. Wang, Nano Res. 2016, 9, 692.

[132] B. Chabot, E. Parthe, Acta Crystallogr., Sect. B: Struct. Crystallogr. Cryst. Chem. 1978, 34, 645.

[133] M. Vigneshwaran, T. Ohta, S. Iikubo, G. Kapil, T. S. Ripolles, Y. Ogomi, T. Ma, S. S. Pandey, Q. Shen, T. Toyoda, K. Yoshino, T. Minemoto, S. Hayase, Chem. Mater. 2016, 28, 6436.

[134] K.-H. Hong, J. Kim, L. Debbichi, H. Kim, S. H. Im, J. Phys. Chem. C 2017, 121, 969.

[135] K. Yamada, H. Sera, S. Sawada, H. Tada, T. Okuda, H. Tanaka, J. Solid State Chem. 1997, 134, 319.

[136] P. C. Harikesh, H. K. Mulmudi, B. Ghosh, T. W. Goh, Y. T. Teng, K. Thirumal, M. Lockrey, K. Weber, T. M. Koh, S. Li, S. Mhaisalkar, N. Mathews, Chem. Mater. 2016, 28, 7496.

[137] B. Saparov, F. Hong, J.-P. Sun, H.-S. Duan, W. Meng, S. Cameron, I. G. Hill, Y. Yan, D. B. Mitzi, Chem. Mater. 2015, 27, 5622.

[138] M. B. Johansson, H. Zhu, E. M. J. Johansson, J. Phys. Chem. Lett. 2016, 7, 3467.

[139] A. J. Lehner, D. H. Fabini, H. A. Evans, C.-A. Hébert, S. R. Smock, J. Hu, H. Wang, J. W. Zwanziger, M. L. Chabinyc, R. Seshadri, Chem. Mater. 2015, 27, 7137.

[140] J. Calabrese, N. L. Jones, R. L. Harlow, N. Herron, D. L. Thorn, Y. Wang, J. Am. Chem. Soc. 1991, 113, 2328.

[141] S. N. Ruddlesden, P. Popper, Acta Crystallogr. 1957, 10, 538.

[142] T. Kataoka, T. Kondo, R. Ito, S. Sasaki, K. Uchida, N. Miura, Phys. Rev. B 1993, 47, 2010.

[143] E. A. Muljarov, S. G. Tikhodeev, N. A. Gippius, T. Ishihara, Phys. Rev. B 1995, 51, 14370.

[144] M. Shimizu, J. I. Fujisawa, J. Ishi-Hayase, Phys. Rev. B 2005, 71, 205306.

[145] K. Tanaka, T. Takahashi, T. Kondo, T. Umebayashi, K. Asai, K. Ema, Phys. Rev. B 2005, 71, 045312.

[146] I. C. Smith, E. T. Hoke, D. Solis-Ibarra, M. D. McGehee, H. I. Karunadasa, Angew. Chem., Int. Ed. 2014, 53, 11232.

[147] T. M. Koh, V. Shanmugam, J. Schlipf, L. Oesinghaus, P. Müller-Buschbaum, N. Ramakrishnan, V. Swamy, N. Mathews, P. P. Boix, S. G. Mhasalkar, Adv. Mater. 2016, 28, 3653.

[148] D. H. Cao, C. C. Stoumpos, O. K. Farha, J. T. Hupp, M. G. Kanatzidis. J. Am. Chem. Soc. 2015, 137, 7843.

[149] K. Yao, X. Wang, Y. Xu, F. Li, L. Zhou, Chem. Mater. 2016, 28, 3131.

[150] Y. Chen, Y. Sun, J. Peng, W. Zhang, X. Su, K. Zheng, T. Pullerits, Z. Liang, Adv. Energy Mater. 2017, 7, 1700162.

[151] J. Rodríguez-Romero, B. Clasen Hames, I. Mora-Seró, E. M. Barea, ACS Energy Lett. 2017, 2, 1969.

[152] B. Cohen, M. Wierzbowska, L. Etgar, Adv. Funct. Mater. 2017, 27, 1604733.

[153] N. Li, Z. Zhu, C. Cheh, H. Liu, B. Peng, A. Petrone, X. Li, L. Wang, A. K.-Y. Jen, Adv. Energy. Mater. 2017, 7, 1601307.

[154] H. Tsai, W. Nie, J. Blancon, C. C. Stoumpos, R. Asadpour, B. Harutyunyan, A. J. Neukirch, R. Verduzco, J. J. Crochet, S. Tretiak, L. Pedesseau, J. Even, M. A. Alam, G. Gupta, J. Lou, P. M. Ajayan, M. J. Bedzyk, M. G. Kanatzidis, A. D. Mohite, Nature 2016, 536, 312.

[155] X. Zhang, G. Wu, S. Yang, W. Fu, Z. Zhang, C. Chen, W. Liu, J. Yan, W. Yang, H. Chen, Small 2017, 13, 1700611.

[156] X. Zhang, X. Ren, B. Liu, R. Munir, X. Zhu, D. Yang, J. Li, Y. Liu, D.-M. Smilgies, R. Li, Z. Yang, T. Niu, X. Wang, A. Amassian, K. Zhao, S. Liu, Energy Environ. Sci. 2017, 10, 2095.

[157] B. Saparov, D. B. Mitzi, Chem. Rev. 2016, 116, 4558.

[158] D. B. Mitzi, C. D. Dimitrakopoulos, L. L. Kosbar, Chem. Mater. 2001, 13, 3728.

[159] M. Yuan, L. N. Quan, R. Comin, G. Walters, R. Sabatini, O. Voznyy, Z. Lu, Nat. Nanotechnol. 2016, 11, 872.

[160] D. Cortecchia, H. A. Dewi, J. Yin, A. Bruno, S. Chen, T. Baikie, N. Mathews, Inorg. Chem. 2016, 55, 1044.

[161] L. Mao, H. Tsai, W. Nie, L. Ma, J. Im, C. C. Stoumpos, M. G. Kanatzidis, Chem. Mater. 2016, 28, 7781.

[162] C. Lermer, S. T. Birkhold, I. L. Moudrakovski, P. Mayer, L. M. Schoop, L. Schmidt-Mende, B. V. Lotsch, Chem. Mater. 2016, 28, 6560.

[163] C. C. Stoumpos, L. Mao, C. D. Malliakas, M. G. Kanatzidis, Inorg. Chem. 2016, 56, 56.

[164] S. Yang, W. Niu, A.-L. Wang, Z. Fan, B. Chen, C. Tan, Q. Lu, H. Zhang, Angew. Chem., Int. Ed. 2017, 56, 4252.

[165] T. J. Huang, Z. X. Thiang, X. Yin, C. Tang, G. Qi, H. Gong, Chem. Eur. J. 2016, 22, 2146.

[166] Z. Xiao, W. Meng, B. Saparov, H.-S. Duan, C. Wang, C. Feng, W. Liao, D. Zhao, J. Wang, D. B. Mitzi, J. Phys. Chem. Lett. 2016, 7, 1213.

[167] R. Willett, H. Place, M. Middleton, J. Am. Chem. Soc. 1988, 110, 8639.

[168] A. O. Polyakov, A. H. Arkenbout, J. Baas, G. R. Blake, A. Meetsma, A. Caretta, T. T. Palstra, Chem. Mater. 2011, 24, 133.

[169] G. Staulo, C. Bellitto, J. Mater. Chem. 1991, 1, 915.

[170] W. D. Van Amstel, L. J. De Jongh, Solid State Commun. 1972, 11, 1423.

[171] J. Han, S. Nishihara, K. Inoue, M. Kurmoo, Inorg. Chem. 2015, 54, 2866.

[172] T. Nakajima, H. Yamauchi, T. Goto, M. Yoshizawa, T. Suzuki, T. Fujimura, J. Magn. Magn. Mater. 1983, 31, 1189.

[173] C. F. Ferreira, E. E. Pérez-Cordero, K. A. Abboud, D. R. Talham, Chem. Mater. 2016, 28, 5522

Conclusiones

Conclusions

Conclusiones

Al final de cada artículo en el *capítulo III,* se encuentra su correspondiente conclusión. En este apartado se presentan las conclusiones generales de toda la investigación realizada durante el periodo de investigación.

1. La mecanosíntesis, ha demostrado ser una técnica extremadamente útil en la síntesis de nuevos materiales basados en estructura de perovskita. Además, demostró ser un método simple, reproducible y eficiente, con la ventaja de poder sintetizar gran cantidad de muestra por síntesis.
2. La técnica de difracción de rayos X ha sido fundamental en todos los estudios realizados. Esta técnica ha permitido determinar la estructura de la perovskita basada en Guanidinio ($GuaPbI_3$) por primera vez. Además, de demostrar la inserción del catión Guanidinio en la estructura 3D de la perovskita mixta $Ma_{1-x}Gua_xPbI_3$.
3. El uso de mezcla de cationes ha resultado ser un planteamiento muy útil para insertar un catión que supera el factor de tolerancia de Goldschmidt, y de esta manera abre un campo a una gran de variedad de cationes que podrían formar perovskitas 3D.
4. Se demostró que al aumentar el uso de puentes de hidrogeno intercambiando el Metilamonio por el Guanidinio la estabilidad del material de perovskita se incrementa.
5. Se ha visto en el recopilatorio bibliográfico que existen un gran número de alternativas a las perovskitas tradicionales debido a la gran flexibilidad estructural y los diferentes tipos de átomos que se pueden emplear.

Conclusions

At the end of each article there is a corresponding conclusion (*Chapter III*). In this section general conclusions of the research are presented.

1. It has been proven that mechanosynthesis is an extremely useful technique in the synthesis of new materials based on perovskite structure. In addition, it is a simple, reproducible and efficient method with the advantage of being able to synthesize a large amount of sample by synthesis.
2. The technique of X-ray diffraction has been fundamental in all the studies carried out. This technique has allowed to determine the structure of the Guanidinium-based perovskite ($GuaPbI_3$) for the first time. In addition, to demonstrate the insertion of the Guanidinio cation in the 3D structure of the mixed perovskite $Ma_{1-x}Gua_xPbI_3$.
3. The use of mixture of cations has proved to be a very useful approach to insert a big cation that exceeds the tolerance factor of Goldschmidt, and thus opens a field to a large variety of cations that could form 3D perovskites.
4. It was demonstrated that by increasing the use of hydrogen bridges by exchanging Methylammonium for Guanidinium the stability of the perovskite material is increased.
5. It has been seen in the bibliographic compilation that there are a large number of alternatives to traditional perovskites due to the great structural flexibility and the different types of atoms that can be used

Apéndices

Appendices

- **Publicaciones derivadas directamente de la Tesis**

– "*Benign-by-Design Solventless Mechanochemical Synthesis of Three-, Two-, and One-Dimensional Hybrid Perovskites"* by Alexander D. Jodlowski, Alfonso Yépez, Rafael Luque, Luis Camacho, and Gustavo de Miguel. *Angew. Chem. Int. Ed.* **2016**, *55*, 14972-14977.

JCR Impact Factor

Impact factor (2016): 11.994

Category: Chemistry, Multidiciplinary.

Decile (2016): 1 **Rank (2016):** 14/171

– "*Large guanidinium cation mixed with methylammonium in lead iodide perovskites for 19% efficient solar cells*" by Alexander D Jodlowski, Cristina Roldán-Carmona, Giulia Grancini, Manuel Salado, Maryline Ralaiarisoa, Shahzada Ahmad, Norbert Koch, Luis Camacho, Gustavo De Miguel and Mohammad Khaja Nazeeruddin, *Nature Energy*, **2017**, *2*, 972–979.

JCR Impact Factor

Impact factor (2017): 46.880

Category: Materials Science, Multidisciplinary

Decile (2017): 1 **Rank (2017):** 2/285

– "*Alternative Perovskites for Photovoltaics*" by AlexanderD Jodlowski, Daily Rodríguez-Padrón, Rafael Luque, Gustavo de Miguel. Adv. Energy Mater. **2018,** 8, 21, 1703120

JCR Impact Factor

Impact factor (2017): 21.875

Category: Chemistry, Physical

Decile (2017): 1 **Rank (2017):** 3/146

– "*Surface passivation of perovskite layers using heterocyclic halides: Improved photovoltaic properties and intrinsic stability*" by Manuel Salado, Alexander D. Jodlowski, Cristina Roldan-Carmona, Gustavo de Miguel, Samrana Kazima, Mohammad Khaja Nazeeruddind and Shahzada Ahmada, *Nano Energy,* **2018**, *50*, 220-228.

JCR Impact Factor

Impact factor (2017): 13.120

Category: Chemistry, Physical

Decile (2017): 1 **Rank (2017):** 9/146

- **Publicaciones no derivadas directamente de la Tesis**

– "*Synthesis of carbon-based fluorescent polymers driven by catalytically active magnetic bioconjugates*" by Daily Rodríguez-Padrón, Alexander D. Jodlowski, Gustavo de Miguel, Alain R. Puente-Santiago, Alina M. Balu, Rafael Luque, Green Chem. **2018**, *20*, 225-229.

JCR Impact Factor

Impact factor (2017): 8.586

Category: Chemistry, Multidisciplinary

Quartile (2017): 1 **Rank (2017):** 21/171

– "*Tenfold increase in efficiency from a reference blue OLED*" by Gonzalo García-Espejo Alexander D. Jodlowski, Alejandra Soriano-Portillo, Gustavo de Miguel, Eulogia Muñoz and Marta Pérez-Morales, Journal of Luminescence, **2018**, *199*, 13-18.

JCR Impact Factor

Impact factor (2017): 2.732

Category: Optics

Quartile (2017): 2 **Rank (2017):** 25/94

- **Patentes**

– "*Optoelectronic device comprising guanidinium in the organic – inorganic perovskite*" Patent No. 17202646.4 – 1212.

- **Premios derivados de la Tesis**

– XVI Premio de Investigación "*Jacobo Cárdenas Torres*" por el trabajo titulado "*Bening-by-Design Solventless Mechanochemical Synthesis of three-, two-, and One-Dimensional Hybrid Perovskites*".

– Nature Energy Poster Prize, en el congreso Stability of Emerging Photovoltaics Conference – from Fundamentals to Application por su poster titulado "*Guanidinium/Methylammonium Lead Iodide Perovskite: An Unexplored Avenue for Stable and 20% Efficient Solar Cells*".

- **Becas y ayudas competitivas**

– Beca de movilidad internacional "*Doctorado Internacional Hacia la Excelencia*" curso 2015/2016, segundo llamamiento.

– Short Term Scientific Mission, COST Action MP1307.

- **Menciones en revistas divulgativas**

– PV Magazine, "*EPFL-led research group seeks to stabilize perovskite solar cells with guanidinium*", **2017**.

– Scitech Daily, "*Guanidinium Helps Stabilizes Perovskite Solar Cells*", **2017**.

– Chem Europe, "*Guanidinium stabilizes perovskite solar cells at 19 percent efficiency*", **2017**.

– Fars News Agency, "*Guanidinium Stabilizes Perovskite Solar Cells at 19 Percent Efficiency*",

– Research & Development, "*Gaunidinium Stabilizes Perovskite Solar Cells at 19 Percent Efficiency*", **2017**.

– Product Design and Development, "*Guanidinium Stabilizes Perovskite Solar Cells at 19 Percent Efficiency*", **2017**.

– AZO Materials, "*Efficiency of Perovskite Solar Cells Stabilized Using Guanidinium*", **2017**.

– Solar Daily, "*Guanidinium stabilizes perovskite solar cells at 19 percent efficiency*", **2017**.

– Boletín TR•UCO. N. 28, **2018**.

La participación en actividades como congresos, summer schools etc. relacionados sobre la línea de investigación, en la que se encuadra la presente Tesis, ha sido una de las acciones objeto del Programa de Formación del doctorando en la realización de su tesis doctoral. De esta forma, se han presentado las siguientes comunicaciones:

– The XXth International Krutyń Summer School 2016, "*Advanced Perovskite, Hybrid and Thin-film Photovoltaics*", June **2016**.

– "*Benign-by-design solventless mechanochemical synthesis of 3-, 2- and 1-dimensional hybrid perovskites*", in 6th EuCheMS Chemistry Congress, Seville (Spain), September **2016**.

– "*Benign-by-design solventless mechanochemical synthesis of Three-, Two- and One-dimensional hybrid perovskites*", in 3rd International Conferences on Perovskite Solar Cells and Optoelectronics, Oxford (United Kingdom), September **2017**.

– Industry Day Printed Electronics and Solar cells, Lisboa, (Portugal), Abril **2017**

– "*Large guanidinium cation mixed with methylammonium in lead iodide perovskites for 19% efficient solar cells*", in VI Congreso Científico de Investigadores en Formación de la Universidad de Córdoba, Córdoba (Spain), January **2018**.

– IV reunión de Jóvenes Investigadores en Coloides e Interfases, Córdoba (Spain), February, **2018**.

– IV Reunión de Jóvenes Investigadores en Coloides e Interfases, Córdoba (España), Febrero **2018**.

– "*Guanidinium/Methylammonium Lead Iodide Perovskite: An Unexplored Avenue for Stable and 20% Efficient Solar Cells*" in *Stability of Emerging Photovoltaics from Fundamental to Applications, Barcelona (*Spain*)*, February **2018**